

INFORMATION TO USERS

This manuscript has been reproduced from the microfilm master. UMI films the text directly from the original or copy submitted. Thus, some thesis and dissertation copies are in typewriter face, while others may be from any type of computer printer.

The quality of this reproduction is dependent upon the quality of the copy submitted. Broken or indistinct print, colored or poor quality illustrations and photographs, print bleedthrough, substandard margins, and improper alignment can adversely affect reproduction.

In the unlikely event that the author did not send UMI a complete manuscript and there are missing pages, these will be noted. Also, if unauthorized copyright material had to be removed, a note will indicate the deletion.

Oversize materials (e.g., maps, drawings, charts) are reproduced by sectioning the original, beginning at the upper left-hand corner and continuing from left to right in equal sections with small overlaps. Each original is also photographed in one exposure and is included in reduced form at the back of the book.

Photographs included in the original manuscript have been reproduced xerographically in this copy. Higher quality 6" x 9" black and white photographic prints are available for any photographs or illustrations appearing in this copy for an additional charge. Contact UMI directly to order.

UMI

A Bell & Howell Information Company
300 North Zeeb Road, Ann Arbor MI 48106-1346 USA
313/761-4700 800/521-0600

Three-Dimensional P-Wave Velocity Structure in the Greater Mount Rainier Area from Local Earthquake Tomography

by

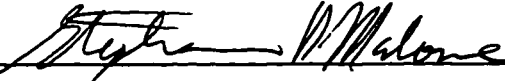
Seth Charles Moran

A dissertation submitted in partial fulfillment
of the requirements for the degree of

Doctor of Philosophy

University of Washington

1997

Approved by 
(Chairperson of Supervisory Committee)

Program Authorized
to Offer Degree Geophysics Program

Date 06/04/97

UMI Number: 9736336

UMI Microform 9736336
Copyright 1997, by UMI Company. All rights reserved.

**This microform edition is protected against unauthorized
copying under Title 17, United States Code.**

UMI
300 North Zeeb Road
Ann Arbor, MI 48103

Doctoral Dissertation

In presenting this dissertation in partial fulfillment of the requirements for the Doctoral degree at the University of Washington, I agree that the Library shall make its copies freely available for inspection. I further agree that extensive copying of this dissertation is allowable only for scholarly purposes, consistent with "fair use" as prescribed in the U.S. Copyright Law. Requests for copying or reproduction of this dissertation may be referred to University Microfilms, 1490 Eisenhower Place, P.O. Box 975, Ann Arbor, MI 48106, to whom the author has granted "the right to reproduce and sell (a) copies of the manuscript in microform and/or (b) printed copies of the manuscript made from microform."

Signature 

Date 6/4/97

University of Washington

Abstract

Three-Dimensional P-Wave Velocity Structure in the Greater Mount Rainier Area from Local Earthquake Tomography

by Seth Charles Moran

Chairperson of the Supervisory Committee: Professor Stephen D. Malone
Graduate Program in Geophysics

One of the most striking features of seismicity in western Washington is the clustering of crustal earthquakes into one of several zones of concentrated seismicity. In this dissertation I explore the hypothesis that geologic structures, in conjunction with regional tectonic forces, are primarily responsible for controlling the location of seismicity in parts of western Washington. The primary tool for testing this hypothesis is a 3-dimensional image of the P-wave velocity structure of the greater Mount Rainier area that I derive using local earthquake tomography. I use P-wave arrival times from local earthquakes occurring between 1980 and 1996 recorded at short-period vertical component stations operated by the Pacific Northwest Seismograph Network (PNSN) and 18 temporary sites operated during a field experiment in 1995 and 1996. The tomographic methodology I use is similar to that described by Lees and Crosson (1989, 1990). In addition, I use the parameter separation method to decouple the hypocenter and velocity problems, don't use station corrections, and use ray-bending for 3-D raytracing, allowing for a full non-linear inversion.

In the upper 4 km several low velocity features show good correlation with the Carbon River, Skate Creek, and Morton anticlines, as well as the Chehalis, Tacoma, and Seattle basins. There is also good correlation between high velocity features and surface exposures of several plutons. One seismic zone, the St. Helens Seismic Zone, correlates well with a planar low velocity feature. This correlation supports the idea that this seismic zone reflects a continuous structure

roughly 50 km in length. A second zone, the Western Rainier Seismic Zone (WRSZ), does not correlate in any simple way with anomaly patterns, suggesting that the WRSZ does not represent a distinct fault. A 10 km-wide low velocity anomaly occurs 8 to 18 km beneath Mount Rainier, which I interpret to be due to a thermal aureole associated with the magmatic system beneath Mount Rainier. Volcano-tectonic earthquakes locate above this feature, and are interpreted to be caused by forces related to hydrothermal circulation and/or the cooling of magmatic bodies at depth.

Table of Contents

List of Figures	iv
List of Tables	vii
I. Introduction	1
1.1 <i>Objectives</i>	1
1.2 <i>Study Area</i>	2
1.2.1 Coast Range	3
1.2.2 Puget Lowlands	4
1.2.3 Cascade Range	5
1.2.4 Columbia Plateau	13
1.2.5 Olympic-Wallowa Lineament	14
1.3 <i>Seismicity</i>	15
1.3.1 Intra-slab Earthquakes	15
1.3.2 Crustal Earthquakes	15
1.3.3 Volcano-Tectonic Earthquakes	19
1.4 <i>Previous Seismological Investigations in the GMR</i>	21
1.4.1 Active Source Studies	21
1.4.2 Passive Source Studies	23
II. Local Earthquake Tomography	24
2.1 <i>Introduction</i>	24
2.2 <i>Basic Theory</i>	25
2.2.1 Wavefronts and Raypaths	25
2.2.2 The Tomographic Problem - Basics	27
2.3 <i>Complications in the Tomographic Method</i>	34
2.3.1 Slowness-Hypocenter Coupling	34
2.3.2 Station Corrections	40
2.3.3 Projecting Points Into a Cartesian Coordinate System	41
2.4 <i>Non-linear inversion</i>	43
2.4.1 Ray-Tracing in 3-D	43
2.4.2 Jumping vs. Creeping	47

2.5 <i>Error Analysis</i>	48
2.5.1 Resolution	48
2.5.2 Variance	50
2.5.3 Trade-off Curve - Selecting λ	52
2.6 <i>LET Procedural Outline</i>	54
III. Data Selection and Collection	57
3.1 <i>Introduction</i>	57
3.2 <i>PNSN Catalog - Selection Criteria</i>	57
3.2.1 Non-earthquake sources	57
3.2.2 Earthquake sources	60
3.3 <i>Field Experiments</i>	62
3.3.1 Experiment #1 - Refraction Profile	62
3.3.2 Experiment #2 - The NEHRP project	66
3.4 <i>Inversion Dataset</i>	75
IV. Results and Interpretations	78
4.1 <i>Inversion</i>	78
4.1.1 One-Dimensional Model	78
4.1.2 Three-Dimensional Model	79
4.2 <i>Error Analysis</i>	80
4.2.1 Checkerboard and Jackknife	80
4.2.2 Blasts	81
4.2.3 Layer-by-Layer Interpretations	83
4.2.4 Comparison to the 1991 Refraction Model	87
4.3 <i>Interpretations of Deeper Anomalies</i>	89
4.3.1 A Buried Eruptive Center for the Crescent Formation	89
4.3.2 Low Velocity Anomaly Beneath Mount Rainier	90
4.3.3 The SWCC - Where is it?	99
4.3.4 Deep Low Velocity Anomalies Beneath the Cascade Crest ...	101
4.3.5 Olympic-Wallowa Lineament (OWL)	113

4.4 <i>Seismotectonic Interpretations</i>	115
4.4.1 <i>St. Helens Seismic Zone (SHZ)</i>	115
4.4.2 <i>Western Rainier Seismic Zone (WRSZ)</i>	118
4.4.3 <i>Other Seismogenic Zones Near Mount Rainier</i>	121
4.4.4 <i>Volcano-Tectonic Earthquakes Beneath Mount Rainier</i>	121
V. Comparison & Contrast	134
5.1 <i>Without Parameter Separation</i>	134
5.2 <i>With Station Corrections</i>	134
5.3 <i>Without New Stations</i>	136
5.4 <i>Comparison with Lees (1989)</i>	140
VI. Conclusions	144
6.1 <i>Summary of Results</i>	144
6.1.1 <i>Geology</i>	144
6.1.2 <i>Seismotectonics</i>	145
6.1.3 <i>Tomography</i>	146
6.2 <i>Future Work</i>	146
Bibliography	149
Appendix A - Rock Velocities	164
Appendix B - Temporary Station Locations	166
Appendix C - How to tie a Bowline	169
Pocket Material: 7 slices through 3-D model	

List of Figures

Figure 1-1: Map of all crustal (depths less than 35 km) earthquakes located within the GMR between 1980 and 1996.	1
Figure 1-2: Map of major physiographic provinces contained in the GMR.	3
Figure 1-3: Map of Bouguer gravity (top) and aeromagnetic (bottom) data in the GMR.	6
Figure 1-4: Simplified map of geology in the GMR. Geology modified from Schuster (1992).	8
Figure 1-5: Map showing location of the SWCC as projected onto the surface. . .	10
Figure 1-6: Segmentation of the Cascade Arc, as defined by Guffanti and Weaver (1988).	12
Figure 1-7: E-W cross-section of crustal and intra-slab earthquakes beneath western Washington.	16
Figure 1-8: Map of SHZ, WRSZ, and all crustal earthquakes with $M_l > 3.0$	17
Figure 1-9: Distribution of lahar deposits from Mount Rainier.	18
Figure 1-10: Cross-sections of seismicity beneath Mount St. Helens and Mount Rainier.	20
Figure 1-11: Locations of seismic experiments performed in the GMR.	22
Figure 2-1: Diagram showing geometry used to derive estimates of ray widths in equation 2.3.	26
Figure 2-2: Diagram of source in a 6-block model with 5 receivers.	38
Figure 2-3: Illustration of the projection problem.	42
Figure 2-4: Illustration of ray bending method from Um and Thurber (1987) . . .	44
Figure 2-5: Trade-off curve showing % reduction in χ^2 misfit and average parameter error for inversions performed with different values of the damping parameter λ	53
Figure 3-1: Plot of all events flagged as blasts (upper) and all shallow events (depth < 3 km) flagged as earthquakes (lower) in the GMR.	58
Figure 3-2: Map showing the locations of all blasts used in the inversion.	60

Figure 3-3: Geometry of the 1994 refraction experiment.	63
Figure 3-4: Composite record section from Centralia refraction experiment.	64
Figure 3-5: Comparison of 1-D model resulting from refraction experiment (bold line) with PNSN "C3" velocity model (dashed line).	65
Figure 3-6: Raypath diagram for all earthquakes with $M_I > 2.0$ occurring between 1990 and 1994.	67
Figure 3-7: Seismograph station distribution in the GMR.	69
Figure 3-8: Diagram of typical station deployed during NEHRP experiment	70
Figure 3-9: Theoretical raypath coverage for the 18 NEHRP locations.	72
Figure 3-10: Raypaths recorded by NEHRP stations.	73
Figure 4-1: Percent reduction in the c_2 misfit within each velocity inversion step.	80
Figure 4-2: Map showing blast relocation test results.	82
Figure 4-3: Velocity contour plots from a N-S cross-section through the 3-D model (top) and a model from the 1991 refraction profile (bottom).	88
Figure 4-4: E-W and N-S cross-sections through Mount Rainier.	91
Figure 4-5: Diagram illustrating geometry for heating of half-space problem.	94
Figure 4-6: Temperature profiles for instantaneous heating of a half-space.	95
Figure 4-7: Layers 2-5 from Plate 1 with the SWCC.	100
Figure 4-8: E-W cross-section through 3-D model along profile 3 in Plate 1.	102
Figure 4-9: Seismograms from 01/29/95 Pt. Robinson earthquake.	104
Figure 4-10: Seismograms from 05/20/95 WRSZ event.	105
Figure 4-11: Seismograms from 01/01/97 event near Yakima.	107
Figure 4-12: Seismogram for station YA2 from the 07/13/97 WRSZ event	108
Figure 4-13: Heat-flow contours from Blackwell et al. (1990) superimposed on Layer 6 of the 3-D velocity model.	110
Figure 4-14: Interpretive cross-section through southern Cascades, modified from Stanley et al. (1996).	112

Figure 4-15: Plot of P axes from all crustal focal mechanisms in Washington. . .	114
Figure 4-16: Proposed new segment for the Cascade volcanic arc.	116
Figure 4-17: WRSZ focal mechanisms in Layers 2 - 5.	119
Figure 4-18: Map and N-S cross-section of Rainier earthquakes located with 1-D model and station corrections	123
Figure 4-19: Map and N-S cross-section of Rainier earthquakes located using 3-D model.	124
Figure 4-20: Locations of Curtis Ridge rockfall	126
Figure 4-21: Focal mechanisms for 11 volcano-tectonic earthquakes beneath Mount Rainier	129
Figure 5-1: 6 slices through the 3-D model derived without the use of parameter separation.	135
Figure 5-2: 6 slices through the 3-D model derived with station corrections. . . .	137
Figure 5-3: 6 slices through the 3-D model derived without data from temporary stations.	139
Figure 5-4: 6 slices through the 3-D model from Lees (1989).	141
Figure 5-5: Illustration of the effect of mislocating a source downwards in depth on lengths of raypaths.	142

List of Tables

Table 2.1: Theoretical Raypath Widths for Different Points Along a Ray	27
Table 3.1: Selection criteria for inversion dataset.	60
Table 3.2: Number of P Arrivals Recorded by Temporary Stations	71
Table 4.1: 1-D Velocity Model Comparison	78
Table 4.2: Comparison of 1-D and 3-D location errors	125
Table A.1: P-Wave Rock Velocities (km/sec) with Increasing Depth.	164
Table B.1: NEHRP Station Locations	166
Table B.2: Refraction Station Locations	166

Acknowledgments

Many, many people have contributed, in many different ways, to the research that has led to this dissertation. First and foremost, I am deeply indebted to my advisor Steve Malone for his support and guidance. His confidence in my scientific abilities helped carry me through many ups and downs over the last 9 years, and his patience allowed me to do things that I needed to do (including taking a leave of absence) to mature not only as a researcher, but as a person. I am also especially grateful to Jonathan Lees for the use of his inversion code, as well as for many spirited conversations concerning "magma chambers" and other scientific topics. I would like to thank my reading committee members Bob Crosson and Ken Creager for their careful reviews of this dissertation, my other committee members William Wilcock and Joe Vance for their respective contributions to this dissertation, and Don Swanson (a former committee member) for bringing me up to speed on the basics of the geology of southwestern Washington. A special thanks is also owed to Chris Newhall, with whom I spent many hours talking and learning about volcanoes. I also benefited from discussions with current and former USGS researchers, including Carol Finn, Sam Johnson, Tom Sisson, Dal Stanley, Craig Weaver, and Dave Zimbelman. My co-workers in the Seismology Lab (Sandra Corso, Pete Lombard, Ruth Ludwin, Tony Qamar, Bill Steele, and Sandy Stromme) provided me with the invaluable experience of working with a community of researchers, as well as many welcome coffee breaks. In addition, I am deeply grateful to my fellow graduate students (both past and present), whose support and camaraderie as well as intellectual stimulation made grad school much less stressful and even fun. In particular, I benefited greatly from conversations with Neill Symons, which were instrumental in developing my intuitive understanding of tomography as well as white-water kayaking. My office-mates over the years (Robert Leet, Sean Walden, Yan Jiang, Gia Khazaradze, Jim Pullen, Gillian Sharer, and Jeff Johnson) gave me lots of support as well as intellectual stimulation. Finally, Gary Davidson was instrumental in helping me overcome many inhibitions and start playing Bluegrass fiddle.

The success of the fieldwork component of my research was highly dependent upon the contributions and hard work of many different people. Allen Strelow

and Jim Ramey taught me the nuts n' bolts of seismometry and telemetry, and John Castle, Rich Lechleitner, Peter Lombard, Steve Malone, Charles Moran, Kay Moran, Jim Pullen, Jeff Schwartz, Gillian Sharer, Allen Strelow, Neill Symons, George Thomas, and Elisa Wells were invaluable assistants and companions in the field. For the refraction experiment in 1994, Will Greenough at the Centralia coal mine graciously allowed and assisted in the deployment of two seismometers in the coal mine, and the Plum Creek Timber Company, Champion International Corporation, Crystal Mountain Resort, and Mount Rainier National Park also granted permission to deploy seismometers on their land for 1-2 weeks. The University of Washington Pack Forest, Champion International Corporation, the White River and Packwood Ranger districts in the Mount Baker-Snoqualmie National Forest, the Naches Ranger district in the Wenatchee National Forest, Crystal Mountain Resort, White Pass Ski Resort, the Cowiche Telephone Company, AT&T, Mount Rainier National Park, and Rick and Jana Gardner ("Pottery by Jana", Ashford, WA), all graciously allowed access to their land for deploying seismometers for 4-6 months in 1995 and 1996. I am especially grateful to Tom Yelin of the USGS for his assistance in acquiring permits for sites on U.S. Forest Service land, and to Rich Lechleitner from Mount Rainier National Park for his assistance in setting up helicopter rides and, in one case, a work party to deploy and retrieve equipment from various high-altitude seismometers in the park. These experiments, as well as the research presented in this dissertation, were funded by USGS cooperative agreement 1434-95-A-1302 and USGS NEHRP grant 1434-95-G-2571.

I wouldn't have made it to graduate school at all without the support of my family. My interest in science began with my grandfather Keith Johnson, who was a living scientific laboratory and demonstrated most days of his life that science at its most fundamental level is fun. It was fostered and allowed to flower by the unwavering support of my parents Charlie and Kay Moran, who took me and my sister Amy on a trip to Iceland to visit Heimaey volcano the year after it erupted, who didn't object when the only books I wanted to read as a kid were about earthquakes and volcanoes, and who still think that what I do is neat. Finally, my wife Elisa Wells, who has known me only as a graduate student, has not only put up with my long hours and occasional swings in emotion, but has also made me feel loved, has helped me laugh, and has supported me to the very end.

I. Introduction

1.1 Objectives

One of the most striking features of seismicity in western Washington is the clustering of crustal earthquakes (Figure 1-1). It is apparent from Figure 1-1 that earth-

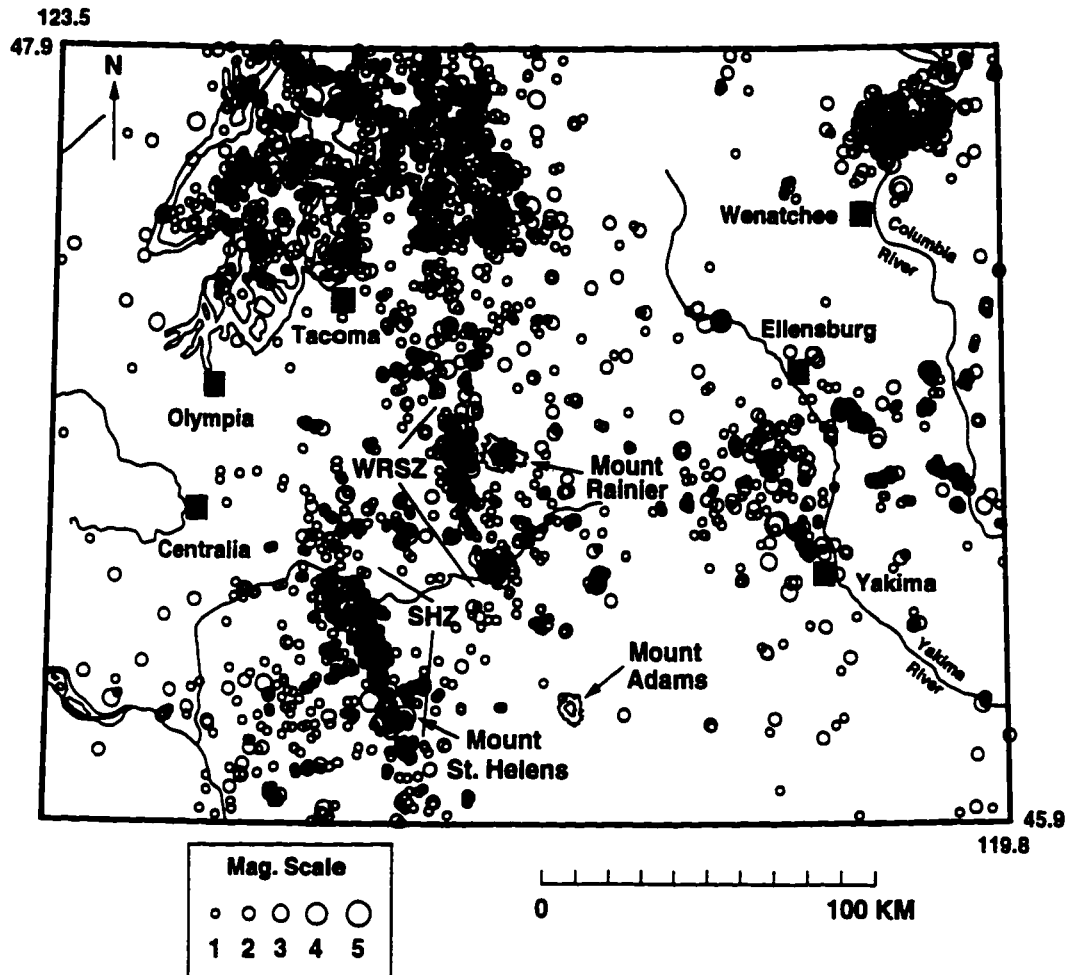


Figure 1-1 Map of all crustal (depths less than 35 km) earthquakes located within the GMR between 1980 and 1996. Mount St. Helens events were excluded, as were all earthquakes with magnitudes < 1.0 , station gap $> 135^\circ$, # of recording stations < 10 , and nearest station > 25 km from event.

quakes do not occur everywhere. Instead, they are concentrated in clusters, or zones, of seismic activity. This clustering has significant implications for seismic hazards assessments. In this dissertation I explore the hypothesis that geologic

structures, in conjunction with regional tectonic forces, are primarily responsible for controlling the location of seismicity (and possibly volcanism) in parts of western Washington. The primary tool for testing this hypothesis is a 3-D velocity image that I derive using local earthquakes recorded by the Pacific Northwest Seismograph Network (PNSN). If an association is found between seismicity patterns, imaged velocity structures, geology, and/or structures imaged from other geophysical datasets, then the structural control hypothesis is supported. If no association is found, then other processes (such as thermal control of the brittle/ductile transition) may be more important in controlling the locus of seismicity. Goals of this work include providing constraints on seismogenic potential (and thus seismic hazards) in this region, as well as providing new information about subsurface structure that can be used to refine and constrain regional tectonic and geologic models.

An important part of my dissertation is the generation of a 3-D P-wave velocity image using local earthquake data from the PNSN catalog. The technique I use, local earthquake tomography (LET), is similar in concept to computerized axial tomography (or CAT) scans used in medicine. LET analyses have been performed before in Washington, most notably by Lees and Crosson (1989, 1990). The LET methodology I use is a refined version of the methodology used by Lees (1989) and Lees and Crosson (1989, 1990), and is described in Chapter II. In Chapter III I describe the dataset used in the inversion, including data gathered during a 2 year field experiment designed to increase ray coverage east of Mount Rainier. The final image is displayed in Plate 1 (located on the inside back cover), and interpretations are discussed in Chapters IV and V.

1.2 Study Area

My study area encompasses a region of remarkable geologic complexity. It contains four main geologic provinces, including parts of the Coast Ranges, the Puget Lowlands, the Cascade Range, and the Columbia Plateau (Figure 1-2). It also contains the NW-SE-trending Olympic-Wallowa lineament (OWL) (Raisz, 1949) and several large stratovolcanos, including Mount Rainier, Mount St. Helens, and Mount Adams. Assigning one name to this region is difficult; however, almost any name is preferable to "my study area." Since my work focuses primarily on seismicity near Mount Rainier and Mount Rainier is visible from most points in my study area, I

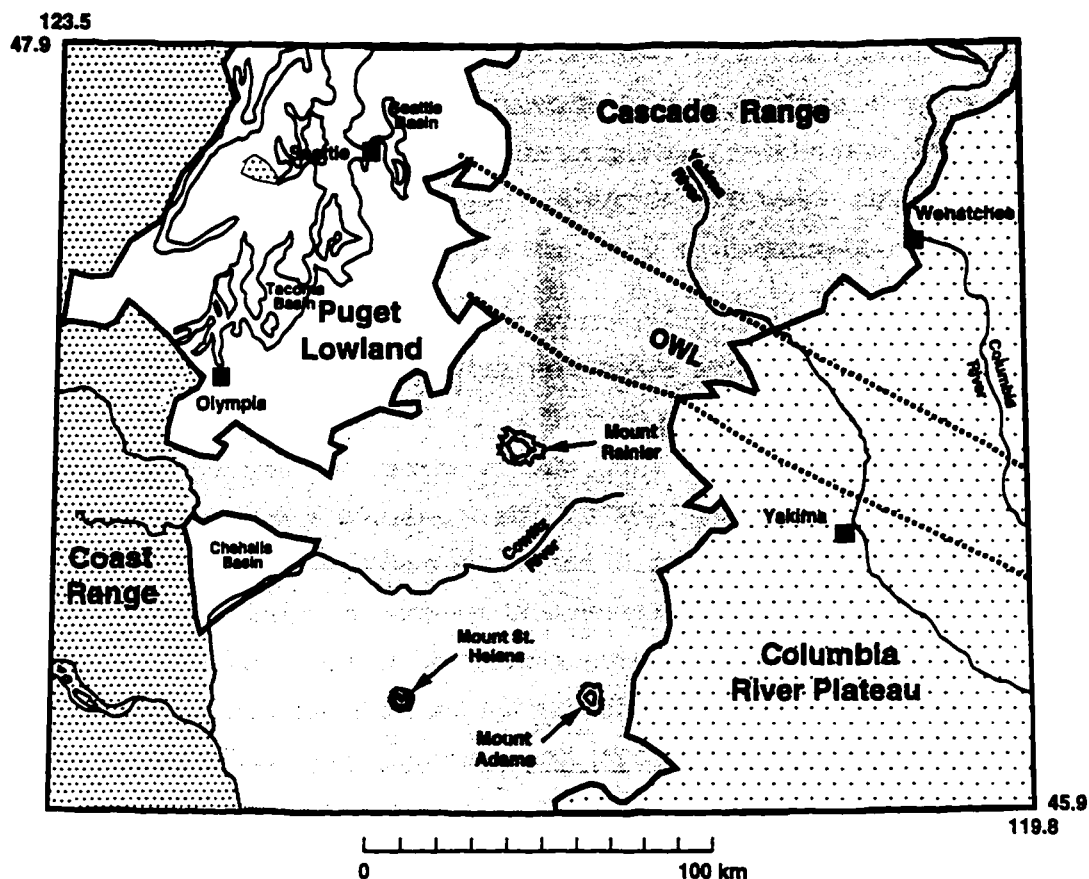


Figure 1-2 Map of major physiographic provinces contained in the GMR. Note that the geographical features shown in this figure (i.e. rivers, volcanoes, etc.) are identical to those shown in all subsequent map-view plots of the GMR.

will refer to my study area as the "greater Mount Rainier area," which for convenience I assign the acronym GMR. Brief descriptions of each of the four provinces in the GMR are given below.

1.2.1 Coast Range

The Coast Range province consists largely of a thick basement of basalts referred to as the Siletz River Volcanics in Oregon, the Crescent Formation in Washington, and the Metchosin Volcanics on southern Vancouver Island (e.g. Snavely and Baldwin, 1948; Tabor and Cady, 1978; Clowes et al., 1987). They are among the most voluminous volcanic deposits in the world, with an estimated total volume of $250,000 \text{ km}^3$, roughly five times the volume of the island of Hawaii (Duncan and Kulm, 1989). The average basalt thickness is estimated to be 3 km, but can be as great as 6 km at

inferred eruptive centers such as the complex exposed near Bremerton, Washington (Duncan and Kulm, 1989; Babcock et al., 1992). The Crescent Formation is divided into two units, an upper unit composed primarily of subaerial basaltic flows and sills, and a lower unit composed primarily of pillow basalts with interbedded sediments (Tabor and Cady, 1978). The lower unit has since been metamorphosed to prehnite-pumpellyite facies basalts (Babcock et al., 1992).

The origin of the basalts is still controversial. They are thought to have formed between 62 and 48 Ma as either a seamount complex that was accreted to the North American margin after formation (Wells et al., 1984; Duncan and Kulm, 1989), or as products of continental margin rifting formed essentially in situ with no post-formation accretion (Babcock et al., 1992). Clasts of quartz diorite found in sediments interbedded with the basalts indicate that they formed close to the North American continent (Cady, 1975). Since formation (and possible accretion), it is thought that this province has acted as a backstop against which slices of oceanic sediments have been offscraped from the subducting Juan de Fuca plate, forming the Olympic core complex (e.g. Cowan, 1986; Brandon and Vance, 1992). The eastward extent of this province is unknown, but models derived from gravity and aeromagnetic data suggest that the Crescent Formation extends several tens of kilometers beyond its easternmost outcrops (Finn, 1990).

1.2.2 Puget Lowlands

The contact, or suture zone, between the Coast Range province and the pre-Tertiary basement of the North American continent is entirely concealed by Tertiary-Quaternary deposits from Cascade volcanism, from Cascade Range-derived sediments, and from deposits of several episodes of continental glaciation (e.g. Johnson, 1984; Walsh et al., 1987). These deposits are thickest in a series of discontinuous basins collectively referred to as the Puget Lowlands. In Washington these basins include the Chehalis, Tacoma, and Seattle basins. The stratigraphy of the Chehalis basin is constrained by several proprietary wells drilled to depths of up to 3.5 km (Stanley et al., 1994). A thin veneer of unconsolidated Quaternary sediments lies on top of a 4-5 km thick section of Oligocene to Eocene deposits including sediments of the Lincoln Creek, Cowlitz/Skookumchuck, and McIntosh formations, and basaltic-to-andesitic rocks of the Northcraft formation (Ise, 1985; Stanley et al., 1994; Johnson and Stanley, 1995). Stanley et al. (1994) infer from seismic reflection profiling results that the entire section is underlain by the Crescent formation.

Strong gravity lows are associated with both the Seattle and Tacoma basins (Figure 1-3) (Bonini et al., 1974; Finn, 1990). Gower et al. (1985) suggest that the steep gradients in the gravity field indicate that the basins are bounded by faults. This idea was independently confirmed by convincing geological evidence for a major earthquake that occurred approximately 1000 years ago along the Seattle Fault (e.g. Bucknam et al., 1992; Atwater and Moore, 1992). This and several other faults have since been detected by seismic reflection profiles (Johnson et al., 1994; Pratt et al., 1997). Pratt et al. (1997) used seismic reflection data to infer a maximum 8 km thickness for deposits in the Tacoma basin and 7.5 km for deposits in the Seattle basin. They also infer that the Crescent Formation forms the basement in both basins.

1.2.3 Cascade Range

Geology

The modern-day Cascade Range is a complex amalgamation of allochthonous terranes accreted during the late Mesozoic that have since been partially covered by Eocene and younger sedimentary and volcanic rocks. Cascade arc volcanism began around 38 Ma (Heller et al., 1987), and the present-day arc extends roughly 1100 km from southern British Columbia to northern California. Before the onset of Cascade volcanism, most of western and central Washington is thought to have been a broad coastal plain with minimal relief (e.g. Evarts and Swanson, 1994). The basement is thought to consist of a series of pre-Tertiary allochthonous terranes accreted onto the North American continent during late Mesozoic/early Cenozoic subduction. South of the Olympic-Wallowa lineament (OWL), exposures of pre-Tertiary terranes in the GMR are limited to the Rimrock Lake Inlier (Clayton, 1983; Vance et al., 1987; Miller, 1989) and small slivers exposed within the OWL northwest of Yakima (e.g. Walsh et al., 1987). Sediments derived from pre-Tertiary terranes were deposited in fault-controlled basins as largely non-marine deltas to the west, forming the middle-to-late Eocene Puget Group that includes the McIntosh, Skookumchuck, Carbonado, Cowlitz, and Renton formations (e.g. Gard, 1968; Johnson and Stanley, 1995). East of the modern-day Cascade Crest the correlative Naches, Roslyn, and Chumstick Formations accumulated as fluvial deposits in local basins (e.g. Tabor et al., 1984). Volcanic activity occurred at widely scattered locations across the Pacific Northwest, and did not concentrate into a margin-parallel belt until the late Eocene, no earlier than 38 Ma (Heller et al., 1987; Evarts and Swanson, 1994).

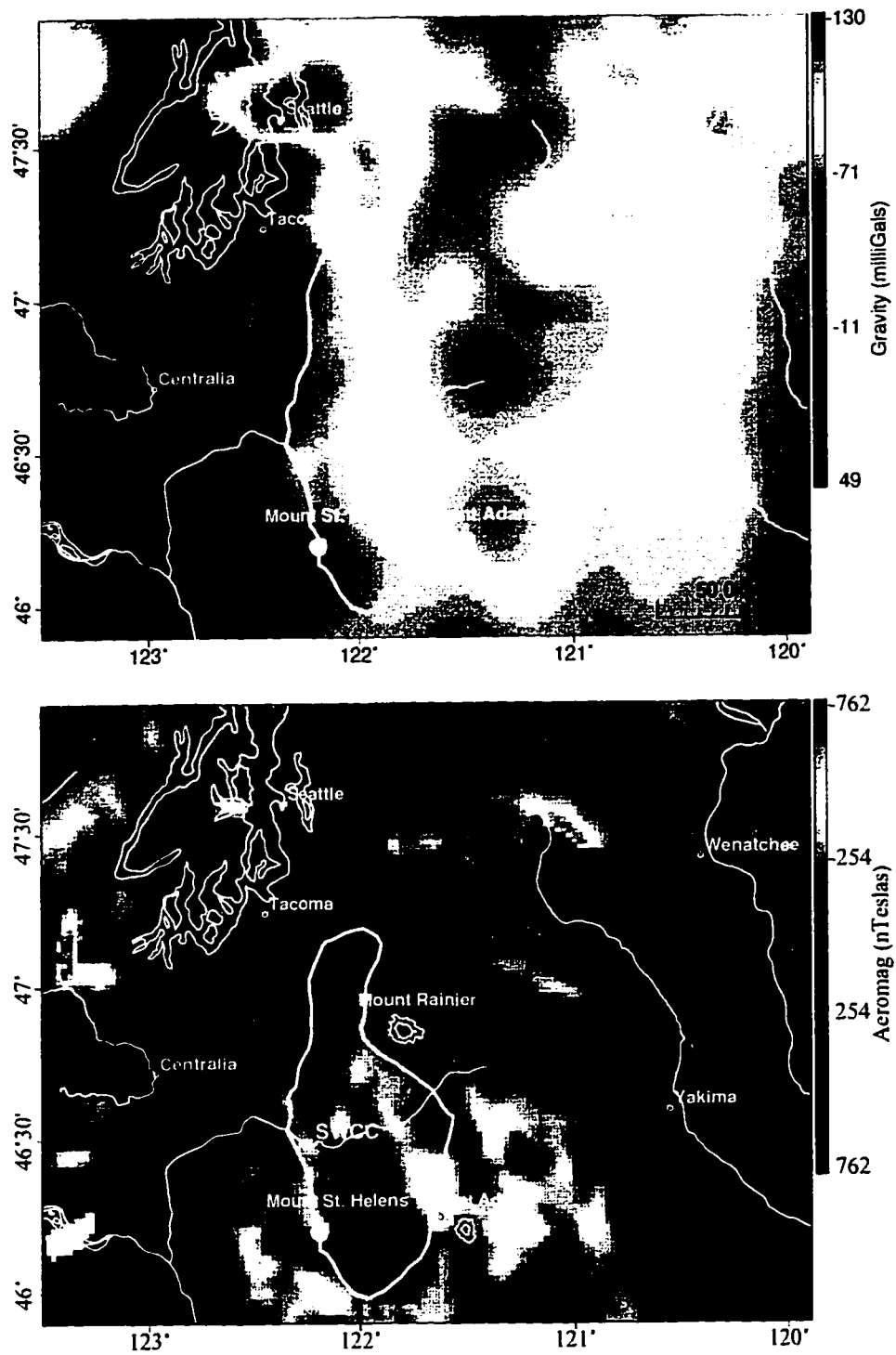


Figure 1-3 Map of Bouguer gravity (top) and aeromagnetic (bottom) data in the GMR. Data are from National Geophysical Data Center (1991), and are plotted using the program Xmap8 (Lees, 1995). The position of the SWCC is drawn (the squash-shaped feature) in both figures.

As Cascade arc volcanism commenced, volcanogenic deposits gradually buried the middle-to-late Eocene deposits. This initial phase of arc volcanism lasted for at least 20 m.y. (Evarts and Swanson, 1994) and formed the volcanogenic deposits of the Northcraft, Ohanapecosh, Stevens Ridge and Fifes Peak Formations (Fiske et al., 1963 & 1964; Walsh et al., 1987; Stanley et al., 1994). Evarts and Swanson (1994) estimate that the maximum stratigraphic thickness of volcanic rocks at the center of the arc is over 7 km. Numerous intrusions also resulted, including the granodioritic to quartz-dioritic Tatoosh and White River plutons exposed in the eastern half of Mount Rainier National Park (Fiske et al., 1963 & 1964; Schasse, 1987), the granitic to granodioritic Bumping Lake pluton east of Mount Rainier (Hammond et al., 1994), the granitic Spirit Lake pluton north of Mount St. Helens (Evarts et al., 1987), as well as many smaller dikes, sills, and stocks exposed throughout the Cascade portion of the GMR (e.g. Schasse, 1987; Walsh et al. 1987; Swanson, 1992).

After the initial burst of volcanism, a relative hiatus in volcanic activity occurred between 17 to 5 Ma in the southern Washington Cascade arc, in contrast to significant late-Miocene volcanism in Oregon (Evarts et al., 1987). The onset of this lull apparently occurred in conjunction with a shift from regional subsidence to regional uplift (Evarts and Swanson, 1994). The absence of mid-to-late Miocene volcanogenic rocks could in part be due to increased erosion associated with this uplift (the regional uplift was likely more significant in the northern Washington Cascades, hence the greater exposure of pre-Tertiary rocks relative to the GMR (Hammond et al., 1994)). Synchronous with this uplift was the onset of a regional folding event, resulting in broad NNW-trending folds such as the Morton anticline, Pole Patch syncline, and Carbon River/Skate Creek anticline (Figure 1-4) (Gard, 1968; Walsh et al., 1987; Evarts and Swanson, 1994). Both the Morton and Carbon River/Skate Creek anticlines are cored by sediments of the mid-Eocene Carbonado Formation (Gard, 1968; Johnson and Stanley, 1995). Seismic reflection data and well-logs from several drill holes indicate that the section of Eocene sediments in the Morton anticline includes both the Carbonado and McIntosh formations, and that the total sediment thickness is approximately 10 km in the core of the anticline (Johnson and Stanley, 1995).

The folded Eocene to Miocene strata are unconformably overlain by basalts from the Columbia River Basalt Group on the eastern edge of the GMR (e.g. Swanson, 1967; Walsh et al., 1987), and elsewhere by volcanogenic deposits from the current

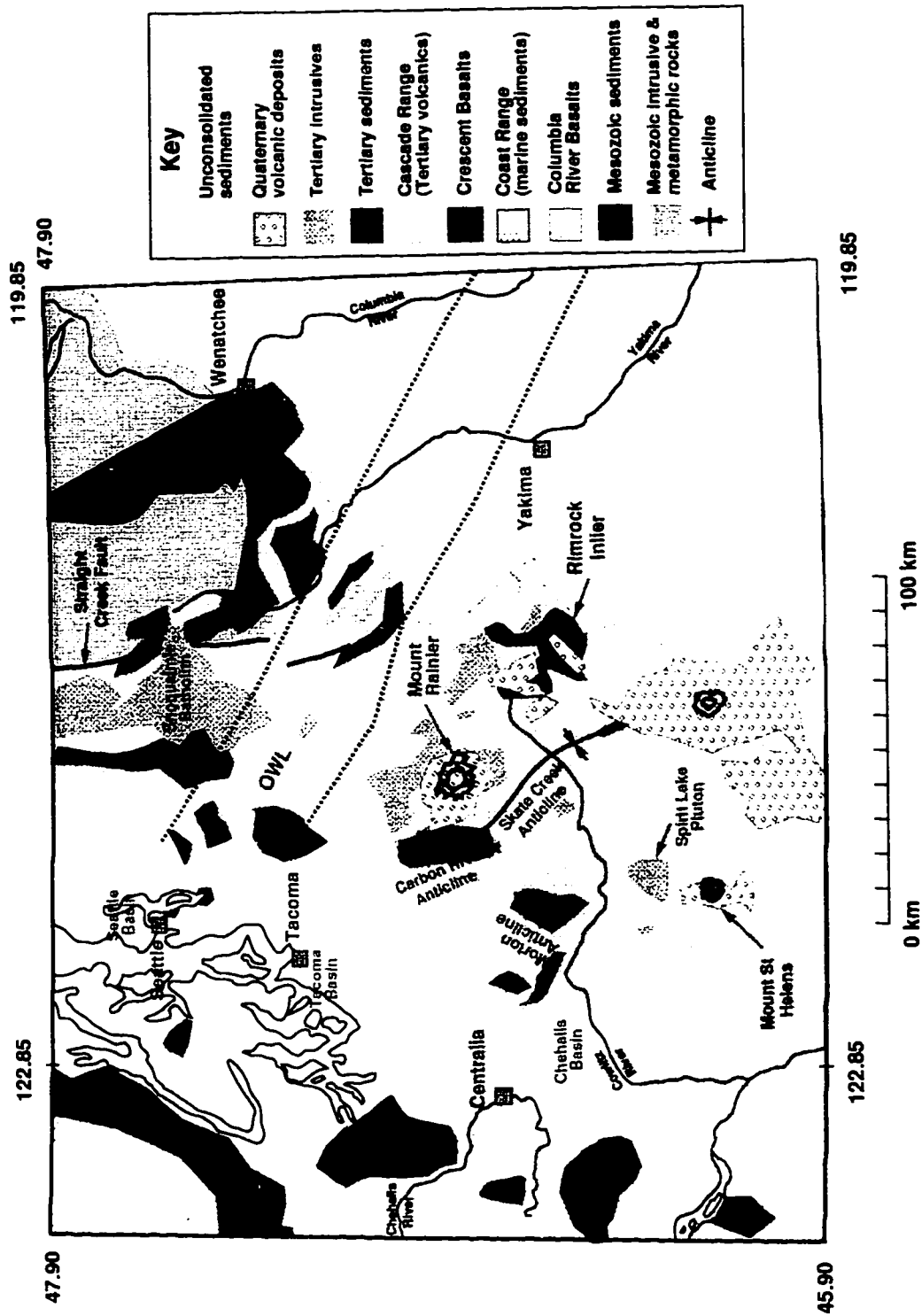


Figure 1-4 Simplified map of geology in the GMR. Geology modified from Schuster (1992).

volcanic phase that began roughly 5 Ma (Guffanti and Weaver, 1988). These deposits include the large Quaternary composite edifices of Mounts Rainier, St. Helens and Adams, the remains of the late-Pliocene to late-Pleistocene Goat Rocks volcano, the Indian Heaven basalt field, and scattered small monogenetic vents (Figure 1-4).

The Southern Washington Cascades Conductor

A major conductivity anomaly beneath the southern Washington Cascades was first identified by Law et al. (1980). This feature has subsequently been mapped in some detail via 2-D magnetotelluric (Stanley, 1984; Stanley et al., 1987; Stanley et al., 1990; Stanley et al., 1992; Stanley et al., 1996), magnetovariational (Egbert and Booker, 1993), and seismic reflection (Stanley et al., 1992) field experiments and modeling, and is referred to as the southern Washington Cascades Conductor (SWCC) (Figure 1-3 and Figure 1-5) (Stanley et al., 1987). The edges of the SWCC appear to correlate with three aeromagnetic lows, although a ridge of relative aeromagnetic highs traverses through its middle (Figure 1-3) (Stanley et al., 1987). However, there is little correlation between the SWCC and anomalies in the Bouguer gravity field (Figure 1-3) (Bonini et al., 1974; Stanley et al., 1987). There is also little evidence for it in 2-D seismic velocity profiles generated by two seismic refraction lines run through the southern Cascades (Gridley, 1993; Miller et al., 1997; Luetgert et al., 1995; Tom Parsons, personal communication). Lees and Crosson (1990) find several low velocity anomalies between 2 and 10 km in their 3-D velocity model derived via local earthquake tomography that generally correspond with the SWCC; however, many of these anomalies may be artifacts caused by poor data quality (see section 5.4). Thus evidence for the SWCC from non-magnetic measurements is somewhat equivocal.

As modeled by Stanley et al. (1992), the SWCC is shallowest along its western edge, where it extends from near the surface to a depth of 10 km, and deepest along its eastern edge, where it extends from 10 to 20 km. Its thickness also increases from north to south. The SWCC is thought to be bounded to the west by the Crescent Formation (Finn, 1990; Johnson and Stanley, 1995), and to the east by pre-Tertiary rocks similar to those exposed in the Rimrock Lake Inlier (Figure 1-5) (Stanley et al., 1992). The source of the high conductivities is not completely understood. The SWCC does not appear to crop out at the surface, making direct lithologic correlation difficult (Stanley et al., 1992). Conductivities in the deeper parts of the SWCC

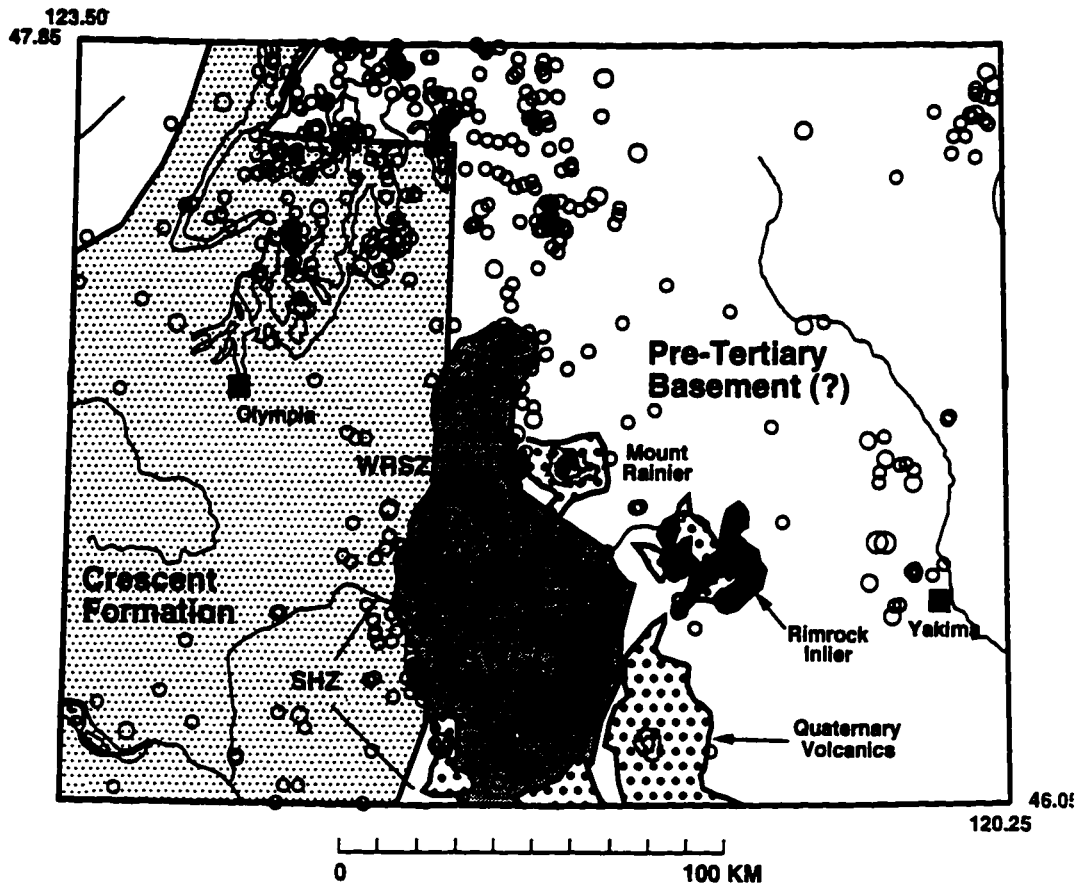


Figure 1-5 Map showing location of the SWCC as projected onto the surface. Also plotted are earthquakes ($M > 2.5$) (open circles) and Quaternary volcanics (dotted pattern). The easternmost extent of the Crescent Formation (inferred by Finn (1990)) is indicated by the stippled pattern.

might be influenced by high temperatures, especially on the eastern boundary where geothermal gradients of up to $50^{\circ}\text{C}/\text{km}$ have been measured (Blackwell, 1990). However, Stanley et al. (1992) note that the upper boundary of the SWCC in cross-section correlates well with the Skate Creek and Morton anticlines, which bring Tertiary marine sedimentary units close to the surface. They also note that an anomaly caused by thermal effects should shallow to the east, not deepen as is the case with the SWCC. Based on these arguments, their preferred interpretation is that the SWCC is composed of a large complex of marine sedimentary rocks (most likely black shale) that was compressed in a fossil suture zone during accretion of the Coast Range in the mid-Eocene.

Stanley et al. (1987) were the first investigators to notice that upper-crustal seismicity and Quaternary volcanic centers cluster along the edges of the SWCC (as projected onto the surface) (Figure 1-5). They postulate that the SWCC is acting as a rigid body rotating in a regional deformational field, and is acting to control the locus of seismicity and volcanism in the GMR. If this is true, then mapping the boundaries of the SWCC in more detail is an important step in assessing seismic hazards in the GMR. Given that the SWCC is thought to be bounded to the west by the Crescent Formation (Figure 1-5), the eastern boundary of the SWCC should in particular be detectable in a LET velocity inversion; it should appear as a vertical contact between the high velocities of the Crescent basalts to the west and the presumably low velocities of the SWCC marine sediments to the east.

Segmentation of the Cascade Arc

There is considerable variability in Pliocene-Holocene volcanic behavior along the axis of the Cascade Range. Guffanti and Weaver (1988) use spatial, temporal, and compositional variations in Pliocene to Holocene volcanism to divide the Cascades in British Columbia, Washington, and central and northern Oregon into three segments (Figure 1-6). The northernmost of these segments extends from southern British Columbia to northern Washington, and is characterized by volcanism occurring at isolated stratovolcanoes such as Glacier Peak and Mount Baker that lie on a basement composed largely of pre-Tertiary allochthonous terranes. The southernmost of these segments extends from central Oregon to the Washington-Oregon border, and is characterized much more voluminous volcanism occurring both at stratovolcanoes such as the Three Sisters and in broad fields of monogenetic vents. The stratovolcanos lie on a basement composed of largely undeformed late-Tertiary mafic volcanic fields (Guffanti and Weaver, 1988). The middle segment extends from the Washington-Oregon border to north of Mount Rainier, and is transitional between the northern and southern segments. Like the northern segment, volcanism is primarily concentrated at stratovolcanoes such as Mount Rainier and Mount St. Helens that lie on a basement of folded early-to-mid-Tertiary Cascade-arc-derived volcanogenic rocks. Like the southern segment, there are isolated fields of mafic rocks (although smaller in volume) erupted from monogenetic vents that lie between the large stratovolcanoes (Walsh et al., 1987).

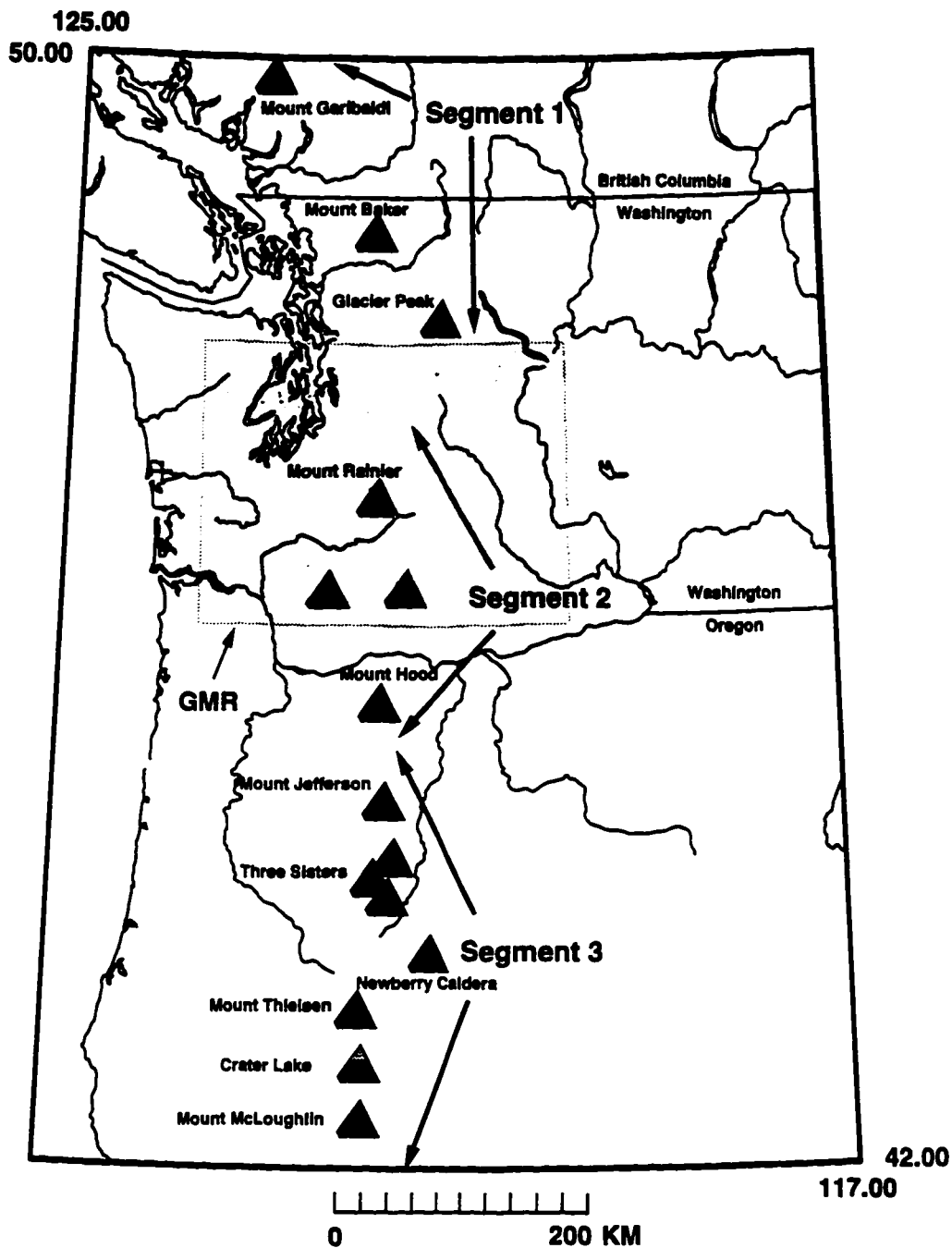


Figure 1-6 Segmentation of the Cascade Arc, as defined by Guffanti and Weaver (1988). Solid triangles correspond to locations of individual volcanoes.

This segmentation is also apparent in other volcano-tectonic features of the Cascade Range, as well as in various geophysical datasets. Sherrod and Smith (1990) demonstrate that Quaternary eruptive rates increase from $0.23 \text{ km}^3 / (\text{km} - \text{m.y.})$

north of Mount Rainier to $1.6 \text{ km}^3 / (\text{km} - \text{m.y.})$ in southern Washington and northern Oregon. Mariner et al. (1990) demonstrate that the rates of convective heat discharge as measured in hot springs increases from $7 \text{ kJ} / (\text{km} - \text{sec})$ in northern Washington to $26 \text{ kJ} / (\text{km} - \text{sec})$ in southern Washington to $230 \text{ kJ} / (\text{km} - \text{sec})$ in Oregon. Blackwell et al. (1990) show that high heat flow rates and geothermal gradients in the northern and southern Washington Cascades are broken by a WNW-trending ridge of low values extending from Seattle to Yakima parallel to the Olympic-Wallowa lineament (see section 1.2.5). This ridge of low heat flow rates also parallels a WNW-trending gravity low (Blakely and Jachens, 1990) and aeromagnetic high (Finn, 1990; personal communication). Finally, Weaver and Michaelson (1985) note that crustal seismicity is diffuse in northwestern Washington, concentrated into a few zones in southwestern Washington, and virtually nonexistent in Oregon. Thus the portion of the Cascade Range in the GMR is a region of along-axis transition in terms of eruptive style, eruptive rates, heat flow rates, geothermal gradients, convective heat discharge, gravity and aeromagnetic trends, and crustal seismicity distribution.

1.2.4 Columbia Plateau

The Cascade Range is bounded to the east by the Columbia Plateau, the youngest flood-basalt province on earth. The flood basalts, collectively known as the Columbia River Basalt Group (CRBG), are a series of thick flows erupted from vents in Idaho and eastern Washington between 17 and 6 Ma, covering most of the eastern half of Washington state as well as northeastern Oregon. Cumulative thickness of the CRBG ranges from 1.5 km to 6 km (Glover, 1985; Catchings and Mooney, 1988). Several of the largest flows reached the eastern flank of the Cascades, largely obscuring the older geologic record (Beeson and Tolan, 1990; Saltus, 1993). Drilling and seismic data show that several Tertiary sedimentary basins were covered by the CRBG near Yakima and Ellensburg, WA (Catchings and Mooney, 1988; Jarchow et al., 1994; Campbell and Reidel, 1994). Gravity modeling also suggests that the CRBG overlies a broad tertiary sedimentary basin that is thickest near Yakima (Saltus, 1993).

Since emplacement of the CRBG the western half of this province has been deformed into a series of NW-striking folds and faults known as the Yakima Fold Belt, with evidence for Quaternary faulting in places (Beeson and Tolan, 1990; Pezopane and Weldon, 1993). The leading edge of CRBG flows that reached the Cas-

ades have been uplifted by 1 km or more in association with the broad regional uplifting of the Washington Cascades. The largest flows, which crossed the axis of the Cascade range prior to uplift and reached as far as the Pacific ocean, also supply perhaps the best constraints on late Cenozoic rotations in the Pacific Northwest (Wells, 1990). Paleomagnetic measurements taken along individual flow units show a progressive westward increase in the amount of clockwise rotation from eastern Washington to the coast. From this spatial pattern Wells (1990) infers that the entire region has undergone dextral shear rotation in response to oblique subduction of the Juan de Fuca plate.

1.2.5 Olympic-Wallowa Lineament

A broad zone of northwest-southeast-trending faults, folds and topographic features extends from the Olympic Mountains southeast to the Wallowa Mountain uplift in northeastern Oregon. This zone is referred to as the Olympic-Wallowa lineament (OWL) (Raisz, 1946; Mann and Meyer, 1993), and stretches across all four of the provinces described above (Figure 1-2 and Figure 1-4). In Washington it is defined by northwest-trending folds in the Yakima Fold belt, faults and folded strata in the Cascades (Walsh et al., 1987; Schuster, 1992), the Seattle Fault (Johnson et al., 1994; Pratt et al., 1997), and the northeast corner of the Olympic Mountains (Raisz, 1946). As noted above, the OWL also parallels northwest-trending anomalies in gravity, heat flow, and aeromagnetic data, and also marks the boundary between the northern and southern segments of the Cascade volcanic arc (Figure 1-6).

Parts of the OWL have unquestionably been active during the Holocene, including the thrust faults of the Seattle Fault and the Yakima Fold Belt (Pezzopane and Weldon, 1993; Johnson et al., 1994) as well as right-lateral strike slip faults in Oregon that have offset Quaternary strata by as much as 2 km (Mann and Meyer, 1993). However, variations from right-lateral strike-slip and oblique normal faulting in the southeast (Pezzopane and Weldon, 1993; Mann and Meyer, 1993) to predominantly thrust faulting in the northwest (e.g. Ludwin et al., 1991) suggest that the OWL is not a single tectonic feature, supporting the idea that it represents a pre-existing weakness or tectonic boundary in the crust that has been reactivated at different locations at different times.

1.3 Seismicity

The Pacific Northwest Seismograph Network, or PNSN (formerly the Washington Regional Seismograph Network), has been in operation since 1969, yielding over a quarter-century-long catalog of accurate earthquake locations in Washington state. During this time it has recorded over 33,000 events, including thousands of earthquakes as well as many hundreds of quarry blasts, rockfalls, avalanches, and other seismic events. Earthquakes in Western Washington can be divided into three categories: intra-slab earthquakes, crustal earthquakes, and volcano-tectonic earthquakes (defined as high-frequency tectonic earthquakes that occur beneath volcanic edifices).

1.3.1 Intra-slab Earthquakes

Intra-slab earthquakes occur within the subducting Juan de Fuca plate and, in cross-section, define a distinct Benioff zone down to 100 km depth (Figure 1-7) (e.g. Ludwin et al., 1991). Several damaging intra-slab earthquakes have occurred this century, including a M 7.2 event in 1949 near Olympia and a M 6.5 event in 1965 between Seattle & Tacoma. Additionally, it is widely thought that M 8 or greater inter-slab earthquakes have occurred along the interface between the Juan de Fuca and North American plates every 300-500 years (e.g. Atwater, 1992).

1.3.2 Crustal Earthquakes

Crustal earthquakes occur in the upper 20 km of the crust except in the Puget Sound basin, where they locate as deep as 30 km (Figure 1-7). Their distribution in map-view is relatively homogeneous in the Puget Sound basin north of Olympia, and very heterogeneous elsewhere (Figure 1-1). Puget Sound basin seismicity is the topic of another research project (Symons and Crosson, 1996), and won't be discussed here. Outside of Puget Sound, crustal earthquakes in the GMR tend to occur in clusters of seismic activity (Figure 1-1 and Figure 1-8). Significantly, these clusters do not correlate with mapped positions of known surface faults. However, two seismic zones have linear appearances in map view, suggesting that earthquakes are occurring along faults that are not exposed at the surface. One of these zones runs NNW-SSE directly beneath Mount St. Helens, and is referred to as the St. Helens seismic Zone, or SHZ (Figure 1-1 and Figure 1-8) (Weaver and Smith, 1983; Grant et al., 1984). Several moderate-sized earthquakes have occurred along the SHZ, including the M_l 5.5 Elk Lake event in 1981. Although there is no evidence for offset

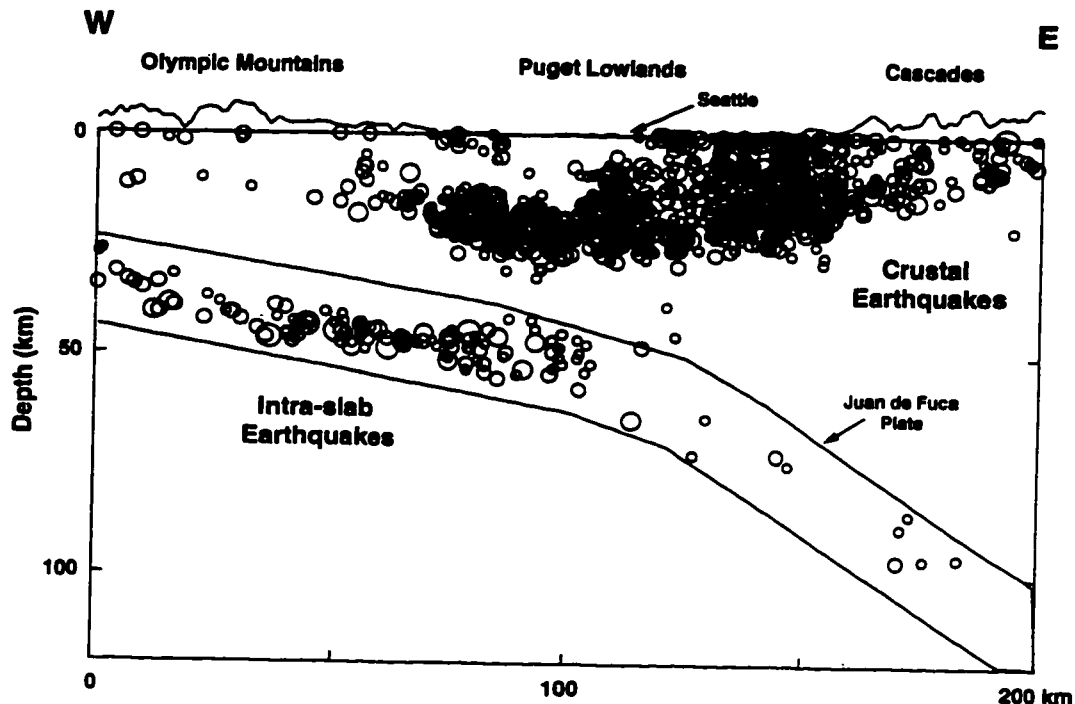


Figure 1-7 E-W cross-section of crustal and intra-slab earthquakes beneath western Washington. The cross-section is centered on Seattle, and includes all earthquakes occurring in a 1° swath with $M_1 > 1.5$ between 1980 and 1996. There is no vertical exaggeration except for topography, which is plotted at 4:1. Note that the drawing of the Juan de Fuca plate is schematic.

on the surface (Evarts and Swanson, 1994), it is thought to represent a distinct right-lateral strike-slip fault. This hypothesis is based both on its linear epicentral trend and on focal mechanisms for SHZ earthquakes which yield fault plane orientations parallel to the epicentral trend (Grant et al., 1984; Weaver et al., 1987) (Note that focal mechanisms from earthquakes directly under Mount St. Helens do not parallel the SHZ trend, and are thought to reflect the state of stress in the volcano's conduit system (Barker and Malone, 1991; Moran, 1994)). Weaver and Smith (1983) use the length of the SHZ (90 km) to suggest that the SHZ is capable of generating up to a M 7.0 earthquake.

The second linear zone trends north-south and is located 15 km to the west of Mount Rainier (Figure 1-1 and Figure 1-8). It is referred to as the Western Rainier Seismic Zone, or WRSZ (Thompson and Qamar, 1989; Malone et al., 1991; National Research Council, 1994). Its relationship to Mount Rainier is unknown, as is its seis-

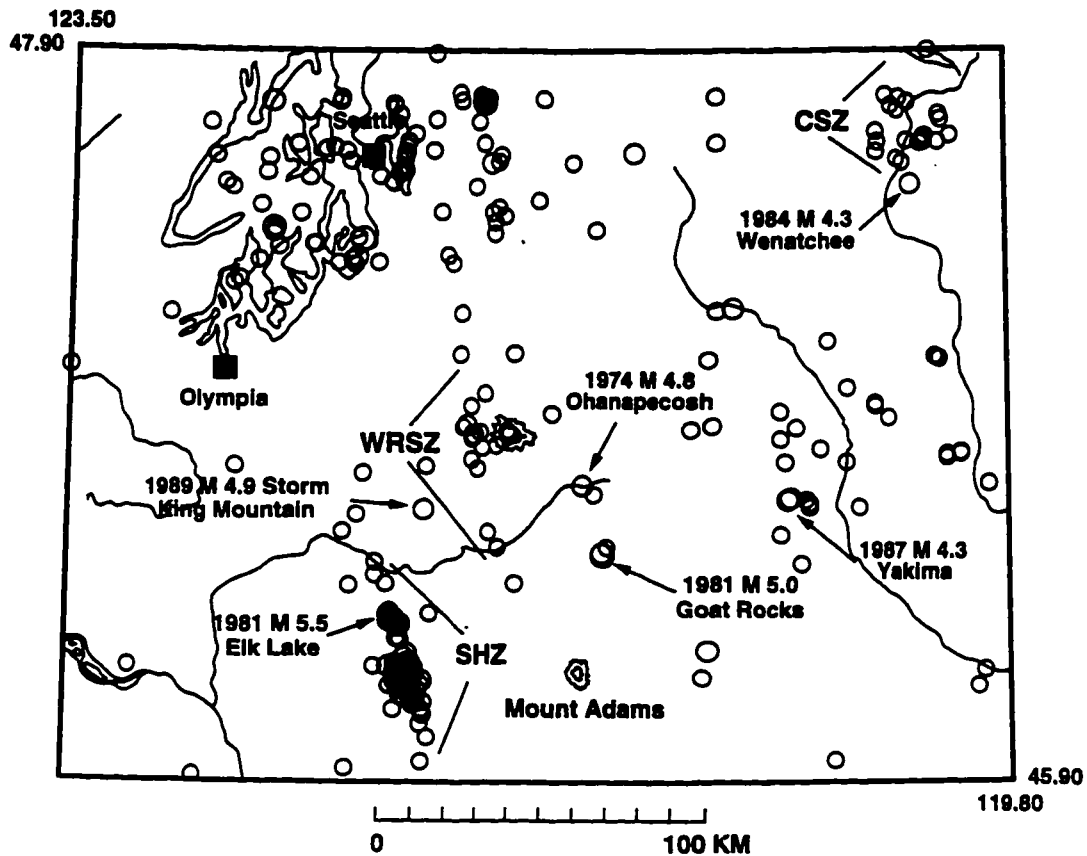


Figure 1-8 Map of SHZ, WRSZ, and all crustal earthquakes with $M_1 > 3.0$.

mogenic potential. The possibility of a large earthquake occurring along the WRSZ is a particular concern because at least 6 large landslides are known to have originated at Mount Rainier in the last 5600 years (Scott et al., 1995), all resulting in lahars that reached the Puget Lowlands (Figure 1-9). If similar-sized lahars were to occur today, they would inundate such moderate-to-densely populated cities as Enumclaw, Orting, Sumner, Auburn, Puyallup, and Kent, not to mention Mount Rainier National Park. While the lahar record is well established, little is known about possible triggers for the landslides. Most appear to not have occurred in conjunction with eruptive activity (Scott et al., 1995). One potential non-eruptive trigger is a large earthquake occurring near Mount Rainier, perhaps along the WRSZ. The largest recorded earthquakes along the WRSZ include several M_1 4.1 earthquakes, most recently in 1995, and a M_1 3.9 in 1973 (Crosson and Frank, 1975). Whether larger earthquakes could occur along the WRSZ is an open question.

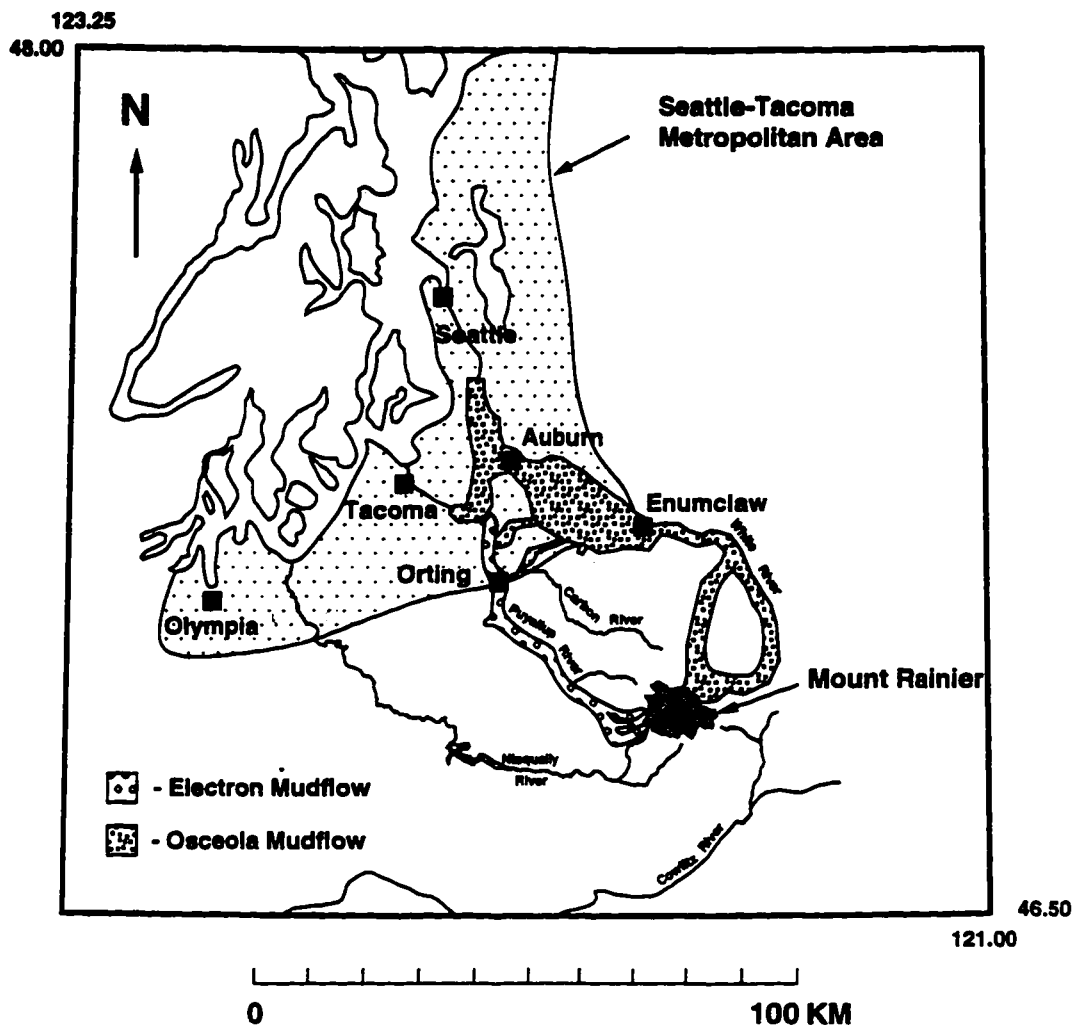


Figure 1-9 Distribution of lahar deposits from Mount Rainier. Shown are the inferred extents of two of the largest Mount Rainier lahars, the Osceola and Electron mudflows (e.g. National Research Council, 1994).

Although focal mechanism studies suggest that it is not a single continuous fault (Malone et al., 1991), no attempt has yet been made to estimate the maximum size of the largest potential earthquake on the WRSZ.

Several other moderate crustal earthquakes have occurred in association with less well-defined seismic clusters. A M_l 4.8 earthquake (5.6 km depth) occurred near Ohanapecosh in Mount Rainier National Park in 1974 (Crosson and Lin, 1975), which I refer to as the Ohanapecosh earthquake (Figure 1-8). Its location lies within a very diffuse band of shallow earthquakes several km east of Mount Rainier (Figure 1-1), and its relationship to the WRSZ is unclear. The M_l 5.0 1981 Goat Rocks

earthquake (7.3 km depth) occurred in a distinct cluster of earthquakes (mainly aftershocks) referred to as the Goat Rocks Zone by Stanley et al. (1996) (Figure 1-8). In 1984 a M_l 4.3 event (8 km depth) occurred roughly 15 km NE of Wenatchee (labeled "Wenatchee" in Figure 1-8) on the southern edge of an oblate cluster of earthquakes that I refer to as the Chelan Seismic Zone (CSZ) (Figure 1-8). The relationship between the CSZ and other seismicity trends, as well as regional tectonics, is not at all clear, and would be a fruitful area for future research. In 1987, M_l 4.3 and M_l 4.1 earthquakes (18 km depth) occurred within two hours of each other roughly 15 km NW of Yakima (labeled "Yakima" in Figure 1-8) in a very diffuse band of seismicity extending from the Tri-Cities area NW to the Cascade Crest, roughly parallel to the Yakima Fold Belt and the OWL. Finally, the M_l 4.9 1989 Storm King Mountain earthquake (18.5 km depth) occurred within a diffuse band of earthquakes that appears in map-view to connect the WRSZ and SHZ (Figure 1-1 and Figure 1-8) (Ludwin et al., 1994; Stanley et al., 1996). This band has been inferred to represent a step-over region where dextral strike-slip motion is transferred from the SHZ to the WRSZ by Stanley et al. (1996).

It is possible, even likely, that most of these zones do not reflect single distinct faults. However, little is known about the 3-D structure in the GMR at the depths (5 - 18 km) of these more diffuse clusters of seismicity. Thus one of the goals of my work is to derive an image of the 3-D velocity structure beneath the GMR and to look for associations between these seismic zones and major structural boundaries in the resultant image. This will hopefully result in a better understanding of seismic hazards in the GMR.

1.3.3 Volcano-Tectonic Earthquakes

Significant numbers of volcano-tectonic earthquakes occur beneath both Mount St. Helens and Mount Rainier (Figure 1-10). Mount St. Helens currently averages between 10 and 20 well-located events per month, whereas Mount Rainier averages between 0 and 5. Depths for Mount St. Helens earthquakes (after 1980) range from 0 to 10 km, and are thought to be directly related to magmatic processes occurring within the conduit system (Barker and Malone, 1991; Mastin, 1994; Moran, 1994). Depths for Mount Rainier earthquakes are quite shallow, although the exact depth range is unknown due to large uncertainties in velocity structure as well as poor station distribution prior to 1989 (Moran et al., 1995; see section 3.2.2).

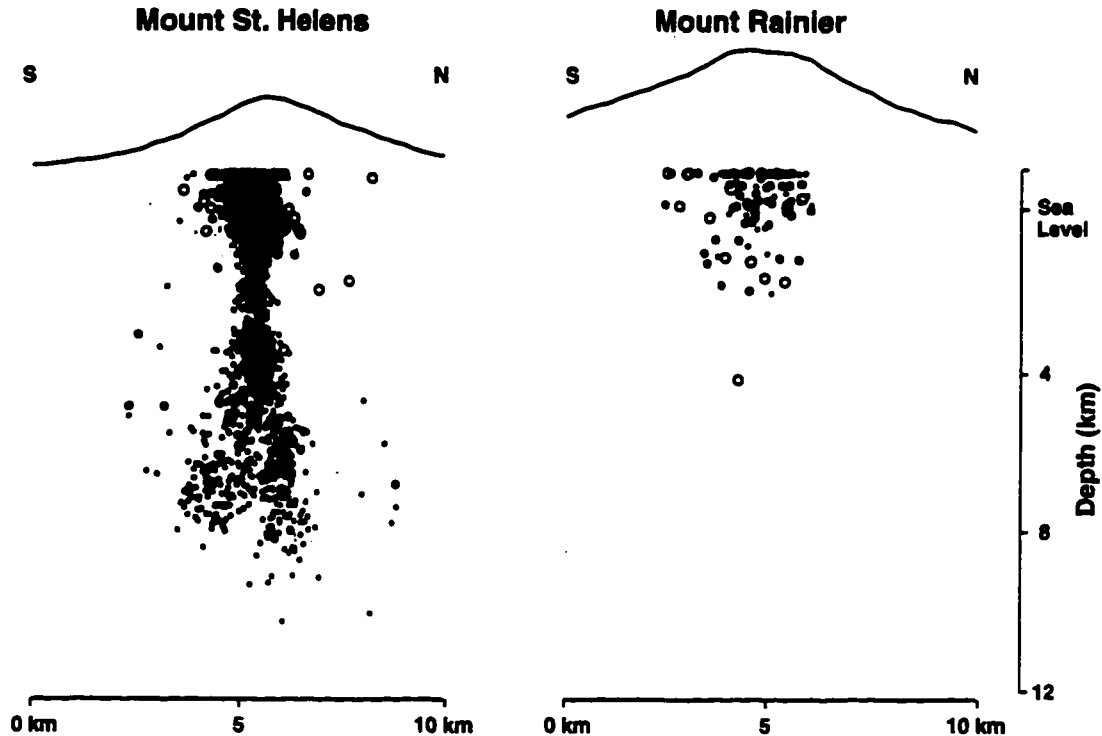


Figure 1-10 Cross-sections of seismicity beneath Mount St. Helens and Mount Rainier. Both plots are drawn to the same scale, and there is no vertical exaggeration. Included are all events occurring between 1981 and 1996. Hypocenters are from the PNSN catalog. Depths have been shifted upwards 1.1 km, the average elevation of stations near each volcano (see explanation in section 4.4.4).

The source of stress for volcano-tectonic earthquakes beneath Mount Rainier is unknown. Candidate stress sources include regional tectonic forces, gravitational forces related to the loading of the crust by the edifice, gravitational forces related to the progressive disintegration of the edifice, volumetric forces associated with an active magmatic intrusion, and volumetric and/or thermal forces associated with cooling magmatic bodies and concomitant hydrothermal circulation. Using routine hypocenters from the PNSN catalog, earthquakes beneath Mount Rainier appear in map-view to define a NE-SW-trending zone across the volcano (see Figure 4-18), suggesting that they are occurring along a fault either below or within the edifice. However, Moran et al. (1995) used a pseudo-Master Event scheme to relocate these earthquakes and found that the new locations grouped in several disconnected clusters. This finding suggests that the linear trend is likely an artifact created by the use of an inappropriate 1-D velocity model in routine PNSN catalog

locations. It also suggests that a 3-D velocity model of the local region around and including Mount Rainier could significantly improve the accuracy of locations beneath Mount Rainier.

1.4 Previous Seismological Investigations in the GMR

Several previous seismological investigations into the subsurface structure of parts of the GMR have been performed, involving both active (i.e. human generated) as well as passive (i.e. naturally occurring) seismic sources. In Chapter IV I compare the results of some of these studies to my LET-derived velocity model. In this section I briefly describe these studies.

1.4.1 Active Source Studies

A series of reversed and unreversed refraction profiles were performed near the western edge of the Columbia Plateau in 1984, the results of which were published by Catchings and Mooney (1988) and Glover (1985) (see "Glover (1985) in Figure 1-11). Results from this work include a contour map of the thickness of the Columbia River Basalts (ranging from 1 to 5 km), an isopach map of Tertiary sediment thickness beneath the basalts (ranging from 3 to 7 km), and a contour map of depths to the crystalline basement beneath the sediments (ranging from 4 to 10 km).

A wide-angle seismic refraction/reflection experiment was carried out on the Columbia Plateau near the cities of Yakima, Ellensburg, and Wenatchee (see "Jarchow et al. (1994)" in Figure 1-11) (Jarchow et al., 1991 and 1994). Results from this experiment include the successful imaging of the base and thickness of the CRBG along the profile, the imaging of a 2-5 km-thick package of Tertiary sediments below the CRBG, and the imaging of basement rocks beneath the sediments including a basement high that is inferred to represent the dividing line between the Swauk and Chumstick basins. These results are independently supported by results from several ~4 km-deep wells drilled near the profile.

Stanley et al. (1992), Gwilliam et al. (1994), and Stanley et al. (1994) published interpretations from a seismic reflection experiment run along an east-west transect through the southern Washington Cascades (see "Stanley et al. (1992)" in Figure 1-11) (the raw data can be found in Gwilliam et al. (1994)). The primary results of this experiment include the apparent imaging of the top of the SWCC, as well as a hypothesized eastward-dipping thrust fault located near Packwood. Several wells

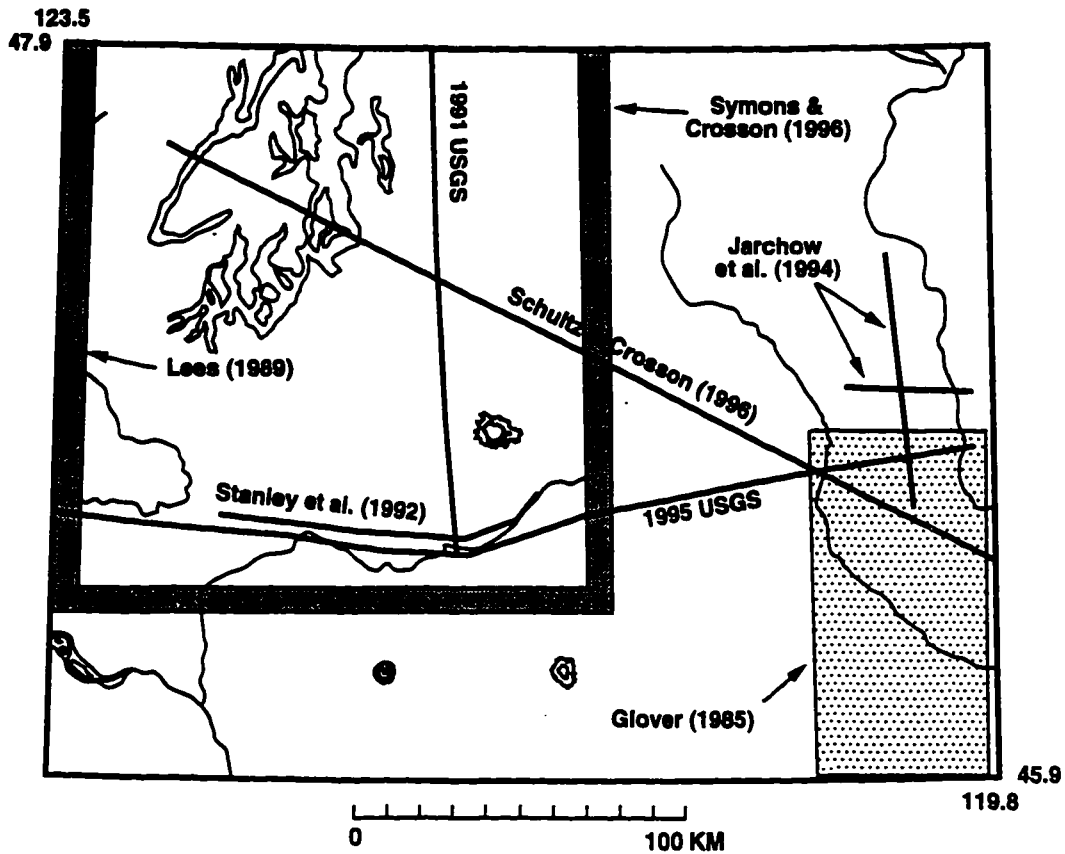


Figure 1-11 Locations of seismic experiments performed in the GMR. See text for explanations of labels.

located on the western end of the profile provide independent support for their interpretations (Stanley et al., 1994); however, there are no such constraints for the eastern end. The seismic data from this experiment are in general of poor quality, and are only adequate for interpretation down to 8-10 km (Stanley et al., 1992).

In 1991 a seismic refraction experiment was performed along a north-south transect through Puget Sound, running approximately 20 km west of Mount Rainier and terminating along the east-west seismic reflection profile described above (see "1991 USGS" in Figure 1-11) (Gridley, 1993; Miller et al., 1997). The resultant velocity model (based on P-wave arrivals) extends from the surface down to 20 km, and can easily be compared to velocity structures in the LET image described in Chapter IV.

Finally, in 1995 a seismic refraction experiment was performed along an east-west transect extending from the coast to the western edge of the Columbia Plateau (see "1995 USGS" in Figure 1-11) (Luetgert et al., 1995; Parsons et al., 1996). Modeling of the upper crust in the profile is still in progress (T. Parsons, personal communication), and a final 2-D P-wave velocity model from this experiment isn't available for direct comparison to the LET image from my work. However, the sources from both the 1995 and 1991 refraction experiments can be used to test the accuracy of earthquake locations in my LET model (see section 4.2.2).

1.4.2 Passive Source Studies

Lees (1989), Lees and Crosson (1989 & 1990), and Lees (1992) performed several LET inversions for P-wave velocity structure both in Puget Sound and at Mount St. Helens (see "Lees (1989)" in Figure 1-11) using data from the PNSN catalog. There is a significant amount of overlap between Lees (1989) study area and the GMR, and it is natural to compare the two sets of images in this area of overlap (see section 5.4).

Schultz and Crosson (1996) performed a seismic refraction study along a profile parallel to the OWL (see "Schultz & Crosson (1996)" in Figure 1-11) using earthquake data recorded on PNSN stations. They derived a 2-D P-wave velocity model that extended from the surface to depths of greater than 50 km. However, the model was most sensitive to velocity and depth variations along the MOHO, and has minimal resolution in the upper crust.

Finally, Symons and Crosson (1996) showed preliminary results from a non-linear inversion for P-wave velocity structure in Puget Sound (see "Symons and Crosson (1996)" in Figure 1-11). They use earthquake data from the PNSN, and perform a simultaneous LET inversion for velocity and hypocenter parameters (see section 2.3.1). Their methodology differs in several ways from the methodology described in Chapter 2. There is significant overlap between their study area and the GMR, so it will be very instructive upon completion of their work to compare their model with the GMR model. Such a comparison can potentially provide important insights into the relative merits of different approaches to LET.

II. Local Earthquake Tomography

2.1 Introduction

One of the primary goals of my dissertation is to derive a 3-D image of the P-wave velocity structure for the GMR extending from the surface to 30 km below sea level. To do this I employ a technique known as Local Earthquake Tomography, or LET (e.g. Thurber, 1993). The term tomography derives from the Greek word 'tomo,' or slice, and the term seismic tomography refers to the reconstruction of a velocity field from the observation of many travel times from seismic waves traveling through the velocity field (Lee and Pereyra, 1993). In LET, the goal is to derive a 3-D image of the velocity structure for some region of the earth using arrival times recorded by a seismograph network from local earthquakes. If the velocity in the medium is constant and the time (origin time) and location (hypo-center) of an earthquake are known, then one can very easily solve for velocity using the basic equation

$$v = \frac{R}{T} \quad (\text{EQ 2.1})$$

where v = velocity (km/sec), R = length (km) of the raypath from earthquake (source) to seismograph station (receiver), and T = travel time (sec) from source to receiver. In this case, one raypath is sufficient to determine the velocity of the medium.

However, LET is in general much more complex. Velocity is usually not constant, which means that raypaths are not straight lines, and the travel time is determined by the integral of the velocity along the raypath;

$$T_i = \int_{\text{raypath}} \frac{dl}{v} \quad (\text{EQ 2.2})$$

where T_i is the travel time of the i th ray and v is the velocity along the a line segment dl along the raypath of the i th ray. Solving equation 2.2 for v is potentially quite problematic, since in general we don't know exactly where or when an earthquake occurred, nor do we know the exact raypath from a source to a receiver. To make things even more complicated, the raypath depends on the velocity structure (which we are trying to determine), making the problem non-

linear and thus potentially very difficult to solve. There are many choices to be made in LET. In this chapter I describe the particular flavor of LET that I use, which is based on the methodology used by Lees (1989) in his inversion for velocity structure in Puget Sound.

2.2 Basic Theory

2.2.1 Wavefronts and Raypaths

The seismogram recorded at a seismograph station is due to the arrival of many different pulses of energy ("wavefronts") generated by the rupturing of the earth along a fault or fault segment. The path that each wavefront travels can be represented by a line drawn normal to the wavefront at any given point (Figure 2-1). This line is often referred to as a ray, and the path traveled by the ray from source to receiver is called the raypath. It is important to note that rays are not physical entities, but are mathematically convenient means for representing the movement of wavefronts through the Earth. The "width" of a ray is often be treated as infinitely thin. This is only valid if the dominant wavelengths are small compared to the size of geological bodies in the region of interest (this is often referred to as the high frequency approximation). However, wavefronts recorded at seismometers are influenced by structure a certain distance away from the calculated raypath, and thus rays can be thought of as having a finite thickness.

Nolet (1987) derives a simple relationship between raypath length, wavelength, and ray "width" which is valuable for gaining intuition into the resolving capabilities of an individual ray. The basic idea comes from Huygen's principle, which states that any point along a wavefront can be considered to be a point source from which secondary wavefronts are emitted. If these wavefronts are in phase with the primary wavefront, then they will constructively interfere, and thus the structure (or velocity) at these secondary sources will influence the wavefront observed at the seismic station. This is graphically demonstrated in Figure 2-1 for a medium with constant velocity. The minimum travel time path from source to receiver is SR. The plane σ represents the wavefront at some intermediate point A. Point B is another point on σ , which emits secondary wavefronts once the initial wavefront reaches it. SB is the minimum travel time path for the initial wavefront from the source to point B, and BR the minimum travel time path for a secondary wavefront from point B to receiver. As long as the difference in distance between SAR and SBR is less than $\frac{\lambda}{4}$

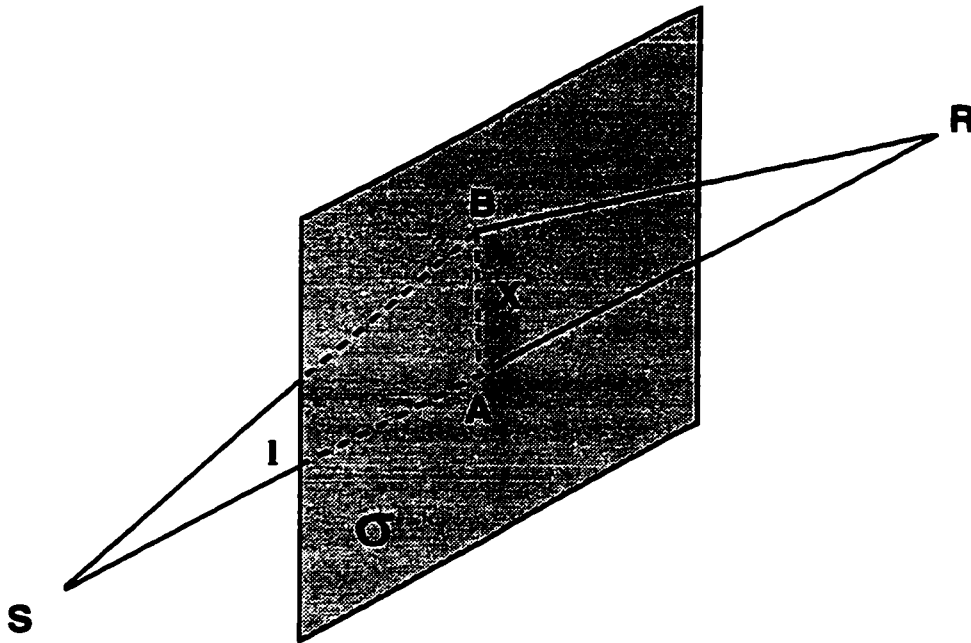


Figure 2-1 Diagram showing geometry used to derive estimates of ray widths in equation 2.3. Figure modified from Nolet (1987). The plane σ represents the wavefront at points A and B.

(where λ is the wavelength), the secondary wavefronts generated at point B will add constructively with the primary wavefront and influence the wavefront observed at R. The maximum distance X that point B can be from A and still contribute wavefronts that will constructively interfere can be written as

$$\sqrt{X^2 + l^2} + \sqrt{X^2 + (R-l)^2} - R \leq \frac{\lambda}{4} \quad (\text{EQ 2.3})$$

where l is the distance along the raypath from the source to point A, and R is the total pathlength along SAR. X can be thought of as the radius of a ray. The dominant frequency, f , of GMR earthquakes is observed to be around 10-12 Hz. Using the relation

$$\lambda = \frac{v}{f} \quad (\text{EQ 2.4})$$

with a velocity v of 6 km/sec, λ is roughly 0.5 km. Table 2.1 shows sample ray widths for different raypath lengths and values of l (note that the raypath width is $2X$).

Table 2.1: Theoretical Raypath Widths for Different Points Along a Ray

Raypath Length (km)	Distance Along Raypath (l, km)	Ray Width (2X, km)
100	0.0	0.25
100	5.0	2.20
100	25.0	4.32
100	50.0	5.0
200	0.0	0.25
200	25.0	4.8
200	50.0	6.14
200	100.0	7.08

As a rule, rays are thinnest at their endpoints and thickest at their midpoints. The raypath thickness can also be thought of as the amount of structure that is being averaged along a single ray. Thus a 200 km long raypath will be sensitive to the average velocity of a 7 km-thick section of rock at its midpoint.

It would seem that the most appropriate way to handle raypaths would be to treat them as ray tubes. However, for a large dataset this would dramatically increase the amount of computation required for a LET experiment, which is already considerable. Thus for simplicity rays in this dissertation are treated as infinitely thin. The longest rays in my LET inversion are 150 km (see section 3.4), thus the maximum width of a raypath is ~6 km. This places a theoretical limit of 6 km (or 2-3 constant velocity blocks; see section 2.2.2) on the minimum size of structures that can be resolved in my LET-derived model, implying that structures in the model that are smaller than 6 km should be interpreted with care.

2.2.2 The Tomographic Problem - Basics

The basic theory of seismic tomography was first described by Aki et al. (1977). The travel time T along a raypath mathematically is described as

$$T = \int_{\text{raypath}} \frac{dl}{v(\mathbf{x})} \quad (\text{EQ 2.5})$$

where dl is the length of a ray segment, \mathbf{x} is the positional vector, and $v(\mathbf{x})$ is the velocity at the location defined by \mathbf{x} . Since T does not linearly depend on $v(\mathbf{x})$ in this

equation, it is mathematically convenient to write T in terms of the slowness $s(\mathbf{x})$, which is simply the reciprocal of the velocity;

$$s(\mathbf{x}) = \frac{1}{v(\mathbf{x})} \quad (\text{EQ 2.6})$$

To simplify notation, I will drop the positional vector term and refer to the slowness simply as s . Equation 2.5 now can be written as

$$T = \int_{\text{raypath}} s dl \quad (\text{EQ 2.7})$$

This is the equation we wish to solve. The forward problem is reasonably straightforward; given a slowness model and a source and receiver, the travel time is computed by taking the integral of the slowness along the raypath. The only tricky part is determining the raypath. However, the inverse problem (solving for the slowness given a travel time) is more problematic. Our ability to construct a raypath is dependent upon our knowledge of the earth's slowness, which in the inverse problem is exactly what we want to solve for. The dependency of the raypath on s makes this problem non-linear. To make the problem soluble, we linearize it by first subdividing s into a reference model s_0 that is known and a perturbational model δs that is unknown. Equation 2.7 then becomes

$$T = \int_{\text{raypath}} s dl = \int_{\text{raypath}} s_0 dl + \int_{\text{raypath}} \delta s dl \quad (\text{EQ 2.8})$$

The raypaths in the reference model s_0 are known. Fermat's Principle states that travel time is to first order invariant for small perturbations to the raypath (Aki and Richards, 1980). This means that if the perturbations in δs are small enough, we can use the raypaths determined in our reference model as our raypaths in the perturbational model (e.g. Aki et al., 1977). Mathematically this can be written as

$$T = \int_{\text{raypath}} s_0 dl + \int_{\text{raypath}} \delta s dl \sim \int_{\text{raypath}_0} s_0 dl + \int_{\text{raypath}_0} \delta s dl \quad (\text{EQ 2.9})$$

This approximation places a great deal of importance on the reference, or starting, model s_0 , since if s_0 is not sufficiently close to the truth, δs will be too large and the approximation made in equation 2.9 will be incorrect. The starting model for this study, and the method used to construct it, is described in section 4.1.1.

Now our problem is effectively linear, since the raypaths are known (to zeroth order), and the travel times can be readily inverted for slowness. Equation 2.9 can be re-written as

$$T - T_0 \sim \int_{\text{raypath}_0} s dl + \int_{\text{raypath}_0} \delta s dl = \int_{\text{raypath}_0} \delta s dl = \delta T \quad (\text{EQ 2.10})$$

where T are the observed travel times, T_0 the computed travel times in the reference model, and δT are travel time residuals. Our goal, simply stated, is to invert equation 2.10 for the slowness perturbations δs . To find the absolute slowness, we simply add δs to s_0 .

In order to solve equation 2.10 in a reasonable amount of computing time, some means for representing the earth in terms of a finite number of parameters is required. Previous investigators have used nodes to parameterize their model, employing a linear or cubic spline interpolation scheme to determine the velocity at each node (e.g. Thurber, 1983; Vandecar, 1991; Shalev, 1993). Other investigators parameterize their models with 3-sided cubes or "blocks", each of which has a single slowness value δs_j (e.g. Aki et al., 1977; Lees and Crosson, 1989). Lees and Shalev (1992) showed that use of different parameterizations does not appear to affect the resultant slowness model. Following Lees (1989), I use constant slowness blocks. This representation allows us to write equation 2.10 in terms of a discrete number of elements,

$$\delta t_i = \sum_{j=1, m} A_{i,j} \delta s_j \quad (\text{EQ 2.11})$$

where $A_{i,j}$ is the partial derivative of δt_i with respect to δs_j (in words, the length of the i th raypath segment in the j th block), and δs_j is the slowness perturbation in the j th block. For many raypaths, this can be written in matrix notation;

$$\delta t = A \delta s \quad (\text{EQ 2.12})$$

where δt is a vector of travel time residuals, δs a vector of slowness perturbations, and A a matrix of partial derivatives (referred to in linear algebra terminology as the Jacobian matrix). The matrix A has dimensions ($n \times m$), where n is the number of observations (rows) and m the number of unknowns (columns).

Our problem can now be boiled down to attempting to compute the inverse of the matrix A and premultiplying it to the vector δt , which will give us δs . However, A is in general not square and not of full rank, and therefore A^{-1} does not exist. In addition, this problem is in general over-determined (more data than unknowns) and inconsistent (dissimilar travel times observed along similar raypaths), meaning that there is no unique solution but an infinite number of "almost-but-not-quite" solutions (Menke, 1984). A logical criterion for selecting one solution is to look for the model that minimizes some measure ϕ of the misfit between the observed and the computed travel times. Mathematically, this is written as

$$\min \{ \phi (\delta t - A\delta s) \} \quad (\text{EQ 2.13})$$

A common approach is to minimize the sum of the squares of the residuals,

$$\min \{ (\delta t - A\delta s)^T (\delta t - A\delta s) \} \quad (\text{EQ 2.14})$$

where $(\delta t - A\delta s)^T$ signifies the transpose of $(\delta t - A\delta s)$. When equation 2.14 is minimized with respect to δs , we get

$$-A^T \delta t + A^T A \delta s = 0, \quad (\text{EQ 2.15})$$

or

$$A^T \delta t = A^T A \delta s \quad (\text{EQ 2.16})$$

Equation 2.16 is solved for δs by inverting the matrix $A^T A$ and premultiplying its inverse to both sides of equation 2.16, giving us an estimate of δs

$$\delta s' = A^\dagger \delta t \quad (\text{EQ 2.17})$$

where A^\dagger is the generalized inverse, and $\delta s'$ is the solution that minimizes the residuals δt in a least squares sense (Crosson, 1976; Aki et al., 1977).

In addition to being over-determined and inconsistent, the problem is also under-constrained, since there are some blocks that are not 'hit' by any rays and are thus not constrained by the data. Because of this, the solution to equation 2.16 will in general be non-unique and highly unstable where there are few or no raypaths. For this reason constraint equations are added, so as to effectively damp out the unstable elements of the solution. In this study I use a second-order differential operator

L (referred to as the horizontal Laplacian) to constrain the model roughness in 2-D to be small (Menke, 1984; Lees, 1989; Lees and Crosson, 1990);

$$\nabla^2 \delta s = L \delta s = 0 \quad (\text{EQ 2.18})$$

This operator is applied to each block (x_i, y_j) in the model via the difference equation

$$4\delta s(x_i, y_j) - \delta s(x_{i+1}, y_j) - \delta s(x_{i-1}, y_j) - \delta s(x_i, y_{j-1}) - \delta s(x_i, y_{j+1}) = 0 \quad (\text{EQ 2.19})$$

These additional constraints (one for each parameter) are added to equation 2.12, giving us (in matrix form)

$$\begin{bmatrix} A \\ \lambda L \end{bmatrix} \delta s = \begin{bmatrix} \delta t \\ 0 \end{bmatrix} \quad (\text{EQ 2.20})$$

where L is the Laplacian operator and λ is a weight referred to as the damping parameter (note that λ no longer represents wavelength).

λ can be varied depending on the degree of smoothing desired. If λ is large, then more weight will be placed on the constraint equations relative to the data, resulting in a smooth model less susceptible to large errors in the data. If λ is small, more weight is given to the data, resulting in a rougher model with more vulnerability to errors in the data, especially in blocks with few or no 'hits'. One of the important and underestimated aspects of LET is selecting the optimal value for λ , since the size of λ can dramatically affect the resulting model. The method that I use for selecting λ is described in section 2.5.3.

As was alluded to above, the data used in LET (phase arrival times) are by no means perfect. There is always a degree of error associated with the estimation (or pick) of the arrival time of a phase. This error depends primarily on data quality and the "eye" of the data analyst. In addition, the pick precision is also influenced by the sample rate used to convert analog seismic signals from seismograph stations into a digital format required for computer manipulation (for example, see section 3.2.2). The routine processing of earthquake information at the PNSN includes the assigning of an uncertainty for each pick. The most precise picks have an uncertainty of ± 0.01 sec, the sampling rate used since 1980 (Steve Malone, personal communication).

This uncertainty estimate can be used to assign a relative weight to each pick, allowing picks from higher quality data to have more influence over the solution. This is accomplished by pre-multiplying equation 2.12 by the inverse of the uncertainty for the i th pick;

$$\frac{1}{\sigma_i} \left(\delta t_i = \sum_{j=1, m} A_{i,j} \delta s_j \right) \quad (\text{EQ 2.21})$$

where σ_i is the uncertainty for the i th pick. To simplify notation a weighting matrix W is formed, which is simply the identity matrix multiplied by the vector of all uncertainties assigned to all n picks;

$$W = \begin{bmatrix} \frac{1}{\sigma_1} & 0 & \dots & \dots & 0 & 0 \\ 0 & \frac{1}{\sigma_2} & \dots & \dots & 0 & 0 \\ \dots & \dots & \dots & \dots & \dots & \dots \\ 0 & 0 & \dots & \dots & \frac{1}{\sigma_{n-1}} & 0 \\ 0 & 0 & \dots & \dots & 0 & \frac{1}{\sigma_n} \end{bmatrix} \quad (\text{EQ 2.22})$$

Now equation 2.21 can be written for all raypaths as

$$W \delta t = W A \delta s \quad (\text{EQ 2.23})$$

and the system of equations becomes

$$\begin{bmatrix} WA \\ \lambda L \end{bmatrix} \delta s = \begin{bmatrix} W \delta t \\ 0 \end{bmatrix} \quad (\text{EQ 2.24})$$

This is referred to as weighted damped least squares (e.g. Lees, 1989). To solve equation 2.24, the functional

$$\|WA \delta s - W \delta t\|^2 + \|\lambda L \delta s\|^2 \quad (\text{EQ 2.25})$$

is minimized with respect to δs , resulting in

$$A^T W^T W \delta t = (A^T W^T W A + \lambda^2 L^T L) \delta s \quad (\text{EQ 2.26})$$

It is equation 2.26 which we seek to solve. Unfortunately, although computing power has grown incredibly fast in the last half decade, it is still too memory intensive to compute and store the matrix $\mathbf{A}^T\mathbf{A}$ for problems with more than a few thousand observations and unknowns, not to mention computing its inverse. For example, in my inversions for the GMR I use a grid of 110,880 constant slowness blocks and approximately 72,000 rays (see section 4.1.2). This results in an \mathbf{A} matrix with $(72,000 * 109,890) = \sim 8$ billion elements. The storage of \mathbf{A} would require roughly 32 gigabytes of RAM, which is available only on high-powered super-computers. Although \mathbf{A} is sparse (each ray hits only a small percentage of the total number of blocks), $\mathbf{A}^T\mathbf{W}^T\mathbf{W}\mathbf{A}$ is dense, so directly solving for $(\mathbf{A}^T\mathbf{W}^T\mathbf{W}\mathbf{A} + \lambda^2\mathbf{L}^T\mathbf{L})^{-1}$ is at present impossible, or at least computational very expensive.

However, there are methods available for approximately solving least squares problems such as equation 2.26 without explicitly forming $\mathbf{A}^T\mathbf{W}^T\mathbf{W}\mathbf{A}$ if \mathbf{A} is sparse. Fortunately \mathbf{A} is sparse in LET, since each ray hits only a small fraction of the total number of blocks in a model (thus most elements in each row will be zero). Several types are in use today in LET, the most common of which are back-projection (e.g. Humphreys and Clayton, 1988) and conjugate-gradient (e.g. Lees, 1989) methods. Spakman and Nolet (1989) demonstrated that the conjugate-gradient method places the least structure in nodes with the fewest 'hits', whereas back-projection methods tended to place the most structure at these nodes. Occam's razor states that one should seek the solution that is the simplest (i.e. that has the least structure), thus conjugate-gradient methods are preferable to back-projection. I use a conjugate-gradient method derived by Paige and Saunders (1982) termed LSQR. This is an iterative method which continues to run until some stopping criterion is reached. Lees (1989) stopped LSQR after 30 iterations, regardless of the rate of convergence. It is more preferable, however, to use some measure of either residual reduction or model change as the stopping criterion, because this threshold will likely vary depending on the convergence properties of a given inversion. I use a measure of the model change Δs , which is computed as follows:

$$\Delta s = \frac{\|\delta s_j - \delta s_{j-1}\|}{\|\delta s_{j-1}\|} \quad (\text{EQ 2.27})$$

In words, Δs is the ratio of two L1 norms; the size of the difference between the models from the current (δs_j) and previous (δs_{j-1}) LSQR iterations (the numerator),

and the size of the previous model perturbation (the denominator). The denominator is a factor that normalizes the numerator. After trial and error, I selected a value of 0.01 for Δs , which usually resulted in ~150 iterations of the LSQR algorithm for each inversion step.

2.3 Complications in the Tomographic Method

The methodology described in section 2.2.2 is reasonably straight-forward and virtually identical to the approach taken by Lees (1989). In this section I describe several not-so-straightforward problems in LET where I diverge from Lees (1989).

2.3.1 Slowness-Hypocenter Coupling

Probably the most important not-so-straightforward problem is the assumption made to this point that the positions of all sources are known. This is in fact only the case when sources have known locations and origin times, such as timed explosions. The positions in space and time for all other sources are estimated by a location program. If the estimated location of a given event does not correspond to the actual location, then there will be a travel time residual associated with the mislocation of that event, in addition to a travel time residual associated with the unmodeled slowness structure. Thus equation 2.23 should be written as

$$W\delta t = WA\delta s + WB\delta x \quad (\text{EQ 2.28})$$

where δx are the 4 hypocenter parameters for each event (x, y, z position and origin time), and B is a Jacobian matrix that contains partial derivatives of the four hypocenter parameters with respect to δt . This equation demonstrates the inherent coupling of slowness and hypocenter parameters. There are two approaches to solving equation 2.28. The first is a joint inversion, where one forms

$$W\delta t = \begin{bmatrix} WA & WB \end{bmatrix} \begin{bmatrix} \delta s \\ \delta x \end{bmatrix} \quad (\text{EQ 2.29})$$

and solves for δs and δx . One potential problem with this approach is that it forces each hypocenter to be located in the same manner, i.e. with the same damping, same number of iterations, etc. Standard location routines (which solve

$$W\delta t = WB \delta x \quad (\text{EQ 2.30})$$

in a linearized damp least squares sense (see for example HYPO71, Lee and Stewart 1981)) commonly allow the number of iterations and degree of damping to vary depending on the convergence properties of the solution for each earthquake. If the solution converges rapidly, iterations are few; if it converges slowly, iterations are many, and the damping is sometimes increased to decrease instabilities in the solution. A joint inversion would not necessarily allow for this location-by-location variability.

An alternative to this approach is the parameter separation method due to Spencer and Gubbins (1980) and Pavlis and Booker (1980). The upshot of this approach is that it allows for the separation of equation 2.28 into two problems which can be solved separately but in a manner that accounts for the intrinsic coupling. This is accomplished via the construction of an annihilation operator \underline{Q} . If the location problem in equation 2.28 is solved first (independently of the velocity model problem) for a single event, we get

$$\delta x' = (\underline{B}^T \underline{B})^{-1} \underline{B}^T W \delta t \quad (\text{EQ 2.31})$$

where $\underline{B} = \underline{W}\underline{B}$ and $\delta x'$ is a least squares estimate of δx . If this estimate of δx is plugged back into equation 2.28, then we get

$$W \delta t = \underline{W}\underline{A} \delta s + \underline{W}\underline{B}(\underline{B}^T \underline{B})^{-1} \underline{B}^T W \delta t = \underline{W}\underline{A} \delta s + \underline{B}\underline{B}^\dagger W \delta t \quad (\text{EQ 2.32})$$

where \underline{B}^\dagger is the generalized inverse. Equation 2.32 can be re-written as

$$(\underline{I} - \underline{B}\underline{B}^\dagger) W \delta t = \delta t' = \underline{W}\underline{A} \delta s \quad (\text{EQ 2.33})$$

where \underline{I} represents the identity matrix and $\delta t'$ is the vector of new weighted travel time residuals created in the relocation step of equation 2.31. This is the approach of Walck and Clayton (1987), Lees (1989), Lees and Crosson (1989, 1990), and others.

The problem with this approach is that the dependence on the source location has been removed from the left-hand side of equation 2.33 (by removing that part of the residual due to mislocation) but not from the right-hand side (Creager and Boyd, 1992). In order to rectify this situation, the part of the location problem that projects into the slowness problem must be removed. A convenient way to do this is to use $\underline{I} - \underline{B}\underline{B}^\dagger$ (the matrix that premultiplies the left-hand side of equation 2.33) as an

annihilation operator. If both sides of equation 2.28 are premultiplied by this operator, then we get

$$\begin{aligned} (I - \underline{BB}^\dagger) W \delta t &= (I - \underline{BB}^\dagger) W A \delta s + (I - \underline{BB}^\dagger) \underline{B} \delta x \\ &= (I - \underline{BB}^\dagger) W A \delta s \end{aligned} \quad (\text{EQ 2.34})$$

The part of the location problem that projects into both sides of equation 2.33 is annihilated from both sides in equation 2.34. This allows us to solve the location and slowness problems separately while still treating the joint problem as coupled.

The computation of $(I - \underline{BB}^\dagger)$ turns out to be relatively trivial. The singular value decomposition (SVD) of the \underline{B} matrix is written as

$$\underline{B} = U \Lambda V^T \quad (\text{EQ 2.35})$$

where U is a matrix of eigenvectors that spans the data space, Λ is a diagonal matrix of eigenvalues, and V is a matrix of eigenvectors that spans the model space (Lanczos, 1961). Using SVD notation, $(I - \underline{BB}^\dagger)$ can be re-written as

$$I - \underline{BB}^\dagger = I - U U^T \quad (\text{EQ 2.36})$$

I use a SVD routine to solve for the location parameters, so computation of $(I - U U^T)$ is straightforward. After each location problem converges, I compute $(I - U U^T)$ and store it in a temporary file to be used later in the slowness problem.

Using equation 2.36, equation 2.34 can be re-written as

$$(I - U U^T) W \delta t = (I - U U^T) W A \delta s \quad (\text{EQ 2.37})$$

To solve the complete slowness problem, we first form the matrix Q ,

$$Q = \begin{bmatrix} (I - U U^T)_1 & 0 & \dots & 0 & 0 \\ 0 & (I - U U^T)_2 & \dots & 0 & 0 \\ \dots & \dots & \dots & \dots & \dots \\ 0 & 0 & \dots & (I - U U^T)_{N-1} & 0 \\ 0 & 0 & \dots & 0 & (I - U U^T)_N \end{bmatrix} \quad (\text{EQ 2.38})$$

which is referred to as the annihilation operator. \mathbf{Q} contains the $(\mathbf{I} - \mathbf{U}\mathbf{U}^T)$ matrices computed for each earthquake. Each $(\mathbf{I} - \mathbf{U}\mathbf{U}^T)$ is a symmetrical matrix with dimensions (nobs x nobs), where nobs is the number of observations for a single earthquake. \mathbf{Q} is also symmetric, but has dimensions of (ntotrays x ntotrays), where ntotrays is the total number of rays in the entire inversion dataset. \mathbf{Q} is quite sparse, with the $(\mathbf{I} - \mathbf{U}\mathbf{U}^T)$ submatrices located along the diagonals. \mathbf{Q} can be thought of as a data covariance matrix (e.g. Crosson, 1976); it contains information about the dependency of a given ray on other rays in the dataset. Equation 2.37 can now be re-written as

$$\mathbf{Q} \mathbf{W} \delta t = \mathbf{Q} \mathbf{W} \mathbf{A} \delta s \quad (\text{EQ 2.39})$$

and equation 2.24 becomes

$$\begin{bmatrix} \mathbf{Q} \mathbf{W} \mathbf{A} \\ \lambda \mathbf{L} \end{bmatrix} \delta s = \begin{bmatrix} \mathbf{Q} \mathbf{W} \delta t \\ 0 \end{bmatrix} \quad (\text{EQ 2.40})$$

One problem with this approach is that the premultiplication of \mathbf{A} by \mathbf{Q} in equation 2.39 results in a matrix that is significantly less sparse than \mathbf{A} . Consider a source in a 6-block model recorded at 5 stations (Figure 2-2):

For this geometry, the \mathbf{A} matrix would look something like

$$\mathbf{A} = \begin{bmatrix} \emptyset \\ \text{Ray1} \\ \text{Ray2} \\ \text{Ray3} \\ \text{Ray4} \\ \text{Ray5} \end{bmatrix} \begin{bmatrix} \text{Block1} & \text{Block2} & \text{Block3} & \text{Block4} & \text{Block5} & \text{Block6} \\ 1 & 0 & 0 & 1 & 1 & 0 \\ 1 & 0 & 0 & 0 & 1 & 0 \\ 0 & 1 & 0 & 0 & 1 & 0 \\ 0 & 0 & 1 & 0 & 1 & 0 \\ 0 & 0 & 1 & 0 & 1 & 1 \end{bmatrix} \quad (\text{EQ 2.41})$$

assuming that the ray segment in each block has unit length. Note that \mathbf{A} is 60% sparse. For this scenario, the \mathbf{Q} matrix would look something like

$$\mathbf{Q} = \begin{bmatrix} a & b & c & d & e & f \\ b & g & h & i & j & k \\ c & h & l & m & n & o \\ d & i & m & p & q & r \\ e & j & n & q & s & t \\ f & k & o & r & t & u \end{bmatrix} \quad (\text{EQ 2.42})$$

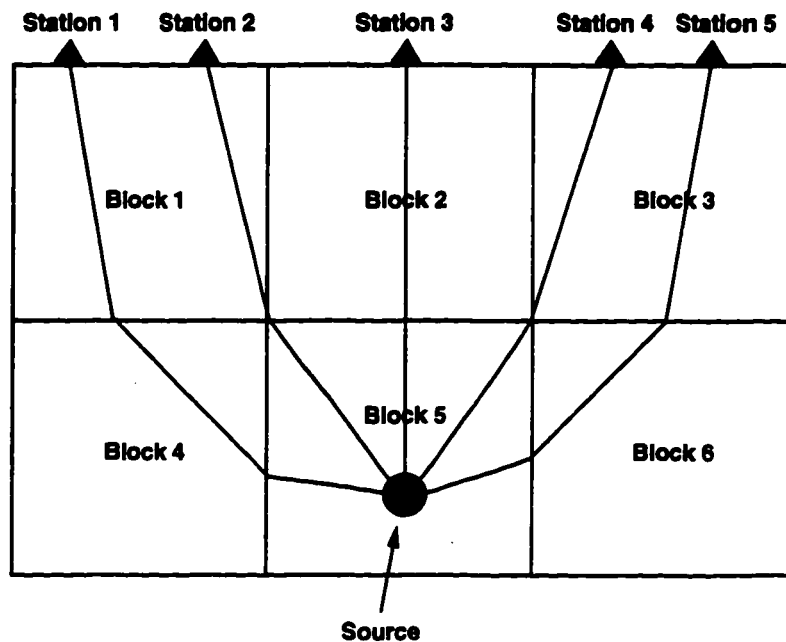


Figure 2-2 Diagram of source in a 6-block model with 5 receivers. Lines correspond to raypaths from the source to each receiver.

where the elements a-u have values ranging from 1 to -1, and are in general non-zero. Pre-multiplying A by Q give us A' ;

$$A' = \begin{bmatrix} a+d+e & (b+i+j) & c+m+n & (d+p+q) & e+q+s & (f+r+t) \\ (a+e) & (b+j) & (c+n) & (d+q) & (e+s) & (f+t) \\ (b+e) & (g+j) & (h+n) & (j+q) & (i+s) & (k+t) \\ (c+e) & (h+j) & (l+n) & (m+q) & (n+s) & (o+t) \\ c+e+f & (h+j+k) & l+n+o & (m+q+r) & n+s+t & (o+t+u) \end{bmatrix} \quad (\text{EQ 2.43})$$

The elements in A' are in general non-zero, meaning that it is 0% sparse. In general, if a block is hit by a ray, it will have a non-zero value for all other rays associated with a given earthquake in the A' matrix, even if the other rays don't hit that particular block. The resultant decrease in sparsity can dramatically increase the amount of RAM and processing time required to invert equation 2.39 (see section 5.1). However, many of these filled-in elements have values close to zero. To reduce RAM requirements CPU time, I introduced a cutoff criterion that zeroed out any elements whose absolute value fell below a certain threshold. Since such a cutoff

can have potentially significant effects on the resultant model, I ran several test single-step inversions, each using all ~75,000 raypaths, with cutoff values ranging from 0 to 10. These tests showed that there was little appreciable difference in resultant models if all elements in A' with absolute values of less than 1.5 were discarded.

To incorporate the parameter separation scheme into the inversion procedure outlined in section 2.2.2, I used the following procedure:

- 1) For each earthquake,
 - 1a) Solve the location problem (equation 2.30) using a damped least squares technique (e.g. Lee and Stewart, 1981). The inverse of B is explicitly calculated using a SVD solver.
 - 1b) Compute $(I - UU^T)$ after the solution has converged and store in a separate file.
- 2) Premultiply the slowness problem $W\delta t = WA\delta s$ (where W is the same weighting matrix used in the location problem) by Q to form equation 2.39.
- 3) Invert equation 2.39 for slowness perturbations $\delta s'$ using LSQR and raypaths traced from the source locations determined in step 1a.

In step 1a) I used a damped least squares location program written by Bob Crosson at the University of Washington. I modified this program to solve the location problem using an SVD algorithm and to compute the annihilation matrix after the final location iteration. Mathematically speaking, use of damping makes the SVD approach incorrect, since damping changes the location problem (equation 2.30) to

$$\begin{bmatrix} WB \\ \alpha \end{bmatrix} \delta x = \begin{bmatrix} W\delta t \\ 0 \end{bmatrix} \quad (\text{EQ 2.44})$$

where α is the damping parameter. This changes $\delta x'$ and makes equation 2.36 incorrect. However, if α is small, then this effect should not be significant. The initial damping value I selected ($\alpha = 0.15$) was chosen so as to both be as small as possible to minimize any possible effects from this problem as well as to be big enough to damp out any large instabilities that arose in the location procedure.

There is a certain amount of controversy about whether or not slowness-hypocenter coupling needs to be formally addressed in seismic tomography. Several investigators (Pavlis and Booker, 1983; Kissling, 1988; Thurber, 1992) have shown that ignoring the coupling can reduce the ability of an inversion to correctly reproduce synthetic velocity/slowness images and earthquake locations, and, more seriously, can cause spurious features to appear in the resultant images. This makes intuitive sense, since a mislocated earthquake will place structure in the wrong part of the model. Because of these and other studies, inversions that have ignored this coupling (e.g. Lees and Crosson, 1989 & 1990) have come under occasionally harsh criticism (e.g. Thurber, 1993). However, although it is unquestionably incorrect from a mathematical point of view to ignore this coupling, solving equation 2.39 can significantly increase computational time and computer memory requirements, as discussed above. The question of whether or not this additional work is worth the effort is addressed in section 5.1, where I compare results from inversions run with and without taking the slowness-hypocenter coupling explicitly into account.

2.3.2 Station Corrections

Station corrections are static time corrections made to all arrival times recorded at a given seismograph station. They are commonly calculated by summing travel time residuals for each station and computing the mean or median. The purpose of the station correction is to account for factors, such as site elevation, site effects, and 3-D velocity (slowness) structure, that are not explicitly included in programs used to calculate travel times. A comparison by Michael (1988) of hypocenters located using a 3-D velocity model with hypocenters located using a 1-D model with station corrections found no significant differences. This indicates that station corrections have a stabilizing influence on locations, justifying their routine use by seismic networks such as the PNSN.

However, their use in LET is potentially problematic. By definition, they contain information about the velocity structure that we want to solve for. If they are removed from the travel time residuals before inversion, then this information is lost. Lees and Crosson (1990) justify the subtraction of station corrections prior to inversion by assuming that most of the velocity information in the correction is due only to structure in the upper 1 km of the crust. Pujol (1995) disputes this claim, however, and suggests that station corrections remove information from at least

the upper 3 km. The upper 1-3 km can be very important for assessing the "correctness" of a 3-D slowness model, since a model should correspond at least broadly to surficial geology (see section 4.2.3).

Can station corrections safely be omitted from an LET inversion? I argue that they can, if the other factors (site effects and site elevation) can be accounted for or can be shown to be negligible. Site elevation can easily be accounted for by tracing rays to the elevation of each seismograph station. Possible site effects include station mislocations as well as systematically biased arrival-times due to structure directly beneath the station. Most PNSN station locations have recently been redetermined with hand-held GPS receivers, which have been shown to be accurate to within 55 meters horizontally and 100 meters vertically (Haase et al., 1995). Errors of that order translate to a reasonably small travel time error of no more than ± 0.02 seconds, so site mislocations can in general be assumed to be insignificant.

If rays are traced to site elevation and site effects can be ignored, then station corrections can be assumed to be due solely to unmodeled velocity structure. Thus their inclusion in LET is undesirable. For these reasons I only use station corrections in the initial location step, where the velocity model is 1-D and thus the potential for mislocation error due to errors in the velocity model is high. The station corrections are determined in a manner similar to Lees (1989). First, earthquakes are fixed at their locations as determined by the PNSN, rays are traced to each station, and the median of all residuals at each station (both within and outside of the GMR) is computed. Next the sources are relocated using the new station corrections, medians are again calculated and added to the station corrections. This procedure is repeated until the station corrections stop changing (usually 3 iterations). The locations determined using these station corrections are then used in the initial step of the slowness inversion; however, the residuals are recalculated without station corrections, so the 3-D velocity structure absorbed by the corrections will instead appear in the slowness model. In section 5.2 I compare slowness models computed with and without stations corrections to estimate their true effect on LET-derived velocity models.

2.3.3 Projecting Points Into a Cartesian Coordinate System

While testing the modifications described above, I encountered an unforeseen problem with the method used by Lees (1989) to project stations and hypocenters from

the global latitude-longitude-depth spherical coordinate system to a local x-y-z cartesian coordinate system (this projection is required to simplify distance calculations and ray tracing within the constant-velocity block parameterization). Lees (1989) uses a method similar to that of Richter (1958) to compute the distance in the x and y direction for each station or hypocenter relative to a reference location (the lower left-hand corner of the model). Lees (1989) then uses these x and y distances as the x and y coordinates for each station or hypocenter in the x-y-z cartesian coordinate system of the model space, computing the distance between pairs of points using the basic distance formula.

The problem with this procedure is illustrated in Figure 2-3. The x and y coordinates for the two stations and one source are computed using the method of Lees (1989) relative to the reference location (0, 0). The x & y coordinates determined in this manner are then used to place sources and receivers in an x-y-z grid (for example, the reference point will be at $x = 0$, station #1 at $x = x_1$, the source at $x = x_2$, and station #2 at $x = x_3$ (these positions are indicated on the x-axis drawn along the bottom of Figure 2-3)). The problem this creates is readily apparent from Figure 2-3; if one uses these x & y coordinates to then determine the distance between points

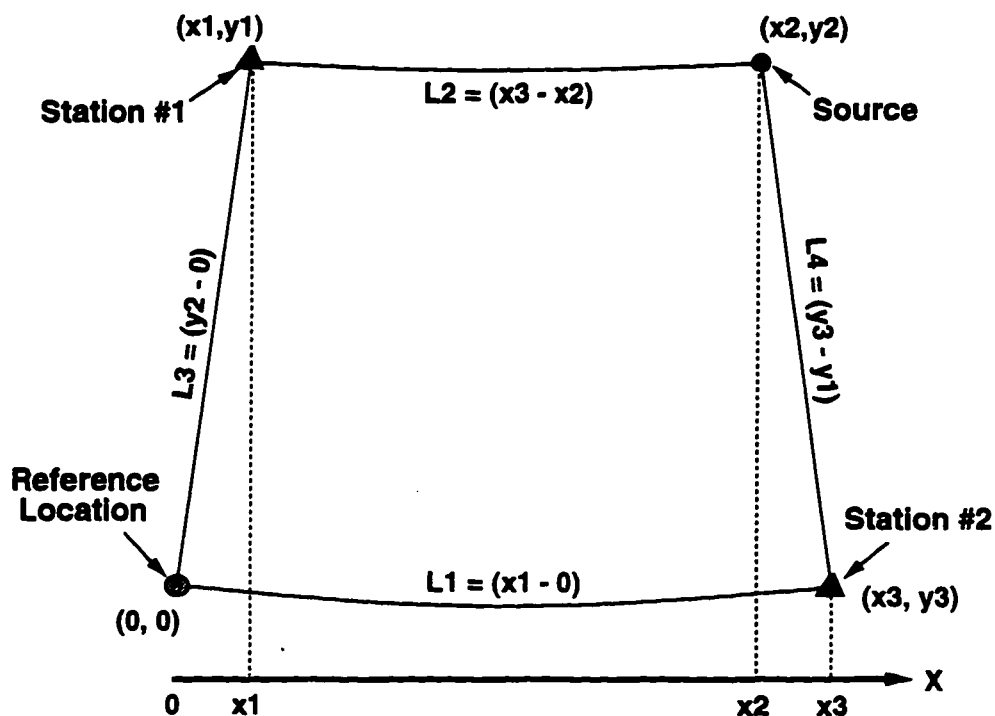


Figure 2-3 Illustration of the projection problem. See text for explanation.

(instead of using Richter's formula), one will come up with a wrong answer. For example, the distance between the source and station #2 in global coordinates is just $L4$ (just the difference between $y2$ and $y3$, since the longitudes of the source and station #2 are the same). However, if one instead computes the distance in the local cartesian coordinate system between the source and station #1 using the x and y coordinates determined relative to the reference location, the resulting distance r is

$$r = \sqrt{(L4)^2 + (x3 - x2)^2} \quad (\text{EQ 2.45})$$

This distance is obviously too large.

The difference between the true distance and the distance computed via the method of Lees (1989) gets progressively larger with increasing distance from the reference location. I found at least one example where the distance was incorrect by more than 2.5 km for a 125 km-long ray. An error of this size would translate into a travel time error of ~0.4 seconds for a medium with a 6 km/sec velocity, on the order of the larger travel time residuals used in my LET inversion. These errors could easily translate into potentially large spurious anomalies in the resultant velocity model. Thus Richter's method (and others resembling it) should not in general be used to project points into a cartesian coordinate system.

To solve this problem, I employed a projection scheme similar to the Lambert Conformal Conic projection used by the U.S. Geological Survey to generate 7.5- and 15-minute topographic maps (Tony Qamar, personal communication). For points projected into the cartesian coordinate system using this pseudo-Lambert Conformal Conic projection, inter-object distances computed using the distance equation were off by only ~60 meters for a 125 km-long ray when compared to distances computed using Richter's method. A distance error of this size would translate into a travel time error of 0.01 seconds, of the same order as the estimated picking error for P-wave arrival times and thus acceptable for a LET inversion.

2.4 Non-linear inversion

2.4.1 Ray-Tracing in 3-D

The theory outlined in section 2.2 and section 2.3 describes a one-step linear inversion, where rays are traced only in the initial 1-D slowness model. The inversion can be made effectively non-linear by iterating over several linear inversion steps. This

requires the retracing of raypaths in each updated model, which in turn requires the ability to raytrace in 3-D. I use an approximate raytracer based on a two-point ray-bending method due to Um and Thurber (1987) and implemented by Lees (1992). Um and Thurber (1987) claim that it is accurate to within 0.1% when compared to an exact raytracer, and almost two orders of magnitude faster.

The basic idea behind the method is illustrated in Figure 2-4. Consider a ray seg-

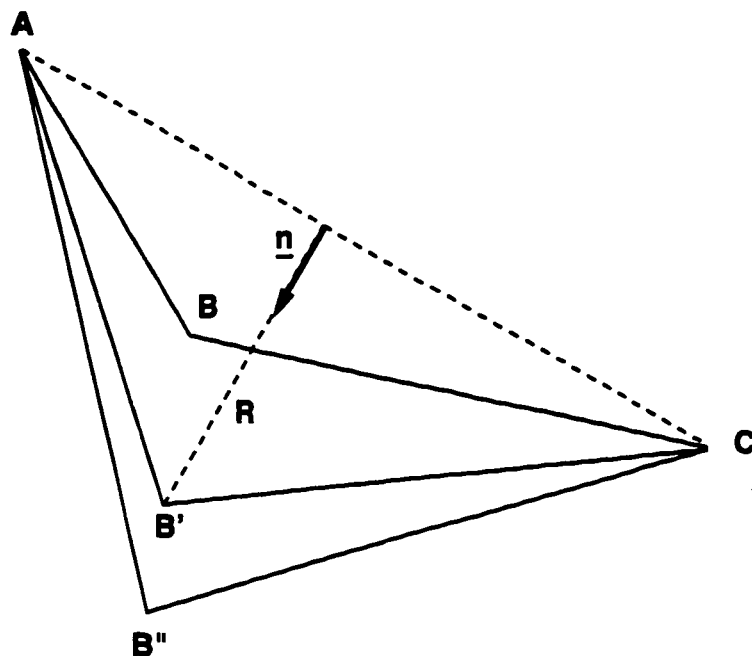


Figure 2-4 Illustration of ray bending method from Um and Thurber (1987).

ment defined by three points, A, B and C. The goal is to move (or bend) point B to a new location B' such that the travel time along the ray segment from A to C is minimized. The direction and amount of movement are both determined relative to the straight line connecting A and C, which approximates the ray vector at point B'. The movement vector \underline{n} is determined using the equation

$$\underline{n} = \nabla V - \frac{(\nabla V \cdot \overline{AC}) \overline{AC}}{\overline{AC}} \quad (\text{EQ 2.46})$$

where \overline{AC} is the unit directional vector of the line connecting points A and C, and \overline{AC} is the length. This equation is derived from the ray equation, which states that the curvature direction of the minimum travel time raypath is antiparallel to the

component of the velocity gradient normal to the ray vector \overrightarrow{AC} (Cerveny et al., 1977) (note that equation 2.46 is simply vector subtraction).

The computation of the amount of movement R is based on the minimization of the following equation, which is derived by using the trapezoidal rule to express the travel time along segments connecting points A , B' and C , with respect to R ;

$$T(R) = \sqrt{L^2 + R^2} \left(\frac{1}{2} \left(\frac{1}{V_A} + \frac{1}{V_C} \right) + \frac{1}{V_{B'}} \right) \quad (\text{EQ 2.47})$$

where L is the distance between C and the midpoint between A and C . The derivation of the equation for R can be found in the appendix of Um and Thurber (1987).

Thus to find B' , we move a distance R along \underline{n} from the midpoint between A and C . This algorithm is applied sequentially to all points along the raypath, leaving only the endpoints unchanged. Since the movement of each point changes the optimal movement vectors and distances for all previous points, a number of iterations are required to reach the approximate minimum travel time path for the entire ray. A raypath is said to have converged if the net travel time decreases by less than a preset travel-time parameter P (the "travel time improvement parameter").

Um and Thurber (1987) found that convergence is generally slow for a raypath with many points, because the amount of movement is underestimated as the number of points along the raypath increases. In order to enhance the rate of convergence, two steps are added. First, the initial ray path is parameterized by only a few points. This initial ray path is 'bent' until travel time convergence is reached. The number of segments along the raypath is then doubled, and the bending process is repeated. Segment doubling continues until a preset maximum number of points N is reached. Second, they added an "enhancement factor" f which changes the location of B' to a new point B'' (Figure 2-4) defined by;

$$B'' = f(B' - B) + B \quad (\text{EQ 2.48})$$

If f is greater than 1, then the amount of perturbation to B is increased, potentially increasing the rate of convergence.

The use of this ray bending algorithm requires two decisions on the part of the user. First, it requires the determination of several input parameters; the maximum number of points N used to define a raypath, the travel time improvement parameter P ,

and the enhancement factor f . A small N , large P (0.1 sec) and large f ($\gg 1$) will result in fast convergence but a large travel time error; a large N , small P (0.0001 sec) and small f (~ 1) will result in slow convergence but a small travel time error. After trial and error, I found that travel times did not decrease appreciably for values of $N \geq 128$, $P \leq 0.001$, and $f \leq 1.1$.

Second, it requires an initial raypath as input into the bending algorithm. Since the bending method is perturbational, the resulting raypath is somewhat dependent upon the initial path. Lees (1992) used the raypath determined by raytracing through a 1-D velocity model as the starting point, and required refracted or direct rays to remain refracted or direct. This requirement is problematic near cross-over points on a travel time curve where the time differences between direct and refracted arrivals can be small. In addition, a direct ray that is slower than a refracted ray in a 1-D model might very well be faster in a 3-D model, and visa versa. These problems are symptomatic of a greater problem, which is that this method (as well as all other ray-shooting and ray-bending methods) only guarantees convergence to a local minimum travel time path, not the global minimum travel time path. In an attempt to overcome this problem, I used both refracted and direct rays as input and selected whichever of the resultant '3-D' raypaths yielded the fastest travel time.

An additional consideration is the use of this algorithm with a model parameterized by constant velocity blocks. The equations for n and R both require knowledge of the velocity (or slowness) gradient, which is not readily available in constant velocity blocks. To compute the velocity gradient field, a single point (node) within each block is assigned the velocity (slowness) of that block, and linear interpolation is used to compute the velocity gradient between each node. However, while testing the ray-bending algorithm I found examples where travel times calculated in the 3-D model along the initial 1-D raypaths were faster than the travel times calculated along the 3-D "bent" raypaths. To ensure that the coded version of the ray bending method was working correctly, I ran further tests and found that the method always converged to at least a local minimum travel time path in the interpolated velocity model. I also examined the 3-D ray paths in the context of the 3-D velocity model, and observed that rays correctly bent away from low velocity features and towards high velocity features. These tests indicate that the raybending algorithm is working properly.

This problem thus appears to be one of mixing apples and oranges. The ray bending method guarantees convergence to a minimum travel time path in a model with continuous first derivatives; however, what is required for my LET scheme is a minimum travel time path in a model parameterized by constant velocity blocks. The fact that 1-D raypaths are occasionally faster in the 3-D constant velocity block model suggests that the only way to guarantee that 3-D rays will always be faster in a constant-velocity block parameterization is to use an algorithm such as the shortest path ray tracing method (e.g. Moser, 1991; Fischer and Lees, 1993) that does not require explicit calculation of velocity gradients. Since the faster 1-D raypaths were in general only a few hundredths of a second quicker than the 3-D raypaths, I chose to use the ray bending method despite this problem. For consistency I always used the faster of the two candidate 3-D raypaths, even when the initial 1-D raypath was faster when traced through the 3-D block velocity model.

2.4.2 Jumping vs. Creeping

The Laplacian smoothing operator as described in section 2.2.2 minimizes the roughness for each individual iteration. However, it is important that the final total perturbational model is smooth; if each model derived at each iteration step is constrained to be smooth (a 'creeping' inversion (Shaw, 1986)), unwanted roughness may be introduced into the final model. To constrain the final total perturbational model (or the total net change from the original 1-D reference model s_0) to be smooth (a 'jumping' inversion (Shaw, 1986)), the final perturbational model after n iterations is written as

$$\sum_{i=1,n} \delta s_i = \delta s_n + \sum_{i=1,n-1} \delta s_i \quad (\text{EQ 2.49})$$

To smooth the final perturbational model, the Laplacian of the right-hand side of equation 2.49 is constrained to be zero;

$$\lambda L \left(\delta s_n + \sum_{i=1,n-1} \delta s_i \right) = 0 \quad (\text{EQ 2.50})$$

After rearranging terms in equation 2.50, we get

$$\lambda L \delta s_n = -\lambda L \left(\sum_{i=1,n-1} \delta s_i \right) \quad (\text{EQ 2.51})$$

This is the final equation needed to solve for δs at iteration n . Note that if $n = 1$, then the right-hand side of equation 2.51 is just 0. Combining equation 2.24, equation 2.39, and equation 2.51, the system of equations for δs at the n th iteration can now be written as

$$\begin{bmatrix} QWA \\ \lambda L \end{bmatrix} \delta s_n = \begin{bmatrix} QW\delta t \\ -\lambda L \sum_{i=1, n-1} \delta s_i \end{bmatrix} \quad (\text{EQ 2.52})$$

This is the system of equations that I used to solve for δs after the first inversion step. Note that if the initial reference model is not smooth (a 1-D model is smooth in 2 dimensions) then one would need to constrain the final model $s_n (= s_0 + \delta s_n)$ to be smooth.

Finally, a method for deciding when to stop the inversion process is required. A non-linear inversion is composed of a series of linear inversions, where each linear inversion consists of a relocation step and a slowness inversion step. The measures I employ are highly qualitative. The inversion is stopped when the model does not change appreciably between inversion steps, and when the change in % reduction in the χ^2 misfit (see equation 2.58) between inversion steps does not decrease significantly. Other more quantitative measures similar to the one described in equation 2.27 could be used. However, given that the model changes little after the second inversion step (see section 4.1.2), any measure of convergence used would likely yield similar results.

2.5 Error Analysis

In LET, the ability to determine what is "real" in an image and what is an artifact is critical. There are two basic measures of the realness, the resolution and the variance. In addition we can test the model's ability to reproduce well-constrained observations, such as surficial geology and blast locations. Each of these tests are discussed below.

2.5.1 Resolution

Resolution is the ability of a particular LET inversion to successfully image structural bodies of a given size and shape. It is primarily controlled by three factors. The first is raypath distribution; if a given block is not 'hit' by any raypaths, then

there is no information about its slowness, and thus its resolution will be zero. The second is model parameterization; if a model is parameterized by 5×5 km blocks, then features smaller than 5 km cannot be resolved. The third is smoothing; if lots of smoothing is used (i.e. λ is large), then sharp structural boundaries will be smeared across several blocks, decreasing resolution of features with sharp edges. Resolution is formally computed by first re-writing equation 2.52 as

$$C \delta s = \delta t' \quad (\text{EQ 2.53})$$

where $\delta t'$ includes both the modified data and smoothing constraints, and C is the combined matrix of spatial derivatives and smoothing constraints. Solving this system using least squares, we get

$$\delta s' = C^\dagger \delta t' = C^\dagger C \delta s \quad (\text{EQ 2.54})$$

where C^\dagger is the generalized inverse of C . $\delta s'$ can be thought of as the version of the truth δs filtered through $C^\dagger C$ (Backus and Gilbert, 1967). The matrix $C^\dagger C$ is the resolution matrix. If $C^\dagger C = I$, then $C^\dagger C$ will impart no distortion on δs ;

$$\delta s' = I \delta s = \delta s \quad (\text{EQ 2.55})$$

The i th row of $C^\dagger C$ corresponding to the i th block in $\delta s'$ is a weighting function which describes the influence of the j th block in δs on the i th block in $\delta s'$ (Lees, 1989). The more closely the i th row resembles a spike (i.e. non-diagonal elements = 0, diagonal = 1), the better the resolution of the i th block. This gives us a quantitative measure of the resolution for each block in $\delta s'$.

However, the computation of $C^\dagger C$ involves storing $C^T C$ and computing its inverse. Because $C^T C$ is never explicitly formed due to computer memory limitations, an approximate method for estimating model resolution is required. One simple and intuitive method is to construct raypath diagrams such as those shown in Chapter III (Figure 3-6). Regions with sparse ray coverage will in general have poor resolution, whereas regions with dense ray coverage will have good resolution. Additionally, regions that have relatively unidirectional ray 'bundles' with few crossing rays (anisotropic ray coverage) will have poor resolution in the direction of the raypaths, resulting in the smearing of slowness structure along the rays. Raypath diagrams are a useful first step in LET, and can be used to determine a) if there is enough data for an inversion, b) if more data should be acquired for a specific

part of the study area, and c) the parameterization scale to use. Another method for estimating resolution is to count the number of 'hits' each block receives and construct hit count diagrams; the more hits a block receives, the better the ability to resolve its velocity relative to its neighboring blocks. Finally, Kissling et al. (1984) introduced the idea of computing a moment of inertia tensor for each block as a measure of the degree of isotropic ray coverage in a single block. This method was used by Lees (1989). Although it more accurately characterizes the nature of the raypath field in an individual block, it suffers from the difficulty of conveying 3-D information (the ray tensor) via 2-D media (paper).

The above methods all estimate the effect of ray distribution on resolution. However, resolution is also influenced by parameterization and smoothing. One method for assessing the combined effect of all three factors is to replace δ_s in equation 2.53 with a spike, where all elements δ_s are zero except for the i th, which is unity. The resulting model δ_s' will just be the i th row of the resolution matrix C^+C (Humphreys and Clayton, 1984; Lees, 1989; Vandecar, 1991).

In order to assess the resolution of each model parameter, the above procedure would have to be repeated n times, once for each model element. An alternative is to construct a model δ_s composed of a series of spikes separated by several blocks. Travel times are recalculated along raypaths already traced in the location problem, and inverting these new travel times for δ_s' . The degree to which δ_s' matches the many-spikes model (referred to as the 'checkerboard' by Spakman and Nolet (1989)) is a measure of the resolution in different parts of the 3-D velocity model. This checkerboard procedure described above is somewhat different from the approach taken by other investigators (e.g. Symons and Crosson, 1996), where earthquakes are relocated and rays retraced in the checkerboard model. The travel times calculated along these new raypaths are then inverted. This latter approach addresses the question, "If the earth looked like a checkerboard, how well would this dataset & inversion machinery reproduce it?" My approach addresses the question, "Given the raypaths already computed, what is the resolving capability of this dataset?"

2.5.2 Variance

Errors in the data, including mislocated earthquakes, mispicked arrivals, mislocated stations and incorrectly traced raypaths, can create errors in the resulting

model. The effect of mislocated earthquakes is mitigated by the parameter separation method described in section 2.3.1 and mislocated stations are assumed to be a small source of error for the PNSN (see section 2.3.2), but the other two error sources can potentially be significant. Thus a means for estimating the amount of error associated with the estimated slowness of each block $\delta s'_i$ is required. In classical least squares the approach would be to compute the covariance of δs ,

$$\text{cov}(\delta s) = \delta s \delta s^T = (C^\dagger \delta t') (C^\dagger \delta t')^T = C^\dagger \text{cov}(\delta t') C^{\dagger T} \quad (\text{EQ 2.56})$$

(Menke, 1984). As with resolution, computing the variance requires the storage of $C^T C$. Thus an approximate method is needed to estimate the variance.

Lees (1989) introduced the idea of using the Jackknife method (e.g. Efron & Tibshirani, 1993) as a means for estimating model error in LET. It is a means for assembling a set of estimates $\delta \bar{s}_{i,j}$ for the slowness perturbation of the i th block. The distribution of these estimates gives an estimate of the standard deviation for each parameter in $\delta s'$, assuming the estimates are normally distributed. This is accomplished by randomly partitioning the dataset into k subsets with each subset containing $n - \frac{n}{k}$ arrival times, where the $\frac{n}{k}$ rays are removed without replacement. An inversion is then run for each subset, yielding $(k = 1, j)$ estimates $\delta \bar{s}_{i,j}$ of the slowness perturbation in the i th block. The standard deviation for the i th block is then estimated by

$$\sigma(\delta s_i) = \sqrt{\frac{\sum_{j=1,k} \delta \bar{s}_{i,j}^2 - \frac{1}{k} \left(\sum_{j=1,k} \delta \bar{s}_{i,j} \right)^2}{k(k-1)}} \quad (\text{EQ 2.57})$$

There are two problems with using the Jackknife in this way to estimate model error. The first problem is that the method followed by Lees (1989) treats each ray as an independent observation, which strictly speaking is incorrect since a ray is linked to other rays that come from the same source. I make a modification to Lees' method by randomly partitioning the dataset into k subsets of $n - \frac{n}{k}$ earthquakes, instead of individual rays. Not only is this more correct from a statistical point of view, but it is also more realistic, since it addresses the question "what effect does removing this earthquake from my dataset have on the solution?" The error estimates can be examined on a block-by-block basis (for example, see Plate 1 on inside

back cover), or can be averaged together to yield an estimate of the average standard error for the entire model.

The second problem is that this method is really only useful for estimating error in a linear inversion. Use of the Jackknife method to estimate error in a non-linear inversion would require k^M inversions, where M is the number of linear inversion steps made in a full non-linear inversion. For any value of $M > 1$ this becomes extremely costly. Thus we are left with the somewhat unsatisfactory position of assuming that the error in the final model is of the same order as the error in any single linear inversion step. Finding a better method for estimating error in a non-linear inversion would be a fruitful area for future research.

2.5.3 Trade-off Curve - Selecting λ

In damped least squares problems such as LET there is in general a trade-off between resolution and variance. If the damping weight λ is large, then instabilities in the solution will be damped, resulting in smaller parameter variance but also poorer resolution of the true parameter values (since greater weight is given to smoothing constraints over the data). Conversely, if the value of λ is small, then instabilities in the solution won't be damped, resulting in large parameter variance but much better resolution. Thus selecting the optimal value for λ can dramatically affect the resultant velocity model, and is an important part of any damped least squares problem.

To select a value for λ , I constructed trade-off curves using percent reduction in the χ^2 (chi-squared) misfit as an estimate of the resolution and the Jackknife method described in section 2.5.2 to estimate the average parameter variance for a given model. χ^2 is computed from either equation 2.26 (for the initial velocity inversion step) or equation 2.52 (for all subsequent velocity inversion steps). For example, χ^2 for the initial inversion step (equation 2.40) is

$$\chi^2 = \left\| \begin{bmatrix} \text{QWA} \\ \lambda L \end{bmatrix} \delta s - \begin{bmatrix} \text{QW}\delta t \\ 0 \end{bmatrix} \right\|^2 \quad (\text{EQ 2.58})$$

The reduction of the χ^2 misfit is a measure of the degree to which the data (including constraint equations) are explained by the model. It is a proxy for resolution because, in general, models with good resolution will have a higher percent reduction in the χ^2 misfit. An alternative method would be to use the checkerboard

method and compute the average difference between the input checkerboard model and the output model, yielding an estimate of the average diagonal values of the resolution matrix.

I generated the trade-off curve by running linear a series of inversions (without earthquake relocation) for a range of values of λ , and computing estimates of the resolution and variance for each λ . The resultant curve is shown in Figure 2-5. It is

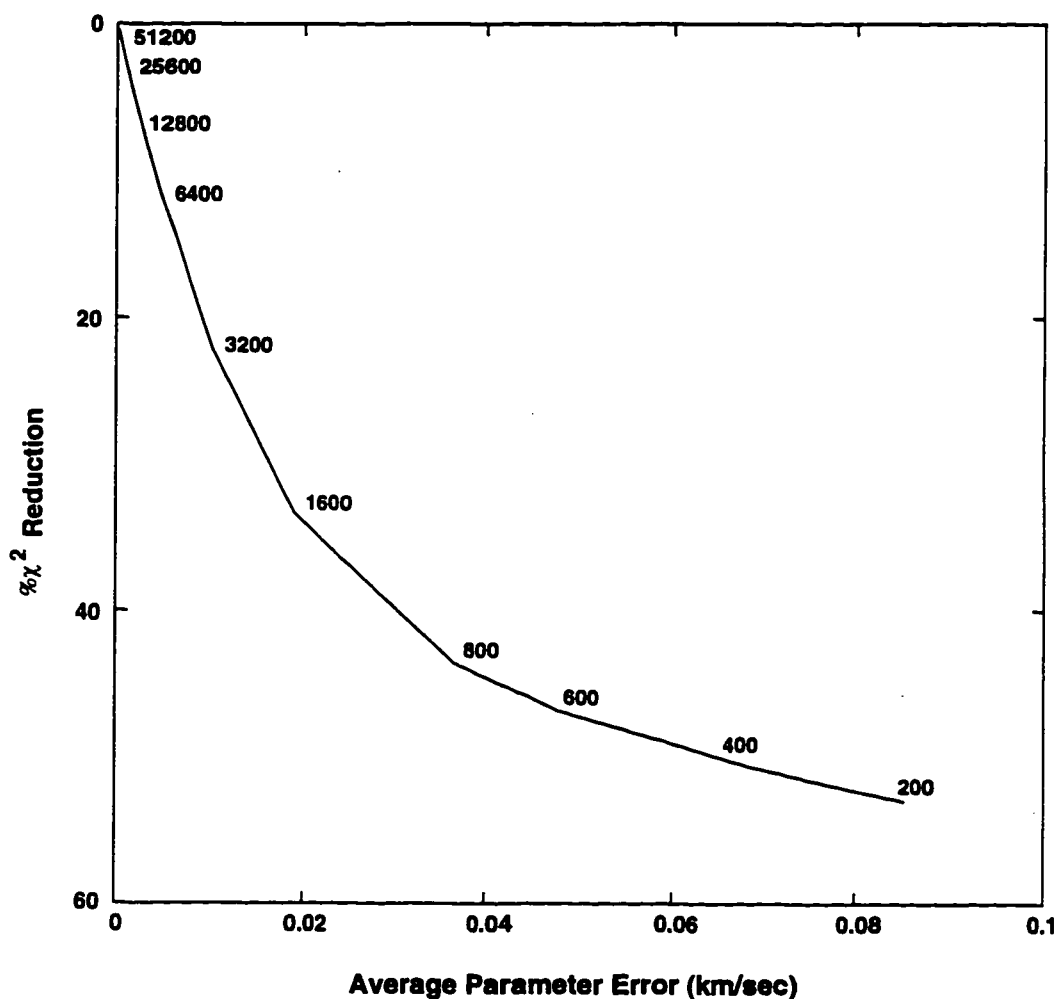


Figure 2-5 Trade-off curve showing % reduction in χ^2 misfit and average parameter error for inversions performed with different values of the damping parameter λ . χ^2 is determined from equation 2.58, and the average error is determined by averaging the estimated errors determined for each parameter from equation 2.57. Based primarily on this graph, a damping value of 600 was selected for all inversions discussed in Chapter IV and Chapter V.

apparent from Figure 2-5 that values of λ ranging from 500 - 1200 will yield models that have both small errors and a significant reduction in the χ^2 misfit. After inspecting the results of checkerboard tests run with values of λ within this range, I chose a λ value of 600 for all of my inversions. It is possible that the optimal value of λ could differ between each inversion step in a full non-linear inversion. However, I found in a series of test runs with much smaller datasets that trade-off curves constructed for several inversion steps did not differ appreciably, indicating that the optimal value of λ probably does not change significantly from inversion step to inversion step.

One limitation of this method for choosing λ is that it is potentially quite time-consuming and expensive. The run-time for each Jackknife estimate is roughly k times longer than the time for one LET inversion run, since the Jackknife involves the inversion of k separate datasets. However, I found that the number of LSQR iterations in each velocity inversion step could be reduced without affecting the shape of the trade-off curve, meaning that the same value of λ would be selected regardless of the number of LSQR iterations. Thus for the trade-off analysis alone I set the convergence criterion Δs for LSQR at 0.25 (see equation 2.27), and reduced the number of subsets k to 5. This reduced the number of LSQR iterations by an order of magnitude, significantly reducing computer costs.

2.6 LET Procedural Outline

The discussion in sections 2.1 - 2.4 can be boiled down to the following procedural outline:

- 1) Select the dataset for LET inversion (see Chapter III).
- 2) Choose or compute the reference 1-D slowness model (see section 4.1.1).
- 3) Compute station corrections (see section 2.3.2):
 - 3a) Fix old locations & compute residuals in reference 1-D model.
 - 3b) Compute P-wave station corrections for all recording stations (within and outside of the GMR).
 - 3c) Relocate earthquakes (equation 2.44) (using only P-wave arrival times) with new station corrections.

- 3d) Repeat step 3b and step 3c until station corrections stop changing.
- 4) Compute final locations in 1-D model using station corrections.
- 5) Perform initial inversion for slowness (velocity) parameters:
 - 5a) Recompute residuals without station corrections prior to inversion.
 - 5b) Remove all raypaths to stations outside the GMR.
 - 5c) Remove all events that drop below the selection criteria used in step 1 because of step 5b.
 - 5d) Use the annihilation matrix \mathbf{Q} (equation 2.38) computed in step 4 to form equation 2.40 (see section 2.3.1), so as to annihilate location dependence from the slowness problem.
 - 5e) Use LSQR to invert equation 2.40 for δs :
- 6) Perform trade-off analysis to select optimal damping weight λ (see section 2.5.3).
- 7) Invert equation 2.40 for δs using the λ determined in step 6, following the same procedure as in step 5.
- 8) Perform next inversion step:
 - 8a) Relocate earthquakes (using only P-waves recorded at stations within the GMR and no station corrections), using ray bending to raytrace in the new 3-D model $\delta s'$ (see section 2.4.1).
 - 8b) Use the annihilation matrix \mathbf{Q} (equation 2.38) computed in step 8a to form equation 2.52, thus annihilating location dependence from the slowness problem.
 - 8c) Use LSQR to invert for a new model $\delta s''$ using the λ determined in step 6.
- 9) Evaluate the resultant model $\delta s''$. If it differs little from $\delta s'$, and the percent reduction in the χ^2 misfit achieved is minimal, go on to step 10. Otherwise, go back to step 8.
- 10) Use the checkerboard (see section 2.5.1) and jackknife (section 2.5.2) methods to estimate resolution and variance in the resultant model.

This is the procedure I used to generate the final images shown in Plate I, as well as the other slowness (velocity) images discussed in Chapter V. To avoid confusion, I will refer to the entire procedure from step 1 to step 9 as the "full inversion", a complete hypocenter/velocity iteration as an "inversion step" (i.e. step 8 is an "inversion step"), and will use the term "iteration" to refer only to iterations made within a single hypocenter or velocity inversion (i.e. the number of LSQR "iterations" required for the velocity inversion in step 8c to converge).

III. Data Selection and Collection

3.1 Introduction

The success of a LET inversion is highly dependent not only on the computational machinery, but also on the quality and quantity of seismic data available for inversion. As I show in section 5.4, the use of poor quality data can easily create false anomalies in the resultant image. Thus it is crucial at the onset of an LET experiment to carefully examine the available data and develop robust criterion for selectively removing poor quality information. In section 3.2 of this chapter I discuss my criteria for selecting data from the PNSN catalog. In section 3.3 I describe two field experiments run between 1994 and 1996 that increased the quantity and quality of seismic data in the GMR.

3.2 PNSN Catalog - Selection Criteria

3.2.1 Non-earthquake sources

The PNSN catalog contains events from 1969 through the present. Included in the catalog are over 33,000 earthquakes located in Washington State. Also included are over 7,800 events from other types of seismic sources, including blasts (from quarries, road construction operations and seismic experiments), low frequency earthquakes (associated primarily with volcanic activity at Mount St. Helens), and surface events such as rockfalls and avalanches (most commonly at Mount St. Helens and Mount Rainier).

An important initial step in selecting a dataset for velocity inversion is to remove non-earthquake sources. Such sources typically have emergent arrivals that are more likely to be mispicked, leading not only to errors in travel time determinations, but also to errors in event location. In addition, station geometry usually provides poor depth constraints for shallow sources, thereby decreasing the accuracy of depth determinations (this is also a problem for shallow earthquakes). Also, inclusion of non-earthquake sources (in particular blasts) can lead to fallacious tectonic interpretations. Figure 3-1 is a plot of all blasts recorded in the GMR between 1980 and 1996, and illustrates this latter point. Several groupings of blasts define linear patterns in map view. These linear trends could easily be misinterpreted as fault zones.

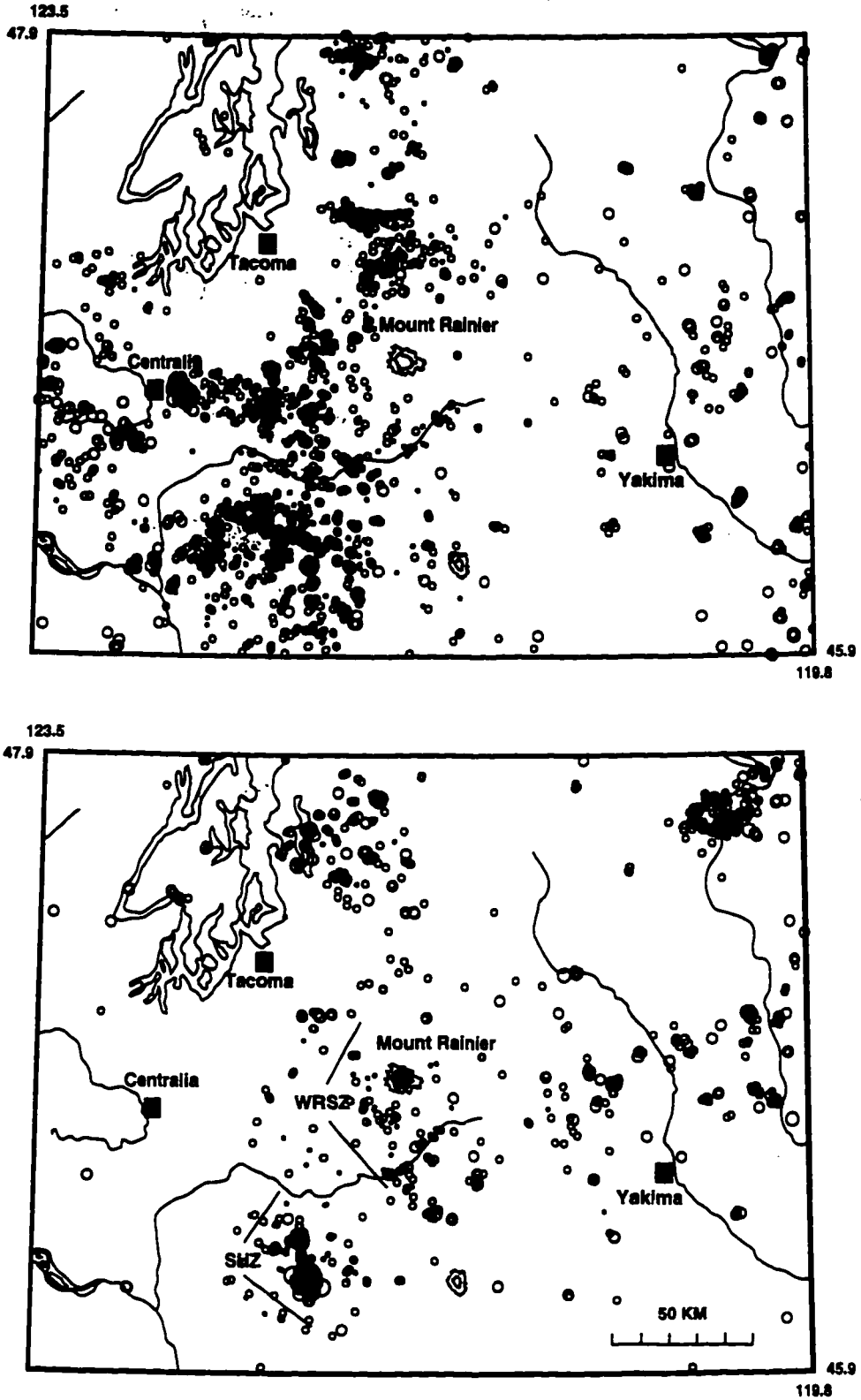


Figure 3-1 Plot of all events flagged as blasts (upper) and all shallow events (depth < 3 km) flagged as earthquakes (lower) in the GMR.

Non-earthquake sources, when they are recognized, receive special flags in the PNSN catalog (e.g. Ludwin et al., 1994), making it very easy to remove these events. However, the occasional non-earthquake source does slip through without being identified as a non-earthquake. This possibility is illustrated by comparing the two plots in Figure 3-1, the upper containing those events identified as blasts and the lower containing events identified as shallow (0 - 3 km) earthquakes in the PNSN catalog. Note that there are some areas of overlap between the two plots, especially near and between Mount Rainier and Mount St. Helens. These areas of overlap suggest that even in areas of known blast activity, the occasional blast has been misidentified as an earthquake by PNSN analysts. In an attempt to quantify the percentage of blasts misidentified as earthquakes in the PNSN catalog, I visually inspected all 1387 events in my dataset that occurred between 1990 and 1993. Using admittedly subjective criteria (such as ringy codas, lower frequency contents and emergent arrivals) that are typically used to distinguish blasts from earthquakes, I identified 49 probable blasts that had been misidentified as earthquakes, or 3.5% of the total number of events examined. This finding suggests that there are probably on the order of 100 other unflagged blasts in my dataset. Because of this, I examined many other shallow (depths < 4 km) earthquakes and identified an additional 20 probable blasts. However, a complete visual inspection of all 'earthquakes' would be a time-consuming process. Since my selection criteria are reasonably strict, I assume that those blasts that do slip into my dataset have reasonably well-constrained locations and won't have any more of an adverse affect on the resulting velocity model than shallow earthquakes.

The above arguments notwithstanding, blasts with known locations and origin times can be extremely useful in LET. Since their locations and origin times are known, any associated travel time residual can be assumed to be due either to velocity anomalies or picking error, a significant advantage over earthquake sources. Also, surface sources contain valuable information about shallow velocity structure that is for the most part not available in earthquake-only datasets, especially in the GMR where most earthquakes locate below 2 km. For these reasons I include 29 well-recorded blasts from USGS refraction experiments in 1991 (Gridley, 1993; Miller et al., 1997) and 1995 (Luetgert et al., 1995), as well as 6 blasts from the Centralia coal mine recorded during a field experiment in 1994 (Figure 3-2) (Moran and Malone, 1994). Arrivals from these blasts were, in general, impulsive and rea-

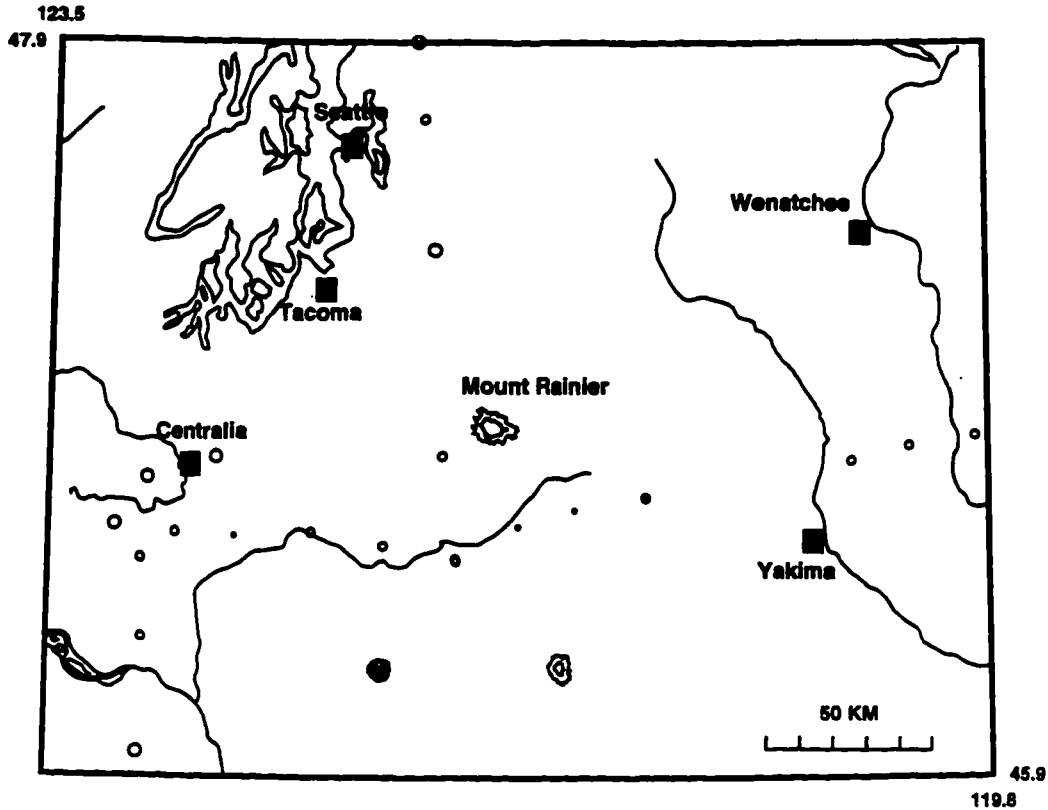


Figure 3-2 Map showing the locations of all blasts used in the inversion.

sonably easy to pick, so picking errors should be comparable to those associated with earthquakes. In Plate 1 these sources are plotted as pink circles (earthquakes are plotted as yellow circles) to ensure that they will not be mistaken for earthquakes.

3.2.2 Earthquake sources

Over 25,700 earthquakes from the PNSN catalog are located within the GMR. Because of this large number, my selection parameters were reasonably conservative (Table 3.1).

Table 3.1: Selection criteria for inversion dataset

Minimum number of P-wave arrivals	10
Maximum station azimuthal gap	135°
Nearest station	15 km

Table 3.1: Selection criteria for inversion dataset

Minimum magnitude	M_l 0.5
Depth range	Surface ^a - 43 km
Latitude range (North)	45.9 - 47.9
Longitude range (West)	119.8 - 123.5
Dates:	800518 - 961231

a. An event is rejected if its depth is above the surface (i.e. an 'air-quake'), which for computational simplicity is represented by the elevation of the nearest station to the epicenter.

Only those earthquakes meeting these criteria were included in the inversion dataset. At Mount St. Helens, the high station density and large number of events (over 9300 locate directly beneath the summit) allowed for the use of stricter selection criteria. The same station gap and maximum depth criteria were used, but the nearest station was required to be within 5 km, and at least 15 P arrivals had to be recorded. In addition, many redundant events were removed by selecting only the largest earthquakes from the energetic swarms preceding the 1980, 1984, 1985, and 1986 eruptions.

An important consideration in selecting the inversion dataset was the change from analog to digital PNSN recording formats that occurred in March of 1980. Before 1980, arrival times were manually picked on a delevelicorder machine. These picks carry a minimum uncertainty of ± 0.05 seconds (Steve Malone, personal communication), in contrast to a minimum uncertainty of ± 0.01 seconds (the sampling rate) for picks made from PNSN digital records. For this reason, all earthquakes that occurred before March 1980 were excluded from the dataset. After 1980, earthquakes were occasionally still picked manually. However, these events received a special flag in the PNSN catalog (Ludwin et al., 1994), and so were easy to selectively remove.

A final special selection criterion was applied to volcano-tectonic earthquakes beneath Mount Rainier. Two stations (RCS and RER) were installed on the edifice of Mount Rainier in June and July of 1989, and a third (RCM) was added in September 1993, doubling the total number of stations within 20 km of the summit (see Figure

3-7). Moran et al. (1995) demonstrated that the variability in depths for Mount Rainier earthquake locations decreased dramatically after 1989, suggesting that the new stations significantly improved location quality. For this reason, only Rainier volcano-tectonic earthquakes occurring after July 1989 were included.

3.3 Field Experiments

The dataset discussed in section 3.2 was augmented by approximately 2,000 additional arrival-time picks recorded on temporary seismographs operated during two field experiments in 1994 and 1995-1996. These two experiments are described below.

3.3.1 Experiment #1 - Refraction Profile

The goal of the first experiment, which ran from July 16, 1994, to August 19, 1994, was to generate a 1-D velocity model for the southern Washington Cascades that could be used as a starting model for LET analysis. To accomplish this I used a combination of PNSN stations and 20 temporary seismographs from the PASSCAL instrument center to form a refraction profile extending from Centralia east towards Ellensburg (Figure 3-3). I did not have the means to generate my own active seismic sources, so I used daily blasts (10-20K lbs) from a coal quarry near Centralia. No controlled sources were available on the eastern end of the profile, so the refraction line was unreversed.

The PASSCAL temporary seismograph stations consisted of a Mark Products L22 4.3 Hz 3-component geophone, a 6-Channel RefTek Data Acquisition System (or DAS) with 500 Mbytes storage capacity, a GPS antenna for accurate timing as well as site location information, and a 12 volt/100 Amp-hour battery. Each DAS unit was programmed to record 3 channels in trigger mode, which usually resulted in 30-40 Mbytes of recorded data (in compressed format) over a 7-day time period. Batteries typically were drained within 7-10 days, and had to be replaced. The design goal was to achieve 1 km station spacing starting just west of the WRSZ. However, in the initial deployments, when the DAS units were programmed with a detrieger threshold, a bug caused the DAS units to shut off. This required the reoccupation of several sites for an additional week, reducing the total number of different sites occupied during the experiment to 47 (see Appendix A for site locations and operation dates). Two sites (NRTH and SOTH) were located at the coal

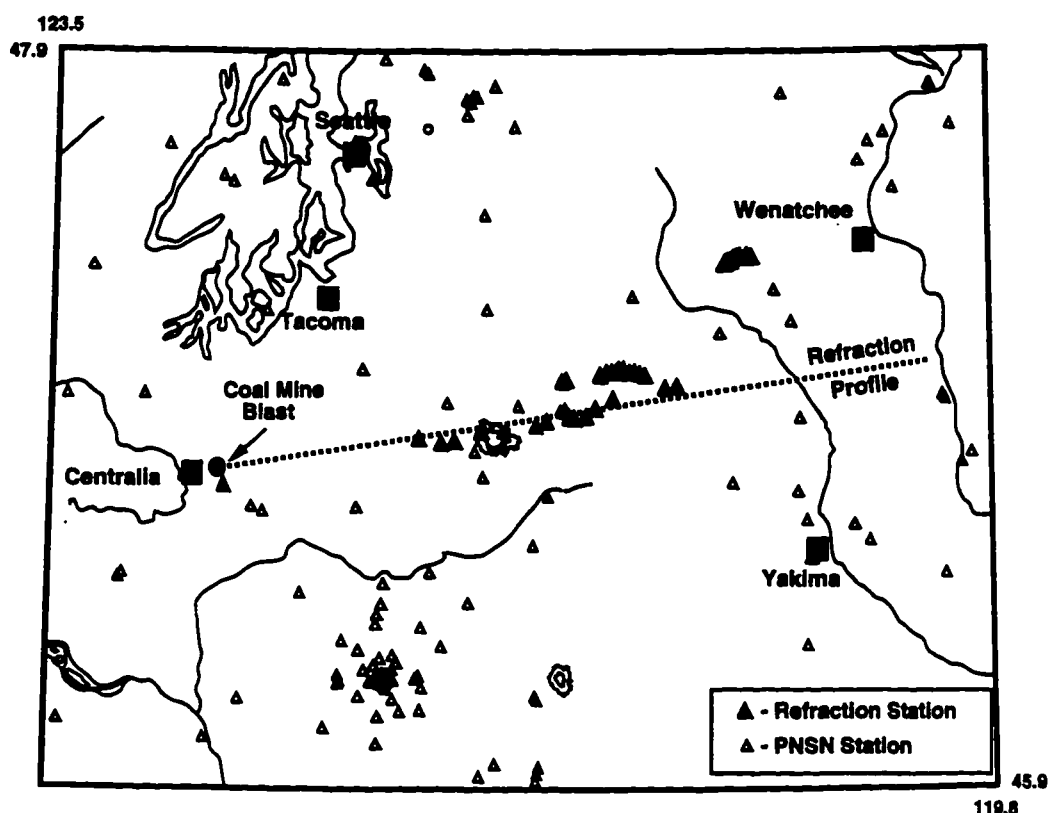


Figure 3-3 Geometry of the 1994 refraction experiment. Solid triangles correspond to refraction stations, open triangles to PNSN stations.

mine for all but the first week of the experiment to provide constraints on the blast origin times (the coal-mine operation could not supply this information with the required accuracy). The estimated uncertainty in the origin times determined from these two sites was 0.1 second. A total of 33 blasts were recorded during the experiment, only 6 of which generated impulsive arrivals at most stations. Recordings of these 6 blasts from the PASSCAL sites and 15 PNSN stations were merged into one datafile, forming a composite record section approximately 170 km long (Figure 3-4). A 1-D model was then derived from first arrivals (Figure 3-5).

Results

The 1-D velocity model that resulted from this experiment is non-unique and poorly constrained. It is non-unique because the profile is unreversed, thus making it impossible to distinguish between apparent velocity and structural dip. It is poorly constrained because of the lack of stations close to the source, the several large gaps in the composite record section, and the uncertainties in first-arrival

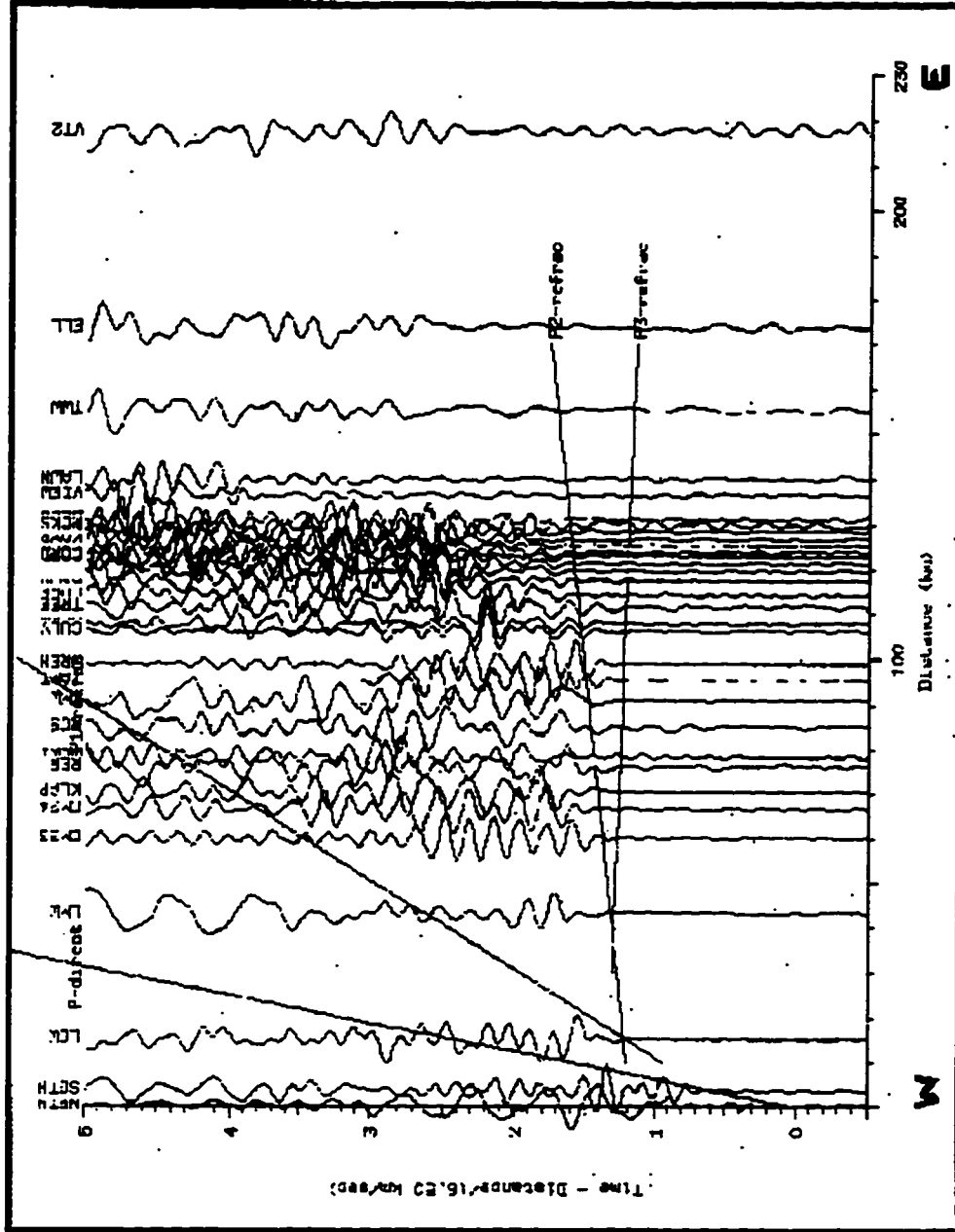


Figure 3-4 Composite record section from Centralia refraction experiment. Section is reduced by 6.5 km/sec. Lines correspond to theoretical phase arrivals from the "CR" velocity model in Figure 3-5.

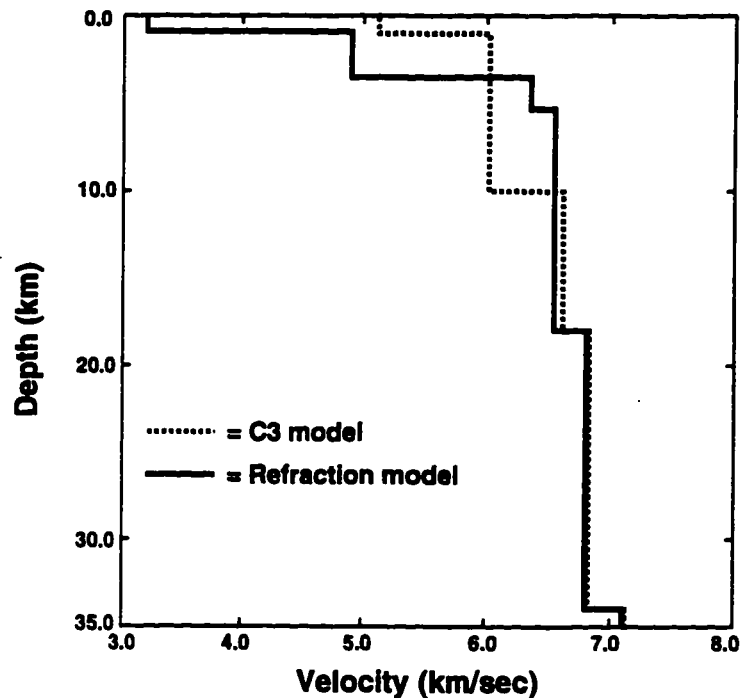


Figure 3-5 Comparison of 1-D model resulting from refraction experiment (bold line) with PNSN "C3" velocity model (dashed line).

picks caused by the variable and non-impulsive nature of the sources. Despite these caveats, two features of the composite record-section and resultant 1-D model are worth pointing out. First, the velocity for layer 3 (6.35 km/sec) is quite high for rocks in this depth range (3.3-5.3 km). Christensen and Mooney (1995) show that typical continental crust has a velocity of 5.80 ± 0.34 km/sec at 5 km, much slower than what I observe. This high apparent velocity could be due to the presence of high velocity rocks close to the surface, or to westward-dipping structure, or to some combination of both. Second, despite the geologic complexity along the profile, the deepest refractor (at 5.3 km depth) is continuous and detectable from 60 to 130 km.

A side-benefit to running the PASSCAL sites in trigger mode was the incidental recording of arrivals from 22 earthquakes located within the GMR. These data were merged with PNSN recordings and repicked, generating 130 new raypaths. These raypaths are included in the dataset used in the LET inversion.

Lessons Learned

This experiment suffered from several factors, the most important of which was the poor quality of the Centralia coal-mine blast recordings. The mine uses ripple-blasting, where individual charges detonate a certain number of milliseconds after their neighbor (Will Greenough, Centralia coal-mine geologist, personal communication). One affect of this is to create a ringy signal with lots of low-frequency energy and emergent first arrivals. These arrivals are hard to pick, especially at distant stations. A second affect is to create different source mechanisms for each blast, making it difficult to look for coherent arrivals on composite record sections assembled from several blasts. Another problem was that the dominant energy in the Centralia blasts is around 1 Hz, well below the 4.3 Hz corner frequency of the geophones used to record the blasts.

A final problem was the fact that the profile was unreversed. Such a profile is not ideally suited to regions like the Cascades where refractors are likely to not be horizontal. The resultant trade-off between structural dip and absolute velocity makes any interpretation of velocities nonunique. Solutions to these problems would include using lower frequency geophones, decreasing station spacing (so one can look for coherent arrivals between several stations as an aide in picking first arrivals), deconvolving the source from individual seismograms, and, perhaps most importantly, reversing the profile with a source on the eastern end.

3.3.2 Experiment #2 - The NEHRP project

The primary goal of the second experiment, which ran from 1995 through July of 1996, was to increase ray coverage, and thus resolution, in the central part of the GMR near Mount Rainier. The rationale for this goal comes from studying raypath diagrams (Figure 3-6). The lines in Figure 3-6 represent horizontal projections of 2-D raypath segments in four different layers from raypaths traced through a 1-D velocity model. The data in Figure 3-6 come from earthquakes with $M_1 > 2.0$ occurring between 1990 and 1994 (i.e. pre-experiment) that meet the criteria listed in Table 3.1. From this figure it is apparent that the pre-experiment ray coverage is quite good for the western half of the GMR, but degrades markedly east of Mount Rainier. Even where there are raypaths in the eastern half, they are dominantly oriented east-west with few crossing raypaths, indicating that resolution east of Mount Rainier is likely to be poor. Note that both the WRSZ and Mount Rainier are on the edge of the poorly-resolved region. The presence of these gaps strongly sug-

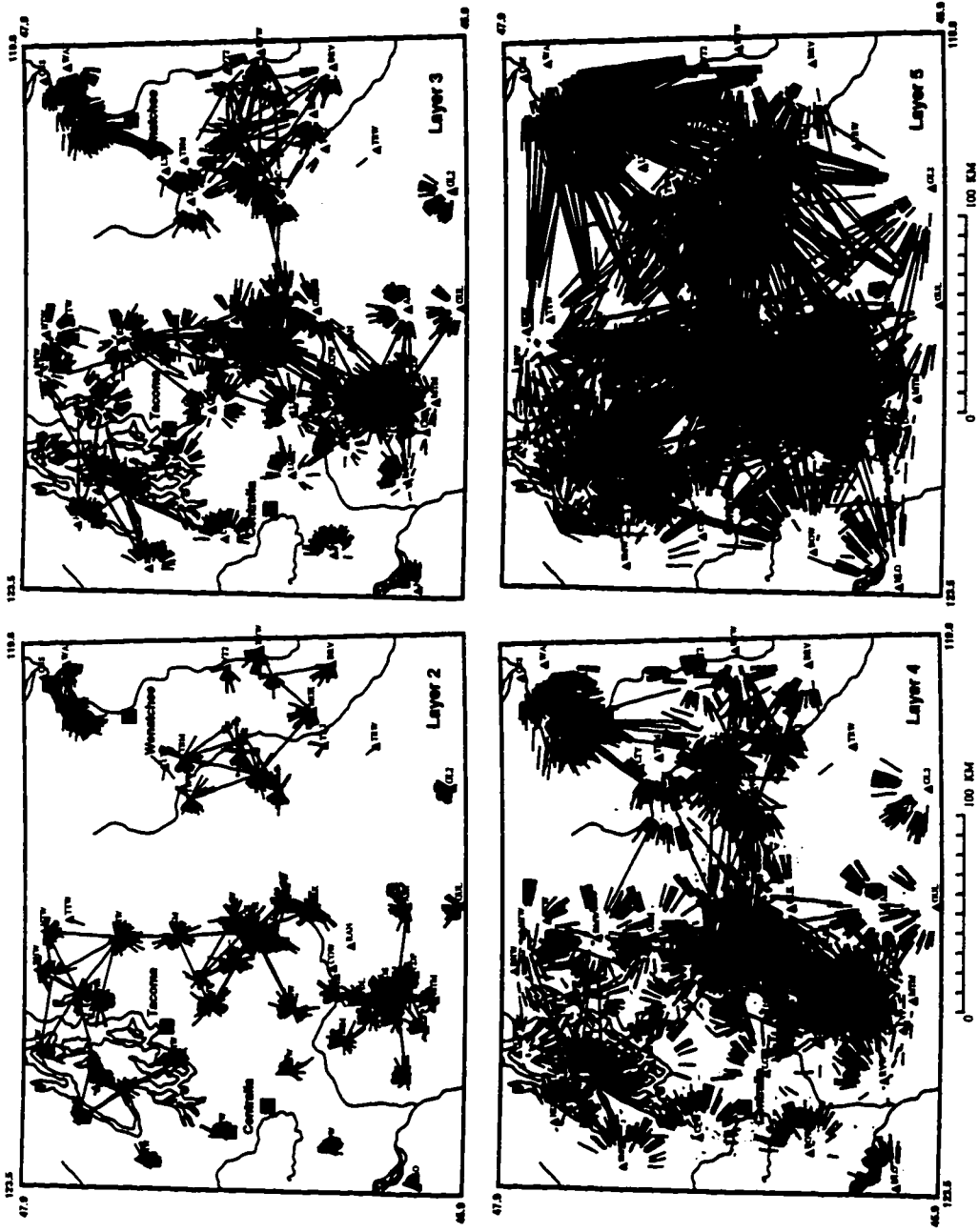


Figure 3-6 Raypath diagram for all earthquakes with $M_j > 2.0$ occurring between 1990 and 1994. Layer 2 extends from 1-4 km, Layer 3 from 4-7 km, Layer 4 from 7-10 km, and Layer 5 from 10-14 km.

gests that resolution of structures east of Mount Rainier will be poor if only the PNSN catalog is used, regions of significant interest in this study.

Experiment Methodology

In order to improve the resolving capabilities of the PNSN dataset in the eastern half of the GMR, a group of 18 seismic stations were temporarily added to the PNSN between 1995 and mid-1996. Sites for these stations were selected so as to fill the ray coverage gaps identified in Figure 3-6. Figure 3-7 shows the locations of these stations, along with the permanent PNSN stations located within the GMR. Only 8 stations were deployed at any one time, due to equipment constraints. Each station consisted of a Mark Products L-4 vertical component 1 Hz seismometer, a Voltage-Controlled Oscillator (VCO), a transmitter and transmitting antenna (typically a 165 MHz Yagi), and a 12-volt 100-amp/hour battery charged by a 32-watt solar panel (Figure 3-8). Since these components are also typical of permanent PNSN stations, the station responses of the temporary stations should be very close to those of the permanent stations. Signals from two stations (ASF and XTL) were linked directly to telephone lines, and didn't require transmitters. In addition, several stations (BDM, CMK, and RAD) were also configured as repeater sites, and so had extra receivers and receiving antennas as well as a summing amplifier.

Signals from the temporary stations were sent to intermediate repeater sites in the PNSN telemetry system, where they were multiplexed with signals from permanent PNSN stations and sent directly to the University of Washington for processing. The use of the PNSN telemetry system placed limits on when and where individual temporary sites could be operated, since a station had to be able to "see" a repeater and there had to be at least one free channel available (each telemetry line can carry a maximum of 8 channels). The weather placed an additional constraint on site location, since elevations above 1 km are typically not accessible in the Cascades from mid-October to mid-June or July.

In the field, final site locations were chosen primarily by searching for a location that had both good southerly exposure for the solar panel and poor visibility from nearby roads to reduce vandalism potential. Little consideration was given to the level of ambient seismic noise prior to installation, but care was taken to not place the site close to an obvious noise producer such as a road or stream. Once a final site was selected, two 2-3' holes were dug, one for the seismometer and one for the

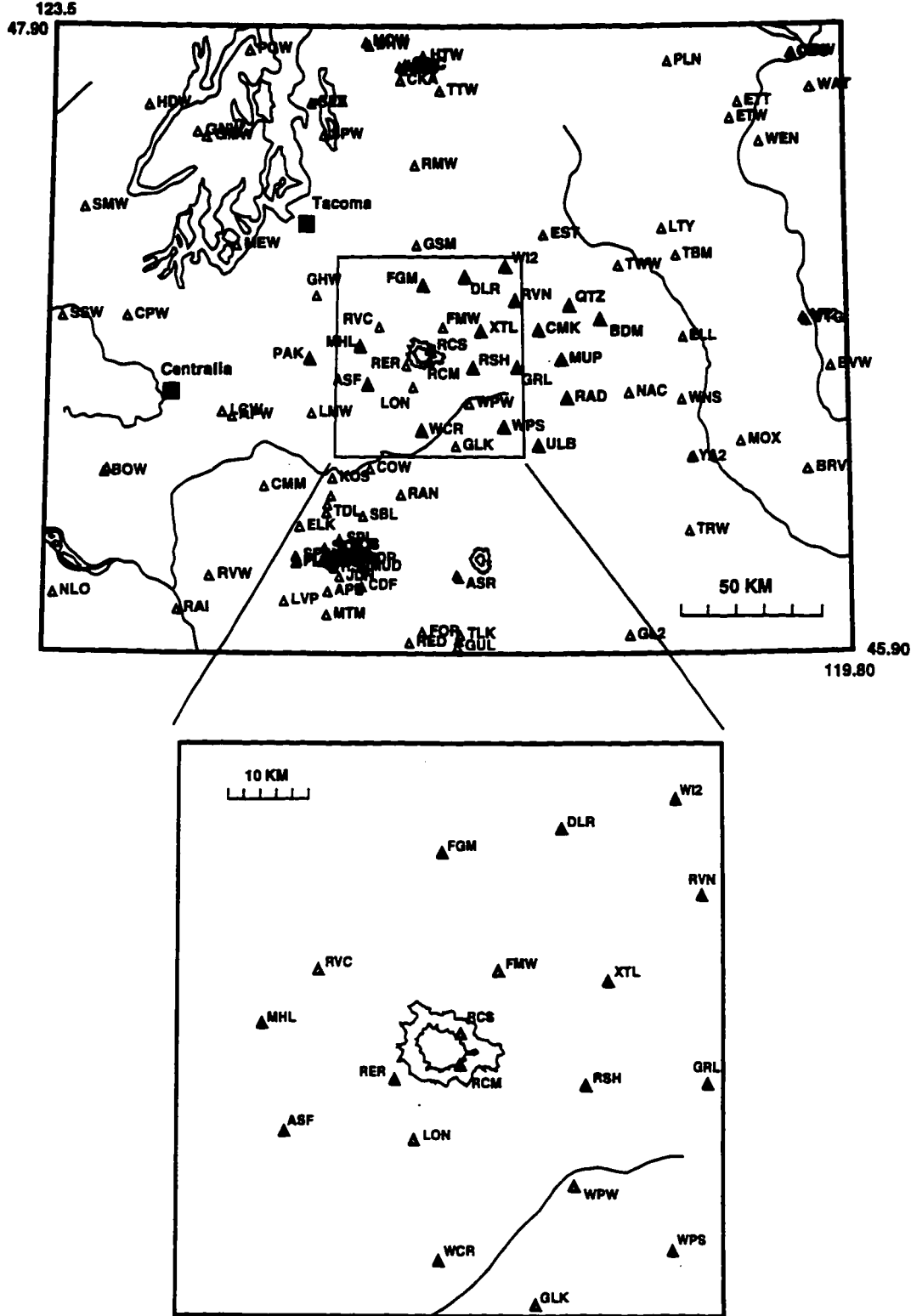


Figure 3-7 Seismograph station distribution in the GMR. Inset shows stations around Mount Rainier. Solid triangles correspond to NEHRP stations, open to permanent PNSN stations.

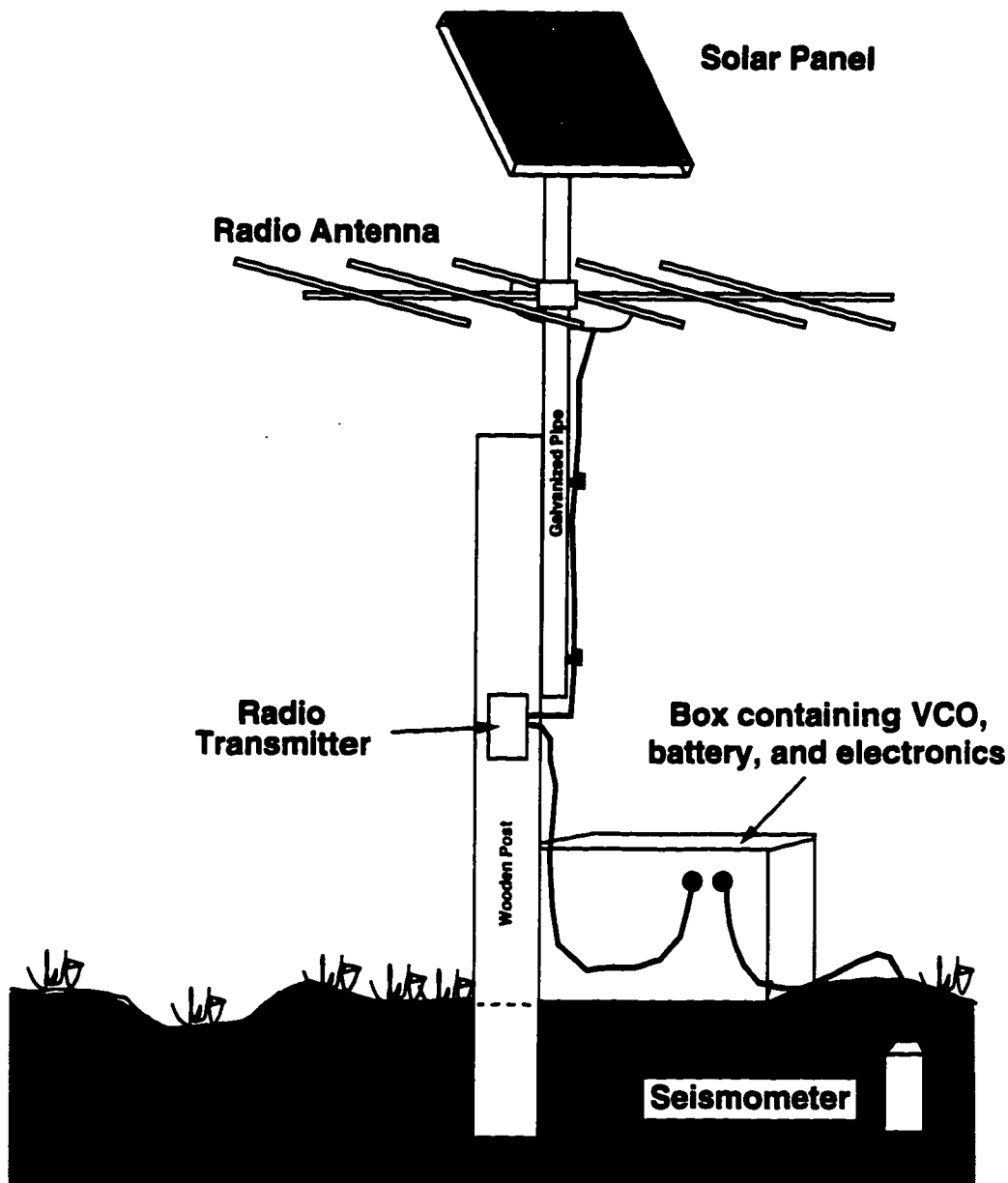


Figure 3-8 Diagram of typical station deployed during NEHRP experiment.

wooden post to which the antenna and solar panel were mounted. At least 10 readings from a hand-held Magellan GPS receiver were averaged to determine a geographic location for the site. As an additional check, the GPS location was compared to visual estimations of location determined in the field on a 7.5' topographic map. The site locations and dates of operation are listed in Appendix A.

Once the signals from the temporary sites reached the University of Washington, they were processed along with signals from permanent PNSN stations by an analyst. Due to initial concerns about mispicks associated with bugs in trace display software used to pick arrival times, I checked all picks for every event that occurred within the GMR to ensure that no significantly bad mispicks (> 0.1 sec) of arrivals at the temporary sites were allowed into the dataset used for the LET analysis.

To judge the success of the experiment, I generated synthetic raypath diagrams for the 18 temporary sites to predict the ray coverage that each site would produce. To do this I selected a set of earthquakes occurring during a random 4 month time period (January-April 1993) in the GMR and assumed that each temporary site would record P-waves from all earthquakes with magnitudes greater than 1 and that met the selection criteria in Table 3.1. The resultant hypothetical raypaths are shown in Figure 3-9. In this idealized scenario, each station recorded 60 arrivals.

Results

The ray coverage recorded during the experiment matched or exceeded this threshold. Figure 3-10 shows this graphically, and Table 3.2 shows the total number of P-wave arrivals recorded from well-located earthquakes recorded at each station.

Table 3.2: Number of P Arrivals Recorded by Temporary Stations

Station	Observed #P-picks	Predicted #P-picks ^a	Dates of Operation
ASF	50	45	950320 - 950612
BDM	40	128	951002 - 960716
CMK	133	128	951006 - 960716
DLR	145	127	950407 - 950919
FGM	90	60	950519 - 950919
GRL	134	128	951002 - 960716
MHL	69	35	950802 - 951011
MUP	101	128	951002 - 960716
PAK	83	90	950202 - 950802
QTZ	133	128	950925 - 960717
RAD	33	45	950629 - 950929

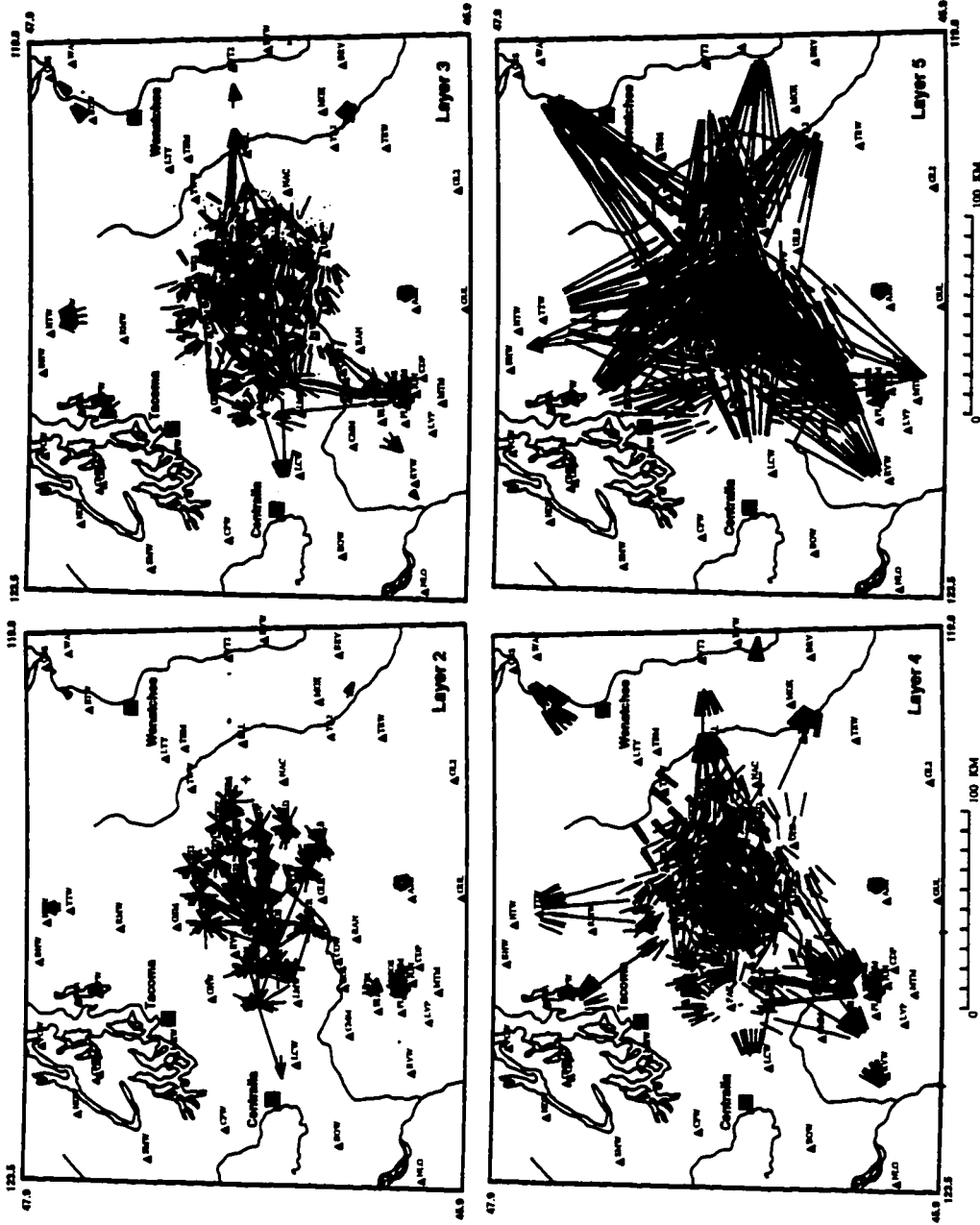


Figure 3-9 Theoretical raypath coverage for the 18 NEHRP locations. See Figure 3-6 for layer depths.

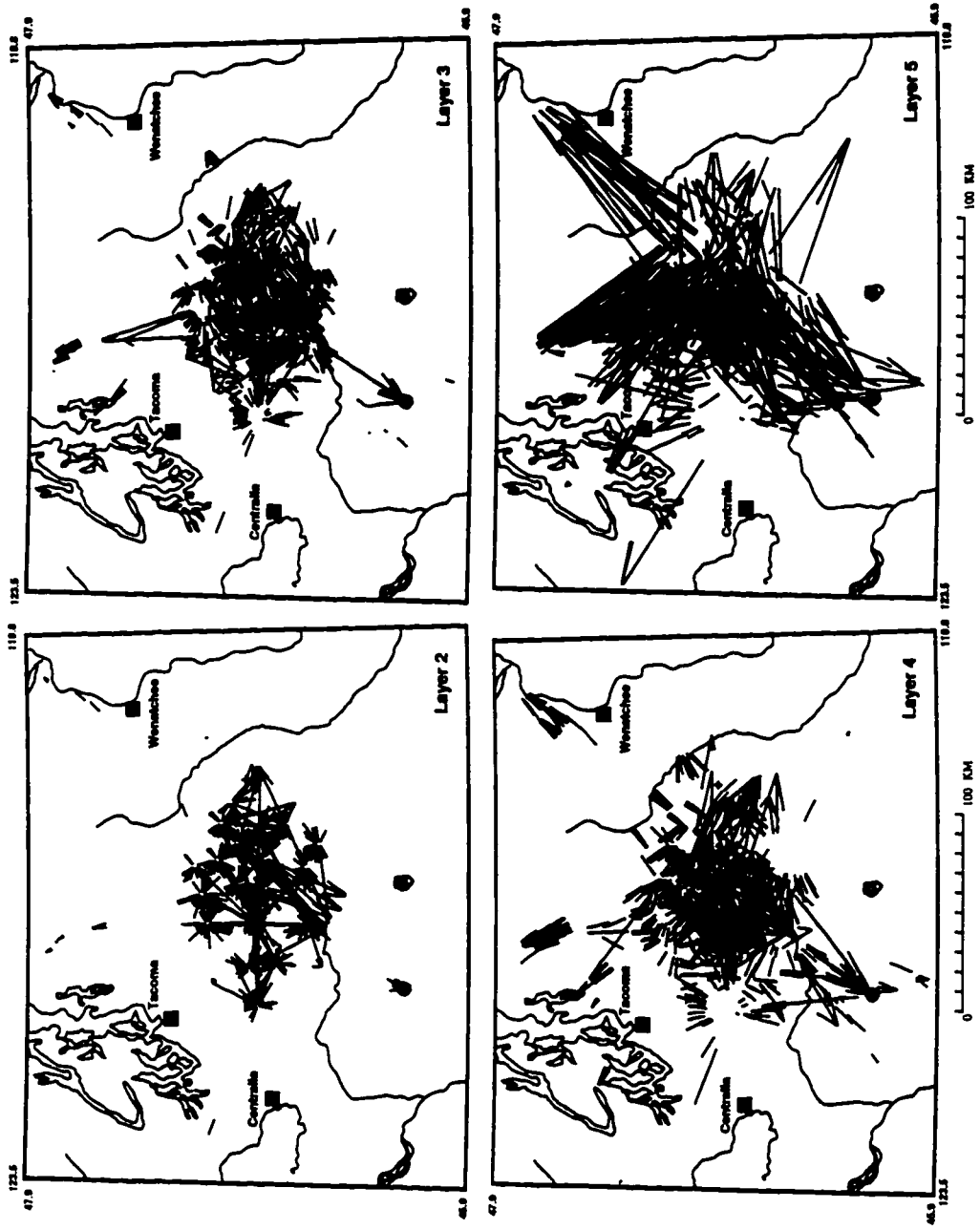


Figure 3-10 Raypaths recorded by NEHRP stations. See Figure 3-6 for layer depths.

Table 3.2: Number of P Arrivals Recorded by Temporary Stations

Station	Observed #P-picks	Predicted #P-picks ^a	Dates of Operation
RSH	89	49	950613 - 950920
RVN	94	128	950925 - present ^b
ULB	82	45	950629 - 950929
WCR	101	50	950612 - 950922
WI2	25	128	950925 - 960717
WPS	61	45	950629 - 950928
XTL	177	128	951011 - present ^b

a. The predicted # of P-picks was calculated by multiplying the number of days each station was in operation by the ratio (60 earthquakes / 120 days (4 months)).

b. RVN and XTL are still in operation; the predicted & observed P-picks are counted through the end of the experiment.

During the experiment, 12 of 18 stations recorded more than 60 arrivals, only 3 stations (BDM, RAD, and WI2) failed to record 75% or more of the anticipated number of P-wave arrivals. BDM was installed along a ridge crest near several trees, and the resultant wind noise was often large enough to obscure arrivals from events below magnitude 2. RAD was installed within 100 meters of a 60-80 ft. antenna tower that generated large amplitude low frequency noise, obscuring many arrivals. WI2 was a good seismic site, but the signal was lost after 3.5 months of operation due to a radio receiver failure at RVN. Despite these 3 disappointments, the total number of new high-quality raypaths recorded during this experiment (1640) vastly exceeded expectations.

Lessons Learned

The fact that the field experiment was successful shows that this type of endeavor is a good way to increase the amount of data available for LET investigations. It is also relatively cost-effective, if the telemetry infrastructure is already in place. Despite the success of the experiment, one problem encountered during the experiment is worth noting. Two of the repeater sites, RVN and BDM, stopped transmitting for roughly one month during January and February. The signals gradually came back after several consecutive sunny days, indicating that the problem was

caused by insufficient charging of the batteries by the solar panels. The current draw for these repeater sites was around 150 milli-amps, roughly double the current at an average station due to the added load of the two additional receivers and summing amplifier. Assuming the 100 Amp/hour batteries were operating at 50% efficiency due to cold temperatures, this load would drain the battery in 14 days without solar charging, compared to 42 days for an average station current draw. Compounding the problem was the fact that at RVN the solar panel was completely in the shadow of a building during the winter months (Vern Wold, AT&T-Yakima, personal communication). Also, at BDM the solar panel, due to its location on a ridgetop underneath trees, was likely covered with snow. The lesson learned is that special care must be taken when positioning solar panels for power-hungry sites to ensure that the solar panel will see a maximum amount of sun during the winter months. In addition, using larger (40 or 60W) panels would probably help, although a voltage regulator would be required to ensure that the battery was not over-charged during the summer.

Another aspect of the experiment that was underappreciated was the contribution the temporary stations made to improving location quality in addition to data quantity. There are several significant gaps in permanent PNSN station distribution west and south of Mount Rainier (Figure 3-7) near the WRSZ and northern terminus of the SHZ. These distribution gaps reduce location qualities, primarily by increasing the distance to the closest station and thus decreasing the quality of constraints on the depth of the source. Three temporary stations, PAK, ASF, and WCR, were placed in these gaps, but only for the first part of the experiment. Thus although many WRSZ earthquakes occurred while stations XTL, RVN, WI2, QTZ, BDM, CMK, GRL, and MUP were in operation, many of these events were not usable because the distance to the nearest station was too great. Future experiments with goals similar to this one should take this factor into account when determining when and where to place seismographs.

3.4 Inversion Dataset

The selection criteria shown in Table 3.1, when combined with additional data recorded by the two field experiments, yield an initial dataset of 4977 earthquakes and 35 blasts (which are not subjected to the earthquake selection criteria). I subject this dataset to several additional criteria during the location process. Two criteria

are applied to individual raypaths. First, rays are used only if the station-receiver distance was less than 150 km. Second, rays are not used if their residuals ((calculated travel times) - (observed travel times)) are greater than ± 1.25 seconds. These criteria were devised after a visual assessment of travel-time pick quality, and are designed to make the inversion more robust by removing those residuals that are most likely to be due to picking errors.

An additional criterion is based on the stability of each location determination. Location stability is measured in two ways. First, if a solution does not converge (here a solution converges if the x and y coordinates change by less than 0.005 km and the depth by less than 0.1 km between location iterations) within a preset number of iterations, then the solution is discarded. Secondly, I use singular-value decomposition (SVD) to invert for hypocentral parameters in the location routine, which allows for the computation of the condition number. The condition number is the ratio of the largest to the smallest singular value in a decomposed matrix, and is a measure of the relative stability of a solution (e.g. Lanczos, 1961). After some experimentation, I decided to reject locations with condition numbers greater than 1100, as events with condition numbers greater than this tended to have unstable locations.

The use of these additional criteria further reduce the number of earthquakes and raypaths available for velocity inversion. In addition, they (in conjunction with the criteria listed in Table 3.1) also impart some variability in the size of the dataset used in each velocity inversion step. For example, of the initial 5012 sources, 4230 events (with 80,973 raypaths) met the selection criteria after the first location step, whereas only 3732 events (74,648 raypaths) met the criteria after the second location step, and 3743 events (74,781 raypaths) after the third. The difference of ~500 events between the first location step and subsequent location steps is largely due to the use of stations outside as well as inside the GMR during the first location step. This was done to stabilize locations along the edges of the model, and resulted in a higher percentage of events satisfying the selection criteria. I found that if external stations were not used in the initial step, then locations along the edges moved substantial distances, and the resulting velocity image showed evidence of severe smearing of structure near the edges. Since I used only stations within the GMR for each subsequent location step after the first, fewer events satisfied the selection criteria (especially the azimuthal gap criterion). Since most of the

500 events that were excluded in subsequent steps are located along the edges of the GMR, I assume that this difference in dataset size between the first and subsequent inversion steps did not affect the resulting model. Likewise, I assume that the smaller variability in dataset sizes used in subsequent inversion steps did not significantly influence the final model, an assumption supported by the observation in section 4.1.2 that the 3-D velocity model did not change appreciably after the second inversion step.

IV. Results and Interpretations

4.1 Inversion

4.1.1 One-Dimensional Model

The initial step in the inversion was to derive a 1-D starting velocity model for subsequent 3-D inversions. I used the PNSN "C3" velocity model as an a priori reference model. The C3 model is the result of two refraction studies, one by Malone and Pavlis (1983) near Mount St. Helens, the other by Leaver (1984) in the Oregon Cascades, and is routinely used by the PNSN to locate events in the Cascades. To improve vertical resolution, I increased the number of layers from 6 to 11, and interpolated velocities from the C3 model to assign velocity values for the new layers. The interpolated model ("C4") is shown in Table 4.1. I then used the inversion methodology described in Chapter 2 and the dataset described in Chapter 3 (minus the blasts) to invert for a new 1-D model. Each layer contained only one block the size of the entire GMR, so the inversion involved only 11 parameters, making it over-constrained. I used simple damping (each parameter is constrained to be zero) instead of Laplacian smoothing, and the damping parameter λ was determined via construction of a trade-off curve between parameter variance and % reduction in the χ^2 misfit. The inversion converged after four iterations, achieving a χ^2 reduction of 7%. The final 1-D model is shown in Table 4.1.

Table 4.1: 1-D Velocity Model Comparison

Layer #	Depth (km) ^a	C4 model (km/sec)	Final 1-D model (km/sec)
1	-3.08	5.10	4.93
2	1.0	6.00	5.90
3	4.0	6.20	6.09
4	7.0	6.40	6.28
5	10.0	6.60	6.53
6	14.0	6.70	6.65
7	18.0	6.80	6.72
8	23.3	6.90	6.88
9	28.7	7.00	7.02
10	34.0	7.10	7.10
11	43.0	7.80	7.80

a. Depth is computed relative to sea level

4.1.2 Three-Dimensional Model

For the 3-D inversion I divided each layer into 10,080 2.5km x 2.5km constant velocity blocks, resulting in a total of 110,880 blocks (or parameters). Note that the lateral dimension of these blocks is slightly less than the vertical. This is because I am primarily interested in lateral velocity contrasts. The vertical velocity structure is assumed to be known to first order, due to the work of Pavlis and Malone (1983) and Leaver (1984), and is not the primary object of my study.

Of the 4230 events and 80,973 raypaths used in the initial step of the 3-D inversion, roughly 3700 events and 75,000 raypaths met the selection criterion in subsequent inversions (as discussed in section 3.4, this difference is due to the use of stations outside the GMR during the initial location step only). This resulted in an A matrix of 2.2×10^{10} elements after the Laplacian constraints were added. Premultiplication by the annihilation operator decreased the sparsity of A from 99.987% to 99.944%, roughly doubling the computation time for the velocity inversion in a single inversion step. Each velocity inversion typically converged after 150 iterations of the LSQR algorithm (see section 2.6 for an explanation of the difference between "full inversion", "inversion step", and "iteration"). The full inversion converged after 7 hypocenter-velocity inversion steps, although there was little significant change in the image after the second inversion step. The net reduction in the χ^2 misfit (from the initial value of χ^2) was 94%, with no appreciable reduction in χ^2 from the initial value after the fifth inversion step. The 94% figure is somewhat of an overestimate, however, since ~6,000 fewer rays were used in each inversion step after the first. A more meaningful statistic is the percent reduction in χ^2 misfit achieved within each inversion step. A reduction of 55% was achieved in the first step, but only a 6.2% reduction was achieved in the last (Figure 4-1). Note that reduction in χ^2 misfit is calculated relative to the value of χ^2 at the beginning of each inversion step. The starting χ^2 is always higher than the χ^2 at the end of the previous step, because the intervening relocation step increased residuals.

The final 3-D model is shown in Plate 1 on the back inside cover. For each layer I show only those blocks that have been 'hit' by at least one ray. Earthquakes contained within each layer are also included in each plot. I have chosen to display the 3-D model in terms of absolute velocities (instead of percent perturbations to the starting 1-D model) because velocities can be more easily related to rock types, greatly facilitating the interpretation of anomalies in terms of rock lithology.

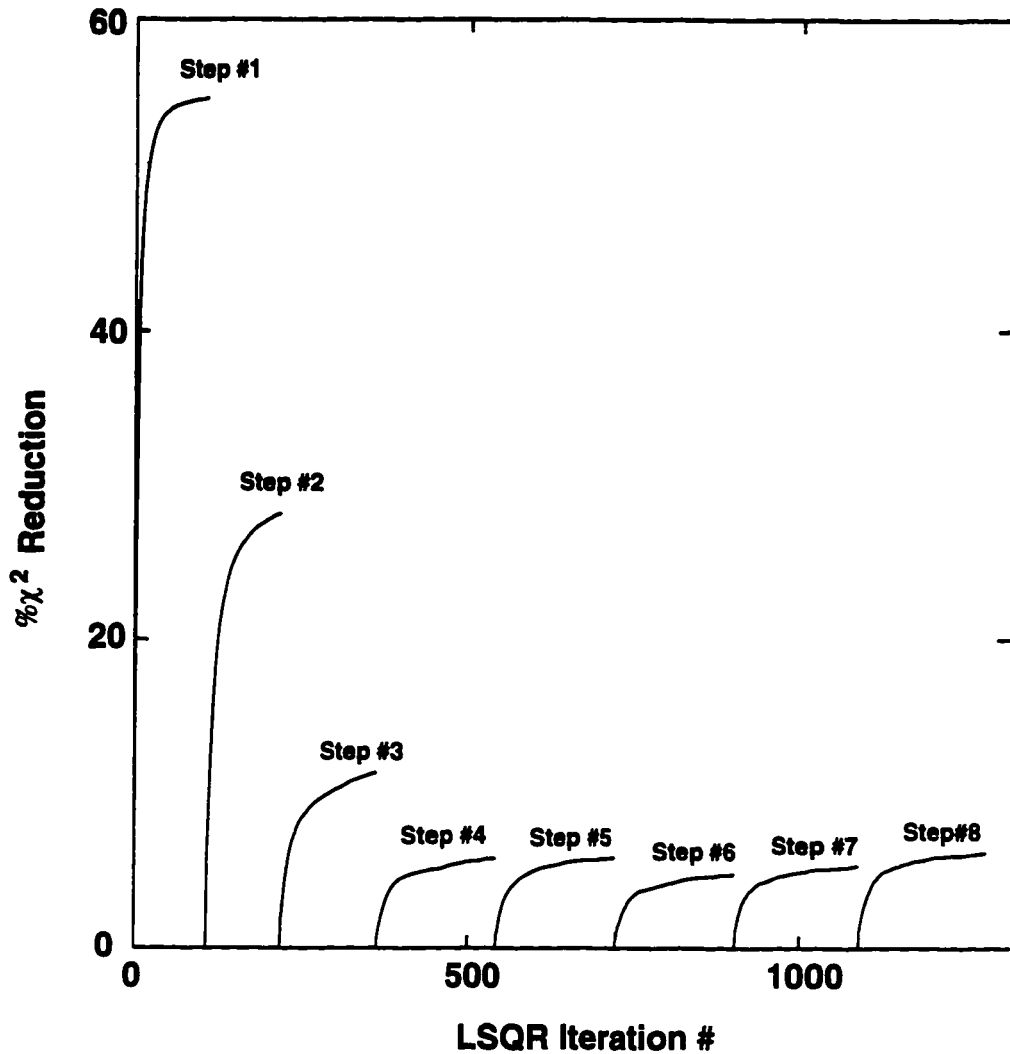


Figure 4-1 Percent reduction in the χ^2 misfit within each velocity inversion step. Misfit reduction is computed relative to the χ^2 value at the start of each inversion step. The LSQR iteration # is treated as continuous between each step for display purposes only. Note that there is no appreciable decrease in the reduction of the χ^2 misfit (relative to the value at the start of each inversion step) after the fourth step.

4.2 Error Analysis

4.2.1 Checkerboard and Jackknife

Resolution and error plots are included beneath each layer in Plate 1. The resolution and error plots are derived from the checkerboard and Jackknife procedures described in section 2.5. Since the checkerboard test was run with data used in the

final iteration and the Jackknife test was run with data used in the first iteration, the pattern of 'hit' blocks varies a little between the two plots. However, the fact that model changed little after the first iteration suggests that these tests are both useful for assessing error and resolution in the final 3-D model.

The input model for the checkerboard test had $\pm 10\%$ perturbations. However, the main utility of the checkerboard test is in estimating the minimum resolvable size of bodies with contrasting velocities in different regions of model space. In order to increase the visibility of resolved anomalies in each plot, each figure is scaled to only $\pm 5\%$ perturbations, with values above $\pm 5\%$ fixed at $\pm 5\%$. For the Jackknife test the dataset was divided into 20 groups of ~ 3500 events. λ was set at 600 for both tests.

4.2.2 Blasts

In addition to resolution and variance, blasts can also be used to assess the accuracy of LET-derived velocity models. If a source with a known location and origin time is relocated in a given velocity model, then the distance in space and time from the new location to the known location is a measure of the expected earthquake relocation error (at least for shallow earthquakes) in that model. This distance also provides a means for evaluating the relative merits of different velocity models. In addition, it can indicate whether a particular velocity model is grossly in error or not, since poor relocations suggest that a given velocity model is a poor representation of the earth.

35 blasts with known locations and origin times locate within the GMR (pink circles in Layer 1 of Plate 1). To relocate these events I used only stations located within the GMR, decreasing the location stability of blasts on the edge of the model and reducing the number of blasts with well-constrained relocations to 27 at 17 different sites (Figure 4-2). The average mislocation in the 3-D model was 1.1 km in 2-D space (map-view), 3.1 km in 3-D space, and the origin time was missed by 0.57 seconds. In contrast, the average mislocation in the 1-D reference model (with station corrections) was 1.2 km in 2-D space, 4.4 km in 3-D, and the origin time was missed by 0.68 seconds. Overall, 20 of the 27 blast relocations were closer to the truth in the 3-D model than in the 1-D model (Figure 4-2), indicating that the 3-D model is an improved version of the earth over the 1-D model with station corrections. 5 of the 7 cases where the 1-D model did better were located near the model edges, where the

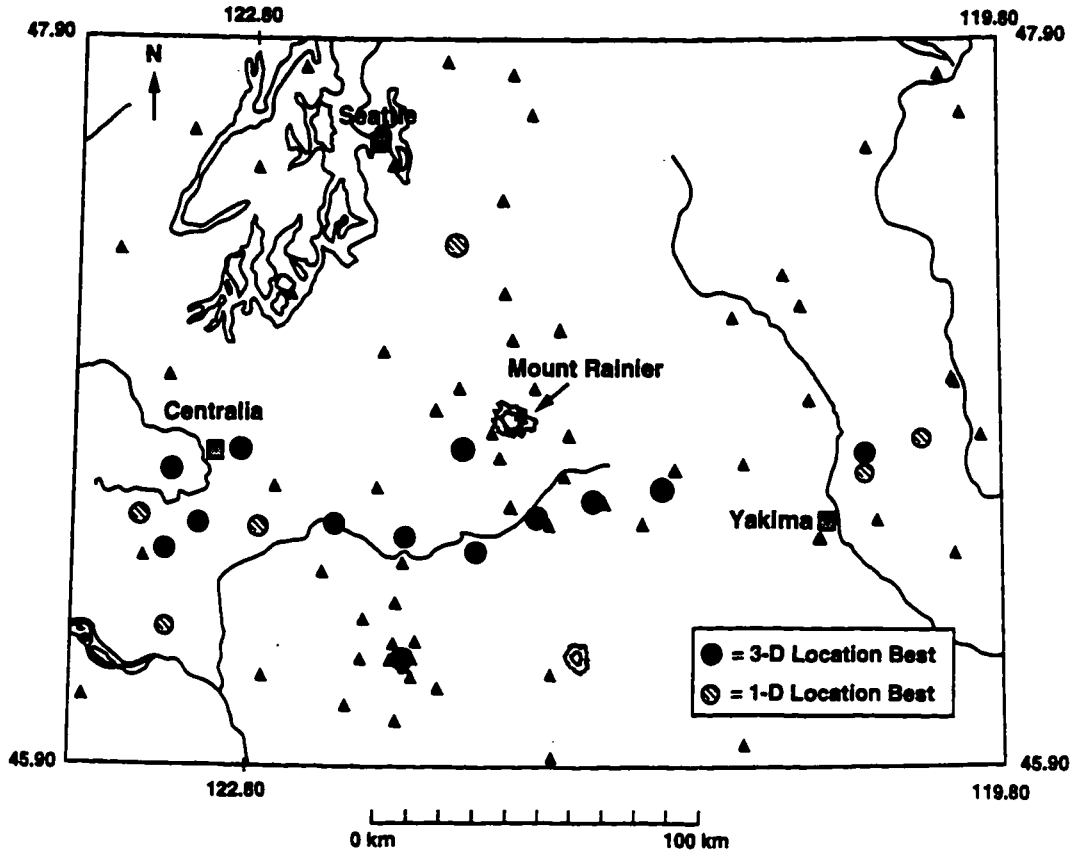


Figure 4-2 Map showing blast relocation test results. Filled circle indicates 3-D locations are best; hachured circle indicates 1-D locations are best.

3-D locations used roughly half of the stations used in the 1-D location. The other 2 cases can't be attributed to poorer station distribution, suggesting that the 3-D model, at least locally, may be in error.

Two comments are worth making regarding this test. First, the improvement in 3-D locations largely represents an improvement in the accuracy of depth determinations. Although the 3-D depths are still off by an average of 2.9 km, it is worth noting that depths of surface sources are usually very difficult to accurately determine. This arises in large part because the elevations of recording stations usually are similar, and are also similar to the true depth of the surface source. This geometry results in a situation where varying the depth of the source by several km does not have an appreciable affect on the travel-time residuals, causing the depth that is determined to be reasonably non-unique and poorly constrained. Thus the 2.9 km absolute error in depths for the 3-D locations is actually quite good for surface

sources that don't have a recording station located very near the epicenter (or recording stations with significantly different elevations). Second, the fact that 75% of the 3-D blast relocations are measurably better than 1-D relocations suggests that our model should also improve the reliability of shallow earthquake relocations in other parts of the GMR, an especially important consideration in areas like Mount St. Helens and Mount Rainier with significant numbers of shallow earthquakes.

4.2.3 Layer-by-Layer Interpretations

Layer 1

The degree to which anomaly patterns and velocities match the mapped geology exposed at the surface is another valuable tool that can be used to assess the reliability of a velocity model. This is problematic in the uppermost layer (Layer 1 (-3.085 - 1 km)), where raypaths are almost exclusively vertical thus providing little horizontal resolution (note that -3.085 km corresponds to the elevation of the highest station in the GMR). However, where there is sufficient resolution (such as near Mount St. Helens, Mount Rainier, and the 1991 and 1995 USGS blasts), there is good correspondence between imaged velocities and local geology as mapped by Fiske et al. (1964), Evarts et al. (1987), Walsh et al. (1987), and Schuster (1992) (see Figure 1-4).

A southwest-northeast trending high velocity that lies southeast of Mount Rainier (located between stations LON and DLR (see Figure 3-7)) correlates well with the mapped extent of the Tatoosh pluton. The Spirit Lake pluton north of Mount St. Helens also coincides with a high velocity anomaly between stations SBL and SOS (see Figure 3-7). The imaged velocities for both granodiorite plutons (5.7 - 6.0 km/sec) are consistent with measured velocities of granodiorite at pressures and temperatures equivalent to 1.5 km depth (Christensen and Mooney, 1995; see Appendix A¹).

Layer 2

Resolution (as estimated by the checkerboard method) is better in Layer 2 (1 - 4 km), although raypaths are still predominantly vertical. Well-resolved anomalies again show good correspondence with local geology as well as with aeromagnetic and Bouguer gravity anomalies. A 40 x 50 km region of high velocities (5.9 - 6.3 km/sec)

1. Appendix A lists measured P-wave velocities for a wide range of rock types at various depths.

extends ESE from the northeastern tip of the Western Rainier Seismic Zone (WRSZ) to the Rimrock Lake area, roughly correlating with the mapped distribution of several Tertiary granitic to granodioritic plutons (including the Tatoosh, White River, and Bumping lake plutons) as well as with resistive bodies detected in magnetotelluric experiments by Stanley et al. (1992). Two other anomalies with similar velocities correlate with the Spirit Lake and Spud Mountain plutons north of Mount St. Helens. Velocities of 5.9 - 6.3 km/sec are consistent with measured velocities of granodiorite at pressures and temperatures equivalent to 5 km depth (Christensen and Mooney, 1995). The fact that all three of these velocity anomalies are larger than the mapped dimensions of their correlative plutons suggests that these plutons are probably much more extensive below the covering of Tertiary volcanoclastic and Quaternary volcanic rocks in the upper 2 km.

A north-south-trending low velocity anomaly (5.0 - 5.5 km/sec) west of Mount Rainier correlates with the trace of the Carbon River/Skate Creek anticline (see geology figure in Plate 1), as well as a linear aeromagnetic low (Figure 1-3) (Stanley et al., 1987). The Carbon River/Skate Creek anticline is cored by Tertiary sediments of the Carbonado formation. The velocities in my LET image are consistent with this lithology; measured velocities of sandstones at pressures and temperatures range from 4.97 km/sec at 2 km depth (surface elevation along the anticline is ~1 km above sea level) to 5.48 km/sec at 5 km depth (Christensen and Szymanski, 1991). A more pronounced velocity low (3.8 - 4.9 km/sec) correlates well with the Chehalis basin, as well as with a low in the Bouguer gravity field (Figure 1-3) (Finn, 1990) and a conductivity high mapped by Egbert and Booker (1993). In addition, a sonic velocity log from the Thompson No. 1 well in the Chehalis Basin shows velocities increasing from ~2.4 km/sec 500m below the surface to ~5.0 km/sec at 3300m depth (Stanley et al., 1994), consistent with the velocities in my LET image. The Jackknife errors are high (greater than ± 0.25 km/sec) for this part of the model, however, so the absolute velocities should be viewed with caution.

Finally, three less well-resolved anomalies in the northwestern corner of the model also correlate well with surface geology. Two low velocity anomalies (3.7 - 4.2 km/sec) correlate with the Seattle and Tacoma basins, as well as with lows in the Bouguer gravity field (see Figure 1-3) (Finn, 1990). While these velocities are higher than the 1.5 - 3.0 km/sec values determined for the upper 3-4 km by Pratt et al. (1997) from seismic reflection data, they are still consistent with laboratory mea-

measurements of dry shale and sandstone velocities at pressures equivalent to 0 - 3 km depth (Christensen and Szymanski, 1991). These two low velocity anomalies extend down to Layer 4 (7 - 10 km), consistent with the maximum basin depths inferred by Pratt et al. (1997). In addition, a high velocity anomaly (6.6 - 6.9 km/sec) centered beneath Green Mountain west of Seattle (near Bremerton) correlates with outcrops of diabase dikes, gabbro, and basalt that are thought to represent an eruptive center correlative with the Crescent Formation (Babcock et al., 1992). Laboratory measurements for gabbros (7.1 km/sec) and diabase (6.7 km/sec) are quite consistent with these lithologies.

Layer 3

Resolution is significantly better in Layer 3 (4 - 7 km), as is apparent in the checkerboard diagram. The best-resolved features are again near Mount St. Helens and Mount Rainier. A region of high velocities (6.4 - 6.7 km/sec) extends east from Centralia to the western edge of the Carbon River anticline, and is discussed in detail in section 4.3.1. The low velocity anomaly in Layer 2 beneath the Carbon River/Skate Creek anticline is also apparent in this layer, with velocities (5.7 - 6.0 km/sec) that are slightly higher than measured velocities for sandstones at pressures equivalent to these depths (5.5 - 5.7 km/sec; Christensen and Szymanski, 1991). The Jackknife error estimates are $\sim \pm 0.05$ km/sec for this part of the model, suggesting that these values are good estimates of the true velocities. One possible explanation for the higher-than-expected velocities is that the Tertiary sediments could be interfingering with higher velocity Tertiary volcanic deposits similar to those found in the Northcraft formation. Alternatively, the sediments could have experienced low-grade metamorphism, which would also increase rock velocities.

A pronounced low velocity anomaly correlates well with the position of the Morton anticline, which is cored by Tertiary sediments of the Carbonado and McIntosh formations inferred by Johnson and Stanley (1995) to extend as far as 10 km below the surface. In addition, several anomalies described in Layer 2 continue in Layer 3, including extensions of the Tatoosh & Spirit Lake plutons and the velocity lows beneath the Seattle and Tacoma basins. Another broad velocity low (4.5 - 5.2 km/sec) extends northwards from Yakima to Ellensburg. The checkerboard and Jackknife diagrams suggest that only broad features are resolvable in this part of the model. However, the velocities are consistent with those determined from seismic

refraction profiling at these depths (Catchings and Mooney, 1988), and probably are a signature of the 2-4 km thick Tertiary sedimentary basins that are inferred to lie beneath the Columbia River Basalts (Catchings and Mooney, 1988; Saltus, 1993; Jarchow et al., 1994).

In general there is good correspondence between velocity anomalies in the first 3 layers of the LET image and surficial geology. This correspondence indicates that the LET velocity image is a good proxy for geology. This in turn indicates that velocity anomalies in deeper model layers can be used with some degree of confidence to infer likely lithologies where resolution is good and the estimated errors in parameter values are small.

Layer 4

Many of the anomaly patterns observed in Layer 3 are also present in Layer 4 (7 - 10 km). These include the low velocity anomalies beneath the Seattle and Tacoma basins, the high velocity anomaly extending east from Centralia, and remnants of the low velocity anomalies associated with the Morton and Skate Creek-Carbon River Anticline. A low velocity anomaly is apparent beneath Mount Rainier. This feature actually extends from Layer 3 (4 km) to at least 14 km, and is discussed in detail in section 4.3.2. In addition, a linear north-south-trending lower velocity trough correlates well with SHZ seismicity. This feature is also visible in Layers 2 and 3, and is discussed in section 4.4.1.

Layer 5

The most visible anomaly patterns in Layer 5 (10 - 14 km) are located in the eastern half of the GMR. The low velocity anomaly beneath Mount Rainier seen in Layer 4 is more distinct in this layer (due to a greater lateral contrast in velocities). The lower velocity trough associated with the SHZ is also apparent. In addition, two broad low velocity anomalies are apparent northeast and southeast of Mount Rainier. These features extend down to at least Layer 7 (23 km), and are discussed in detail in section 4.3.4. Many of the other anomaly patterns discussed in Layers 1 - 4 are not apparent in Layer 5.

Layer 6

The two broad low velocity anomalies seen in the eastern half of Layer 5 are even more extensive in Layer 6 (14 - 18 km). The low velocity anomaly beneath Mount Rainier appears to merge with the southern of these two anomalies. In addition, a ridge of higher velocities appears to bisect the two broad low velocity anomalies. This ridge is parallel to the OWL, and is discussed in section 4.3.5. Velocities beneath Puget Sound, which were quite low in Layers 2-4, are quite high (6.8 - 7.1 km/sec) in this layer, perhaps corresponding to deeply buried sections of the Crescent Formation.

Layer 7

The two broad low velocity anomalies are also present in Layer 7 (18 - 23 km), although somewhat less extensive. The high velocity ridge bisecting the two anomalies is also apparent. No new anomaly patterns are visible in this layer.

Layers 8 - 11

Although velocities were computed for blocks in Layers 8 - 11 (23 - 43 km), the number of 'hit' blocks is small and the resolution is in general quite poor, so these layers are not included in Plate 1, and are not discussed in the rest of this Chapter.

4.2.4 Comparison to the 1991 Refraction Model

Figure 4-3 shows cross-sectional contour plots of velocity variations with depth in the model resulting from the 1991 refraction experiment in Puget Sound (see section 1.4.1) (Miller et al., 1997) and in my 3-D model (the location of the 1991 refraction profile is labeled "USGS 1991" in Figure 1-11). There are general similarities between these plots, including a decrease in near-surface velocities north of the 100 km position on each profile and a general increase in velocities from north to south above 5 km. However, there are also some differences, most notably the higher velocities in the tomographic model relative to the refraction model below 5 - 7 km (although they match quite well above 5 - 7 km). These differences are in large part due to different resolving capabilities of the two datasets. The refraction profile has good ray coverage from the surface to 7 - 11 km (Kate Miller, personal communication), whereas ray coverage is reasonably poor in the upper 1 - 2 km for the tomographic dataset but quite good from 2 to 23 km, especially in the southern half of the profile (see Plate 1). Where the resolution is good in both models (2 - 7

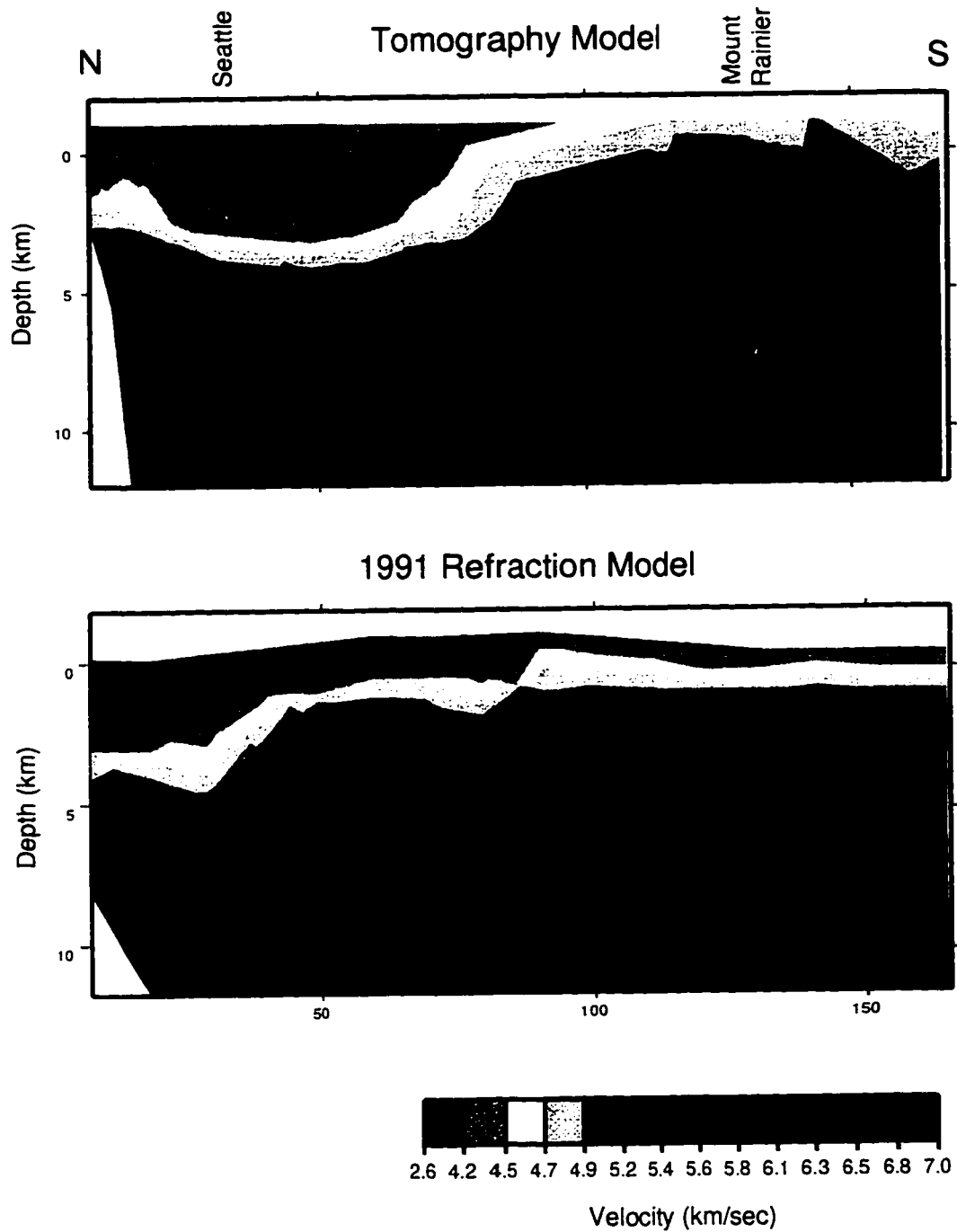


Figure 4-3 Velocity contour plots from a N-S cross-section through the 3-D model (top) and a model from the 1991 refraction profile (bottom). The top cross-section is drawn parallel to the 1991 refraction profile (see Figure 1-11 for the 1991 profile location). The velocity scale for each plot is identical, and is similar to the scale used in all other plots of the tomographic model.

km), the velocities match quite well; thus the disagreements are most likely due to poor resolution.

The differences in resolving capabilities of each dataset limit the utility of making direct comparisons between these two profiles. However, the 1995 refraction profile traversed through a region of excellent ray coverage in the GMR, so comparisons between the two models will hopefully not be as limited by resolution. A final model is not yet available for the 1995 refraction profile (Tom Parsons, personal communication). Figure 4-8 in section 4.3.4 is a cross-section through my 3-D model drawn approximately parallel to the 1995 profile, and can be used to facilitate comparisons when the refraction model is completed.

4.3 Interpretations of Deeper Anomalies

4.3.1 A Buried Eruptive Center for the Crescent Formation

A broad well-resolved high velocity anomaly (6.4 - 6.7 km/sec) in Layers 3 and 4 (4 - 10 km) extends eastwards from Centralia to the western edge of the Carbon River anticline, where it also appears to correlate with the western boundary of the SWCC (see Figure 4-7). It lies beneath sediments of the southernmost Puget Lowlands and an uplift of Paleogene sediments and volcanics that form the northern boundary of the Chehalis Basin. It correlates well with an aeromagnetic high (Figure 1-3) interpreted by Stanley et al. (1987) and Finn (1990) to be a buried remnant of the Crescent Formation. It also correlates with a high velocity (6.35 km/sec) layer detected between 3.5 and 5.5 km with data recorded during an unreversed refraction survey in 1994 (Moran and Malone, 1994; see section 3.3.1).

Lithologies that are consistent with the LET-derived velocities include zeolite and prehnite-pumpellyite facies basalt, both of which have measured velocities of around 6.25 km/sec at pressures and temperatures equivalent to 5 km depth (Christensen and Mooney, 1995), and diorite (measured velocities of 6.41 km/sec). Since there are no exposures of diorite at the longitude of this anomaly in the GMR, I consider diorite to be an unlikely lithology. Low-grade metamorphosed basalt is a satisfying hypothesis because it corresponds to the lithologies found in the lower member of the Crescent Formation (e.g. Tabor and Cady, 1978), exposed just a few kilometers west of this anomaly. However, the measured velocities of zeolite facies basalt are somewhat lower than the LET velocities. One explanation for the slightly

higher LET velocities is the possibility that the metamorphosed basalts are locally juxtaposed with diabase dikes and sills (measured velocities of 6.64 km/sec) and/or small amounts of gabbro (measured velocities of 7.05 km/sec). These latter rock types are found along with basalt at an inferred eruptive center west of Bremerton that is correlative with the Crescents (Babcock et al., 1992). Thus a logical interpretation of this anomaly is that it represents a buried eruptive center of the Crescent Formation, composed primarily of altered basalts with minor amounts of gabbro and/or diabase.

4.3.2 Low Velocity Anomaly Beneath Mount Rainier

One of the more remarkable features in the velocity image is a ~10 km-wide constant-velocity cylinder (5.95 km/sec) directly beneath Mount Rainier that extends from 1 km to 14 km depth. In cross-sectional view it is even more apparent (Figure 4-4; see also Plate 1). Resolution is excellent in the vicinity of Mount Rainier (3-6 km, or 1-2 block widths) and estimated errors are small (~0.01 km/sec), indicating that this feature is real and well-resolved. As discussed above in section 4.2.3, ~6 km/sec velocities near the surface are consistent with measured velocities in granodiorite (Christensen and Mooney, 1995). However, 6 km/sec velocities at depths of 10-18 km are consistent with velocities of altered rocks such as slate, phyllite, and granitic gneiss. Volcanic rocks as a group have velocities slower than 6 km/sec at these depths (for example, andesite is ~5.56 km/sec), and intrusive rocks are faster (granodiorite is ~6.23 km/sec). Thus it is difficult to explain this anomaly at depth simply by the presence of igneous rocks. Either the lithology is non-igneous, or there are other processes acting to lower intrusive rock velocities (or raise volcanic rock velocities) beneath Mount Rainier.

I believe that this cylindrical anomaly is, at least in part, a manifestation of thermal effects associated with the magmatic system beneath Mount Rainier. Low velocity anomalies beneath volcanoes are often interpreted by tomographers to be regions of hot rock and/or "magma chambers" (e.g. Lees, 1992; Iyer, 1993), an interpretation usually based on the coincidence of the anomaly's location beneath a volcano. At Mount Rainier, several additional arguments can be used to support the hypothesis that the cylindrical anomaly is due to the presence of hot (but not necessarily liquid) rock. The first comes from the observation that no earthquakes locate within the cylindrical anomaly. In addition, earthquake depths outside the cylinder progressively decrease from all directions as its edges are approached (Figure 4-4).

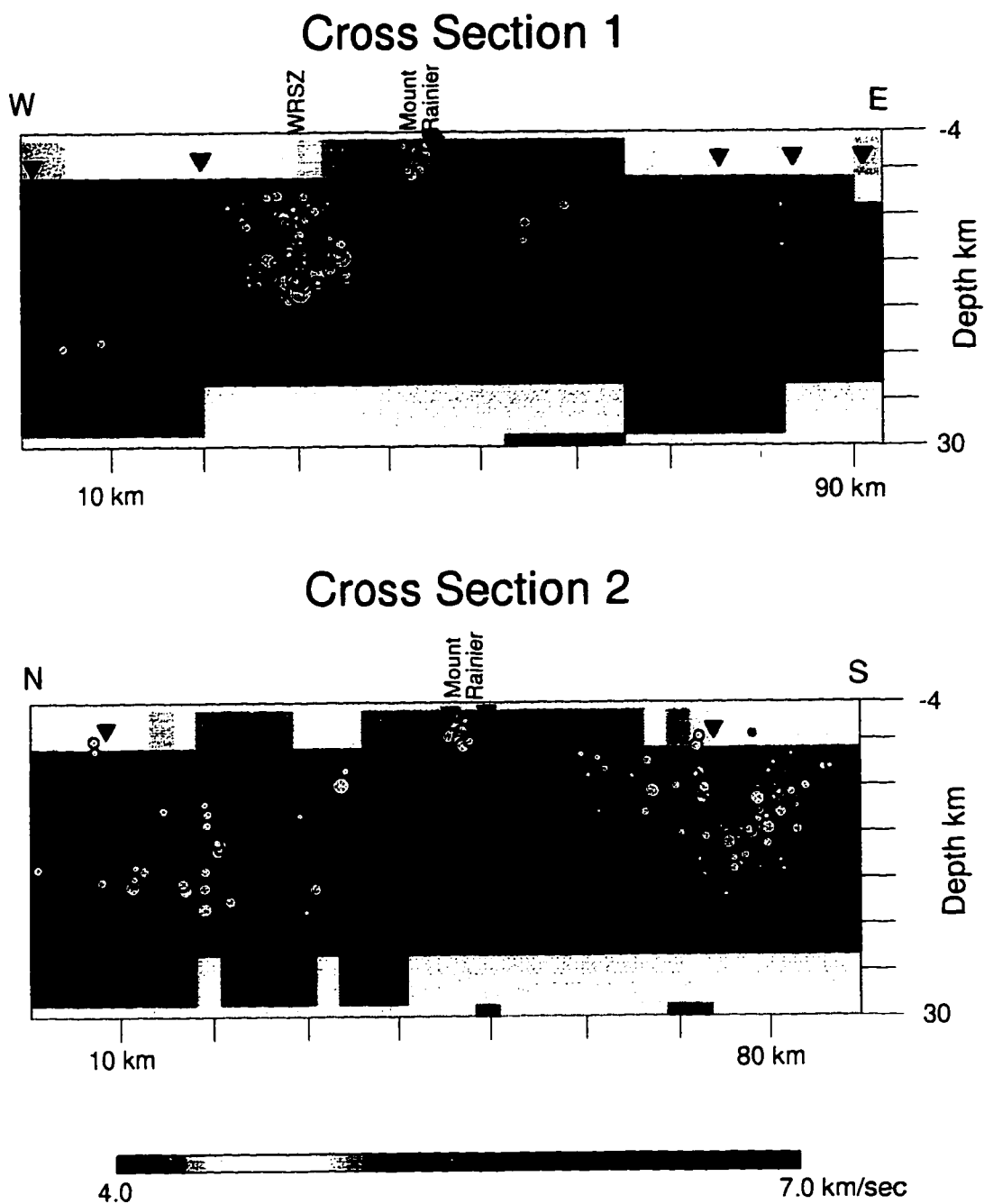


Figure 4-4 E-W and N-S cross-sections through Mount Rainier. Note the zone of lower velocities beneath Mount Rainier, and the shallowing of hypocenters as this zone is approached from any direction. The profile positions are indicated in Layer 1 of Plate 1. The velocity scale is identical to the one used in Plate 1.

These two observations suggest a shallowing of the brittle-ductile transition as the edifice is approached, which, if true, indicates that the rock within the low velocity cylinder is hot.

The second argument is a negative one. If it is assumed that the 5.95 km/sec anomaly is solely due to composition, then the likely lithologies at 10-18 km depths are phyllite, slate, and granitic gneiss (see Appendix A). However, the only xenoliths found to date in the andesites and dacites of Mount Rainier are cognate andesitic-to-mafic inclusions and olivine gabbro xenoliths (McKenna, 1994). No xenoliths of non-igneous origin have been found (Tom Sisson, personal communication). At Mount St. Helens, Heliker (1995) found abundant gabbroic xenoliths, with smaller amounts of quartz diorite, metamorphosed basalt, dacite, andesite, and vein quartz. Aside from the gabbros (which are thought to be cumulates), each of these lithologies is consistent with the presumed composition of the conduit wall rock beneath Mount St. Helens from the surface to at least 6 km depth. The lack of any phyllite, slate, or granitic gneiss xenoliths at Mount Rainier suggests that they are in fact not present beneath the volcano. If this is true, then composition alone cannot explain the anomaly.

The third argument is directly related to the second argument. If other lithologies can be ruled out due to lack of evidence from xenoliths, then the most likely lithology to expect beneath an andesitic volcano like Mount Rainier is dacite. Granodiorite (compositionally close to dacite) has velocities of 6.22 km/sec at pressures equivalent to 10-20 km depth. If this is in fact the lithology, then some mechanism (such as elevated temperatures) is required to lower the velocities by ~4.5%.

These arguments support the idea that temperatures are elevated within the anomaly, and that the velocities are not due to composition alone. I consider two end-member hypotheses to explain these observations. The first calls upon the presence of magma to explain the low velocities (the "magma" hypothesis). Assuming a P-wave velocity of 2.5 km/sec for an andesitic magma with no crystals (Murase and McBirney, 1973), the anomaly could be explained by the presence of 7% (by volume) andesitic melt evenly distributed throughout the anomaly. The second hypothesis is that low velocities are caused elevated temperatures due to conductive cooling of magmatic bodies, resulting in a thermal aureole with temperatures approaching (but not reaching) the solidus of the country rock (the "hot rock"

hypothesis). In the first hypothesis, the presence of magma would be enough to lower velocities. In the second hypothesis, the lowered velocities would be due to a negative slope of velocity/temperature derivatives as temperature increase to near the solidus. The first hypothesis could be tested by looking for evidence of seismic attenuation and/or changes in the V_p/V_s ratio across the anomaly, which would require 3-component and (for attenuation) broadband data. However, current instrumentation near Mount Rainier consists of 1 broadband 3-component and 9 short-period vertical-component stations. Thus data limitations make the first hypothesis difficult to test. A logical first step, then, is to perform thermal modeling to attempt to confirm or refute the second hypothesis.

Thermal Modeling

Can cooling magmatic intrusions beneath Mount Rainier affect temperatures in the surrounding wall rock enough to influence seismicity and/or rock velocity to the extents observed Figure 4-4 and Plate 1? I use equations from Carslaw and Jaeger (1959) and Turcotte and Schubert (1982) for temperatures resulting from the instantaneous heating of a half space to attempt to address this question. (The geological equivalent of the instantaneous heating of a half-space is the instantaneous heating associated with the injection of a dike of magma into a region of rock at a constant, relatively cool temperature T_o). These equations assume a scenario where at time $t = 0$ the surface $r = 0$ (the dike/country rock contact) is suddenly brought up from the ambient temperature T_o to a temperature T_m (see Figure 4-5). Temperatures are calculated for times $t > 0$ assuming that the surface at $r = 0$ is held at a constant temperature T_m , and that the intrusion cools only via conduction. The resulting equation for temperatures $T(r,t)$ at distances $r > 0$ and $t > 0$ is

$$T(r, t) = T_o + (T_m - T_o) \operatorname{erfc}\left(\frac{r}{2\sqrt{\kappa t}}\right) \quad (\text{EQ 4.1})$$

where erfc is the complementary error function and κ the thermal diffusivity, which can be computed via the relationship

$$\kappa = \frac{K}{\rho c} \quad (\text{EQ 4.2})$$

(Turcotte and Schubert, 1982), where K is the thermal conductivity, ρ the density, and c the specific heat of the medium. Assuming a thermal conductivity of $3 \text{ J} / (\text{m}$

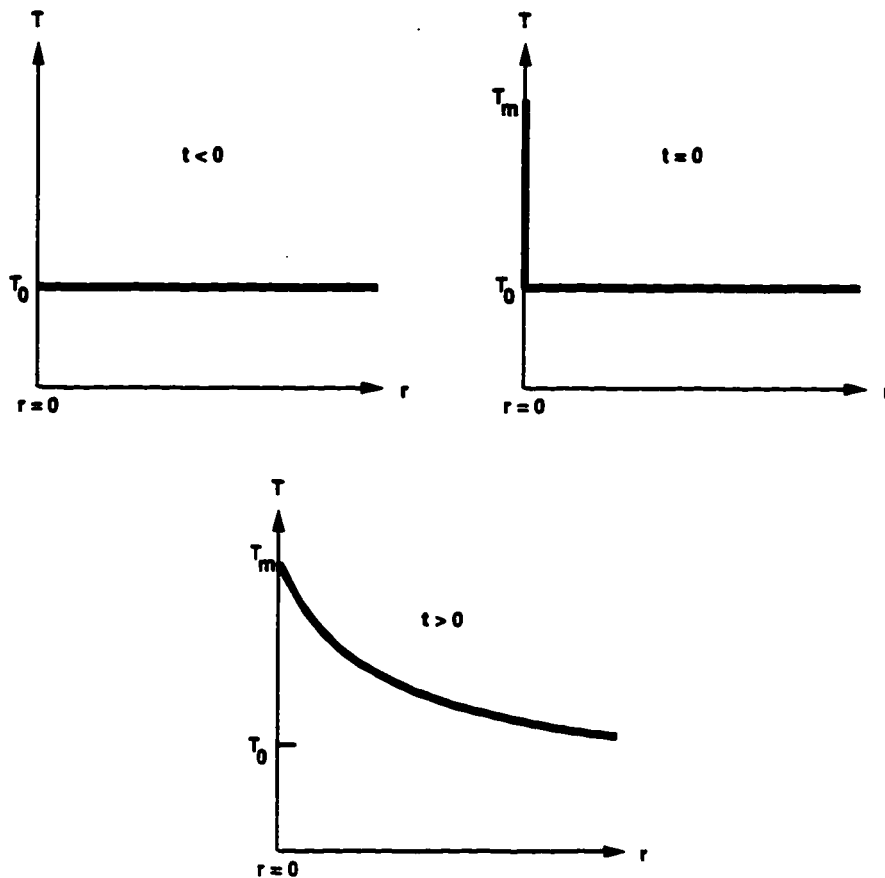


Figure 4-5 Diagram illustrating geometry for heating of half-space problem.

sec $^{\circ}\text{C}$) (Turcotte and Schubert, 1982), a density of 2700 kg/m^3 (e.g. Turcotte and Schubert, 1982), and a specific heat of $820 \text{ J/(kg } ^{\circ}\text{C)}$ (Ozisik, 1993), κ is $1.35 \times 10^{-6} \text{ m}^2/\text{sec}$.

T_0 is estimated from heat flow measurements collected by Blackwell et al. (1990), which indicate that the geothermal gradient is $\sim 30^{\circ}\text{C}/\text{km}$ in the region around Mount Rainier. This gradient yields estimates for T_0 of 100°C at 3.5 km depth (or 2 km below sea level, assuming an average terrain elevation of 1.5 km), 200°C at 7 km depth (5.5 km below sea level), and 300°C at 10 km depth (8.5 km below sea level). To estimate T_m , I assume that the wall-rock immediately adjacent to a dike is kept at or near its melting temperature. I assume that the wall-rock is granodioritic in composition, and use laboratory measurements of the granodiorite solidus (e.g. Best, 1982) at pressures equivalent to upper crustal depths to estimate a value of 700°C for T_m . Using these values in equation 4.1, a range of values for $T(r,t)$ can be

computed for a range of times $t > 0$ and distances r from the intrusion. The resulting temperature vs. distance profiles are plotted in Figure 4-6 for a range of times after intrusion.

Two horizontal lines of constant temperature are drawn in each of the 3 plots in Figure 4-6. The first line ($T = 350^\circ\text{C}$) represents an estimate of the temperature at which deformation of crustal rocks changes from brittle (seismogenic) to ductile (aseismogenic) behavior as determined from laboratory and field experiments (e.g. Hyndman and Wang, 1993). For $T_0 = 100^\circ\text{C}$ (2 km below sea level), all curves exceed 350°C at distances less than 1.5 km from the intrusion, and the ductile region extends out to 5 km at $t = 500,000$ years. For $T_0 = 200^\circ\text{C}$ (5.5 km below sea level), the ductile region extends outward to from 2 km at $t = 50,000$ years to ~ 7 km at $t = 500,000$ years. Finally, for $T_0 = 300^\circ\text{C}$ (8.5 km below sea level), the ductile region extends from 3 km at 50,000 years to ~ 10 km at 500,000 years. Beneath Mount Rainier the "seismic gap" extends 7-10 km (3-4 blocks) from the center of the low veloc-

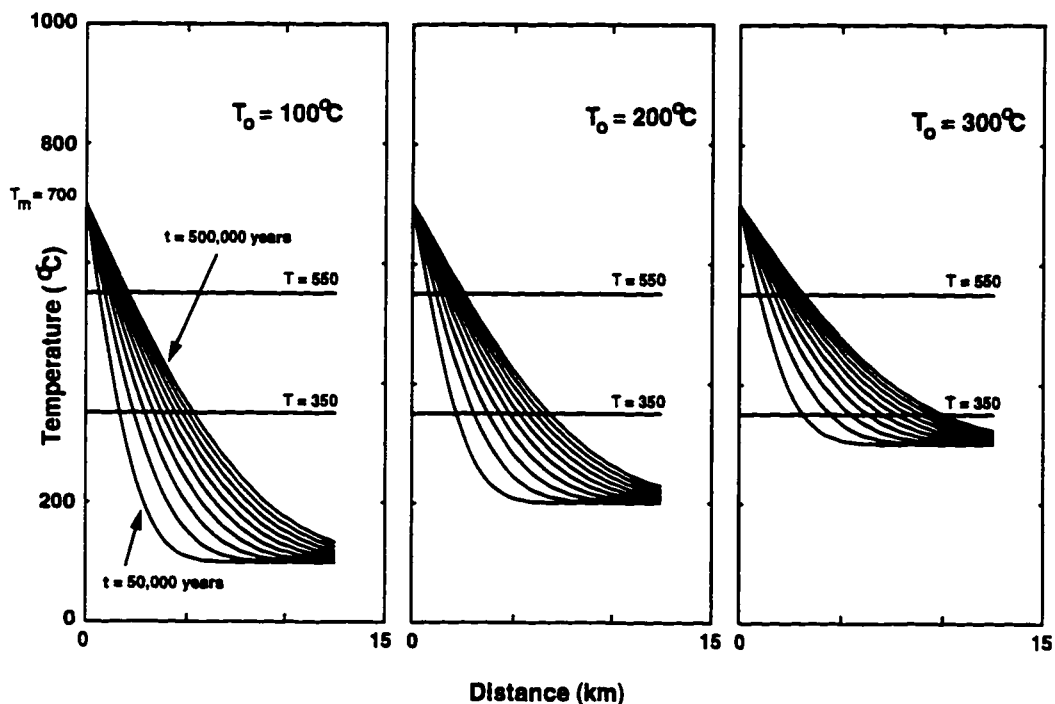


Figure 4-6 Temperature profiles for instantaneous heating of a half-space. Each plot is for a different T_0 corresponding to different depths below the surface, and contains profiles computed at 50,000-year time intervals.

ity zone (Figure 4-4), consistent with the ductile zone extents along the computed temperature profiles at times $t > 450,000$ for $T_0 = 200^\circ\text{C}$ and 300°C .

A second horizontal line in Figure 4-6 at 550°C represents my best estimate of the temperature above which compressional velocities of granodiorite drop significantly with increased temperature. This estimate is extrapolated from the very few laboratory measurements of compressional velocities at crustal pressures and near-solidus temperatures (Sato, 1989; Iyer and Dawson, 1993; Christensen and Mooney, 1995). Christensen and Mooney (1995) show that P-wave velocities for granodiorite drop ~1% from room temperature to 138°C at pressures equivalent to 5 km depth, ~1.5% from room temperature to 263°C at 10 km depth, and ~2.3% from room temperature to 381°C at 15 km depth. Murase and McBirney (1973) measured P-wave velocities for several different types of magma at atmospheric pressure, and demonstrated that P-wave velocities for andesite only drop after temperatures have exceeded the solidus. However, more recent results presented by Sato et al. (1989) for dry peridotite indicate that compressional velocities decrease by 5-6% starting at 220°C below the peridotite solidus, with most of the decrease occurring within 150°C of the solidus (e.g. Figure 1 in Sato et al., 1989). Due to a lack of similar measurements for granodiorite, I assume that a similar relationship holds for granodiorite, which leads to the threshold temperature of 550°C plotted in Figure 4-6. At 10 km depth, a 5% reduction in granodiorite velocities (~6.2 km/sec) translates to a velocity of 5.9 km/sec, just below the observed 5.95 km/sec (to exactly match the observed value, only a ~4.5% reduction in the velocity of granodiorite is needed).

In Figure 4-6, all curves for $T_0 = 100^\circ\text{C}$ exceed 550°C at distances less than 0.5 km from the intrusion, and region of lowered velocities extends out to 2 km at $t = 500,000$ years. For $T_0 = 200^\circ\text{C}$ the lowered velocity region extends out to 2.5 km at $t = 500,000$ years, and for $T_0 = 300^\circ\text{C}$ it extends out to 3.2 km at $t = 500,000$ years. In Figure 4-4 the core of the region of lowered velocities has a radius of ~3.75 km (~1.5 blocks), reasonably close to the maximum extent of the lowered-velocity regions for profiles computed with $t = 400,000 - 500,000$ years and $T_0 = 200$ and 300°C (Figure 4-6).

The reasonably good correspondence between the theoretical extents of both the ductile and lowered-velocity regions at times $t > 450,000$ years with the observed extents of the aseismic zone and low velocity anomaly beneath Mount Rainier provide some quantitative support for the hypothesis that elevated temperatures beneath Mount

Rainier due to magmatic intrusion are affecting both seismicity and seismic velocities beneath Mount Rainier. Furthermore, these estimates for t match quite well with the age of Mount Rainier, which has been determined from preliminary age-dating to be no younger than 466,000 years old (Tom Sisson, personal communication).

However, there are some potential problems with the simple model I use to test this hypothesis. One significant problem is that it assumes infinite dike dimensions in the x and z directions, when a more appropriate geometry for Mount Rainier's conduit system is a cylindrical shape. The infinitely wide dike will result in some over-estimation of temperatures, especially at distances far from the edge of the intrusion. Unfortunately, attempts to derive an easy-to-use analytic solution similar to equation 4.1 for a cylindrical geometry using both paper and Mathematica (Wolfram, 1991), were unsuccessful. A literature search yielded solutions for temperatures outside cooling one-time intrusions with cylindrical and spherical shapes (e.g. Carslaw and Jaeger, 1959; Furlong and Myers, 1985; Furlong et al., 1991), which are inappropriate models for a volcanic system that has experienced multiple intrusions throughout its ~466,000-year history. (This point is illustrated by the fact that temperature profiles computed using these one-time intrusion solutions yielded ductile and lowered-velocity extents much smaller than the observed aseismic zone and low velocity anomaly). It also yielded a quote from Carslaw and Jaeger (1959) to the effect that the solution for a continuous cylindrical source "is not expressible in terms of tabulated functions." Numerical modeling (e.g. Ozisik, 1993) would likely overcome these obstacles, but is beyond the scope of this dissertation.

Another potential problem is the mechanism for maintaining the constant temperatures T_m along the edge of the dike intrusion. The time t_s required for a dike to completely solidify (again assuming conductive cooling) is

$$t_s = \frac{b^2}{4\kappa\lambda^2} \quad (\text{EQ 4.3})$$

where b is the dike half-width, and λ is graphically estimated from

$$\frac{L\sqrt{\pi}}{c(T_{\text{mag}} - T_o)} = \frac{e^{-\lambda^2}}{\lambda(1 + \text{erf}(\lambda))} \quad (\text{EQ 4.4})$$

where T_{mag} is the temperature of the intrusion and L is the latent heat of crystallization (Turcotte and Schubert, 1982). Using estimated intrusion temperatures of 930°C derived for Mount St. Helens dacite (Rutherford et al., 1985) for T_{mag} and assuming a value of 320 kJ/kg for L (Turcotte and Schubert, 1982) and a dike width of 0.2 km , equation 4.3 yields a t_s of 200 years for $T_o = 100^{\circ}\text{C}$, $t_s \sim 360$ years for $T_o = 200^{\circ}\text{C}$, and $t_s \sim 635$ years for $T_o = 300^{\circ}\text{C}$. Thus a new intrusion would be required on the order of every 500 years or so. If each intrusion was cylindrically shaped, had a radius of 0.1 km (half the dike width), and extended from 4 to 14 km (the depth range of the low velocity anomaly), each intrusion would contain $\sim 0.31 \text{ km}^3$ of magma. This translates into a magma supply rate of $6.2 \times 10^{-4} \text{ km}^3/\text{year}$, or a total volume of $\sim 290 \text{ km}^3$ of magma that had to solidify underground over the lifespan of Mount Rainier in order to maintain the temperature T_m (the granodiorite solidus) at the intrusion interface. If this in fact occurred, then there at present should be a 6 km -wide cylinder of dacitic intrusions (at various stages of cooling) below the volcano. For comparison, the total volume of eruptive products at Mount Rainier is estimated to be 140 km^3 (Sherrod and Smith, 1990), implying that only one-third of the volume of each batch of magma intruded beneath Mount Rainier actually reaches the surface. Although this may seem like a low percentage, Ryan (1987) points out that magmatic intrusions achieve neutral buoyancy at some depth below the surface, resulting in the eruption of only a fraction of the original magmatic volume. Thus it is not inconceivable that a temperature T_m could have been maintained for the length of time required to yield temperatures at large enough distances from the intrusion (Figure 4-6) to produce the observed seismicity and seismic velocity patterns in Plate 1.

This simple model of a cooling dike provides some support for the "hot rock" hypothesis as an explanation for both the velocity patterns and seismicity distribution near Mount Rainier. The actual numbers calculated above should be taken with several grains of salt, or even a small shakerfull. As discussed above, they are derived using a model that neglects the likely cylindrical shape of intrusions beneath Rainier (which would reduce the extent of the aseismic ring), that assumes only conductive cooling (the presence of a hydrothermal system indicates convective cooling at least in the near-surface), and that assumes no heat loss at the top of the intrusion. It is likely that a more realistic model would produce smaller values for the extent of ductile and lowered-velocity regions than those shown in Figure 4-

6, and any definitive statements about the "hot rock" hypothesis will need to wait until more realistic modeling using cylindrical geometries is performed. However, the model I use does provide useful zeroth-order estimates that suggest that a long-lived periodically recharged conduit system can potentially have a significant effect on both the distribution of earthquakes and the velocity field in the surrounding country rock.

4.3.3 The SWCC - Where is it?

Figure 4-7 shows layers 2-5 of the 3-D velocity model with the boundaries of the Southern Washington Cascades Conductor (SWCC), as projected into map-view, indicated in each layer (these are the layers corresponding to the depth extents of the SWCC inferred by Stanley et al. (1987) and Stanley et al. (1992)). From this figure it is apparent that the expected low velocity signal from the marine sediments that are thought to make up the SWCC (Stanley et al., 1992) is in general not present. Indeed, most of the anomalies within the SWCC boundaries have higher-than-average velocities, not lower. The only significant low velocity regions within the SWCC are along some of its margins in layers 2-4, features that I attribute to be due to several anticlines that are cored by Tertiary sedimentary rocks (section 4.2.3).

One hypothesis to explain the apparent absence of the SWCC in my velocity model is that the high conductivities that define the SWCC are not lithologically controlled, but instead reflect the presence hydrothermal fluids, brines, graphite, or other non-lithological factors that would result in high conductivities. Another hypothesis is that the SWCC does reflect a lithologically distinct rock unit, but that this unit is pockmarked with plutons (such as the Spirit Lake pluton) that intruded the SWCC after its formation. Since plutonic rocks in general have very high seismic velocities, it is conceivable that if enough plutons are present in the SWCC, the signal from the lower velocity sediments of the SWCC will either be averaged out or will be lost due to diffraction of raypaths around the conductive rocks within the SWCC. Diffraction in particular can severely limit the ability to image small (on the order of several wavelengths) low velocity bodies, a widely recognized problem in LET (Weilandt, 1987).

A third hypothesis is that the SWCC is not a coherent lithologic block. Although many earthquakes do occur along the margins, there are also significant numbers of earthquakes that occur within its boundaries. In particular, the southern portion of

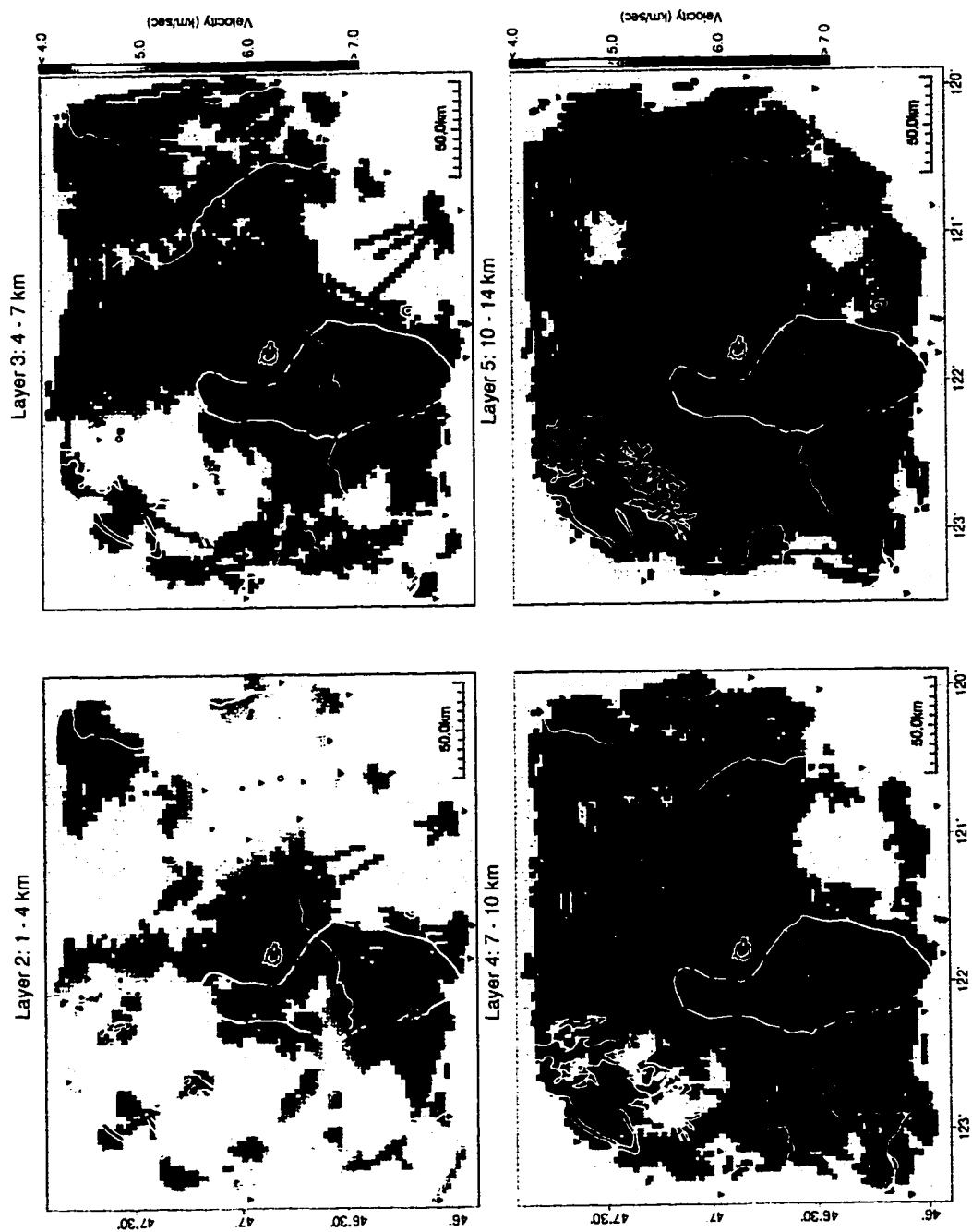


Figure 4-7 Layers 2-5 from Plate 1 with the SWCC. The position of the SWCC is outlined by the bold-white line.

the WRSZ, which has earthquakes extending from the surface down to depths of ~15 km, occurs exactly in the middle of the SWCC as imaged by Egbert and Booker (1993). A fourth hypothesis is that the SWCC does reflect a lithologically distinct rock unit which has been metamorphosed after formation. Such metamorphism would induce crystal growth into pore spaces in sedimentary rocks, raising velocities significantly but presumably either maintaining or improving conductance. Indeed, it seems likely that rocks at depth would be metamorphosed to some degree, given that this region has been exposed to ~40 million years of high heat flow rates associated with arc volcanism.

Regardless of the true mechanism, however, the lack of any strong correlation between velocity and conductivity anomalies (Figure 4-7) indicates that the SWCC is a lithologically complex body. In addition, it also raises the possibility that, despite the apparent correlations between its boundaries and seismic zones as well as volcanic centers, the SWCC does not represent a distinct tectonic block acting to control seismicity and volcanism in the GMR. Everts and Swanson (1994) also raise this possibility, noting that along the SHZ (the inferred western boundary of the SWCC),

“the lack of evidence for such a major boundary in the overlying Cascade volcanic section is puzzling.”

4.3.4 Deep Low Velocity Anomalies Beneath the Cascade Crest

Two eye-catching low velocity anomalies (5.9 - 6.4 km/sec) appear in Layers 5 - 7 (10 - 23 km depth; see Plate 1). In map-view they are separated by a northwest-trending high velocity ridge which parallels the OWL (see section 4.3.5). The northern anomaly lies directly beneath the trace of the Straight Creek Fault and the Snoqualmie batholith (see Plate I). The southern anomaly begins just south of the OWL and extends southward to Mount Adams, with the lowest velocities located directly beneath the Rimrock Inlier. In addition, the cylindrical anomaly beneath Mount Rainier appears to merge with this anomaly at depths below 14 km, suggesting that it is perhaps related to these two deeper anomalies. Finally, earthquakes appear to shallow as the southern anomaly is approached (Figure 4-8)

Cross Section 3

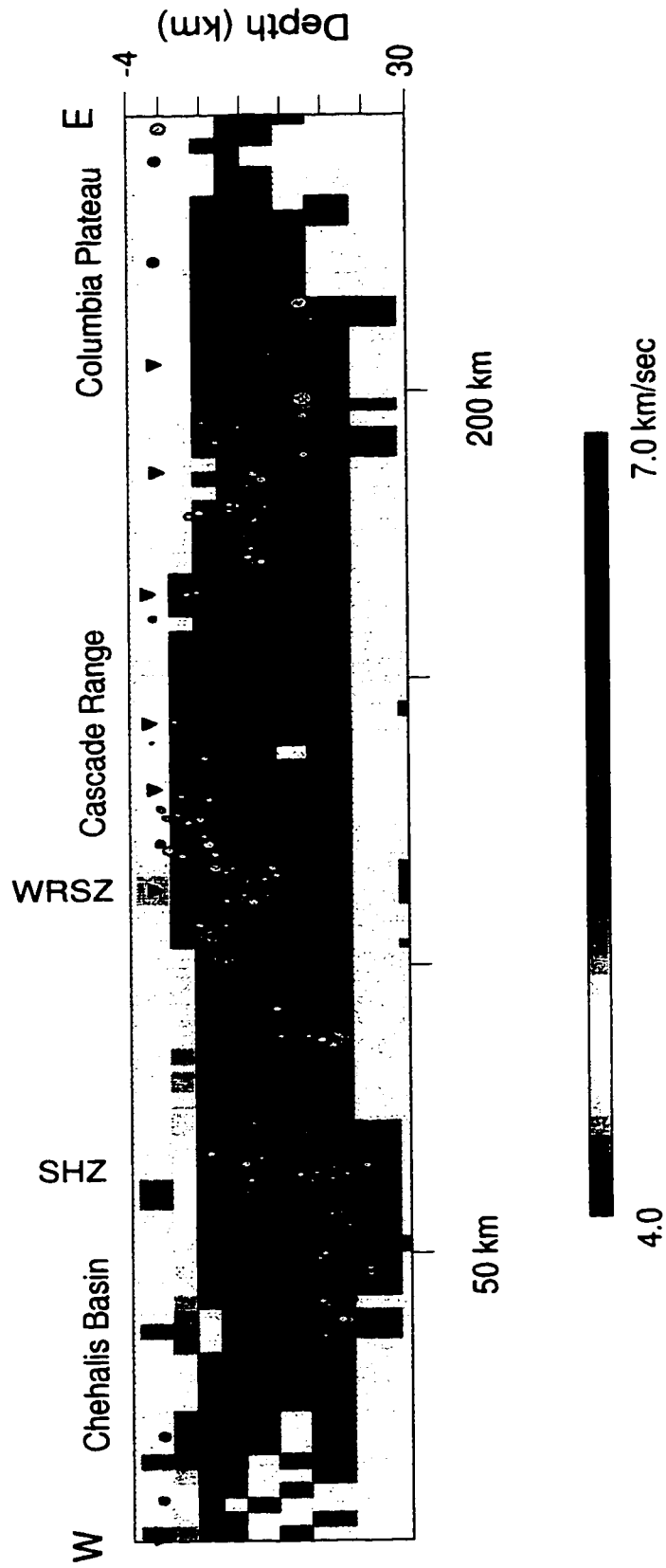


Figure 4-8 E-W cross-section through 3-D model along profile 3 in Plate 1. Note the low velocity anomaly near the 150 km marker, and the shallowing of hypocenters in association with this anomaly. Also note that this profile is parallel to the 1995 refraction profile.

Are They Real?

The first question that comes to mind upon viewing these anomalies is, how real are they? Resolution is reasonably poor in this part of the model (~15-20 km, or 5-8 block widths), as indicated by the checkerboard diagrams (Plate 1), by the raypath diagrams (see Figure 3-6), and by gaps corresponding to un-hit blocks in the southern anomaly (indicating poor ray coverage). Estimated errors are also modestly high (± 0.1 km/sec). However, the dimensions of the anomalies exceed these resolution limits and the estimated errors are much less than the anomaly sizes, suggesting that they are real features that reflect a signal in the data.

This in turn raises the question, is the signal in the data real? Most of the raypaths that traverse these anomalies are on the order of 100 km or greater in length. As a general rule, the longer the raypath, the greater the dissipation of seismic energy due to geometric spreading, diffraction, and attenuation, as well as to encounters with scattering bodies. If the amplitude of the first arrival is attenuated too much, then identification of the first arrival becomes very difficult. Thus the chances of mispicking arrival times increases with increasing distance from the source.

A confirmation that this signal is at least in part real comes from the examination of travel-time residual patterns from energetic events ($M_1 \sim 4$ or greater) at stations where rays from the source likely traversed these anomalies. Three such events are examined here. The first is the January 29, 1995, M_1 5.1 Point Robinson earthquake that occurred 17 km beneath Vashon Island. Figure 4-9 contains seismograms from stations ETW, ELL, and YA2 (see Figure 3-7 for station locations). Arrivals for each of these stations are impulsive, and thus picking errors should only be on the order of a few hundredths of a second. Thus the associated residuals are presumably due solely to velocity structure, not picking error.

The residuals at each station match what is expected from the anomaly pattern. The raypath from the source to ETW traverses through the heart of the northern low velocity anomaly, and the residual at ETW is 0.6 seconds. The raypath to ELL travels along the northwest-trending high velocity ridge that separates the two low velocity anomalies, and its residual is -0.34 seconds. The raypath to YA2 traverses through the southern low velocity anomaly, and its residual is 1.0 seconds. Similar-sized residuals are also observed at the nearby stations MOX and TRW.

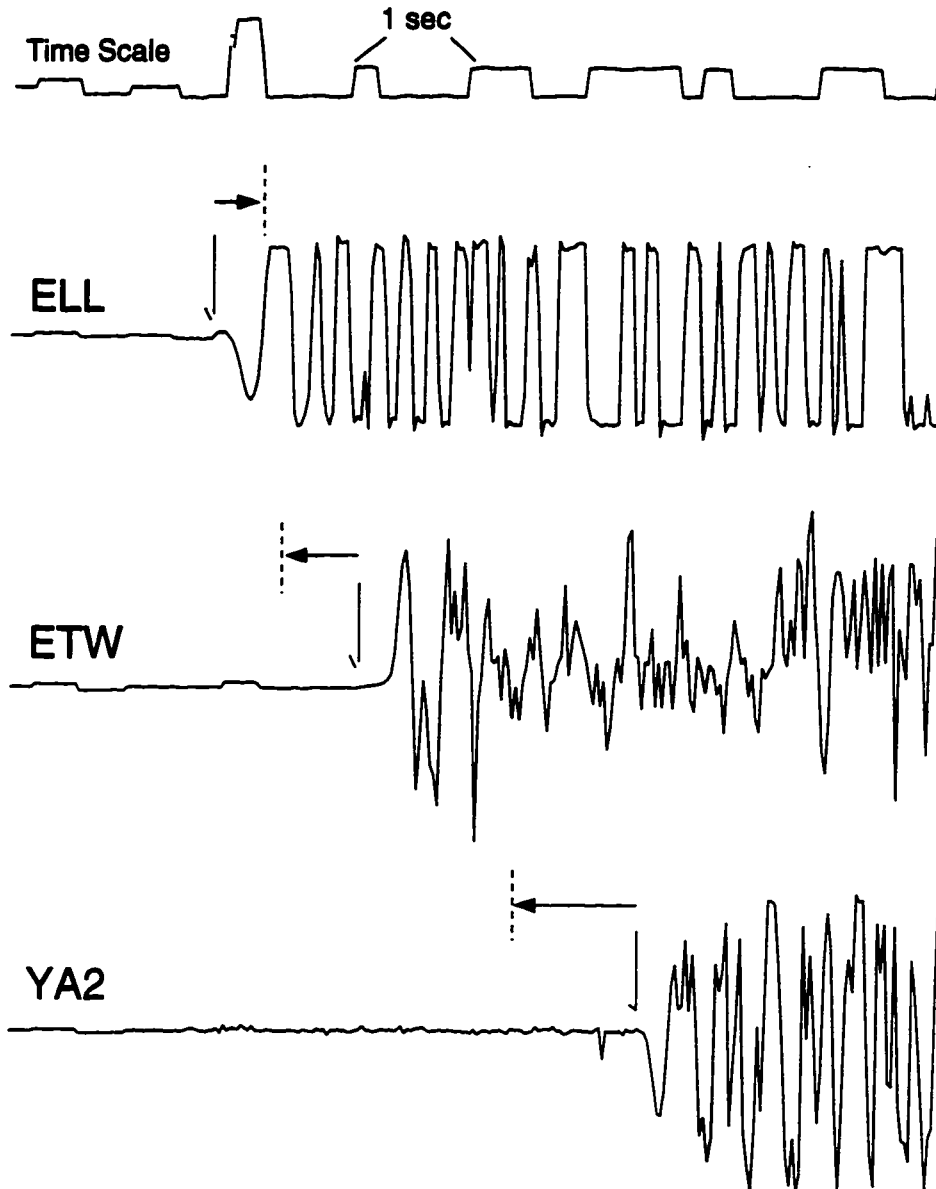


Figure 4-9 Seismograms from 01/29/95 Pt. Robinson earthquake. The vertical half-arrow corresponds to the P-pick. The vertical dashed line indicates the calculated P-arrival time using a 1-D model with station corrections. The length of the horizontal arrow corresponds to the size of residual; the arrow points to the left for positive residuals and to the right for negative.

The second test event is the May 20, 1995, M_1 4.1 earthquake along the WRSZ at a depth of 13 km. Figure 4-10 shows seismograms from stations ETW, ELL, and YA2. The path to ETW nicks the edges of the two low velocity anomalies, and the associated residual is 0.17 seconds, almost 0.5 seconds higher than for the first event. The

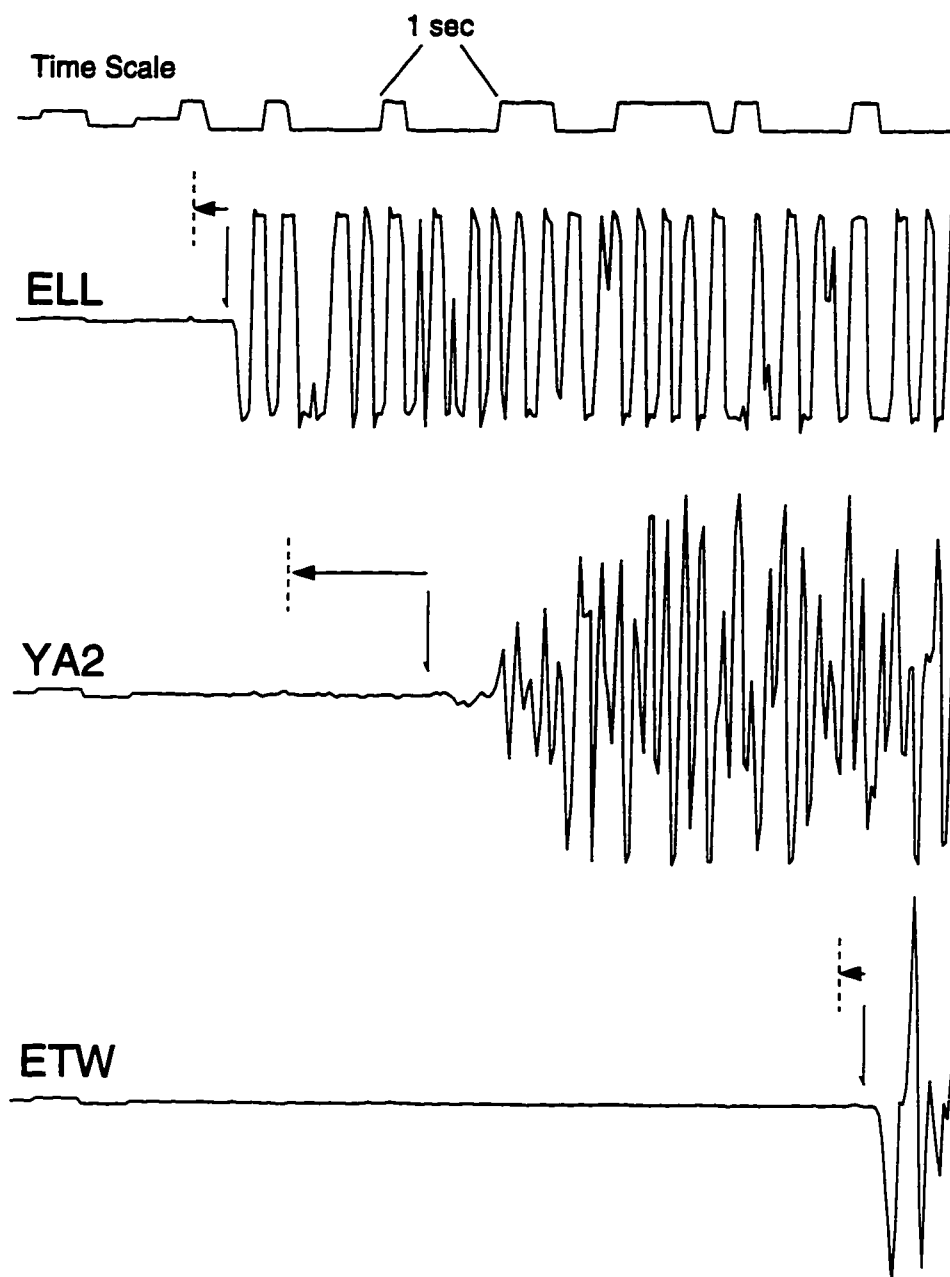


Figure 4-10 Seismograms from 05/20/95 WRSZ event. The symbols are the same as in Figure 4-9. Note the attenuated arrival at YA2.

path to ELL encounters the low velocity cylinder beneath Mount Rainier as well as the edge of the southern anomaly, and the residual at ELL is 0.24 seconds, 0.5 seconds lower than for the first event. Finally, the path to YA2 goes through the heart of the southern low velocity anomaly, and the associated residual is 1.14 seconds. In addition, there is a notable difference in the signal characters between ELL and YA2.

Each station is an equivalent distance from the source, yet the first arrival is much more emergent at YA2 than at ELL. This could be a source effect, since YA2 is near a nodal plane. However, the difference in waveforms could also indicate that the low velocity anomaly through which the YA2 raypath traveled is also highly attenuative.

The third test event is the January 1, 1997, M_1 3.7 earthquake near Yakima at a depth of 19 km. Figure 4-11 shows seismograms from stations GSM, RVC, and KOS. The path to GSM travels along the high velocity ridge, and its associated residual is -0.14 seconds. The path to RVC is along the northern edge of the southern low velocity anomaly, and its associated residual is 0.33 seconds. The path to KOS is through the heart of the southern low velocity anomaly, and its associated residual is 0.59 seconds. Again, there is a noticeable difference in the signal character between stations, this time between RVC and KOS; the waveform at KOS is very attenuated in comparison to RVC. In this case both stations are equally far from nodal planes; thus this is likely not a source effect. This observation provides further support for the idea that at least the southern low velocity anomaly is also attenuative.

These events all indicate that the low velocity signal in the data is real, and thus interpretable. However, the apparent attenuation at YA2 in the Figure 4-10 and KOS in the Figure 4-11 suggests that first arrivals from smaller events may be attenuated so much as to be hidden in the noise, leading to systematically late picks of arrival times. Evidence for this can be seen in a M_1 3.7 9 km deep event along the WRSZ that occurred on July 13th, 1995 (Figure 4-12). Note that there is a very low amplitude emergent arrival roughly 1 second before the main energy pulse. For events much smaller than M_1 3.7, this low amplitude pulse would not rise above the noise level, and would in most cases not be picked. Instead, the main energy pulse would be picked, introducing a 1 second pick error that would translate into low velocities in a velocity inversion.

Thus the answer to the question of whether or not these low velocity anomalies are real is complicated. There do appear to be two resolvable regions that dramatically delay travel times and/or attenuate first arrival energy. However, the attenuation also likely causes picks of P-arrivals to be systematically late for smaller ($M_1 < 3.7$) events, where low amplitude first arrivals are likely to be hidden in the ambient

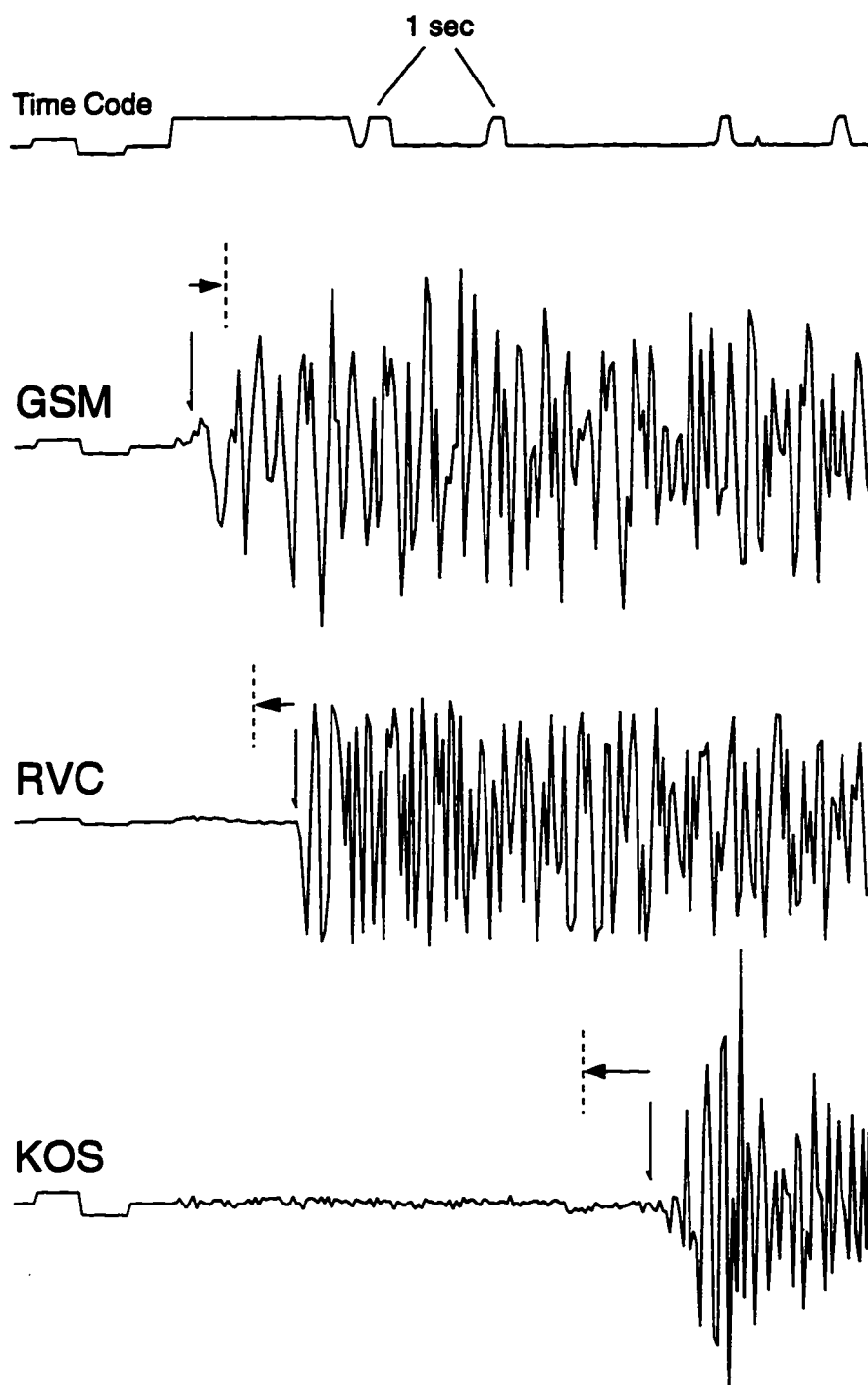


Figure 4-11 Seismograms from 01/01/97 event near Yakima. Symbols are the same as in Figure 4-9. Note the attenuated arrival at KOS.

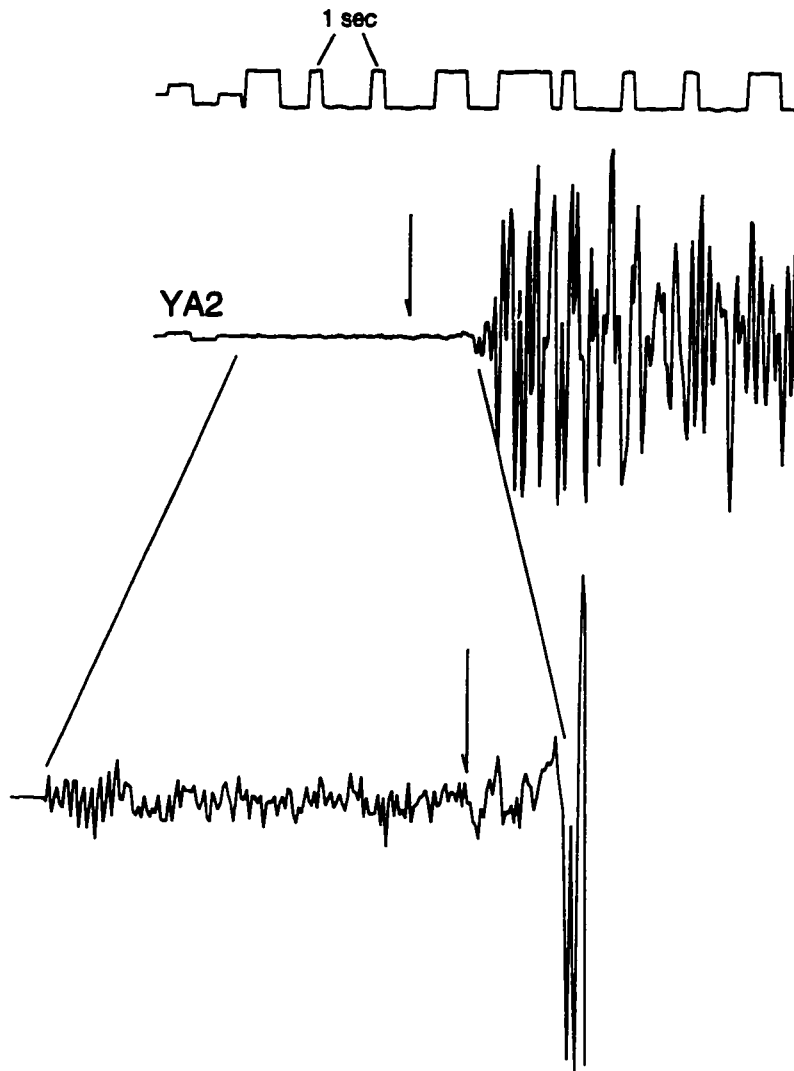


Figure 4-12 Seismogram for station YA2 from the 07/13/97 WRSZ event. The first four seconds of the upper trace are magnified in the lower trace. Note the low amplitude first arrival (marked by arrow) that precedes a much more impulsive arrival roughly 1 second later.

seismic noise level. Such a systematic mispicking of arrivals will result in an overestimate of the amplitude of the velocity anomaly. Therefore, the velocity anomalies are probably real, but their velocities (5.9 - 6.4 km/sec) are probably artificially low.

What Are They?

Interpretations of these anomalies are made problematic by the fact that the absolute velocity values are likely in error by an unknown amount due to the systematic mispicking problem discussed above. In addition, the range of velocities in these anomalies (5.9 to 6.4 km/sec) is consistent with a wide range of lithologies, including granite-granodiorite (6.2 km/sec), diorite (6.4 km/sec), slate and phyllite (6.1 km/sec), granitic gneiss (6.1 km/sec), and zeolite facies basalt (6.3 km/sec) (Christensen and Mooney, 1995). Thus velocity information alone is non-unique.

One hypothesis is that these anomalies are associated with regions of elevated temperatures. This hypothesis is supported by several pieces of evidence. One, a cross-sectional plot across the southern anomaly (Figure 4-8) shows that earthquake depths shallow noticeably as the anomaly is approached from either side. In addition, few earthquakes locate within the anomalies. These observations suggest (as do similar patterns beneath Mount Rainier) a shallowing brittle-ductile zone in association with these anomalies. Further support for this hypothesis comes from heat flow measurements by Blackwell et al. (1990), who found two regions of anomalously high heat flow that broadly correlate with these two anomalies (Figure 4-13). Furthermore, the high heat flow regions are separated by a region of lower heat flows that parallels the high velocity ridge between the two anomalies (Figure 4-13).

One possible source for such elevated temperatures is the presence of cooling and/or partially molten magma bodies. This idea is supported by the possible evidence for P-wave attenuation observed at stations YA2 for event 2 and KOS for event 3. Such attenuation could be caused by seismic waves traversing through regions of partially molten and/or fluid-filled rock. In addition, the possible deep zones of high conductivities east of the SWCC discussed by Stanley et al. (1987, 1990) and Egbert and Booker (1993) could also be explained by the presence of geothermal fluids associated with cooling magmatic bodies, which could in turn give rise to the observed high heat flow rates.

It is unlikely that such a broad region would consist entirely, or even primarily, of molten rock, for several reasons. One, such a broad magmatic region would have a much greater impact on velocities. Laboratory measurements of compressional velocities for 75% crystalline peridotitic melts at 15 km depth are ~4 km/sec (Sato et al., 1989), well below the imaged velocity values in a region that is presumably

Layer 6: 14 - 18 km

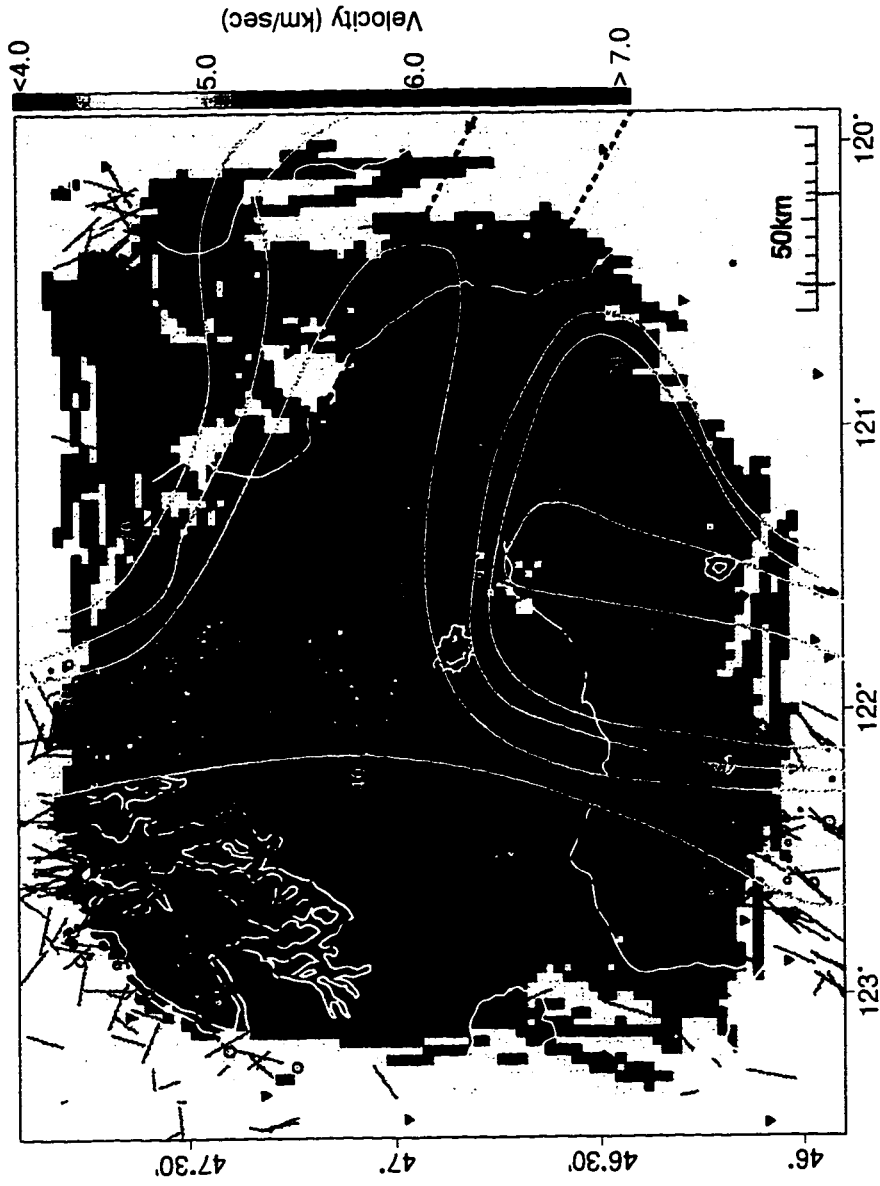


Figure 4-13 Heat-flow contours from Blackwell et al. (1990) superimposed on Layer 6 of the 3-D velocity model. The approximate position of the OWL is also indicated by the brown dashed line. P-axes from the PNSN catalog (as projected onto the surface) are indicated by green lines.

much less mafic than peridotite. Two, if such a region did exist, then there should be more evidence (in the form of volcanic and/or geothermal activity) of elevated temperatures at the surface. Such evidence does exist at volcanic centers such as the Yellowstone caldera (with dimensions similar to these anomalies and several low velocity bodies that are thought to be primarily magmatic) in the form of extensive geyser and fumarolic fields, as well as exceedingly high heat flow rates (e.g. Lehman et al., 1982). Aside from elevated heat flow rates (more than 10 times lower than the values observed at Yellowstone by Lehman et al. (1982)), the only surficial evidence above the southern low velocity anomaly are a few Quaternary volcanic centers and one inferred small Quaternary caldera north of Goat Rocks (Don Swanson, personal communication). There is no evidence of Quaternary volcanic activity above the northern anomaly.

However, velocities can be affected by the presence of hot rock without requiring the presence of magma, as discussed in section 4.3.2. Using equation 4.3 from section 4.3.2, a dike with a width of 20 km (roughly half the width of the two anomalies and also the resolution in this part of the model) would take ~4.4 million years to solidify, and elevated temperatures above 550°C (the threshold temperature above which velocities begin to decrease) would presumably last for several more millions of years. Thus elevated temperatures are a plausible hypothesis for the cause of these low velocity anomalies.

A second hypothesis is that these anomalies represent the continuance of the SWCC underneath the Cascades and into the Columbia Plateau. This hypothesis is suggested in part by models of the SWCC from Stanley et al. (1996) (see Figure 4-14), and also by the observation that the western boundary of the southern anomaly almost exactly parallels the eastern boundary of the SWCC (see Figure 4-7). It is supported by results from magnetic and seismic reflection studies in the GMR. Stanley et al. (1987, 1992) infer from magnetotelluric profiles that the SWCC extends from 10 to 20 km depth along its eastern boundary and dips steeply to the east, although their resolution is poor. They also suggest that the SWCC could continue further eastward, underthrusting the eastern Cascades and western Columbia Plateau. This idea also is supported by data from a seismic reflection profile along Highway 12 that are interpreted by Stanley et al. (1992) to show, among other things, that the top of the SWCC is bounded by a thrust fault. In addition, Egbert and Booker (1993) note that there is a suggestion of a deeper conductivity anomaly

to the east of the SWCC in their magnetovariational dataset, supporting the possible continuance of the SWCC beyond its eastern boundary.

However, there are several observations that argue against the underthrusting hypothesis as an explanation for the low velocity anomalies. One, no similarly extensive low velocity anomalies are apparent at shallower depths within the boundaries of the SWCC (see section 4.3.3). This suggests that perhaps there is no strong velocity signal associated with the SWCC, and thus detection of it at greater depths is questionable. Two, the northern anomaly does not correlate with any mapped conductive body. Indeed, Stanley et al. (1990) find no evidence for any anomalously high conductive zones from the SWCC north to Mount Baker. Thus the northern anomaly is linked to the conductivity hypothesis only by inference. Three, the true eastern edge of the SWCC is not well constrained by the reflection or magnetotelluric data, and both datasets have very poor resolution below depths of 10 km. Thus the evidence for the continuance of the SWCC beyond its eastern boundary is at best equivocal.

The fourth and final argument is that the amount of shortening required by the underthrusting hypothesis is problematic. The amount of horizontal motion can be estimated from Figure 4-14, which is modified from a cross-section by Stanley et al. (1996). It is apparent from Figure 4-14 that at least 25 km of westward horizontal

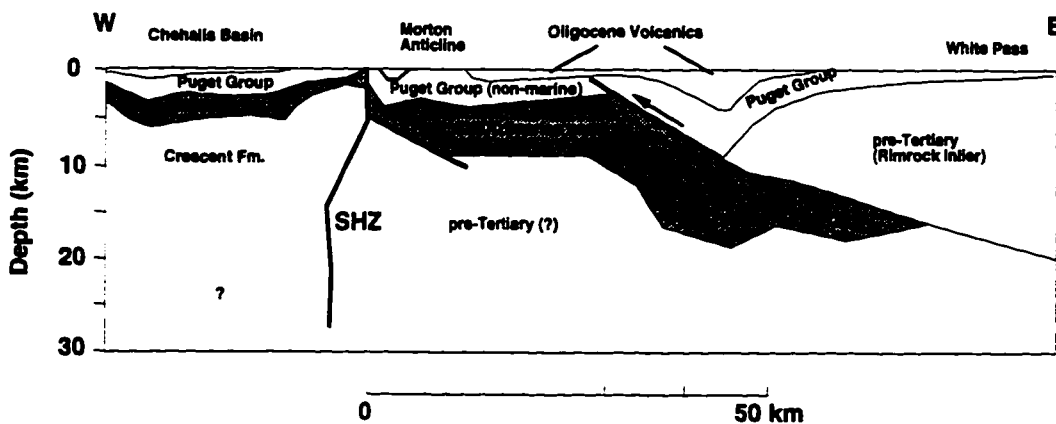


Figure 4-14 Interpretive cross-section through southern Cascades, modified from Stanley et al. (1996). The profile is parallel to cross-section 3 (Plate 1).

motion is required to bring the SWCC (thought to be composed of Eocene marine sediments) back from underneath the pre-Tertiary Rimrock Inlier. Conservation of

mass requires that this 25 km of westward motion be accommodated either by a significant thickening of the SWCC (if its western end is fixed) or by a horizontal shear zone between the SWCC and overlying Eocene sediments that would allow the entire SWCC to move 25 km without thickening. Significant thickening would require original depositional thicknesses of ~10 km or more on the eastern edge of the formation, roughly three times greater than the maximum estimated thickness of the McIntosh Formation beneath the Chehalis Basin and the Morton Anticline (Johnson and Stanley, 1995). The shear zone hypothesis suffers from a lack of any evidence of a decollement between the McIntosh and Puget Group formations in well logs from the Chehalis Basin (Johnson and Stanley, 1995). Thus it seems unlikely that the two low velocity anomalies could be due to Tertiary marine sediments underthrust beneath the Rimrock Inlier and its pre-Tertiary equivalents.

4.3.5 Olympic-Wallowa Lineament (OWL)

One striking aspect of the northwest-trending high velocity ridge that separates the two low velocity anomalies in layers 5 - 7 (10 - 23 km depth) (see section 4.3.4) is that it directly parallels the trace of the OWL through the Cascades, with its northern boundary lying directly beneath the southern edge of the OWL (as defined by the White River fault and the Naches River valley (e.g. Hammond et al., 1994)). This anomaly pattern is somewhat suspect, since checkerboard diagrams show evidence of northwestward smearing of velocity structure parallel to the high velocity ridge (see Plate 1), primarily due to a lack of northeastward-trending raypaths. However, arrival times from well-recorded earthquakes are noticeably early for raypaths traveling parallel to this ridge (see discussion of event 1 in section 4.3.4), indicating that this feature is real even if its imaged outline is likely to be smeared.

Velocities along the ridge range from 6.3 - 6.6 km/sec in Layer 5 to 6.5 - 6.8 km/sec in Layer 7. These velocities correspond to a wide range of lithologies, including diorite, diabase, prehnite-pumpellyite facies basalt, granulite, and marble (Christensen and Mooney, 1995). However, only diorite fits within these ranges for all 3 layers, suggesting that perhaps this ridge is predominantly dioritic in composition.

Importance in Regional Tectonics?

Presuming for the moment that the shape of this feature is real, there are several fascinating coincidences which, taken together, may indicate that this ridge could play an important role in regional tectonics. First, the ridge parallels the OWL (see Fig-

ure 4-13), inferred by several researchers to represent a possible tectonic boundary (e.g. Pezzopane and Weldon, 1993). Second, this ridge parallels a ridge of lower temperatures discussed briefly in section 4.3.4 (see Figure 4-13). Third, its southern boundary roughly correlates with the northernmost extent of Quaternary volcanic vents in the southern Washington Cascades segment of the Cascade arc (see section 1.2.3). Fourth, an apparent change in the orientation of P axes from focal mechanisms appears to occur along an axis parallel to the trend of the OWL and high velocity anomaly (Figure 4-13 and Figure 4-15). Figure 4-15 shows the orienta-

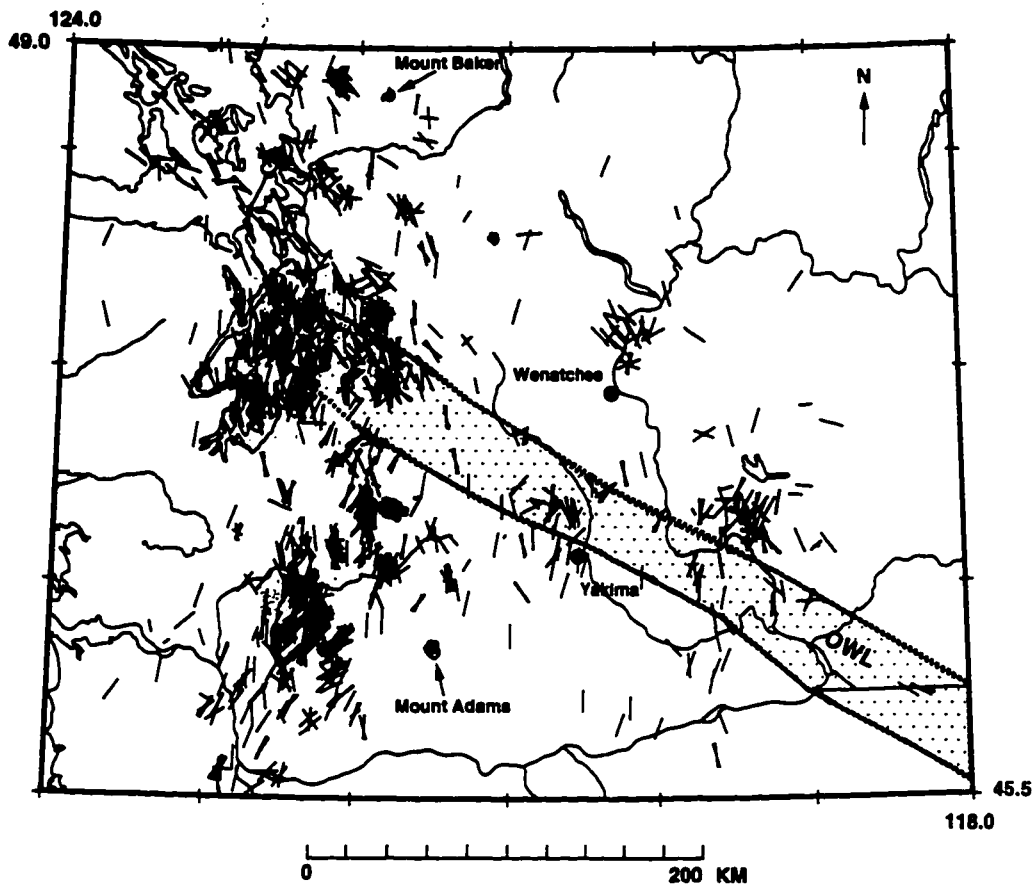


Figure 4-15 Plot of P axes from all crustal focal mechanisms in Washington. P axes are projected into X-Y plane, so the longest P axes reflect horizontal compressive stresses and the shortest reflect vertical stresses.

tions of all P-axes (or directions of maximum compressive stress) from well-constrained focal mechanisms in the PNSN catalog (derived using 1-D velocity models) for all of Washington. It is apparent from this diagram that there is a general change in P-axis orientations from north-northeast south of the OWL to north-

northwest north of the OWL. This change is part of a more regional trend apparent in Plate 1 of Zoback (1992), where directions of maximum compressive stress change from north-northeast to north-northwest along a linear trend extending from Puget Sound southeast to Idaho (the southeastern limit of the OWL). The P-axes return to a north-northeast orientation well north of the OWL in Canada (Zoback, 1992). Thus there is an apparent perturbation in the regional stress field associated with the OWL and/or with the high velocity ridge.

The high velocity ridge thus appears to correlate with four other features; the OWL, a ridge of low heat flow values, the northern limit of Quaternary volcanoes in southern Washington, and the axis along which P axes change from north-northeast to north-northwest. The coincidence of these features with the high velocity ridge suggests the possibility that it could be playing an important role in regional tectonics. Determining the nature of this role is beyond the scope of my dissertation. However, on the basis of the correlation of all these observations I propose the addition of a new fourth segment to the segmentation of the Cascade arc in Washington and Oregon as defined by Guffanti and Weaver (1988) (Figure 4-16). The new segment ("Segment 4" in Figure 4-16) separates the isolated strato-volcanoes of the northern Washington Cascades ("Segment 1" in Figure 4-16) and the more extensive volcanism of the southern Washington Cascades ("Segment 2"), and is defined by the area where all of the features described above coincide.

4.4 Seismotectonic Interpretations

4.4.1 St. Helens Seismic Zone (SHZ)

A 5 to 10 km-wide low-velocity trough extending from 1 to 14 km in depth stretches 50 km northwards from Mount St. Helens to the northern end of the Morton anticline. All seismicity associated with the SHZ north of Mount St. Helens occurs within the southern 40 km of this trough, suggesting the possibility that this feature is the signature of a fault or fault zone. The length of a fault can be related to magnitude via equations from Brune (1970) derived for a circular model of earthquake rupture,

$$M_o = \frac{17}{6} r^3 \sigma \quad (\text{EQ 4.5})$$

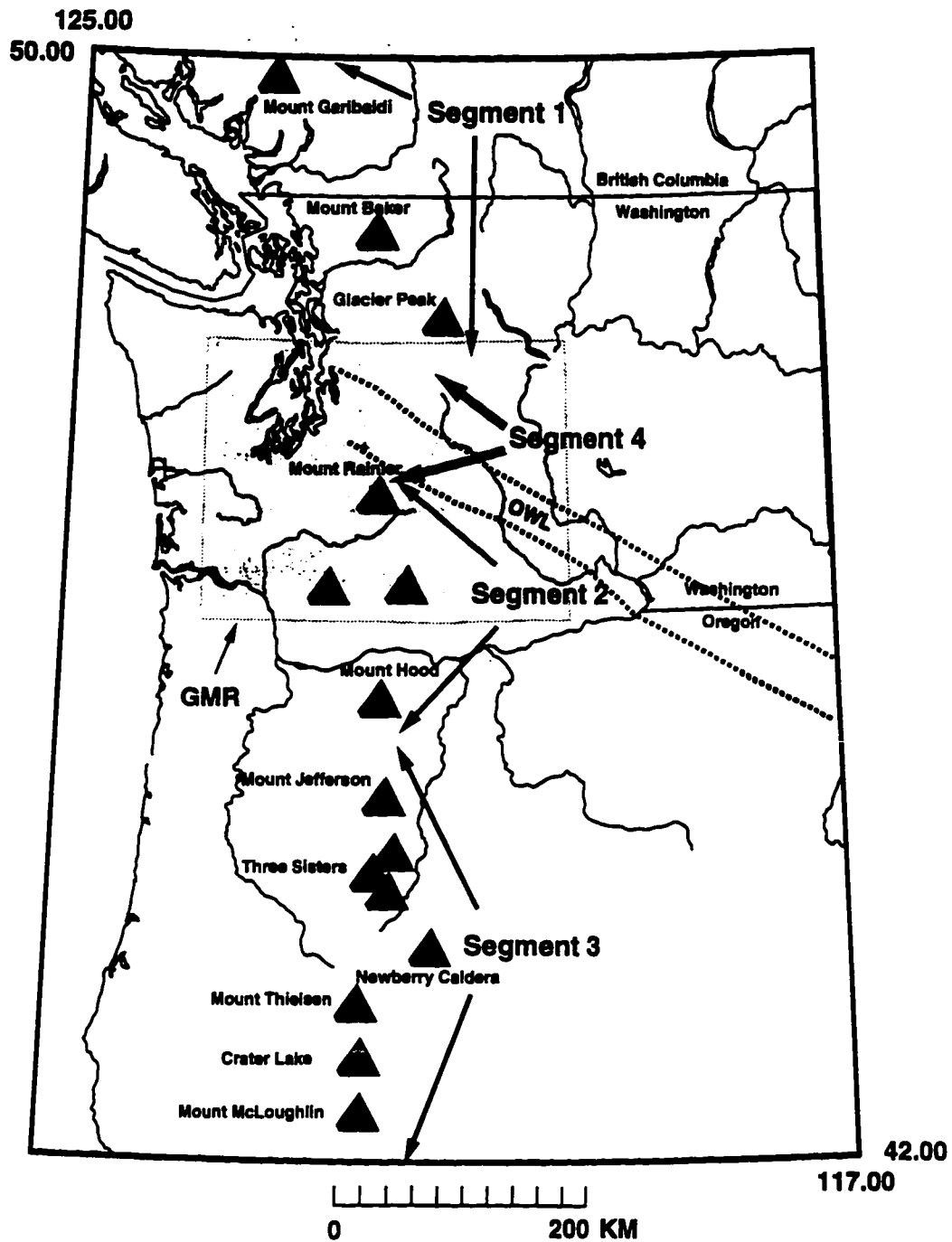


Figure 4-16 Proposed new segment for the Cascade volcanic arc. Original segmentation is defined by Guffanti and Weaver (1988) (see Figure 1-6 for comparison).

where M_0 is the moment magnitude, r the source radius (in centimeters), and σ the stress drop in megapascals (or MPa). M_0 is related to magnitudes determined using coda lengths (M_1) via an empirical scale determined by Hanks and Kanamori (1978),

$$\log M_0 = 1.5M_1 + 16.1 \quad (\text{EQ 4.6})$$

Assuming a stress drop of 1 MPa, a rupture with a 20 km radius would generate a M_1 6.8 earthquake. If the rupture involved only a half circle instead of a full circle (as might be the case for a near-surface rupture), a M_1 6.6 would result. If the entire 50 km of this trough were to rupture, then a M_1 of 6.7 - 7.0 would result. These magnitude estimates are consistent with those from Weaver and Smith (1983), who used an empirical relationship between magnitude and rupture length from Mark (1977) to estimate that a rupture of half the length of the SHZ (determined from seismicity alone) would result in a M_1 7.0 earthquake. They are also consistent with moment magnitude estimates of 6.3 - 6.9 derived using an updated empirical scale from Wells and Coppersmith (1994). An earthquake of this size would cause considerable shaking not only at the nearby communities of Randle and Packwood, but also at Mount St. Helens (possibly generating flank collapses of the edifice) and at Riffe Lake and Mayfield Reservoir, both located at the northern end of the SHZ. Each of these water bodies was formed by the damming of the Cowlitz River. A M_1 6.6 - 7.0 SHZ event could cause damage to these structures, possibly creating a catastrophic flood that would threaten the downstream communities of Toledo, Castle Rock, and Kelso.

However, there are two additional factors that need to be considered in the estimation of seismogenic potential of the SHZ. The first factor is the lack of evidence to date for any surface rupture above the SHZ (Weaver and Smith, 1983; Evarts and Swanson, 1994). If the SHZ is capable of generating a M_1 7.0 event, then presumably events of similar size have occurred in the past. An earthquake of this magnitude would generate displacements on the order of one meter (Brune, 1970), which would surely be noticeable at the surface. Assuming a brittle-ductile transition depth of 24 km (the depth of the deepest SHZ earthquakes), the largest radius for a rupture that does not break the surface is 12 km for an earthquake located at 12 km depth. Assuming a stress drop of 1 MPa, this translates to a M_1 6.3 earthquake. The second factor is the 5-10 km width of the SHZ, which is apparent both in the distri-

bution of earthquakes and in the imaged anomaly. This width suggests the possibility that earthquakes are occurring along parallel (as indicated by virtually identical focal mechanisms) but separate fault planes. If this is in fact the case, then the length of any single fault is likely to be only a fraction of the total length of the SHZ. For example, a fault of 10 km would generate a M_l 5.6 earthquake, similar in size to the M_l 5.5 Elk Lake event that occurred at a depth of 9.5 km along the SHZ in 1981. Although these two factors do not rule out the possibility of a M_l 7.0 event occurring along the SHZ, they do reduce its likelihood.

4.4.2 Western Rainier Seismic Zone (WRSZ)

Unlike the SHZ, the WRSZ does not appear to relate in any simple way to features in the velocity model. The one exception to this is in Layer 5 (see Plate 1), where the eastern edge of the WRSZ coincides with the western edge of the low velocity cylinder beneath Mount Rainier (see section 4.3.2). It is possible that this correlation indicates the presence of a lateral brittle-ductile transition, an idea supported by the apparent shallowing of depths near the low velocity feature (see cross-section in Figure 4-4).

The general lack of any simple correlation between the WRSZ and the 3-D velocity model indicates that the WRSZ is probably not a single fault or zone of parallel faults. This interpretation is consistent with and supported by results from previous seismological studies of the WRSZ. Thompson and Qamar (1989) studied the aftershocks associated with the July 29 1988 M_l 4.1 earthquake, and found that they defined a northeast-trending plane parallel to one of the fault planes from the focal mechanism for the mainshock. This suggests that the rupture occurred along a northeast-trending plane, roughly 45° different from the north-south orientation of the WRSZ. Malone et al. (1991) also noted that most WRSZ fault plane solutions in general do not parallel the WRSZ. This is apparent in Figure 4-17, which shows all WRSZ mechanisms in the PNSN catalog. An additional complexity also apparent in Figure 4-17 is the occurrence of primarily dextral-slip events between 1 and 7 km and reverse or oblique-reverse events between 7 and 14 km. These observations conflict with interpretations by other investigators that motion along the WRSZ is primarily dextral slip in character (e.g. Stanley et al. (1996)).

The lack of parallelism between fault planes and the epicentral trend, along with the occurrence of a significant number of thrust events, is quite different from the

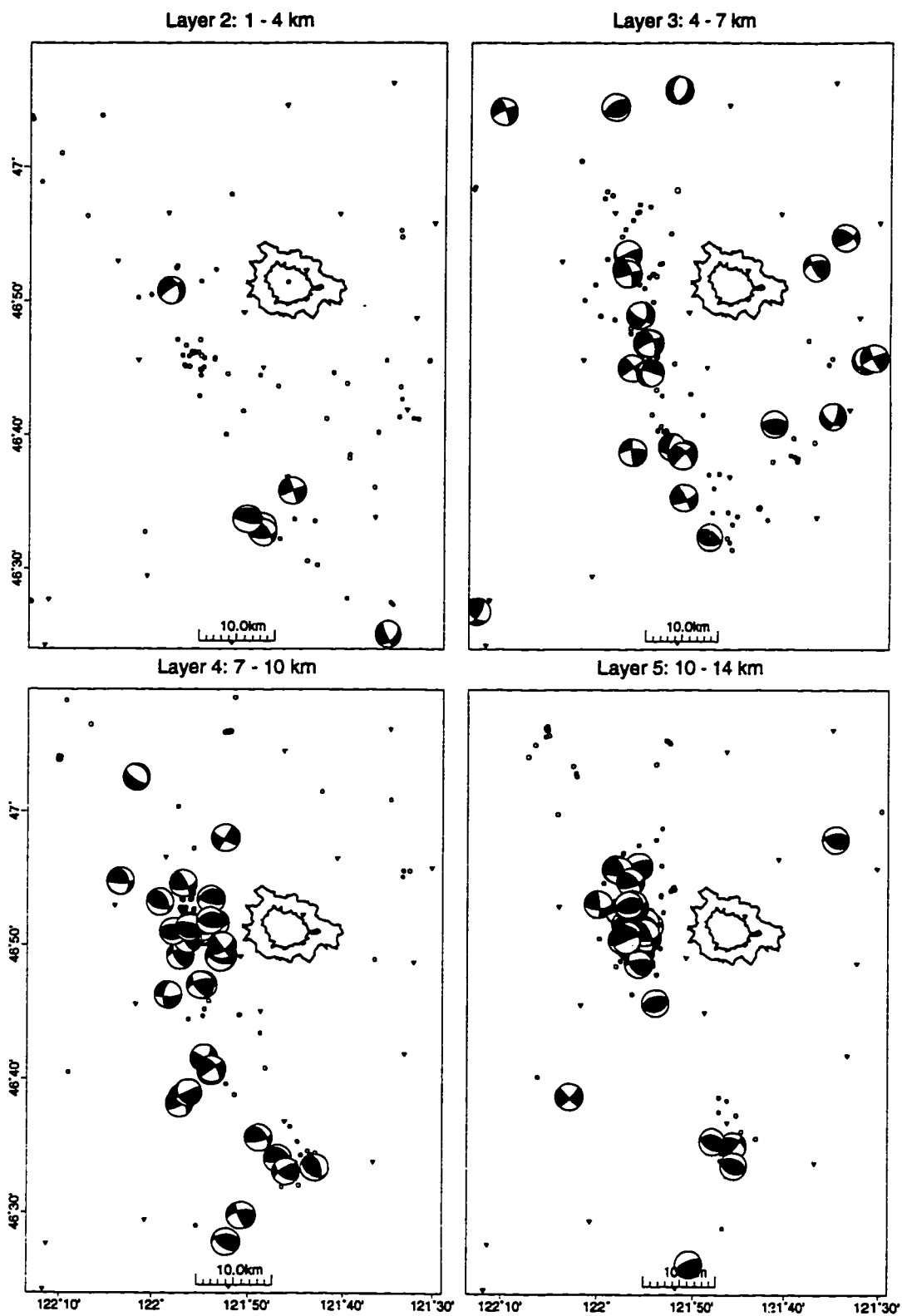


Figure 4-17 WRSZ focal mechanisms in Layers 2 - 5. Plotted are all mechanisms from the PNSN catalog. Note that most events with reverse mechanisms appear to occur in the lower two layers.

SHZ. This (along with the lack of association of WRSZ seismicity with structure in the velocity model) indicates that the WRSZ is more complex than the SHZ, and that it likely does not represent a single fault or zone of parallel faults. Instead, it is likely composed of a series of relatively small northeast-to-northwest-trending en echelon faults that rupture independently of each other. The WRSZ is ~12 km wide as measured in map-view both to the northeast and the northwest. Assuming that this represents the maximum potential length for a single fault in the WRSZ, equation 4.5 and equation 4.6 yield an estimate of M_1 5.5 for the largest potential earthquake along the WRSZ, much lower than the M_1 6.9 estimate that results from using its length in the north-south direction.

This estimate of the maximum magnitude earthquake to expect along the WRSZ has potentially significant implications in terms of estimating the hazard posed to Mount Rainier by the WRSZ (see section 1.3.2). Although little is known about the seismic response of Mount Rainier's edifice to shaking associated with earthquakes of different magnitudes and epicentral distances, the amplitude of ground motion associated with a M_1 5.5 will be ~25 times less than that associated with a M_1 6.9. Thus it can be said that, if this model of the WRSZ is correct, the hazard posed to Mount Rainier by the WRSZ is relatively small.

Whether or not a M_1 5.5 event could trigger a flank collapse depends on a wide range of factors, including the composition and degree of alteration in the edifice and the presence of pre-existing zones of weakness (both of which influence the structural integrity of the edifice), as well as the properties of the earthquake (i.e. location, focal mechanism, directivity of the rupture, etc.). The historical record contains only two examples of earthquake-triggered flank collapses at volcanoes. The first is the 1980 eruption at Mount St. Helens, which began as a large landslide that occurred at the same time as a M_s 5.2 earthquake located directly beneath the volcano (e.g. Malone et al., 1981; Kanamori et al., 1984). The second is the flank collapse that occurred at On-take Volcano in Japan in 1984. The landslide was apparently triggered by a M 6.8 earthquake located 10 km southeast of the volcano (Newhall and Dzurisin, 1988). This event was preceded by 6 years of seismicity in the same general area as the mainshock, which included events as large as M 5.3 (Newhall and Dzurisin, 1988). One interpretation of this sequence is that the M 5.3 event wasn't big enough to trigger the landslide, but the M 6.8 event was. Thus in the historical record there is one example of a M_s 5.2 earthquake located directly

beneath a volcano that (arguably?) triggered a flank collapse, and one example of a M_l 5.3 earthquake located 10 km from a volcano that arguably failed to trigger a collapse. These examples suggest that, under certain conditions (perhaps similar to those that existed at Mount St. Helens prior to the May 18, 1980, eruption), a M_l 5.5 near Mount Rainier could trigger a collapse. However, they also illustrate the difficulty of drawing any inferences about the effect of a M_l 5.5 earthquake at a volcano like Mount Rainier without knowing more about the edifice's intrinsic stability and its response to ground shaking.

4.4.3 Other Seismogenic Zones Near Mount Rainier

Although the WRSZ does not appear to pose a significant seismic hazard to Mount Rainier, there are other seismogenic regions nearby that arguably pose a greater threat. The largest earthquake to have been recorded within Mount Rainier National Park is the M_l 4.8 Ohanapecosh event in 1974 (see section 1.3.2). While the location is not well constrained, especially in depth (Crosson and Lin, 1974), its epicentral location does lie within a diffuse cloud of seismicity in the southeastern corner of the park. It also lies along the northwest-trending boundary of a high velocity anomaly in layers 2 and 3, and possibly layer 4, that I interpret to be a granodioritic pluton (see section 4.2.3). The focal mechanism for this event has one fault plane directly parallel to this boundary, suggesting that this boundary could represent a possible buried active fault. If this is the case and the length of this boundary (25 km) represents the length of the active fault, then a M_l 6.4 event is possible (assuming a 1 MPa stress drop). Such an event occurring close to Mount Rainier could very conceivably generate significant ground accelerations in the edifice. Thus this feature, if an active fault, represents a potentially more significant hazard to Mount Rainier than the WRSZ, as well as a hazard to nearby communities such as the town of Packwood.

4.4.4 Volcano-Tectonic Earthquakes Beneath Mount Rainier

Figure 4-18 and Figure 4-19 are map views and north-south cross-sections of well-constrained hypocenters for 64 volcano-tectonic earthquakes beneath Mount Rainier. Figure 4-18 shows hypocenters located with the "C3" PNSN 1-D velocity model and station corrections, and Figure 4-19 shows hypocenters located in the 3-D velocity model computed in this study. Note that in Figure 4-18 I manually adjusted the depth of each earthquake upwards by 1.1 km from its original depth. This is done to account for the fact that the PNSN location routines do not trace rays to the eleva-

tion of each station, instead (for computational simplicity) stopping at 0 km. The residual resulting from this procedure is absorbed by the station correction for each station. Locations computed using these station corrections will then have depths determined relative to a datum that is the average elevation of all stations used in the location, instead of sea level. This average elevation is 1.1 km for PNSN stations near Mount Rainier, meaning that an earthquake with a depth of 1.1 km as determined by the PNSN actually has a depth of 0 km relative to sea level.

There are two intriguing patterns in the distribution of hypocenters in these two figures. One, the 1-D locations in map view define a diffuse band trending north-east-southwest across the summit, suggesting the possibility of a fault directly beneath the edifice. However, no such linear trend is seen in the 3-D locations. In addition, the 3-D locations are systematically shifted several hundred meters to the north-northeast, and group into two clusters separated by a ~0.3 km-wide seismic gap (Figure 4-19). This gap is more than twice the size of the average estimated epicentral error for the 3-D locations (0.14 km), suggesting that this feature is real. Two, 3-D depths range from 0.8 km below sea level to 2.85 km above, with an average depth of 0.1 km above sea level, 0.4 km below the average depth of the 1-D locations. Significantly, 61 of the 64 3-D locations are below the inferred base of the edifice (~2 km above sea level (e.g. Fiske et al., 1964)).

These seismicity patterns are almost identical to those seen in Moran et al. (1994), where earthquakes were relocated using a pseudo-Master Event technique. Taken together, they have potentially significant implications for the nature of the stress sources responsible for volcano-tectonic earthquakes beneath Mount Rainier.

Evaluation of New Locations

Before interpreting their significance, however, it is important to estimate the accuracy of the 3-D relocations. One means for the assessing the relative quality of the 3-D locations is to compare their estimated formal errors with those from the original 1-D locations. Table 4.2 shows the average location errors and the average root-mean-square (rms) misfit of observed to calculated travel times for both the 3-D locations and the 1-D PNSN locations. (Note that these errors are estimated errors computed by the location routine, and do not necessarily reflect the true errors in location.).

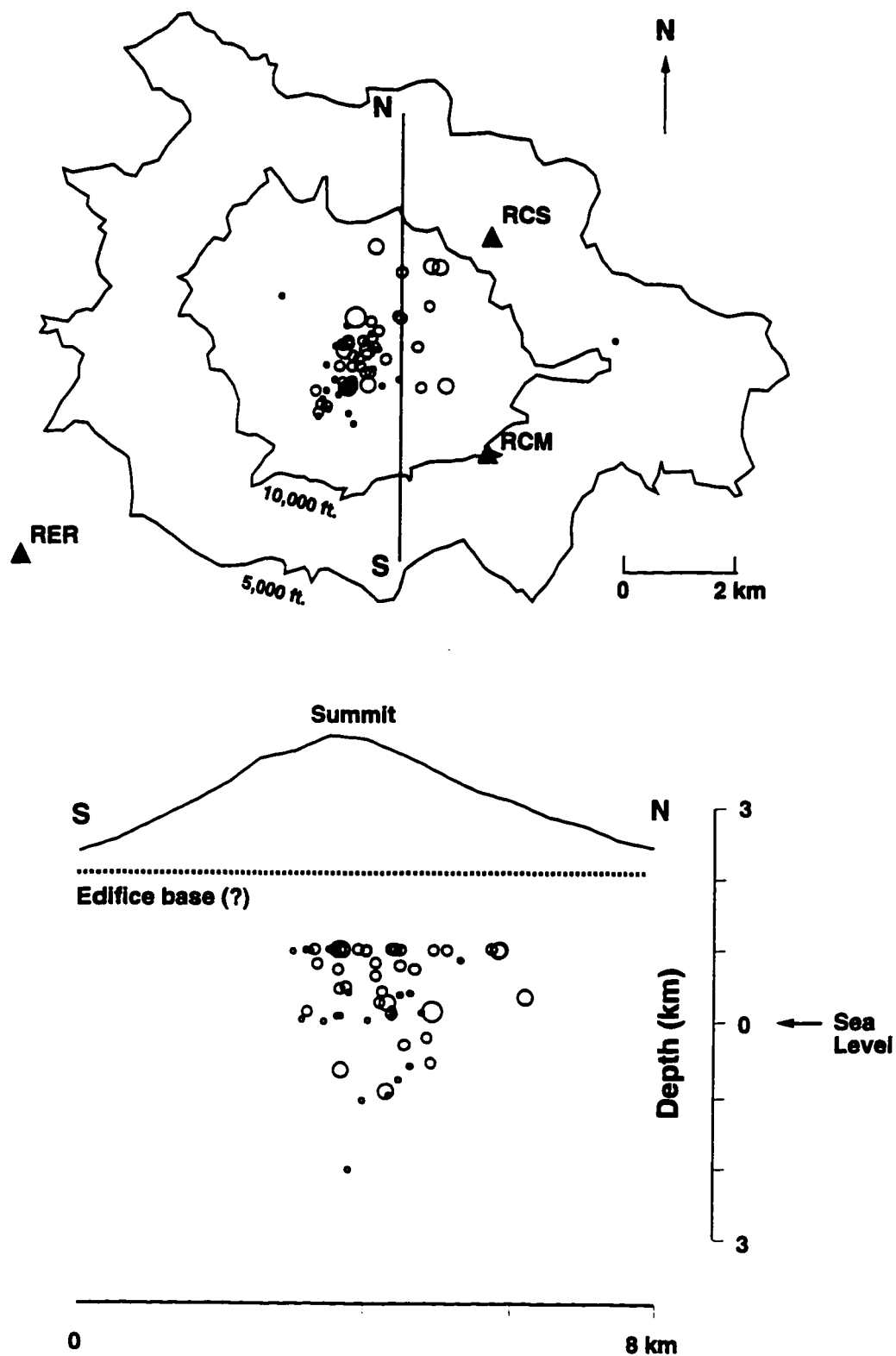


Figure 4-18 Map and N-S cross-section of Rainier earthquakes located with 1-D model and station corrections. The cross-section profile is indicated on the map.

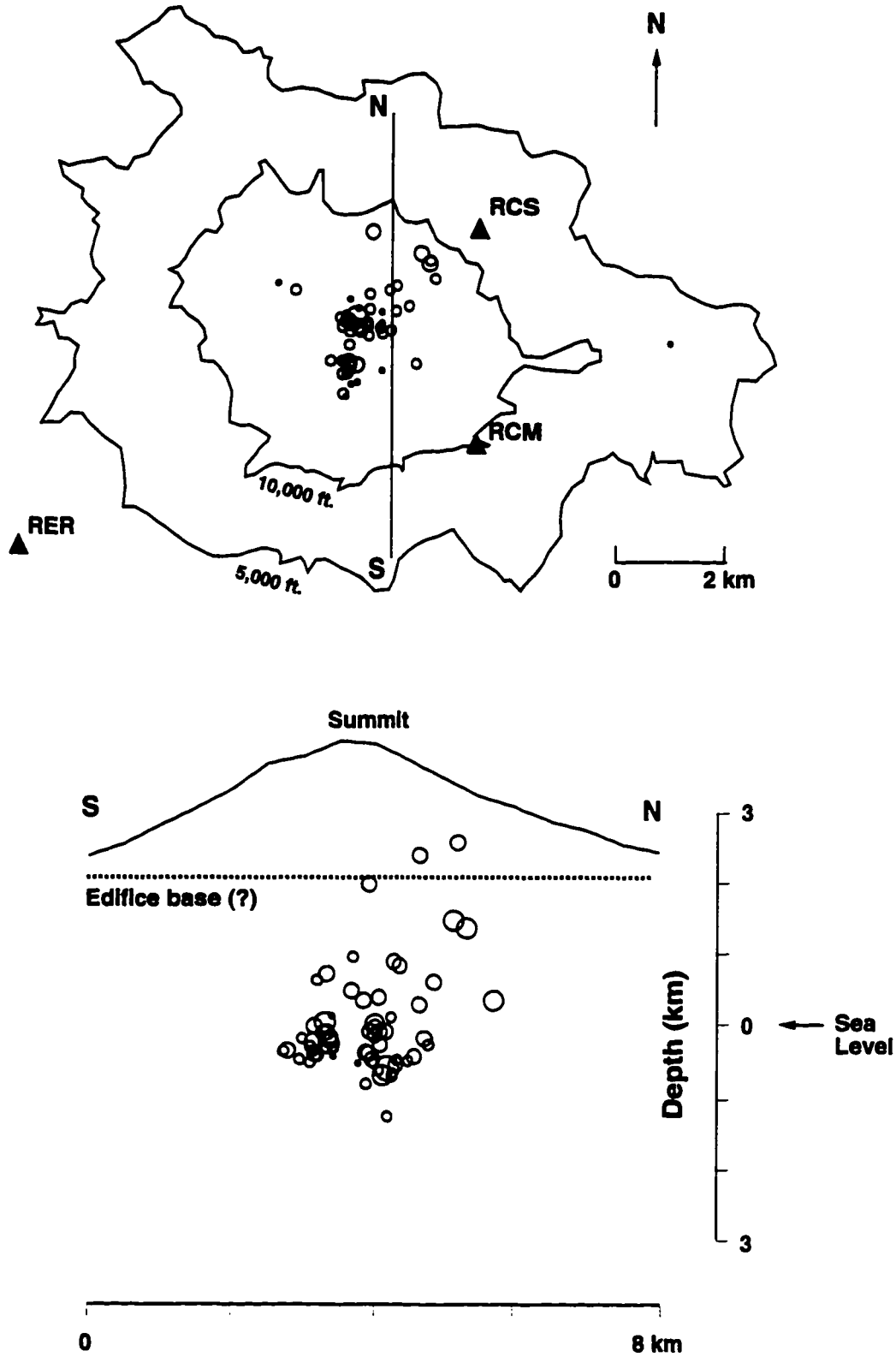


Figure 4-19 Map and N-S cross-section of Rainier earthquakes located using 3-D model.

Table 4.2: Comparison of 1-D and 3-D location errors

Error Type	1-D locations	3-D locations
X error	0.25 km	0.14 km
Y error	0.24 km	0.12 km
Depth error	0.55 km	0.27 km
RMS misfit	0.18 sec	0.11 sec

As can be seen from Table 4.2, the 1-D location errors are almost twice the size of the 3-D location errors, and the rms misfit for 3-D locations is almost 40% lower than the 1-D locations. These relative measures of error indicate that the 3-D locations are more precise than the 1-D locations, and suggest that they are more accurate.

Another means comes from comparing the degree of mislocation of the one source on the edifice with a known location, the August 16, 1989, rockfall off Curtis Ridge (Norris, 1994). This event was recorded on PNSN stations as far as 200 km from the source and generated an impulsive phase that was picked at 15 stations (Rick Benson, personal communication), enough to compute a well-constrained location. It also left a very visible scar, allowing for the estimation of its source location at North $46^{\circ} 52' 18.1''$, West $121^{\circ} 45' 4.9''$, and an elevation of 11,200 feet, or 3.4 km (Norris, 1994). This location is shown in Figure 4-20, along with locations derived using the 1-D and 3-D velocity models. The 3-D location is only 0.4 km from the true location in map view, whereas the 1-D location is 1.1 km distant. The depths for both locations are at or near sea level, roughly 3.5 km below the depth of the true source.

Two statements can be made on the basis of this test. One, 3-D locations as a group are likely more accurate (i.e. closer to the actual locations) than the 1-D locations. This is based primarily on the fact that the 3-D location of the Curtis Ridge rockfall is closer to the true location than the 1-D location. It is also based on the observation that the 0.5 km northeastward shift in map view from the 1-D epicentral location to the 3-D epicentral location (Figure 4-20) matches the general north-northeastward shift between 1-D and 3-D epicenters for all Rainier volcano-tectonic earthquakes (Figure 4-18 and Figure 4-19). The fact that these two trends are parallel indicates that the systematic north-northeastward shift for all earthquakes probably moves the epicenters closer to their true locations.

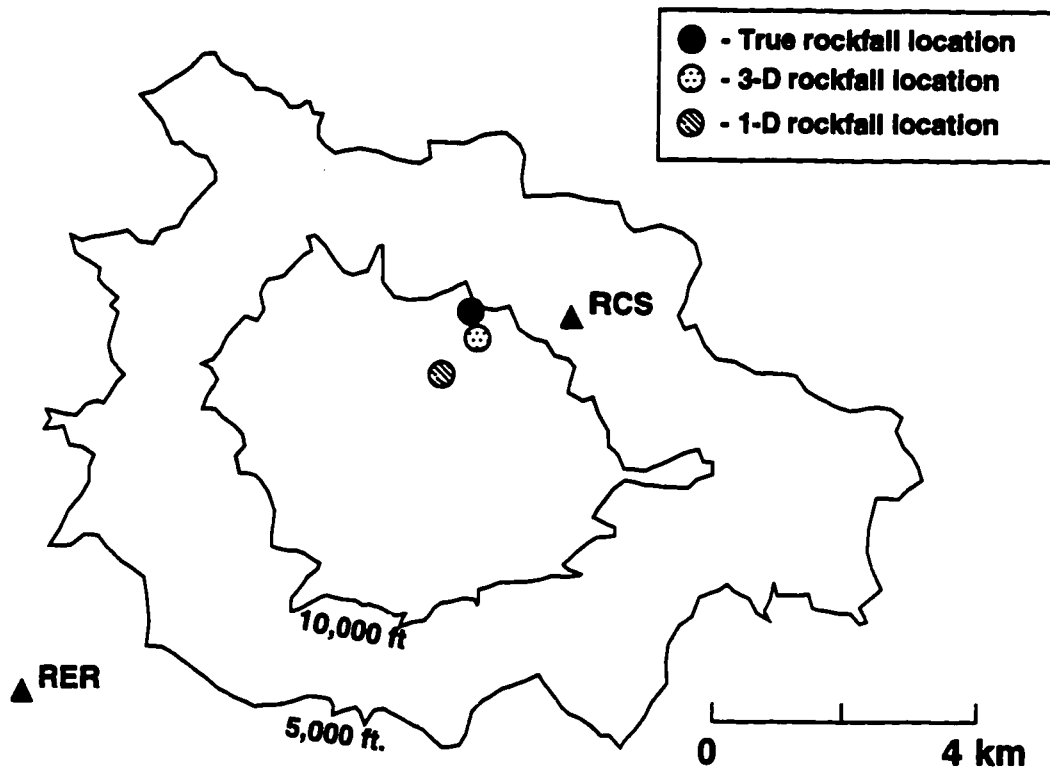


Figure 4-20 Locations of Curtis Ridge rockfall. The true location is indicated by the black circle, the PNSN location (using a 1-D model) by the hachured circle, and the location computed in the 3-D velocity model by the spotted circle.

Two, the fact that depths for both the 1-D and 3-D rockfall locations are 3.5 km below the true location suggests that depth determination may be problematic for events occurring within the edifice. This is supported by depths determined using both S and P-wave arrivals picked at the two closest stations to these earthquakes, RCM (3.1 km elevation) and RCS (2.9 km elevation). The difference between the arrival times (the "S-P time") provides a good constraint on the source-receiver distance X via the equation

$$X = V_p \times \frac{(S_{\text{time}} - P_{\text{time}})}{\left(\frac{V_p}{V_s} - 1\right)} = V_p \times \frac{\Delta T}{0.732} \quad (\text{EQ 4.7})$$

where V_p is the P-wave velocity, V_s the S-wave velocity, and V_p/V_s is 1.732 assuming a Poisson's ratio of 0.25 (e.g. Christensen, 1996). Using arrival-time picks for

reasonably impulsive S and P phases from a volcano-tectonic earthquake occurring on March 6th, 1994, at 0227 GMT, S-P times for RCM and RCS are 0.38 and 0.67 seconds, respectively. Assuming a V_p of 5 km/sec, these times translate to 3-D distances of 2.6 km and 4.6 km, respectively. Using these distances as radii and the epicentral distances from the two stations as x and y coordinates, the two resulting spheres intersect at a depth of 0.4 km below both stations (or 2.5 km above sea level). This is 2.2 km above the depth determined in the 3-D model using only P-wave arrivals. (Note that X will be smaller if the V_p/V_s ratio is larger than 1.732 (as is likely in volcanic environments, where V_s is more sensitive to the presence of fluids than V_p), resulting in an even shallower depth and greater disparity with the depths determined using only P-wave arrivals.)

The known mislocation in depth of the Curtis Ridge rockfall, coupled with the apparent mislocation in depth of the March 6th, 1994, earthquake, suggests that depth determinations for all volcano-tectonic earthquakes may be 2 - 3.5 km too deep. Such systematic mislocations could be caused by an erroneous velocity model. In general, depths will be deeper if the uppermost layer has low velocities, and shallower if it has high velocities (see Figure 5-5 and discussion in section 5.4). Thus one means for making the depths shallower at Mount Rainier is to increase the velocities in the uppermost layer. However, P-wave velocities for the uppermost layer at Mount Rainier are 5.4 - 5.7 km/sec in the 3-D model. Given that the edifice is predominantly composed of andesite (~5.2 km/sec) that is highly altered in places (<< 5.2 km/sec) (e.g. National Research Council, 1994; Sisson, 1995), increasing velocities in the uppermost layer at Mount Rainier is geologically objectionable.

Thus if volcano-tectonic earthquakes are systematically mislocated 2 - 3.5 km below their true depths, it is probably not because of errors in the velocity model. If other factors such as mispicks and mislocation of stations can be ruled out (and I believe they can), then the most likely cause of these mislocations is poor seismograph station geometry on the edifice. Given the demonstrated improvement in the precision of depth determinations after installation of the flank stations RER, RCS, and RCM (Moran et al., 1995), it is likely that further improvement in depth determinations would be achieved by installing a station at the summit.

In summary, although there is an apparent improvement in the precision of the locations of volcano-tectonic earthquakes using the 3-D model, there is also evi-

dence that suggests that these earthquakes are systematically mislocated below their true depths. As will be discussed in the next section, knowledge of their true depths is critical to any interpretation of their significance. Future seismic research at Mount Rainier should focus on resolving this depth determination problem, either by using controlled sources to more accurately assess location capabilities and/or by installing a seismograph station at the summit, directly over the hypocenters, to improve the accuracy of depth determinations.

Significance of Volcano-Tectonic Earthquakes

As was briefly discussed in section 1.3.3, the source of stress for these earthquakes is unknown. Possible hypotheses for why earthquakes are occurring beneath Mount Rainier include: a) earthquakes occurring along faults below and/or within the edifice in response to tectonic forces (the "tectonic hypothesis"); b) earthquakes occurring along faults beneath the edifice in response to gravitational loading of the crust by the weight of the edifice (the "loading hypothesis"); c) earthquakes occurring along faults within the edifice in response to processes related to the progressive crumbling apart of the edifice (the "disintegration hypothesis"); d) earthquakes occurring in response to volumetric and/or thermal forces and locally increased pore pressures associated with the magmatic/hydrothermal system that is known to exist within the edifice (the "hydrothermal hypothesis"); e) earthquakes occurring in response to magmatic intrusion (the "magmatic hypothesis").

I consider the tectonic hypothesis to be the least likely of these candidate hypotheses. This statement stems in part from the observation that many of these earthquakes locate above sea level, where tectonic forces are likely not as strong relative to other stress sources likely operating in a volcanic environment (such as hydrothermal or magmatic forces). A more important piece of evidence comes from focal mechanisms calculated for 11 of these events using the new 3-D model (Figure 4-21) (note that there is little difference between these mechanisms and those computed using the 1-D velocity model). 8 of the 11 mechanisms are normal or oblique-normal, in contrast to mechanisms along the WRSZ, which are predominantly reverse or dextral-slip in character (see Figure 4-17). In addition, the P axes for these 11 events are oriented either vertically or horizontally in a NW-SE direction, quite different from the regional horizontal P-axis trend of N23°E determined by

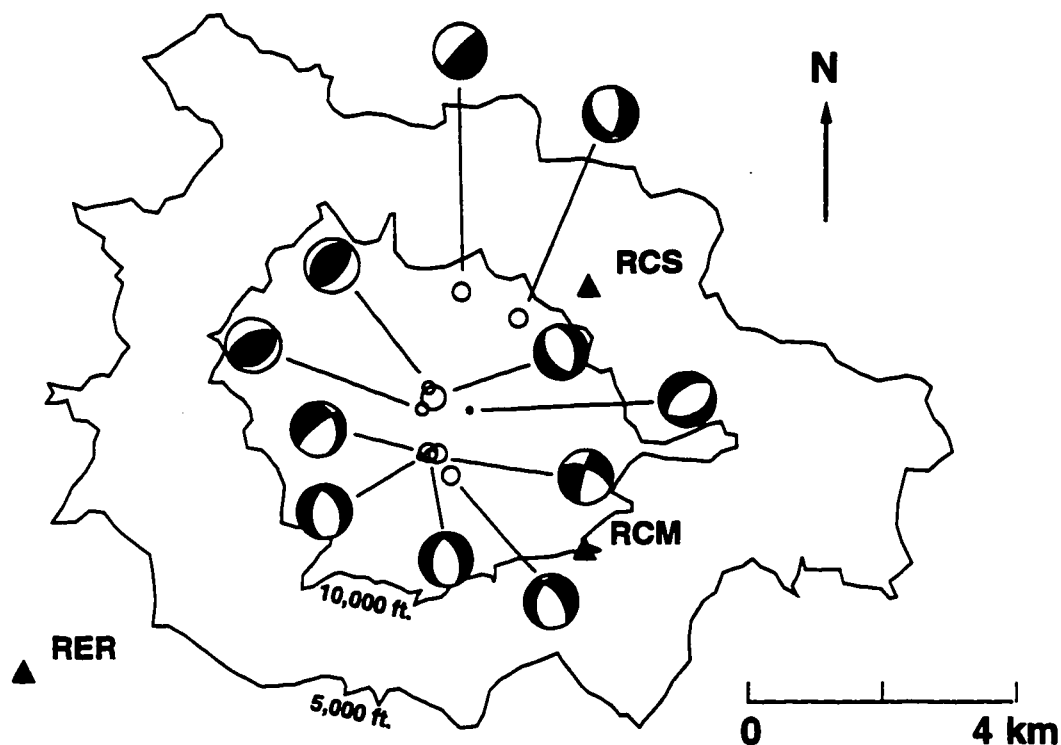


Figure 4-21 Focal mechanisms for 11 volcano-tectonic earthquakes beneath Mount Rainier. Note that the majority of the mechanisms are normal or oblique-normal.

Ma et al. (1991). This difference indicates that the volcano-tectonic earthquakes are occurring in response to local, not regional, stresses.

The observation that favors the tectonic hypothesis is the NE-SW distribution of epicenters determined using the 1-D velocity model (Figure 4-18). This trend suggests the possible presence of a fault or fault zone within or beneath the edifice. As can be seen in Figure 4-19, however, the 3-D locations show no such trend; instead, the epicenters appear to group in several tight clusters. This pattern argues against the presence of a single through-going fault. In addition, focal mechanisms show no preferential P or T-axis orientations, suggesting that they are occurring in response to highly localized stresses. Development of one through-going structure is unlikely in an environment of locally varying stress regimes, since failure along a single fault would be enhanced by the stress field operating in one region and inhibited in another.

An equally unlikely explanation for these earthquakes is the magmatic hypothesis. A magmatic intrusion into the edifice would certainly be accompanied by an increase in the number and/or magnitude of earthquakes as well as other types of precursory activity. However, there has been no evidence of any such occurrence from seismicity (e.g. Malone et al., 1991), heat-flow measurements (e.g. Frank, 1995), or deformation studies (Don Swanson, personal communication). In addition, the chemistry of fumaroles and hot springs at Mount Rainier contain only trace amount of gases commonly associated with magmatic intrusions (Frank, 1995). Thus it is highly unlikely that the volcano-tectonic earthquakes are occurring in response to magmatic intrusion.

The third least-likely explanation is the loading hypothesis. This hypothesis is supported by the fact that 8 of the 11 mechanisms in Figure 4-21 are normal or oblique-normal, with the P-axes oriented vertically as one might expect if the crust is bending in response to the weight of the edifice. However, there are two arguments against this hypothesis. One, if loading is the primary stress source, then the distribution of volcano-tectonic earthquakes should be broader both in map-view and in depth, roughly reflecting the dimensions of the edifice. Instead, they occur only in tight clusters directly beneath the summit; the area beneath the rest of the edifice is aseismic (Figure 4-19). Two, if this is a viable stress source, then earthquakes should also occur beneath other volcanoes with volumes similar to Mount Rainier. However, the crust beneath Mount Adams, the only Washington volcano with a volume similar to Mount Rainier, is completely aseismic.

The primary piece of evidence against the disintegration hypothesis comes from the depths of the 3-D locations. If the average depth of the 3-D locations is truly 2 km below the presumed base of the edifice, then it is unlikely that these earthquakes are related to the volcano falling apart. However, the possibility that depths may be overestimated by 2 to 3.5 km cannot be overlooked. Shifting all locations upwards by 2 km would bring almost every event to a position within or just below the edifice (as well as a few that would locate in the air above the edifice!). In addition, the predominantly normal sense of focal mechanisms in Figure 4-21 agrees with what one might expect from slumping sources on outward-dipping faults. However, the predominantly north-south orientation of most of the fault plane solutions is counter to the primarily east-west orientation of structural discontinuities and zones of geothermal alteration in the edifice (Zimbelman et al.,

1995). These zones are thought to act as geologic controls that concentrate flank collapses on the eastern and western flanks of Mount Rainier. Thus it is uncertain whether the progressive disintegration of the edifice is a viable mechanism for earthquake generation at Mount Rainier.

I believe that the most likely stress source is thermal and/or volumetric forces created by hydrothermal and/or magmatic processes occurring within the plumbing system beneath Mount Rainier. This statement is arrived at partly by process of elimination; the other candidates simply have more arguments against them. The primary piece of evidence that supports this hypothesis is the tight clustering of hypocenters directly beneath the summit. This clustering is consistent with what would be expected to occur above a pressurized magmatic intrusion. If the cylindrical velocity anomaly beneath Mount Rainier is the signal of a magmatic system, then the concentration of volcano-tectonic earthquakes above this feature could indicate that they are occurring in response to magmatic forces occurring within this system. This idea is supported by a study of the theoretical stress field around a 3-D ellipsoidal pressurized intrusion by Koide and Bhattacharji (1975). For any shape other than a sphere, they find that maximum stresses occur directly above the intrusion. Knapp and Norton (1981) also find that fracturing in response to thermal stresses associated with a cooling intrusion concentrates primarily above the intrusion.

The clustering of earthquakes is also consistent with a model proposed by Frank (1995) for the hydrothermal system operating within and beneath Mount Rainier's edifice. Mount Rainier is known to have a vigorous hydrothermal system, with fumaroles keeping parts of the summit snow-free year round (e.g. National Research Council, 1994; Frank, 1995). The hottest and most widespread fumarolic activity is found at the summit, with progressively cooler and smaller fields found on the upper and lower flanks of the volcano. Frank (1995) uses this pattern to suggest that the hydrothermal system is fed by hot gas-rich thermal fluids that migrate upwards from an unknown depth through a narrow central conduit to form an upper-level aquifer at about 1 km below the summit. This aquifer then interacts with groundwater to feed both the summit and flank fumaroles. The fact that earthquakes cluster in several narrow groups directly beneath the summit vents, but well below the postulated aquifer, suggests that these earthquakes could be caused by forces associated with the rising hot gas-rich fluids. The presence of such fluids

could encourage failure in the country rock near the conduit walls by locally increasing pore-fluid pressures along pre-existing fractures, by lowering the intrinsic strength of the wall rock via progressive alteration to clay, and/or by contraction and expansion of the surrounding wall-rock in response to thermal and/or volumetric forces.

This hypothesis is also consistent with interpretations of high-frequency earthquakes at other volcanoes. Montalto (1994) examined seismicity beneath the La Fossa cone at Vulcano, Italy, and concluded that the volcano-tectonic earthquakes were most likely occurring in response to semibrittle hydraulic microfracturing that occurred whenever pore pressures exceeded a certain threshold. Nishi et al. (1996) examined seismicity at White Island, and found intriguing similarities to Mount Rainier earthquakes. They observed that most volcano-tectonic events had magnitudes ranging from 0.7 to 2.7 (the largest observed earthquake at Mount Rainier was a M_l 3.0), and a composite focal mechanism was normal (most Rainier mechanisms are normal). Nishi et al. (1996) infer that these earthquakes are occurring in response to elevated pore pressures and geochemical weakening in the country rock associated with the presence of a shallow hydrothermal system.

One important issue regarding this hypothesis is understanding how such processes could lead to the stress drops and/or source dimensions that are theoretically required for the 11 M_l 2.0 and greater earthquakes that have occurred beneath Mount Rainier since 1989. The source radius r can be estimated from equation 4.5 and equation 4.6 (see section 4.4.1). Assuming a stress drop of 1 MPa, a M_l 2 event will have a source radius of 82 meters and an M_l 3 event will have a source radius of 260 meters (independent confirmation of these numbers comes from the Curtis Ridge rockfall, which had an M_l of ~ 2.0 and a surface area of 15,000 m² (Norris, 1994) corresponding to a circle with a radius of 70 meters). Thus the largest earthquakes at Mount Rainier should have rupture lengths of 150 - 500 meters. Unfortunately, there are few constraints on fault dimensions in magmatic environments. The stress drop value of 1 MPa used above is consistent with theoretical values determined by Koide and Bhattacharji (1975) for a stress field generated by magmatic forces. The fault lengths determined above are also consistent with mapped dimensions of faults associated with plutonic bodies such as the 6 km-diameter Diamond Joe stock in western Arizona (Gerla, 1988), where fault lengths ranged from several centimeters to over a kilometer. Gerla (1988) used results from theo-

retical modeling to infer that most of these fractures likely occurred in response to thermal forces related to cooling of the pluton after emplacement. Thus the theoretical fault dimensions determined above for the largest Mount Rainier earthquakes are consistent with results from other studies of fracture patterns associated with magmatic and/or hydrothermal systems.

In summary, although volcano-tectonic earthquakes beneath Mount Rainier could be caused by several processes, the most likely are volumetric and/or thermal forces associated with the hydrothermal system and/or a cooling intrusive body beneath Mount Rainier. However, evidence for possible systematic mislocation of these earthquakes indicates that more work needs to be done to delineate the exact depth range in which these events are occurring before any firm conclusions can be reached about the process(es) responsible for these earthquakes.

V. Comparison & Contrast

Chapter II describes in detail several major modifications made to the methodology used by Lees (1989). An important question is raised by these modifications, namely "How much difference did they make?" In this Chapter I look at two of these modifications; the incorporation of parameter separation (section 5.1), and the exclusion of station corrections (section 5.2). In addition, in section 5.3 I examine the degree to which resolution was improved by earthquake data collected during the two field experiments described in section 3.3.

5.1 Without Parameter Separation

Figure 5-1 shows the 3-D model computed without using parameter separation. The inversion was run until convergence was achieved, which occurred after 8 full iteration steps. The net reduction in the χ^2 misfit was 94%.

Comparing Figure 5-1 to Plate 1 (generated with parameter separation), it is apparent that there is little significant difference between these two models. The most significant differences are located along the edges of the model, where ray-path coverage is weakest and thus most vulnerable to erroneous hypocenter locations. A more subtle difference is in the size of the anomalies; the amplitudes of low and high velocity anomalies in Figure 5-1 tend to be marginally larger than in Plate 1. However, the broad similarity between these two models suggests that it is by and large not necessary to jointly invert for both hypocenter and velocity parameters where ray coverage is sufficiently dense. Thus previous inversions that did not address the intrinsic coupling of the location and velocity problems (e.g. Lees, 1992) are probably not significantly biased because of this neglect. However, this may conclusion may only be applicable in regions such as the GMR where hypocenters are (apparently) well-constrained and thus not likely to be significantly in error.

5.2 With Station Corrections

Figure 5-2 shows the model that results from an inversion run with station corrections (note that parameter separation was used in this inversion). There are several significant differences between Figure 5-2 and the 3-D model presented in Plate 1. Most of the differences occur in the upper 4 layers, largely in association

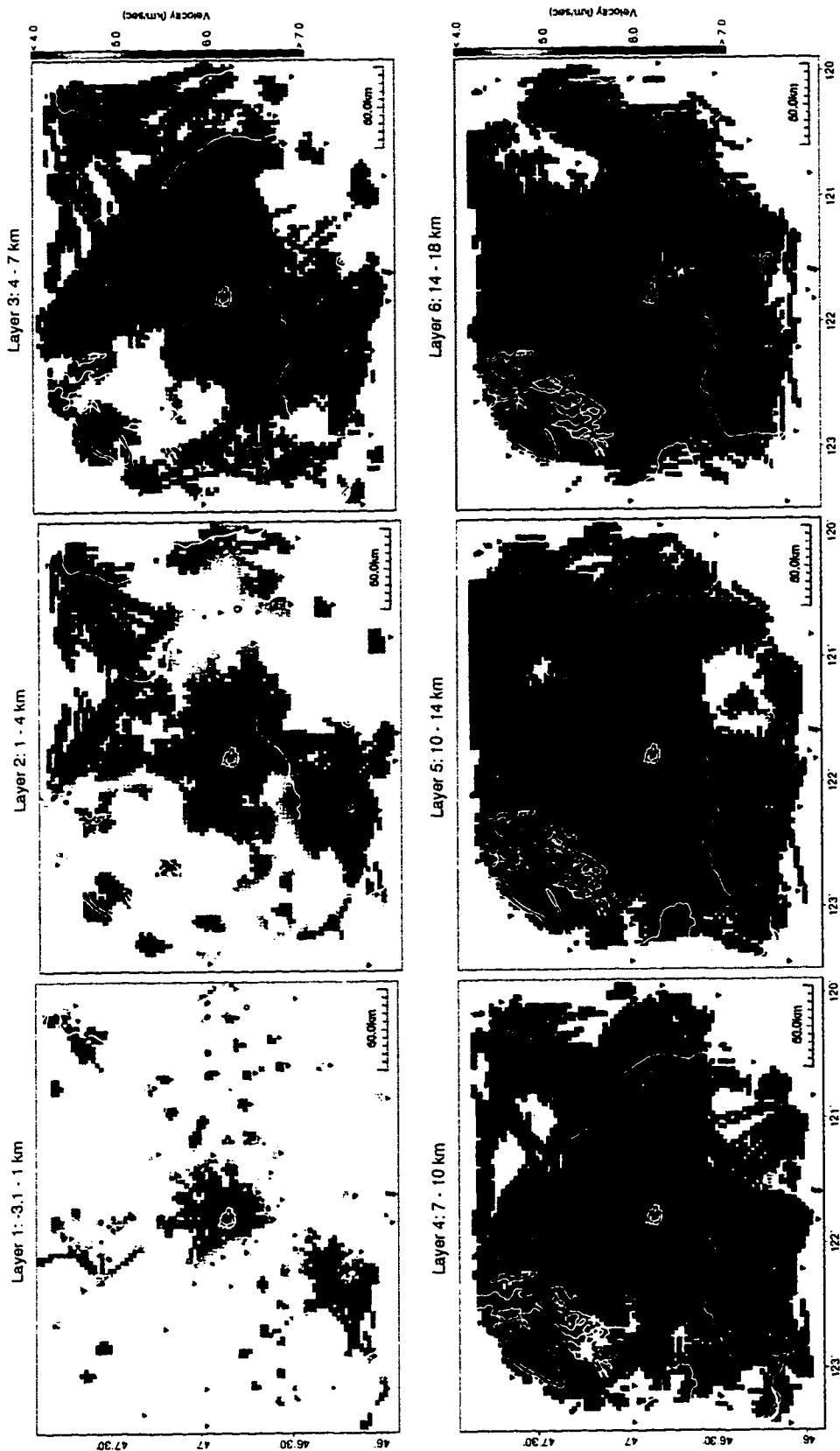


Figure 5-1 6 slices through the 3-D model derived without the use of parameter separation. Velocity scale and landmarks are the same as in Plate 1. Note that there is little difference between this model and Plate 1.

with stations that have the largest corrections. The most noticeable difference occurs beneath the Seattle and Tacoma basins, where there is an almost complete absence in Figure 5-2 of the low velocity anomalies associated with the basins apparent in Layers 1 - 4 of Plate 1. Beneath the basins velocities range from 5 to 6.5 km/sec in the model generated with station corrections (Figure 5-2), well above the 3.7 - 5 km/sec velocities determined without station corrections (Plate 1). Velocities determined from seismic reflection data range from 1 - 3 km/sec in the upper 4 km (Pratt et al., 1997), indicating that the image derived without station corrections is much closer to the truth. Two stations, SPW and MEW, are primarily responsible for this difference (see Figure 3-7 for station locations). The station corrections for SPW and MEW are 0.78 and 0.77 seconds, respectively. If these corrections are removed before the inversion for velocity parameters is performed, then positive (i.e. late) residuals will decrease in size, resulting in the higher velocities seen below these stations in Figure 5-2. For example, a vertical raypath will take 2.5 seconds to travel through a 10 km-thick layer that has an average velocity of 4 km/sec. If a correction of 0.77 seconds is removed from this time, then the average velocity of this layer must increase to 5.8 km/sec, similar in size to the velocity differences observed.

It is apparent from this comparison that the use of station corrections in LET can cause potentially significant biases in the resulting model. This could explain the failure of Lees and Crosson (1989), who used station corrections, to image the Seattle Basin (see Figure 5-4 in section 5.4). However, the differences are most significant in the upper 3 layers, indicating that station corrections only have significant effects in the uppermost few layers. Nevertheless, if rays are traced to station elevation, and station locations are not significantly in error, then there is no real need to use station corrections in LET except to stabilize locations in the initial location run. Given that their inclusion does result in notable biases, their use in LET should be avoided.

5.3 Without New Stations

Figure 5-3 shows the model that results from an inversion performed without data recorded by the 40+ refraction and 18 NEHRP temporary stations deployed during the experiments described in section 3.3.1 and section 3.3.2 (note that parameter separation was used in this inversion, but station corrections were not). 3633 events

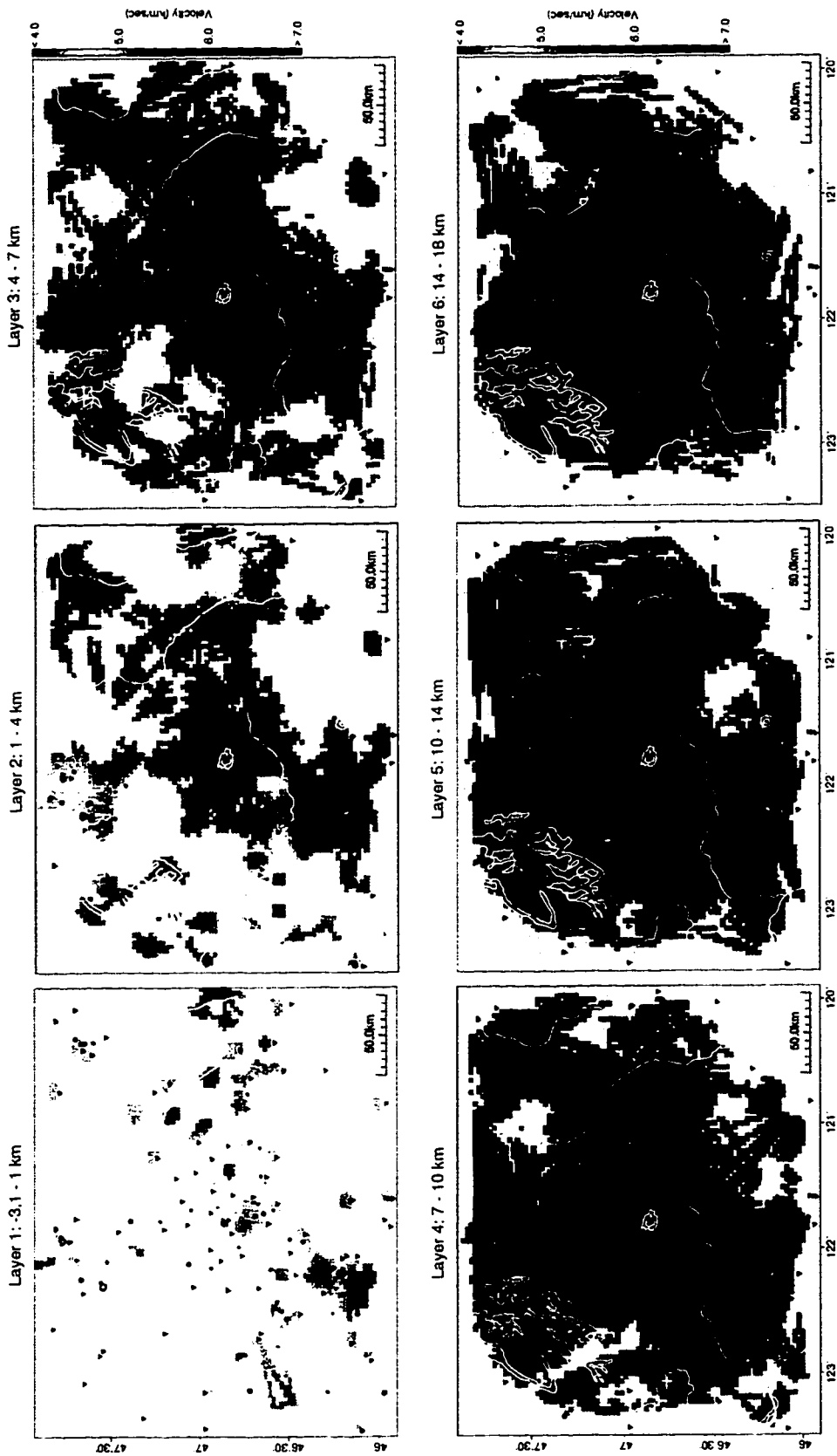


Figure 5-2 6 slices through the 3-D model derived with station corrections. Velocity scale and landmarks are identical to Plate 1. Note that there are quite significant differences between this model and Plate 1, especially in the upper 3 layers.

with 71,724 rays were used in the final iteration, 130 fewer events and 3320 fewer rays than were used in the final iteration for the model shown in Plate 1. Thus the field projects described in section 3.3 resulted in a 4.6% increase in the number of raypaths available for a LET inversion in the GMR.

The most significant differences between the models derived with (Plate 1) and without (Figure 5-3) the temporary stations occur in the upper three layers near Mount Rainier and the temporary stations. In Layer 1, the high velocity anomaly beneath Mount Rainier (interpreted in section 4.2.3 to be the signal of the Tatoosh pluton) is less extensive in Figure 5-3, and its edges are less well defined. In Layers 2 and 3 the region of high velocities beneath Mount Rainier (interpreted in section 4.2.3 to be Tertiary plutons) is also less extensive in Figure 5-3 and its edges (especially its eastern edges) are poorly defined, whereas the edges are very well defined in Plate 1. In addition, the north-south lower velocity anomaly associated with the Carbon River/Skate Creek anticline is better defined in Plate 1, and a high velocity anomaly due west of Mount Rainier on the eastern edge of the SWCC is non-existent in Figure 5-3. Not coincidentally, these two later anomalies locate directly beneath three of the temporary NEHRP stations (PAK, MHL, and ASF). In Layer 3, the north-south lower-velocity body beneath the Carbon River anticline is narrower in Plate 1. In addition, the western and northern edges of the broad low velocity anomaly north of Yakima (interpreted in section 4.2.3 to be due to Tertiary sediments buried beneath the CRBG) is improved in Plate 1. In deeper layers the differences are more subtle, and wouldn't affect interpretations.

The improved resolution of the high velocity body beneath Mount Rainier in Layers 1 - 3, as well as its edges, is perhaps the most important improvement in the model resulting from the additional data collected by the temporary seismograph stations. The improved resolution of this high velocity anomaly has improved our ability to detect potentially hidden active faults near Mount Rainier, an important part of the assessment of seismic hazards in this region. For example, the improved resolution allowed me to speculate with some degree of confidence that the 1974 Ohanapecosh earthquake possibly occurred along a fault associated with the southern edge of this high velocity region (see section 4.4.3). In addition, improved resolution of bodies associated with the WRSZ allowed for a more reliable assessment of its seismogenic potential (see section 4.4.2).

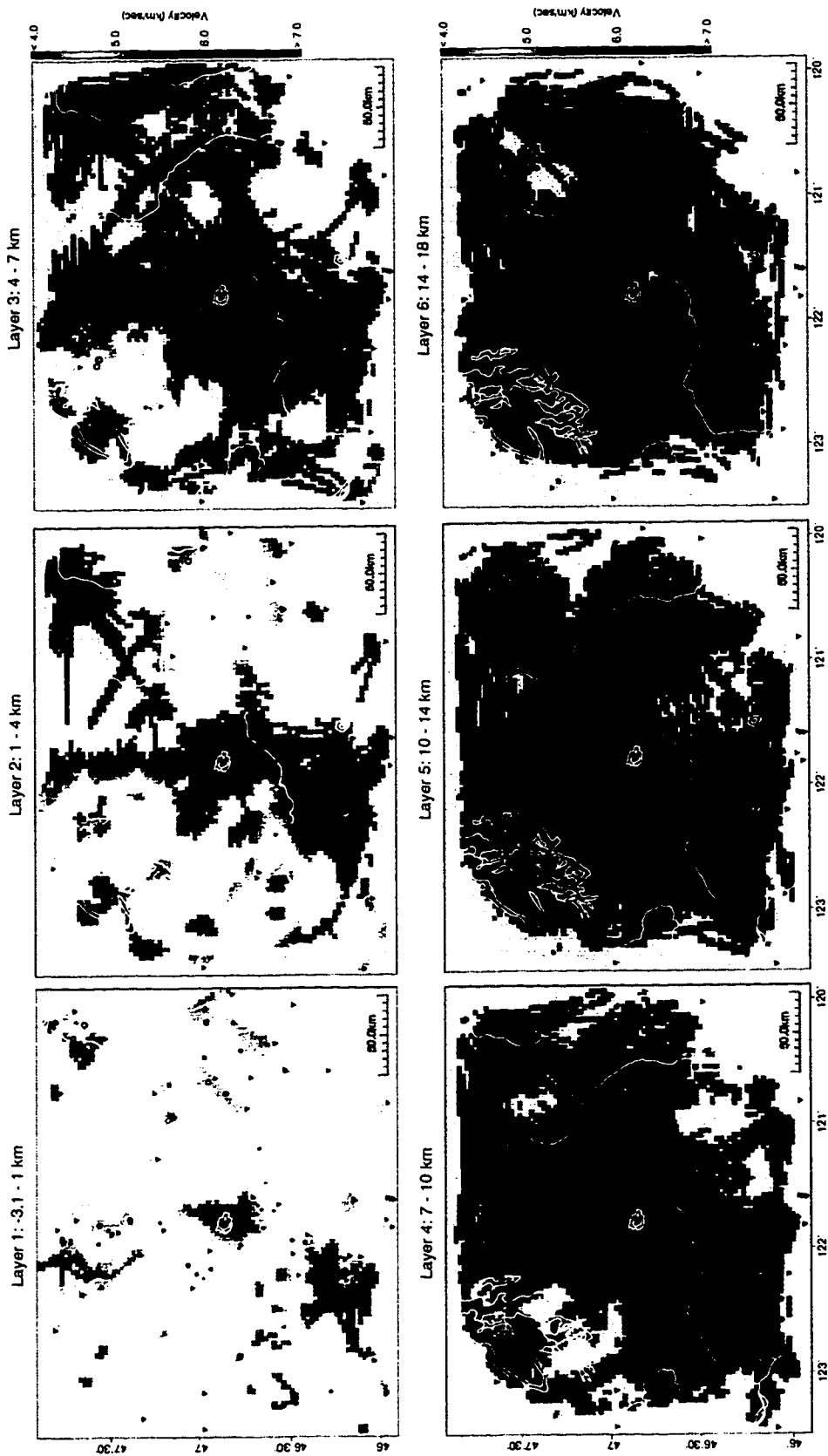


Figure 5-3 6 slices through the 3-D model derived without data from temporary stations. Velocity scale and landmarks are identical to Plate 1. Note that most of the increased resolution in Plate 1 occurs east of Mount Rainier in the upper 3 layers.

Overall, the degree of difference between Figure 5-3 and Plate 1 is less than was originally expected. This statement leads to two conclusions. One, the fact that 3300 additional rays did little to fundamentally change the model where ray coverage already existed indicates that the P- wave velocity signals contained within the PNSN earthquake catalog are robust. Two, the fact that the model changed mainly where ray coverage did not previously exist indicates that future field experiments with goals similar to mine should concentrate on filling gaps in ray coverage. Adding raypaths to regions that already have some ray coverage doesn't appear to have much influence on the resulting model.

5.4 Comparison with Lees (1989)

Figure 5-4 shows depth slices through the 3-D P-wave velocity model of Puget Sound derived by Lees (1989) and published in Lees and Crosson (1990). It is immediately apparent that this image differs markedly from my image shown in Plate 1. The differences are in part due to differences in methodology used in the two inversions. Lees (1989) performed just a one-step linear inversion, used station corrections (see section 2.3.2), incorrectly projected hypocenters and stations into x-y-z coordinates of the 3-D model (see section 2.3.3), and used a different starting model. Also, since the geographical areas examined by the two studies are different, resolving capabilities are likely different in the area of overlap.

However, probably the most significant factor is the differing quality of data used in the two inversions. Different criteria were used to select earthquakes, and unquestionably the criteria used by Lees (1989) (azimuthal gap $\leq 180^\circ$, number of stations ≥ 5 , nearest station ≤ 50 km, rms residual < 0.5 sec, and magnitude > 0.0) were less strict than those that I use (see Table 3.1). The more liberal criteria resulted in at least two related spurious anomalies in the Puget Sound image; a high velocity anomaly beneath LMW in Layer 1, and a low velocity anomaly beneath LMW in Layers 2 and 3. The only source of velocity information for the blocks in this region comes from the many shallow sources located in the upper 5 km. A careful comparison of the dataset used by Lees (1989) with the PNSN catalog shows that most of the sources in this region are actually blasts or probable blasts from local logging operations and quarries. Thus most of these sources were actually located at the surface. However, the average depth for these sources in the dataset used by Lees (1989) is 3 km. The cartoon in Figure 5-5 illustrates the result-

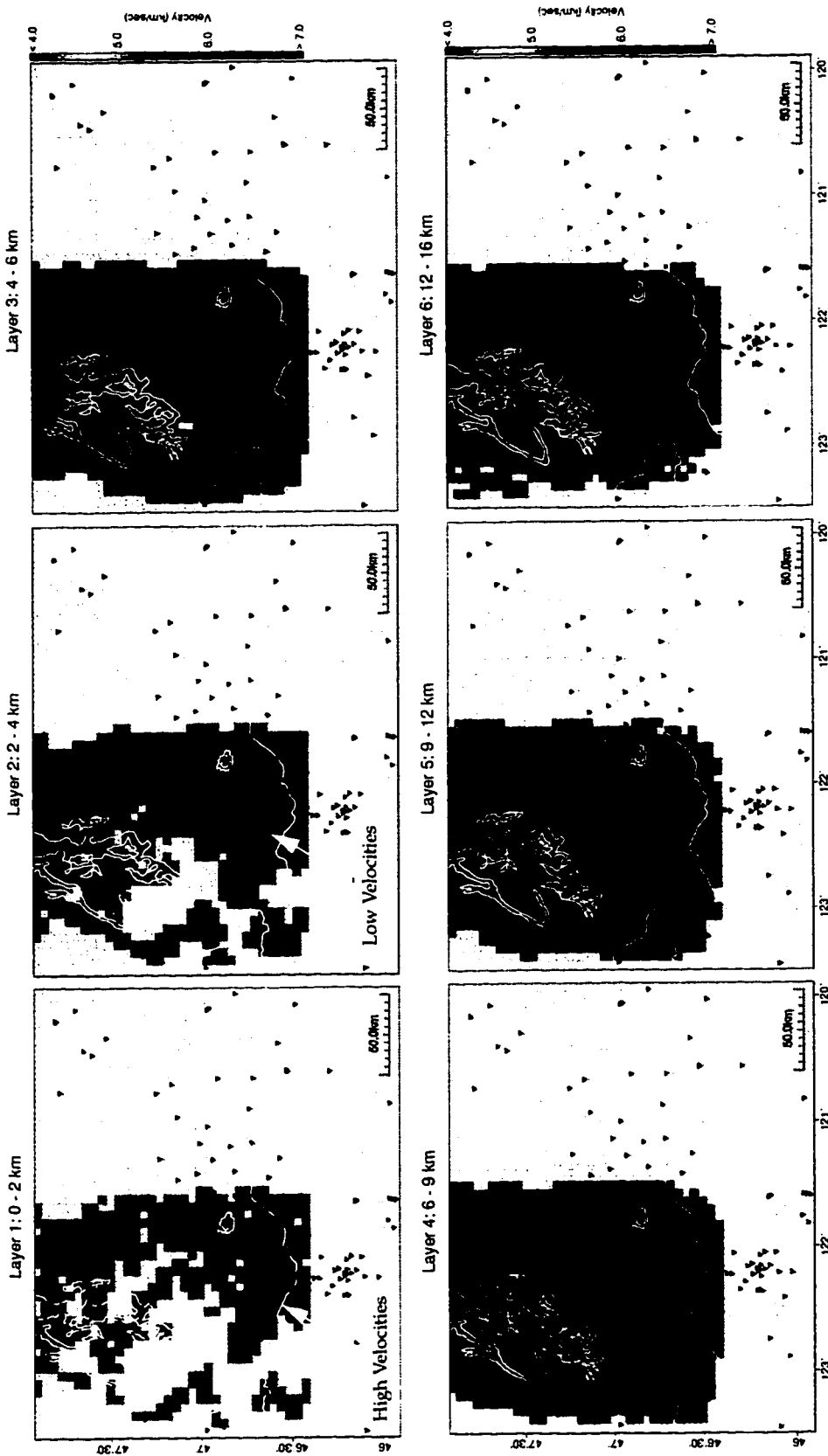


Figure 5-4 6 slices through the 3-D model from Lees (1989). Shown is the portion that overlaps the GMR. The velocity scale and landmarks are identical to Plate 1. Note that there are very significant differences between these images and the model shown in Plate 1. Arrows in Layers 1&2 point to the spurious anomalies discussed in the text.

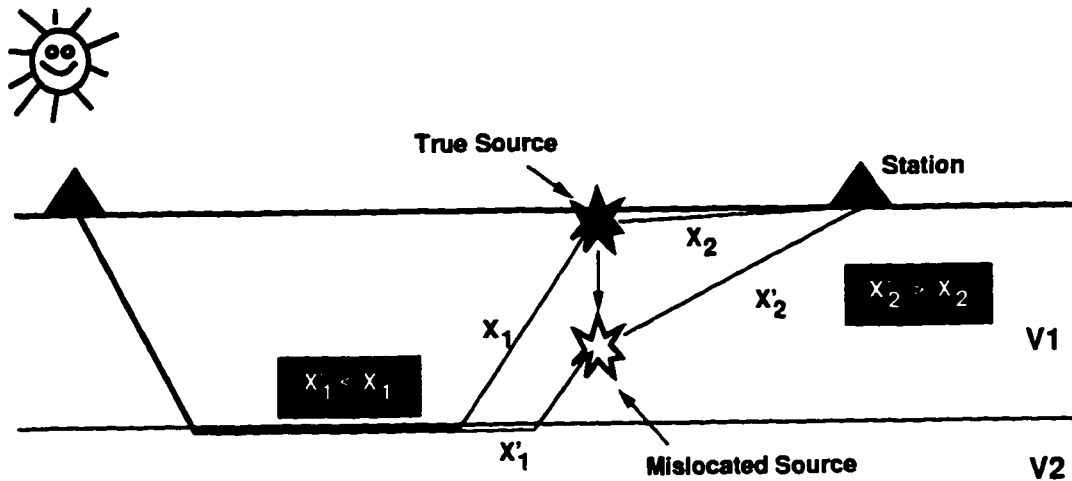


Figure 5-5 Illustration of the effect of mislocating a source downwards in depth on lengths of raypaths. See text for explanation.

ing problem. If a source is mislocated several km below the surface, then the ray-path length (X_i) will increase for upgoing rays and decrease for downgoing rays. Since

$$\text{Travel Time} = \frac{\text{Distance } (X_i)}{\text{Velocity } (V_i)}$$

an increase in the raypath distance (i.e. $X'_2 > X_2$ in Figure 5-5) will result in a higher velocity, and a decrease (i.e. $X'_1 < X_1$ in Figure 5-5) will result in a lower velocity (assuming that the travel time remains relatively constant). This is exactly the pattern observed near LMW in Layers 1, 2, and 3 in Figure 5-4. Layer 1 contains rays traveling upwards to LMW that are longer than they should be due to the mislocation of the blast depths, resulting in a high velocity anomaly. Layers 2 and 3 contain raypaths traveling downward to other stations that are shorter than they should be, resulting in low velocity anomalies. This illustrates that the systematic mislocation of many sources in a particular region can easily create spurious anomalies in the resultant image.

There are several possible reasons why these blasts are systematically mislocated in depth. The main reason is likely because of inadequate station geometry. Depths for shallow sources are in general difficult to accurately determine, because the sources occur at roughly the same elevation as the stations. The resulting time

derivatives with respect to depth will therefore vary little over a reasonably large range of depths, making the location unstable with respect to depth. This problem is alleviated somewhat by the presence of a station close to the source, hence my more conservative requirement that the nearest station be within 15 km of the source. Another possible reason for the systematic mislocations is that the velocity structure of the upper 1 km of the crust (which raypaths from surface sources must travel through not once but twice) is very complex and in general poorly known. Finally, waveforms from blasts are generally of poorer quality than earthquakes, with lower frequency and more emergent arrivals. Thus arrival time picks will have a greater tendency to be in error.

If Lees (1989) had performed a non-linear inversion and had accounted for hypocenter-velocity coupling, then it is possible that these spurious anomalies would have disappeared. However, many of the depths from relocations of the USGS blasts in my final 3-D model are also several kilometers below the surface (see section 4.2.2), suggesting that factors such as distance to the nearest recording station and azimuthal gap are more important in accurate depth determination than perfect knowledge of 3-D velocity structure and/or accounting for hypocenter-velocity coupling. The possibility that these two spurious anomalies were caused by overly liberal selection criteria calls into question the practice of using more liberal selection criteria to increase the number of events in regions that would otherwise have relatively sparse ray coverage (e.g. Protti et al., 1996). It also demonstrates that it is well worth the time and effort to ensure that one is using only well-constrained earthquake sources in a LET inversion. No matter how fancy one gets with inversion theory, if bad data are used, erroneous anomalies will result.

VI. Conclusions

6.1 Summary of Results

In this dissertation I have described a LET experiment performed in the Greater Mount Rainier area (GMR). The most important results from this work fall into three categories; geology, seismotectonics, and tomography.

6.1.1 Geology

The P-wave velocity model described in Chapter IV provides important constraints on the structure and lithology of the upper crust beneath the GMR. There is in general excellent agreement between the upper 3 layers of the model and geology. Significant findings include:

- Two low velocity anomalies that lie directly beneath the Morton and Carbon River-Skate Creek anticlines, extending from the surface to 10 km. These anomalies likely correspond to Tertiary sediments of the Carbonado and McIntosh formations.
- Low velocity anomalies that correlate with the positions of the Seattle, Tacoma, and Chehalis basins.
- A broad high velocity anomaly extending from the surface to 10 km, correlating at the surface with the Tatoosh, White River, and Bumping Lake plutons.
- A broad high-velocity anomaly in Layers 2-3 due west of the SWCC that lies beneath the sedimentary cover of the Puget Lowlands. The velocities in this anomaly are consistent with a body composed of altered basalts with minor amounts of gabbro and diabase. I interpret this feature to be a buried eruptive center of the Crescent formation.
- A cylindrical low-velocity anomaly that extends from 1 to at least 10 km beneath Mount Rainier. This anomaly is interpreted to be caused by heating of country rock in association with the cooling of bodies of magma in the conduit system beneath Rainier.
- Two mid-crustal low velocity anomalies beneath the Cascades. These could also be caused by increase in temperatures.

6.1.2 Seismotectonics

The association (or lack thereof) between seismicity patterns and structures in my P-wave velocity model has significant implications for seismic hazards and seismotectonics in the GMR. These include:

- The association of the St. Helens seismic Zone (SHZ) with a narrow, north-south, 50-km long trough of lower velocities extending from near the surface to at least 14 km. This association supports the hypothesis that the SHZ represents a distinct fault or fault zone. Using a length of 50 km, the maximum expectable earthquake along this fault is between 6.7 and 7.0.
- The general lack of association of the Western Rainier Seismic Zone (WRSZ) with a single distinct feature in the velocity model. This, combined with the more diffuse nature of WRSZ seismicity, suggests that the WRSZ does not represent a distinct fault or fault zone. I estimate that the maximum expected earthquake along the WRSZ is 5.5, more than an order of magnitude smaller than the SHZ.
- The apparent association of a M_l 4.8 event near Ohanapecosh with a north-east-trending lateral velocity contrast. This suggests the possibility that this event occurred along a previously unidentified fault, which (based on the length of this boundary) could generate a M_l 6.4.
- The general lack of a systematic relationship between velocity patterns and the inferred location of the SWCC. This lack of association indicates that there is no single velocity signature associated with the SWCC, and raises the possibility that it is not a distinct lithologic feature.
- The apparent correlation of a high velocity ridge with the southern boundary of the OWL. Based on the additional correlation of these two features with a ridge of heat flows and an apparent change in the orientation of P-axes from focal mechanisms, I propose the addition of a fourth segment to the segmentation scheme of Guffanti and Weaver (1988) for the Washington and Oregon Cascades.
- The apparent location of volcano-tectonic earthquakes at depths below the base of the edifice of Mount Rainier, indicating that they are probably not occurring in response to the disintegration of the edifice. These earthquakes

are interpreted to be occurring most likely in response to thermal and/or volumetric forces related to the hydrothermal/magmatic system beneath Mount Rainier.

6.1.3 Tomography

In addition to the above geologic and seismotectonic interpretations, several findings are also applicable to the general field of seismic tomography.

- Images derived with and without parameter separation were insignificantly different except where ray coverage was sparse. Thus models from previous studies derived without accounting for the intrinsic coupling of hypocenter and velocity parameters via parameter separation or true simultaneous inversion (e.g. Walck and Clayton, 1987; Lees, 1989) are probably not significantly biased because of this neglect, unless their ray coverage and/or data quality were poor.
- Images derived with and without station corrections indicate that station corrections do remove velocity structure from the upper several layers of a velocity model. Thus station corrections should not be used in LET, except to stabilize the initial locations.
- Poor data quality can result in large spurious anomalies in LET images. As a general rule, data quality should come before data quantity.

6.2 Future Work

There are several seismology-related projects that would yield important additional constraints on geologic interpretations in the GMR. One such project that should be performed is a higher resolution LET inversion for P-wave velocity structure at Mount Rainier. In my study the whole of the Mount Rainier edifice was represented by 9 constant-velocity blocks extending from the surface to 1 km below sea level, hardly an ideal parameterization for a highly complex system like Mount Rainier. There is arguably sufficient data for such an inversion now in the PNSN catalog, although there are some gaps in the northwest quadrant due to poor station coverage. The resultant model would likely improve the accuracy of locations in the edifice. It would also provide important constraints on the location

of low velocity and/or attenuating bodies in the edifice that could correspond to zones of hydrothermal alteration.

More work is also needed to improve our understanding of the significance of volcano-tectonic earthquakes beneath Mount Rainier. Based on my findings in section 4.4.4, some uncertainty remains regarding the depth range in which these earthquakes are occurring. This uncertainty is primarily due to the distribution of seismograph stations on the volcano. A seismometer located on the summit of Rainier would greatly improve the station geometry, and would greatly improve the accuracy of PNSN hypocentral determinations for volcano-tectonic earthquakes occurring beneath Rainier. Since knowledge of earthquake depths is crucial for their interpretation (i.e. are they occurring above or below the base of the edifice?), I believe it is vital for the PNSN to install a new, permanent station at the summit.

Another important direction of future research is the development of a 3-D S-wave velocity model for the GMR (as well as the Puget Sound). S-wave models can provide important additional constraints on the lithology and/or attenuative properties of rocks, and have recently been used with great success by Benz et al. (1996) to infer the existence of a magma conduit beneath Redoubt Volcano. Deriving such a model using the current PNSN dataset is somewhat problematic, since the vast majority of S-picks are made on traces recorded by vertical-component stations and thus will have at least an order-of-magnitude higher picking error than P-picks. However, it would still be a good first step to perform a tomographic inversion using the available S-picks in the PNSN catalog, and to compare the resulting model to existing P-wave velocity models.

Three other important projects would require some field work to acquire the necessary data. The first is the deployment of temporary three-component seismometers around Mount Rainier, in an effort to acquire sufficient data to perform a P and S wave attenuation study (e.g. Ponko and Sanders, 1994). The second is the deployment of vertical-component seismometers in the region between Mount St. Helens and Mount Hood, where there is seismicity but very few stations. The objective would be to look for any major structural link between the SHZ beneath Mount St. Helens and a smaller north-south trending band of earthquakes beneath Mount Hood. The third is the deployment of vertical-component seismometers in the Wenatchee-Lake Chelan area, with the objective of developing a model that could

be used to help improved our understanding of the tectonic significance of earthquakes occurring in a diffuse band south of Lake Chelan, as well as to estimate their seismogenic potential.

A final recommendation is to use my GMR model to perform 3-D wave propagation experiments. By comparing calculated waveforms with waveforms observed at the few available PNSN 3-component stations, one could (for example) assess the realness of the two broad mid-crustal anomalies beneath the Cascades.

In addition to these seismology projects, the attempt in section 4.3.2 to link low velocities beneath Mount Rainier with heated (but not molten) granodiorite demonstrates the real need for more laboratory measurements of the seismic velocities of rocks at or near their solidus temperatures. There are few such measurements made at pressures corresponding to upper-crustal depths, making any conclusions regarding the presence or lack of melt based on velocities determined from tomography tenuous at best.

Bibliography

- Aki, K., A. Christoffersson, and E. S. Husebye, Determination of the three-dimensional seismic structure of the lithosphere, *J. Geophys. Res.*, 82, 277-296, 1977.
- Aki, K., and P. G. Richards, *Quantitative seismology: Theory and methods*, W. H. Freeman and Company, New York, pp. 63-121, 1980.
- Atwater, B. F., Geologic evidence for earthquakes during the past 2000 years along the Copalis River, southern coastal Washington, *J. Geophys. Res.*, 97, 1901-1919, 1992.
- Atwater, B. F., and A. L. Moore, A tsunami about 1000 years ago in Puget Sound, Washington, *Science*, 258, 1614-1617, 1992.
- Babcock, R. S., R. F. Burmeister, D. C. Engebretson, and A. Warnock, A rifted margin origin for the Crescent Basalts and related rocks in the northern Coast Range Volcanic Province, Washington and British Columbia, *J. Geophys. Res.*, 97, 6799-6821, 1992.
- Backus, G. E., and J. F. Gilbert, Numerical application of a formalism for geophysical inverse problems, *Geophys. J. R. Astr. Soc.*, 13, 247-276, 1967.
- Barker, S. E., and S. D. Malone, Magmatic system geometry at Mount St. Helens modeled from the stress field associated with post-eruptive earthquake, *J. Geophys. Res.*, 96, 11,883-11,894, 1991.
- Beeson, M. H., and T. L. Tolan, The Columbia River Basalt Group in the Cascade range: A middle Miocene reference datum for structural analysis, *J. Geophys. Res.*, 95, 19,547-19,559, 1990.
- Benz, H. M., B. A. Chouet, P. B. Dawson, J. C. Lahr, R. A. Page, and J. A. Hole, Three-dimensional P and S wave velocity structure of Redoubt Volcano, Alaska, *J. Geophys. Res.*, 101, 8111-8128, 1996.
- Best, M. G., *Igneous and metamorphic petrology*, W. H. Freeman and Company, New York, pp. 261-266, 1982.
- Blackwell, D. D., J. L. Steele, and S. Kelley, Heat flow in the state of Washington and thermal conditions in the Cascade Range, *J. Geophys. Res.*, 95, 19,495-19,516, 1990.

- Blakely, R. J., and R. C. Jachens, Volcanism, isostatic residual gravity, and regional tectonic setting of the Cascade volcanic province, *J. Geophys. Res.*, 95, 19,439-19,451, 1990.
- Bonini, W. E., D. W. Hughes, and Z. F. Danes, Complete Bouguer gravity anomaly map of Washington, Gravity Anomaly Map GM-11, Washington Division of Geology and Earth Resources, scale 1:500,000, 1974.
- Brandon, M. T., and J. A. Vance, Tectonic evolution of the Cenozoic Olympic subduction complex, Washington State, as deduced from fission track ages for detrital zircons, *Am. J. Sci.*, 292, 565-636, 1992.
- Brune, J. N., Tectonic stress and the spectra of seismic shear waves from earthquakes, *J. Geophys. Res.*, 75, 4997-5009, 1970.
- Bucknam, R. C., E. Hemphill-Haley, and E. B. Leopold, Abrupt uplift within the past 1700 years at southern Puget Sounds, Washington, *Science*, 258, 1611-1614, 1992.
- Cady, W. M., Tectonic setting of the Tertiary volcanic rocks of the Olympic Peninsula, Washington, *J. Res. U.S. Geol. Surv.*, 3, 573-582, 1975.
- Campbell, N. P., and S. R. Reidel, Further exploration for gas warranted in Columbia basin, *Oil Gas J.*, 92, 127-130, 1994.
- Carslaw, H. S., and J. C. Jaeger, *Conduction of heat in solids*, Oxford University Press, Oxford, pp. 53-62 & 258-262, 1959.
- Catchings, R. D., and W. D. Mooney, Crustal structure of the Columbia Plateau: Evidence for continental rifting, *J. Geophys. Res.*, 93, 459-474, 1988.
- Cerveny, V., I. A. Molotkov, and I. Psencik, *Ray method in seismology*, University of Karlova Press, Prague, Chechoslovakia, 1977.
- Christensen, N. I., Seismic velocities, in *Handbook of physical properties of rocks, Volume II*, edited by R. S. Carmichael, pp. 1-227, CRC Press, Inc., Boca Raton, Florida, 1982.
- Christensen, N. I., Poisson's ratio and crustal seismology, *J. Geophys. Res.*, 101, 3139-3156, 1996.
- Christensen, N. I., and D. L. Szymanski, Seismic properties and the origin of reflectivity from a classic Paleozoic sedimentary sequence, Valley and Ridge province, southern Appalachians, *Geol. Soc. of Am. Bull.*, 103, 277-289, 1991.

- Christensen, N. I., and W. D. Mooney, Seismic velocity structure and composition of the continental crust: A global view, *J. Geophys. Res.*, 100, 9761-9788, 1995.
- Clayton, G. A., Geology of the White Pass area, south-central Cascade Range, Washington, M.S. thesis, 212 pp., Univ. of Wash., Seattle, 1983.
- Clowes, R. M., M. T. Brandon, A. G. Green, C. J. Yorath, A. Sutherland Brown, E. R. Kanasewich, and C. J. Spencer, LITHOPROBE - southern Vancouver Island - Cenozoic subduction complex images by deep seismic reflections, *Can. J. Earth Sci.*, 24, 31-51, 1987.
- Cowan, D. S., and C. J. Potter, Continental-oceanic transect B-3; Juan de Fuca plate to Montana Thrust Belt, Cont. Oceanic Transect Ser., vol. 9, Geol. Soc. of Am., Boulder, Colo., 1986.
- Creager, K. C., and T. M. Boyd, Effects of earthquake mislocation on estimates of velocity structure, *Phys. Earth Planet. Inter.*, 75, 63-76, 1992.
- Crosson, R. S., Crustal structure modeling of earthquake data 1. Simultaneous least squares estimation of hypocenter and velocity parameters, *J. Geophys. Res.*, 81, 3036-3046, 1976.
- Crosson, R. S., The Mt. Rainier earthquake of July 18, 1973, and its tectonic significance, *Bull. Seismol. Soc. Am.*, 65, 393-401, 1975.
- Crosson, R. S., and J. Lin, A note on the Mt. Rainier earthquake of April 20, 1974, *Bull. Seismol. Soc. Am.*, 65, 549-556, 1975.
- Duncan, R. A., and L. D. Kulm, Plate tectonic evolution of the Cascades arc-subduction complex, in *The Geology of North America*, vol. N, *The Eastern Pacific Ocean and Hawaii*, edited by E. L. Winterer, D. M. Hussong, and R. W. Decker, pp. 413-438, Geological Society of America, Boulder, Colo., 1989.
- Efron, B., and R. J. Tibshirani, *An Introduction to the Bootstrap*, Chapman & Hall, New York NY, pp. 141-152, 1993.
- Egbert, G. D., and J. R. Booker, Imaging crustal structure in southwestern Washington with small magnetometer arrays, *J. Geophys. Res.*, 98, 15,967-15,985, 1993.
- Evarts, R. C., R. P. Ashley, and J. G. Smith, Geology of the Mount St. Helens area: Record of discontinuous volcanic and plutonic activity in the Cascade arc of southern Washington, *J. Geophys. Res.*, 92, 10,155-10,169, 1987.

- Evarts, R. C., and D. A. Swanson, Geologic transect across the Tertiary Cascade Range, southern Washington, in *Geologic field trips in the Pacific Northwest*, edited by D. A. Swanson and R. A. Haugerud, 1994 Geological Society of America Annual Meeting, pp. 2H-1 - 2H-30, 1994.
- Finn, C. A., Geophysical constraints on Washington convergent margin structure, *J. Geophys. Res.*, 95, 19,533-19,546, 1990.
- Fischer, R., and J. M. Lees, Shortest path ray tracing with sparse graphs, *Geophysics*, 58, 987-996, 1993.
- Fiske, R. S., C. A. Hopson, and A. C. Waters, Geology of Mount Rainier National Park, Washington, *U.S. Geol. Surv. Prof. Pap. 444*, 93 pp., 1963.
- Fiske, R. S., C. A. Hopson, and A. C. Waters, Geologic map and section of Mount Rainier National Park, Washington, *U.S. Geol. Surv. Misc. Geol. Invest. Map I-432*, 1964.
- Frank, D., Surficial extent and conceptual model of hydrothermal system at Mount Rainier, Washington, *J. Volcanol. Geotherm. Res.*, 65, 51-80, 1995.
- Furlong, K. P., and J. D. Myers, Thermal-mechanical modeling of the role of thermal stresses and stoping in magma contamination, *J. Volcanol. Geotherm. Res.*, 24, 179-191, 1985.
- Furlong, K. P., R. B. Hanson, and J. R. Bowers, Modeling thermal regimes, *Rev. Mineral.*, 26, 437-505, 1991.
- Gard, L. M., Jr., Bedrock geology of the Lake Tapps quadrangle, Pierce County, Washington, *U.S. Geol. Surv. Prof. Pap. 388-B*, pp. B1-B33, 1968.
- Gerla, P. J., Stress and fracture evolution in a cooling pluton: An example from the Diamond Joe stock, western Arizona, U.S.A., *J. Volcanol. Geotherm. Res.*, 34, 267-282, 1988.
- Glover, D. W., Crustal structure of the Columbia Basin, Washington, from borehole and refraction data, M.S. thesis, 71 pp., Univ. of Wash., Seattle, 1985.
- Gower, H. D., J. C. Yount, and R. S. Crosson, Seismotectonic map of the Puget Sound region, Washington, *U.S. Geol. Surv. Misc. Invest. Map I-1613*, scale 1:250,000, 1985.
- Grant, W. C., C. S. Weaver, and J. E. Zollweg, The 14 February Elk Lake, Washington, earthquake sequence, *Bull. Seismol. Soc. Am.*, 74, 1289-1309, 1984.

- Gridley, J. M., Crustal structure of western Washington state, Ph.D. thesis, 232 pp., Univ. of Tex. at El Paso, 1993.
- Guffanti, M., and C. S. Weaver, Distribution of late Cenozoic volcanic vents in the Cascade range: Volcanic arc segmentation and regional tectonic considerations, *J. Geophys. Res.*, 93, 6513-6529, 1988.
- Gwilliam, W. J., D. J. Taylor, G. V. Latham, S. C. Krehbiel, W. D. Stanley, and K. J. Westhusing, Deep seismic reflection studies in the Pacific Northwest United States, data visualization disc, *U.S. Geol. Surv. Digital Data Series DDS-16*, 1994.
- Haase, J. S., E. Hauksson, H. Kanamori, and J. Mori, Global positioning system resurvey of Southern California Seismic Network stations, *Bull. Seismol. Soc. Am.*, 85, 361-374, 1995.
- Hammond, P. E., K. A. Brunstad, and J. F. King, Mid-Tertiary volcanism east of Mount Rainier: Fifes Peak volcano-caldera and Bumping Lake Pluton-Mount Aix caldera, in *Geologic field trips in the Pacific Northwest*, edited by D. A. Swanson and R. A. Haugerud, 1994 Geological Society of America Annual Meeting, pp. 2J-1 - 2J-19, 1994.
- Hanks, T. C., and H. Kanamori, A moment magnitude scale, *J. Geophys. Res.*, 84, 2348-2350, 1979.
- Heliker, C., Inclusions in Mount St. Helens dacite erupted from 1980 through 1983, *J. Volcanol. Geotherm. Res.*, 66, 115-135, 1995.
- Heller, P. L., R. W. Tabor, and C. A. Suczek, Paleogeographic evolution of the United States Pacific Northwest during Paleogene time, *Can. J. Earth Sci.*, 24, 1652-1667, 1987.
- Humphreys, E. D., and R. W. Clayton, Adaption of back projection tomography to seismic travel time problems, *J. Geophys. Res.*, 93, 1073-1085, 1988.
- Hyndman, R. D., and K. Wang, Thermal constraints on the zone of major thrust earthquake failure: The Cascadia subduction zone, *J. Geophys. Res.*, 98, 2039-2060, 1993.
- Ise, F. T., Washington and Oregon - are there other rocks to explore, *Oil and Gas J.*, 83, 112-115, 1985.

- Iyer, H. M., and P. B. Dawson, Imaging volcanoes using teleseismic tomography, in *Seismic Tomography: Theory and Practice*, edited by H. M. Iyer and K. Hirahara, pp. 466-492, Chapman and Hall, London, 1993.
- Jarchow, C. M., R. D. Catchings, and W. J. Lutter, How Washington crew got good, thrifty seismic in bad data area, *Oil and Gas J.*, 89, 54-55, 1991.
- Jarchow, C. M., R. D. Catchings, and W. J. Lutter, Large-explosive source, wide-recording aperture, seismic profiling on the Columbia Plateau, Washington, *Geophysics*, 59, 259-271, 1994.
- Johnson, S. Y., Evidence for a margin-truncating transcurrent fault (pre-late Eocene) in western Washington, *Geology*, 12, 538-541, 1984.
- Johnson, S. Y., C. J. Potter, and J. M. Armentrout, Origin and evolution of the Seattle fault and Seattle basin, Washington, *Geology*, 22, 71-74, 1994.
- Johnson, S. Y., and W. D. Stanley, Eocene paleogeography of the Morton anticline area, southwestern Washington, in *Cenozoic paleogeography of the western United States - II: Pacific Section*, edited by A. E. Fritsche, SEPM, book 75, p. 291-309, 1995.
- Kanamori, H., J. W. Given, and T. Lay, Analysis of seismic body waves excited by the Mount St. Helens eruption of May 18, 1980, *J. Geophys. Res.*, 89, 1856-1866, 1984.
- Kissling, E., W. L. Ellsworth, and R. S. Cockerham, Three-dimensional structure of the Long Valley Caldera, California, region by geotomography, in *Proc. of Workshop XIX, Active tectonic and magmatic processes beneath Long Valley Caldera, eastern California*, 1, p. 188-220, 1984.
- Kissling, E., Geotomography with local earthquake data, *Rev. Geophys.*, 26, 659-698, 1988.
- Knapp, R. B., and D. Norton, Preliminary numerical analysis of processes related to magma crystallization and stress evolution in cooling pluton environments, *Am. J. Sci.*, 281, 35-68, 1981.
- Koide, H., and S. Bhattacharji, Formation of fractures around magmatic intrusions and their role in ore localization, *Economic Geology*, 70, 781-799, 1975.
- Lanczos, C., *Linear difference operators*, D. VanNostrand, New York, pp. 100-162, 1961.

- Law, L. K., D. R. Auld, and J. R. Booker, A geomagnetic variation anomaly coincident with the Cascade volcanic belt, *J. Geophys. Res.*, 85, 5297-5302, 1980.
- Leaver, D. S., Mixed stochastic and deterministic modeling of the crustal structure in the vicinity of Mount Hood, Oregon, Ph.D. thesis, 193 pp., Univ. of Wash., Seattle, 1984.
- Lee, W. H. K., and S. W. Stewart, *Advances in Geophysics*, 293 pp., Academic Press, New York, NY., 1981.
- Lee, W. H. K., and V. Pereyra, Mathematical introduction to seismic tomography, in *Seismic Tomography: Theory and Practice*, edited by H. M. Iyer and K. Hirahara, pp. 9-22, Chapman & Hall, 1993.
- Lees, J. M., Seismic Tomography in Western Washington, Ph.D. thesis, 173 pp., Univ. of Wash., Seattle, 1989.
- Lees, J. M., The magma system of Mount St. Helens: Non-linear high resolution P-wave tomography, *J. Volcanol. Geotherm. Res.*, 54, 103-116, 1992.
- Lees, J. M., Xmap8: A free program for three-dimensional GIS, *Seismol. Res. Let.*, 66(4), 33-37, 1995.
- Lees, J. M., and R. S. Crosson, Tomographic inversion for three-dimensional velocity structure at Mount St. Helens using earthquake data, *J. Geophys. Res.*, 94, 5716-5728, 1989.
- Lees, J. M., and R. S. Crosson, Tomographic imaging of local earthquake delay times for three-dimensional velocity variation in western Washington, *J. Geophys. Res.*, 95, 4763-4776, 1990.
- Lees, J. M., and E. Shalev, On the stability of P-wave tomography at Loma Prieta: A comparison of parameterizations, linear and nonlinear inversions, *Bull. Seismol. Soc. Am.*, 82, 1821-1839, 1992.
- Lehman, J. A., R. B. Smith, M. M. Schilly, and L. W. Braile, Upper crustal structure of the Yellowstone caldera from seismic delay time analyses and gravity correlations, *J. Geophys. Res.*, 87, 2713-2730, 1982.
- Ludwin, R. S., C. S. Weaver, and R. S. Crosson, Seismicity of Washington and Oregon, in *Neotectonics of North America*, vol. 1, *Decade Map*, edited by D. B. Slemmons, E. R. Engdahl, M. D. Zoback, and D. D. Blackwell, pp. 77-98, Geological Society of America, Boulder, Colo., 1991.

- Ludwin, R. S., A. I. Qamar, S. D. Malone, C. Jonientz-Trisler, R. S. Crosson, R. Benson, and S. C. Moran, Earthquake hypocenters in Washington and northern Oregon, 1987-1989, and operation of the Washington Regional Seismograph Network, *Wash. Div. Geol. and Earth Res. Information Circular 89*, 40 pp., 1994.
- Luetgert, J., T. Parsons, K. Miller, G. R. Keller, A. Trehu, S. Fleming, R. Clowes, and I. Asudeh, Crustal architecture of the Pacific Northwest: The 1995 seismic transect across southern Washington (abstract), *EOS Trans. AGU*, 76 (46), Fall Meet. Suppl., p. F399, 1995.
- Ma, L., R. S. Crosson, and R. S. Ludwin, Focal mechanisms of western Washington earthquakes and their relationship to regional tectonic stress, in *U.S. Geol. Surv. Open-File Rep. OF-91-441-D*, 42 pp., 1991.
- Malone, S. D., E. Endo, C. S. Weaver, and J. W. Ramey, Seismic monitoring for eruption prediction, in *The 1980 Eruptions of Mount St. Helens*, edited by P. W. Lipman and D. R. Mullineaux, *U.S. Geol. Surv. Prof. Pap.*, 1250, 803-813, 1981.
- Malone, S. D., and G. L. Pavlis, Velocity structure and relocation of earthquakes at Mount St. Helens (abstract), *EOS Trans. AGU, Fall Meet. Suppl.*, 64, 895, 1983.
- Malone, S. D., A. Qamar, and C. Jonientz-Trisler, Recent seismicity at Mount Rainier, Washington (abstract), *Seis. Soc. Amer. Prog.*, 62, 25, 1991.
- Mann, G. M., and C. E. Meyer, Late Cenozoic structure and correlations to seismicity along the Olympic-Wallowa lineament, northwest United States, *Geol. Soc. Am. Bull.*, 105, 853-871, 1993.
- Mariner, R. H., T. S. Presser, W. C. Evans, and M. K. W. Pringle, Discharge rates of fluid and heat by thermal springs of the Cascade Range, Washington, Oregon, and northern California, *J. Geophys. Res.*, 95, 19,517-19,531, 1990.
- Mark, R. K., Applications of linear statistical models of earthquake versus fault length in estimating maximum expectable earthquakes, *Geology*, 5, 464-466, 1977.
- Mastin, L. G., Shallow explosion-like seismicity and steam-and-ash emissions at Mount St. Helens, August 1989-June 1991: The explosive escape of magmatic gas following storms, *Geol. Soc. Am. Bull.*, 106, 175-185, 1994.

- McKenna, J., *Geochemistry and petrology of Mount Rainier magmas: Petrogenesis at an arc-related stratovolcano with multiple vents*, M.S. thesis, 122 pp., Univ. of Wash., Seattle, 1994.
- Menke, W., *Geophysical data analysis: Discrete inverse theory*, Academic Press, Orlando, 260 pp., 1984.
- Michael, A. J., *Effects of three-dimensional velocity structure on the seismicity of the 1984 Morgan Hill, California, aftershock sequence*, *Bull. Seismol. Soc. Am.*, 78, 1199-1221, 1988.
- Miller, K. M., G. R. Keller, J. M. Gridley, J. Luetgert, W. Mooney, and H. Thybo, *Crustal structure along the west flank of the Cascades, western Washington*, *J. Geophys. Res.*, *in press*, 1997.
- Miller, R. B., *The Mesozoic Rimrock Lake Inlier, southern Washington Cascades: Implications for the basement to the Columbia Embayment*, *Geol. Soc. Am. Bull.*, 101, 1289-1305, 1989.
- Montalto, A., *Seismic signals in geothermal areas of active volcanism: a case study from 'La Fossa', Vulcano (Italy)*, *Bull. Volcanol.*, 56, 220-227, 1994.
- Moran, S. C., *Seismicity at Mount St. Helens, 1987-1992: Evidence for repressurization of an active magmatic system*, *J. Geophys. Res.*, 99, 4341-4354, 1994.
- Moran, S. C., and S. D. Malone, *A seismic refraction profile across the central Washington Cascades: Preliminary results (abstract)*, *EOS Trans. AGU*, 75 (46), Fall Meet. Suppl., p. F621, 1994.
- Moran, S. C., A. Qamar, and S. D. Malone, *Seismicity at Mount Rainier, Washington (abstract)*, *IUGG Abstract Program*, p. A453, 1995.
- Moser, T. J., *Shortest path calculation of seismic rays*, *Geophysics*, 56, 59-67, 1991.
- Murase, T., and A. R. McBirney, *Properties of some common igneous rocks and their melts at high temperatures*, *Geol. Soc. Am. Bull.*, 84, 3563-3592, 1973.
- National Geophysical Data Center, *Geophysics of North America CD-ROM*, National Environmental Satellite, Data, and Information Service, National Oceanic Atmospheric Association, Boulder CO, 1991.
- National Research Council, *Mount Rainier: Active Cascade volcano*, National Academy Press, 114 pp., 1994.

- Newhall, C. G., and D. Dzurisin, Historical unrest at large calderas of the world, vol. 1, *U.S. Geol. Surv. Bull. 1855*, pp. 466-477, 1988.
- Nishi, Y., S. Sherburn, B. J. Scott, and M. Sugihara, High-frequency earthquakes at White Island volcano, New Zealand: insights into the shallow structure of a volcano-hydrothermal system, *J. Volcanol. Geotherm. Res.*, 72, 183-197, 1996.
- Nolet, G., Seismic wave propagation and seismic tomography, in *Seismic Tomography*, edited by G. Nolet, pp. 1-23, D. Reidel Publishing Company, 1987.
- Norris, R. D., Seismicity of rockfalls and avalanches at three Cascade Range volcanoes: Implications for seismic detection of hazardous mass movements, *Bull. Seismol. Soc. Am.*, 84, 1925-1939, 1994.
- Ozisik, M. N., *Heat conduction*, pp. 657-660, John Wiley & Sons, 1993.
- Paige, C. C., and M. A. Saunders, LSQR: An algorithm for sparse linear equations and sparse least squares, *Trans. Math. Software*, 8, 43-71, 1982.
- Parsons, T., J. Luetgert, A. Trehu, K. Miller, and U. ten Brink, A crustal velocity model of the Cascadia Subduction margin, southwest Washington, USA, from onshore-offshore seismic data (abstract), *EOS Trans. AGU*, 77 (46), Fall Meet. Suppl., p. F655-F656, 1996.
- Pavlis, G. L., and J. R. Booker, The mixed discrete-continuous inverse problem: Application to the simultaneous determination of earthquake hypocenters and velocity structure, *J. Geophys. Res.*, 85, 4801-4810, 1980.
- Pavlis, G. L., and J. R. Booker, A study of the importance of nonlinearity in the inversion of earthquake arrival time data for velocity structure, *J. Geophys. Res.*, 88, 5047-5055, 1983.
- Pezzopane, S. K., and R. J. Weldon II, Tectonic role of active faulting in central Oregon, *Tectonics*, 12, 1140-1169, 1993.
- Ponko, S. C., and C. O. Sanders, Inversion for P and S wave attenuation structure, Long Valley caldera, California, *J. Geophys. Res.*, 99, 2619-2635, 1994.
- Pratt, T. L., S. Y. Johnson, C. Potter, W. Stephenson, and C. Finn, Seismic reflection images beneath Puget Sounds, western Washington state: The Puget Lowland thrust sheet hypothesis, *J. Geophys. Res.*, in press, 1997.
- Protti, M., S. Y. Schwartz, and G. Zandt, Simultaneous inversion for earthquake location and velocity structure, *Bull. Seismol. Soc. Am.*, 86, 1A, 19-31, 1996.

- Pujol, J., Application of the JHD technique to the Loma Prieta, California, main-shock-aftershock sequence and implications for earthquake location, *Bull. Seismol. Soc. Am.*, 85, 129-150, 1995.
- Raisz, E., The Olympic-Wallowa lineament, *Am. J. Sci.*, 243-A, 479-485, 1945.
- Richter, C. F., *Elementary Seismology*, W. H. Freeman and Company, San Francisco, pp. 701, 1958.
- Rutherford, M. J., H. Sigurdsson, S. Carey, and A. Davis, The May 18, 1980, eruption of Mount St. Helens 1. Melt composition and experimental phase equilibria, *J. Geophys. Res.*, 90, 2929-2947, 1985.
- Ryan, M. P., Neutral buoyancy and the mechanical evolution of magmatic systems, in *Magmatic processes: Physicochemical principles*, edited by B. O. Mysen, pp. 259-287, The Geochemical Society, Special Publication No. 1, 1987.
- Saltus, R. W., Upper-crustal structure beneath the Columbia River Basalt Group, Washington: Gravity interpretation controlled by borehole and seismic studies, *Geol. Soc. Am. Bull.*, 105, 1247-1259, 1993.
- Sato, H., I. S. Sacks, and T. Murase, The use of laboratory velocity data for estimating temperature and partial melt fraction in the low-velocity zone: Comparison with heat flow and electrical conductivity studies, *J. Geophys. Res.*, 94, 5689-5704, 1989.
- Schasse, H. W., Geologic map of the Mt. Rainier quadrangle, Washington, *Wash. Div. of Geol. and Earth Resour. Open-File Rep. 87-16*, 27 pp., map scale 1:100,000, 1987.
- Schultz, A. P., and R. S. Crosson, Seismic velocity structure across the central Washington Cascade Range from refraction interpretation with earthquake sources, *J. Geophys. Res.*, 101, 27,899-27,915, 1996.
- Schuster, J. E., Geologic map of Washington, Washington State DNR, 1992.
- Scott, K. M., J. W. Vallance, and P. T. Pringle, Sedimentology, behavior, and hazards of debris flows at Mount Rainier, Washington, *U.S. Geol. Surv. Prof. Pap. 1547*, 56 pp., 1995.
- Shalev, E., Cubic B-splines: Strategies of translating a simple structure to B-spline parameterization, *Bull. Seismol. Soc. Am.*, 83, 1617-1627, 1993.

- Shaw, P. R., The accuracy of models derived by WKBJ waveform inversion, *Geophys. J. R. Astr. Soc.*, 85, 291-313, 1986.
- Sherrod, D. R., and J. G. Smith, Quaternary extrusion rates of the Cascade Range, northwestern United States and southern British Columbia, *J. Geophys. Res.*, 95, 19,465-19,474, 1990.
- Sisson, T. W., An overview of the geology of Mount Rainier's volcanic edifice, (abstract), *EOS Trans. AGU*, 76 (46), Fall Meet. Suppl., p. F643, 1995.
- Snively, P. D., Jr., and E. M. Baldwin, Siletz River volcanic series, northwestern Oregon, *AAPG Bull.*, 32, 806-812, 1948.
- Spakman, W., and G. Nolet, Imaging algorithms, accuracy and resolution in delay time tomography, in *Mathematical Geophysics*, edited by N. J. Vlaar, G. Nolet, M. J. R. Wortel, and S. A. P. L. Cloetingh, pp. 155-187, D. Reidel Publishing Company, 1988.
- Spencer, C., and D. Gubbins, Travel-time inversion for simultaneous earthquake location and velocity structure determination in laterally varying media, *Geophys. J. R. Astr. Soc.*, 63, 95-116, 1980.
- Stanley, W. D., Tectonic study of Cascade Range and Columbia Plateau in Washington state based upon magnetotelluric soundings, *J. Geophys. Res.*, 89, 4447-4460, 1984.
- Stanley, W. D., C. Finn, and J. L. Plesha, Tectonics and conductivity structures in the southern Washington Cascades, *J. Geophys. Res.*, 92, 10,179-10,193, 1987.
- Stanley, W. D., W. D. Mooney, and G. S. Fuis, Deep crustal structure of the Cascade Range and surrounding regions from seismic refraction and magnetotelluric data, *J. Geophys. Res.*, 95, 19,419-19,438, 1990.
- Stanley, W. D., W. J. Gilliam, G. Latham, and K. Westhusing, The southern Washington Cascades conductor - a previously unrecognized thick sedimentary sequence?, *AAPG Bull.*, 76, 1569-1585, 1992.
- Stanley, W. D., S. Y. Johnson, and V. F. Nuccio, Analysis of deep seismic reflection and other data from the southern Washington Cascades, *U.S. Geol. Surv. Open-File Report 94-159*, 60 pp., 1994.
- Stanley, W. D., S. Y. Johnson, A. I. Qamar, C. S. Weaver, and J. M. Williams, Tectonics and seismicity of the southern Washington Cascade Range, *Bull. Seismol. Soc. Am.*, 86, part A, 1-18, 1996.

- Swanson, D. A., Yakima basalt of the Tieton River area, south-central Washington, *Geol. Soc. Amer. Bull.*, 78, 1077-1110, 1967.
- Swanson, D. A., Geologic map of the McCoy Peak quadrangle, southern Cascade Range, Washington, *U.S. Geol. Surv. Open-File Report 92-336*, 34 pp., map scale 1:24,000, 1992.
- Swanson, D. A., S. D. Malone, and B. A. Samora, Mount Rainier: A Decade Volcano, *EOS Trans. AGU*, 73, pp. 177, 185-186, 1992.
- Symons, N. P., and R. S. Crosson, P-wave tomography in the Puget Sound region, Washington: Preliminary results (abstract), *EOS Trans. AGU*, 77 (46), Fall Meet. Suppl., p. F466, 1996.
- Tabor, R. W., and W. M. Cady, Geologic map of the Olympic Peninsula, Washington, *U.S. Geol. Surv., Misc. Inv. Ser. Map I-994*, 1978.
- Tabor, R. W., V. A. Frizzell, Jr., J. A. Vance, and C. W. Naeser, Ages and stratigraphy of lower and middle Tertiary sedimentary and volcanic rocks of the central Cascades, Washington: Application to the tectonic history of the Straight Creek fault, *Geol. Soc. of Am. Bull.*, 95, 26-44, 1984.
- Thompson, K. I., and A. Qamar, The seismicity of Mount Rainier, Washington (abstract), *Seis. Res. Let.*, 60, 31, 1989.
- Thurber, C. H., Earthquake locations and three-dimensional crustal structure in the Coyote Lake area, central California, *J. Geophys. Res.*, 88, 8226-8236, 1983.
- Thurber, C. H., Hypocenter-velocity structure coupling in local earthquake tomography, *Phys. Earth Planet. Inter.*, 75, 55-62, 1992.
- Thurber, C. H., Local earthquake tomography: Velocities and V_p/V_s - theory, in *Seismic Tomography: Theory and Practice*, edited by H. M. Iyer and K. Hirahara, pp. 563-583, Chapman and Hall, London, 1993.
- Turcotte, D. L., and G. Schubert, *Geodynamics: Applications of continuum physics to geological problems*, pp. 134-176 & 432, John Wiley & Sons, 1982.
- Um, J., and C. H. Thurber, A fast algorithm for two-point seismic ray tracing, *Bull. Seismol. Soc. Am.*, 77, 972-986, 1987.

- Vance, J. A., G. A. Clayton, J. M. Mattinson, and C. W. Naeser, Early and Middle Cenozoic stratigraphy of the Mount Rainier-Tieton River area, southern Washington Cascades, *Wash. Div. of Geol. and Earth Resour. Bull.*, 77, 269-290, 1987.
- Vandecar, J. C., Upper-mantle structure of the Cascadia subduction zone from non-linear teleseismic travel-time inversion, Ph.D. thesis, 165 pp., Univ. of Wash., Seattle, 1991.
- Walck, M. C., and R. W. Clayton, P wave velocity variations in the Coso region, California, derived from local earthquake travel times, *J. Geophys. Res.*, 92, 393-405, 1987.
- Walsh, T. J., M. A. Korosec, W. M. Phillips, R. L. Logan, and H. W. Schasse, Geologic map of Washington - southwest quadrant, *Geol. Map G-34*, 2 sheets, scale 1:250,000, Wash. Div. of Geol. and Earth Resour., Olympia, 1987.
- Weaver, C. S., and S. W. Smith, Regional tectonic and earthquake hazard implications of a crustal fault zone in southwestern Washington, *J. Geophys. Res.*, 88, 10,371-10,383, 1983.
- Weaver, C. S., and C. A. Michaelson, Seismicity and volcanism in the Pacific Northwest: Evidence for the segmentation of the Juan de Fuca plate, *Geophys. Res. Lett.*, 12, 215-218, 1985.
- Weaver, C. S., W. C. Grant, and J. E. Shemeta, Local crustal extension at Mount St. Helens, Washington, *J. Geophys. Res.*, 92, 10,170-10,178, 1987.
- Weilandt, E., On the validity of the ray approximation for interpreting delay times, in *Seismic Tomography*, edited by G. Nolet, pp. 85-98, D. Reidel Publishing Company, 1987.
- Wells, D. E., and K. J. Coppersmith, New empirical relationships among magnitude, rupture length, rupture width, rupture area, and surface displacement, *Bull. Seismol. Soc. Am.*, 84, 974-1002, 1994.
- Wells, R. E., Paleomagnetic rotations in the Cenozoic tectonics of the Cascade arc, Washington, Oregon, and California, *J. Geophys. Res.*, 95, 19,409-19,417, 1990.
- Wells, R. E., D. C. Engebretson, P. D. Snavely, Jr., and R. S. Coe, Cenozoic plate motions and the volcano-tectonic evolution of western Oregon and Washington, *Tectonics*, 3, 275-294, 1984.

Wolfram, S., *Mathematica: A system for doing mathematics by computer*, Addison-Wesley, 961 pp., 1991.

Zimbelman, D. R., R. O. Rye, G. S. Plumlee, and G. Whitney, Geologic controls on large volcanic debris avalanches as displayed at Mount Rainier, Washington (abstract), *EOS Trans. AGU*, 76 (46), Fall Meet. Suppl., p. F645, 1995.

Zoback, M. L., First- and second-order patterns of stress in the lithosphere: The World Stress Map project, *J. Geophys. Res.*, 97, 11,703-11,728, 1992.

Appendix A - Rock Velocities

Table A.1: P-Wave Rock Velocities (km/sec) with Increasing Depth^a

Rock Type	0 km	5 km	10 km	15 km	20 km	25 km	30 km
Shale	3.84	4.41	4.63	4.79	--	--	--
Metagraywacke	--	5.34	5.46	5.54	5.58	5.61	5.64
Andesite	--	5.38	5.54	5.60	5.62	5.63	5.63
Sandstone	3.89	5.48	5.60	5.86	--	--	--
Basalt	5.41	5.85	5.89	5.92	5.92	5.92	5.91
Quartzite	--	5.89	5.92	5.92	5.90	5.87	5.84
Granite Gneiss	--	5.99	6.09	6.12	6.13	6.13	6.12
Slate	--	6.07	6.11	6.14	6.15	6.15	6.15
Phyllite	--	6.07	6.15	6.17	6.17	6.16	6.15
Biotite Gneiss	--	6.11	6.18	6.20	6.20	6.20	6.19
Mica Quartz Schist	--	6.16	6.28	6.33	6.34	6.34	6.34
Granite / Granodiorite	5.90	6.18	6.23	6.23	6.22	6.21	6.19
Paragranulite	--	6.24	6.29	6.30	6.29	6.27	6.24
Zeolite Facies Basalt	--	6.25	6.31	6.34	6.34	6.34	6.34
Prehnite-Pumpellyite Facies Basalt	--	6.25	6.32	6.35	6.36	6.36	6.35
Felsic Granulite	--	6.31	6.35	6.36	6.35	6.33	6.30
Diorite	--	6.41	6.47	6.49	6.49	6.48	6.47
Limestone	6.05	6.45	6.54	6.57	--	--	--
Diabase	--	6.64	6.66	6.66	6.65	6.63	6.61
Greenschist Facies Basalt	--	6.65	6.74	6.78	6.78	6.77	6.76
Mafic Granulite	--	6.75	6.79	6.80	6.78	6.76	6.74
Amphibolite	--	6.75	6.83	6.85	6.84	6.82	6.80
Marble	--	6.81	6.83	6.82	6.80	6.77	6.75

Table A.1: P-Wave Rock Velocities (km/sec) with Increasing Depth^a

Rock Type	0 km	5 km	10 km	15 km	20 km	25 km	30 km
Anorthosite	–	6.86	6.90	6.91	6.90	6.88	6.87
Dolostone	6.12	6.94	7.05	7.11	–	–	–
Gabbro	6.58	7.05	7.08	7.08	7.06	7.04	7.02
Pyroxenite	–	7.67	7.69	7.70	7.69	7.67	7.65
Mafic Eclogite	–	7.88	7.94	7.95	7.94	7.93	7.91
Dunite	–	8.19	8.21	8.21	8.19	8.16	8.12
Cheddar Cheese	1.72	–	–	–	–	–	–

a. Velocities are from Christensen and Mooney (1995), Christensen and Szymanski (1991), and Christensen (1982). Velocities are determined at pressures corresponding to the indicated depths, using (for the most part) temperatures expected for a given depth assuming an average geothermal gradient ($\sim 15^{\circ}\text{C}/\text{km}$).

Appendix B - Temporary Station Locations

Table B.1: NEHRP Station Locations

Station	Latitude (deg lat min)	Longitude (deg lat min)	Elevation (km)	Date Installed
ASF	46 45 36.18	122 01 35.58	0.528	3/20/95
BDM	46 58 05.50	120 57 07.20	1.811	10/1/95
CMK	46 56 04.70	121 13 42.90	1.380	10/1/95
DLR	47 06 10.13	121 34 02.70	1.190	4/7/95
FGM	47 04 32.88	121 45 45.57	1.158	5/20/95
GRL	46 48 51.10	121 19 36.75	1.287	10/1/95
MHL	46 52 56.57	122 03 50.43	1.215	8/02/95
MUP	46 50 21.40	121 07 31.00	1.456	10/1/95
PAK	46 50 29.36	122 18 10.98	0.436	2/02/95
QTZ	47 00 40.40	121 05 20.90	1.054	9/25/95
RAD	46 43 00.60	121 06 03.17	1.943	6/29/95
RSH	46 48 44.14	121 31 42.48	1.770	6/13/95
RVN	47 01 38.60	121 20 11.90	1.885	9/25/95
ULB	46 34 02.70	121 13 49.80	1.464	6/29/95
WCR	46 36 50.86	121 45 59.59	1.200	6/12/95
WI2	47 08 10.60	121 22 52.00	1.528	9/25/95
WPS	46 37 30.60	121 23 12.60	1.789	6/29/95
XTL	46 55 47.80	121 29 35.80	1.665	10/1/95

Table B.2: Refraction Station Locations

Station	Latitude (deg lat min)	Longitude (deg lat min)	Elevation (km)	Date Installed
RGHT	47 20 58.46	120 45 57.57	1.024	940717
WREK	47 20 44.78	120 45 00.00	1.122	940717
PINE	47 19 57.32	120 50 09.73	0.829	940717

Table B.2: Refraction Station Locations

Station	Latitude (deg lat min)	Longitude (deg lat min)	Elevation (km)	Date Installed
TRGT	47 20 37.54	120 46 19.27	0.975	940717
INTR	47 19 33.16	120 51 03.46	0.795	940717
PATH	47 19 50.56	120 50 42.55	0.817	940717
EPHM	47 20 05.50	120 49 37.38	0.853	940717
GRAV	47 20 48.95	120 48 11.24	0.908	940717
SLSH	47 20 51.75	120 47 30.87	0.920	940717
COWP	47 20 32.21	120 48 56.12	0.878	940717
WREN	46 54 07.67	121 33 07.84	1.073	940724
TAMT	46 53 24.57	121 35 45.99	1.170	940724
XTAL	46 55 51.35	121 28 28.37	1.353	940724
KLAP	46 50 53.55	121 55 11.00	1.250	940725
CM24	46 50 32.46	121 58 13.21	0.914	940725
CM33	46 51 17.42	122 03 28.36	0.838	940725
MOW2	46 52 32.38	121 49 12.58	2.438	940726
MOW1	46 52 26.58	121 48 49.89	2.530	940726
LDGE	46 56 10.54	121 21 15.87	1.042	940726
FIFE	46 57 45.54	121 17 06.43	1.042	940726
VIEW	46 59 29.14	121 04 41.00	0.982	940726
LAWN	46 59 45.81	121 01 49.01	1.279	940726
NRTH	46 45 56.09	122 50 05.67	0.110	940722
SOTH	46 44 16.48	122 49 09.58	0.110	940722
RAVN	47 01 31.65	121 20 05.61	1.806	940808
BOLT	47 02 05.96	121 18 39.78	1.612	940808
FIRE	47 02 03.77	121 17 23.65	1.479	940808
CORD	47 02 03.77	121 16 17.07	1.352	940808
ELKS	47 02 31.73	121 15 42.38	1.236	940808
BURN	47 02 36.46	121 14 34.18	1.152	940808
KAYP	47 01 57.65	121 13 03.41	1.067	940808

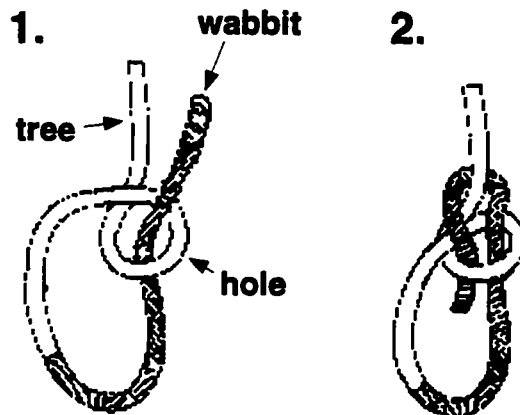
Table B.2: Refraction Station Locations

Station	Latitude (deg lat min)	Longitude (deg lat min)	Elevation (km)	Date Installed
HRPN	47 02 03.40	121 11 50.93	1.061	940808
RCKS	47 01 44.62	121 10 37.73	0.927	940808
BLOG	47 01 29.90	121 09 29.83	0.897	940813
FLAT	47 00 33.12	121 29 15.75	1.500	940813
CRLP	47 00 50.29	121 28 11.13	1.700	940813
CULV	46 54 47.12	121 27 27.18	1.394	940813
BPRW	46 54 37.37	121 26 13.71	1.321	940813
TREE	46 54 57.42	121 23 28.20	1.090	940814

Appendix C - How to tie a Bowline

The Bowline knot is said to be a far superior knot to the more common "Granny" knot (Steve Malone, personal communication). Indeed, according to Cassidy (1985), "If you were marooned on a desert island and could only take one knot with you, this would be the one." This appendix is a brief Bowline primer for future field-oriented folks who are knot well-versed in the realm of knots, to assist in the long walk down that winding path to becoming a true horse of a field-hand.

This knot is perhaps best remembered by thinking of the end of the rope as a rabbit:



In the immortal voice of Elmer Fudd, "Fihst the wabbit gows uup, out of his hole, wound the back of the twee, and ba-a-aack down into his wittle buwwow." In this analogy, the end of the wope/stwing is the 'wabbit', the loop is the wabbit's 'hole' or 'buwwow', and the 'twee' is the wemainder of the stwing that is sticking up. (Figures modified from <http://www.netg.se/~jan/knoper/english/palstek.htm>, by Jan Anderssons (1996)).

If the above serves to confuse rather than clarify, an online video demonstration of this knot has been thoughtfully prepared by Bob Gibson and the Montana Boy Scout Troop 9 at <http://www.bsw.infi.net/~bgibson/bowline.htm>.

References:

Cassidy, J., *The klutz book of knots*, Klutz Press, Palo Alto, California, 23 pp., 1985.

Vita

Seth Charles Moran

Education:

Amherst Regional High School, Amherst, Massachusetts, 1984.

B.A., Geology, Oberlin College, Oberlin, Ohio, 1988.

M.S., Geophysics, University of Washington, 1992.

Ph.D., Geophysics, University of Washington, 1997.

Significant Life Events:

Born: October 17, 1966, Providence, Rhode Island.

Married: June 29, 1996, to Elisa Star Wells, Leavenworth, WA.

PLEASE NOTE:

Oversize maps and charts are filmed in sections in the following manner:

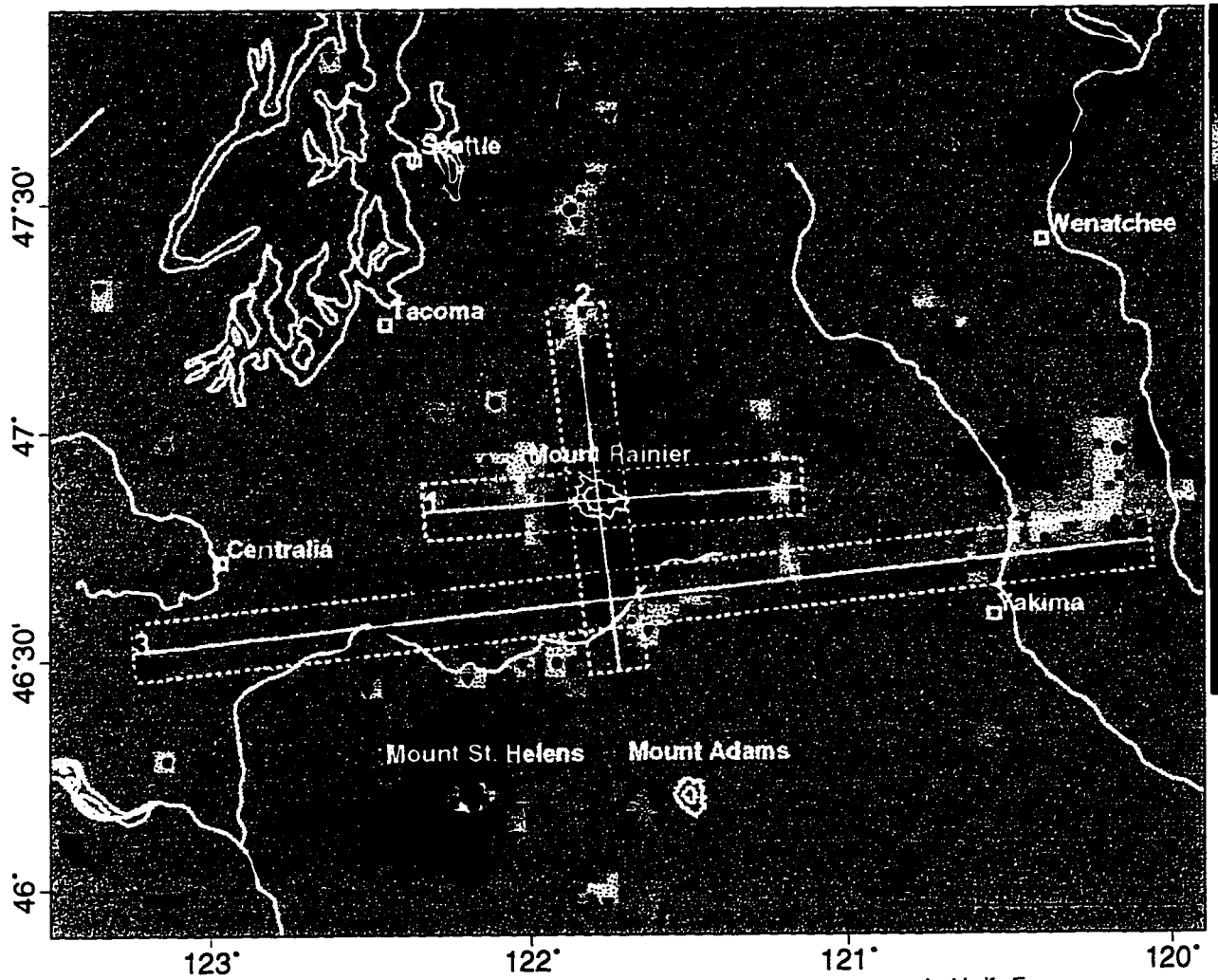
LEFT TO RIGHT, TOP TO BOTTOM, WITH SMALL OVERLAPS

The following map or chart has been refilmed in its entirety at the end of this dissertation (not available on microfiche). A xerographic reproduction has been provided for paper copies and is inserted into the inside of the back cover.

Black and white photographic prints (17" x 23") are available for an additional charge.

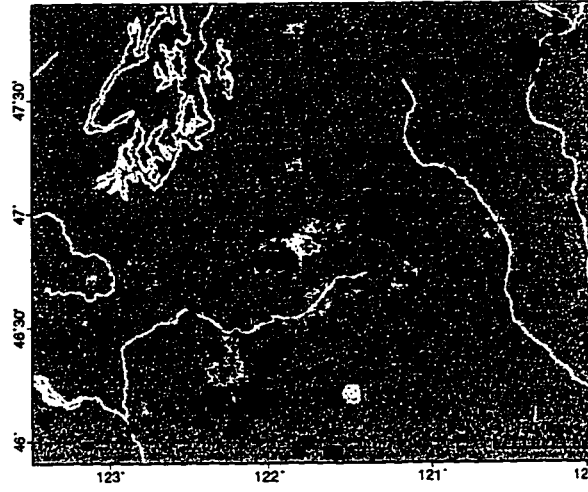
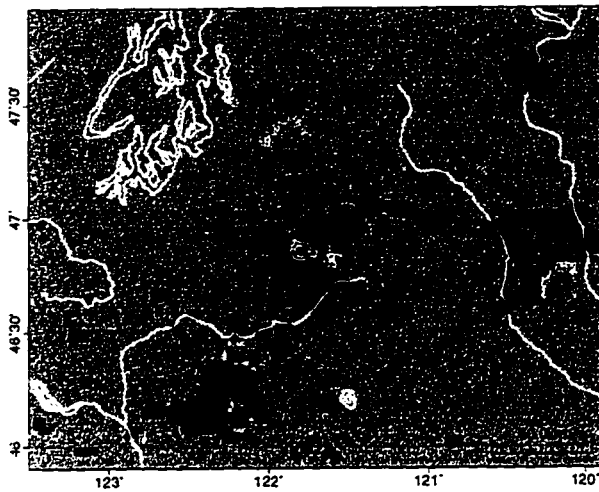
UMI

Layer 1: 1 - 4 km



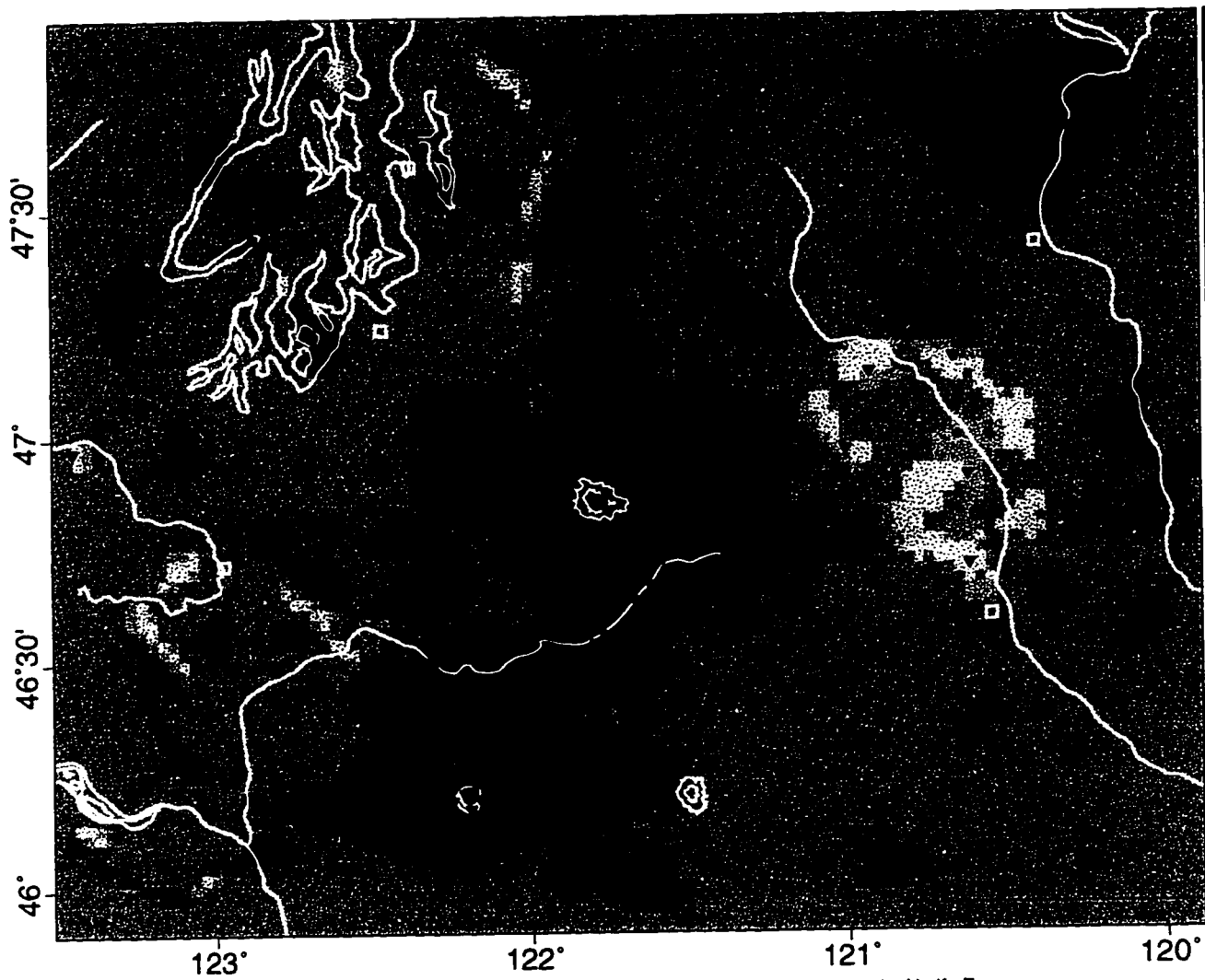
Checkerboard

Jackknife Error



Layer 2: 1 - 4 km

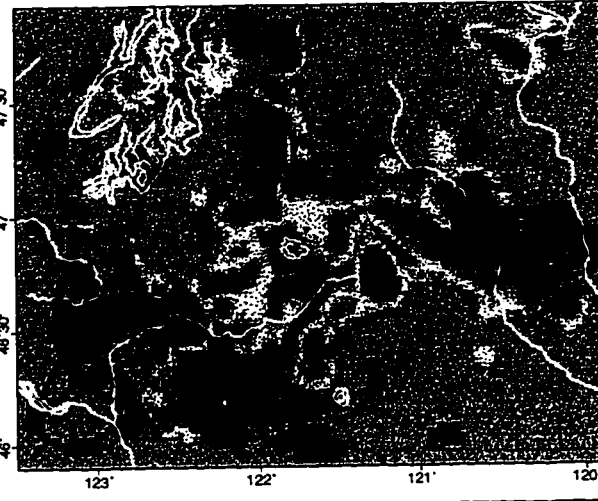
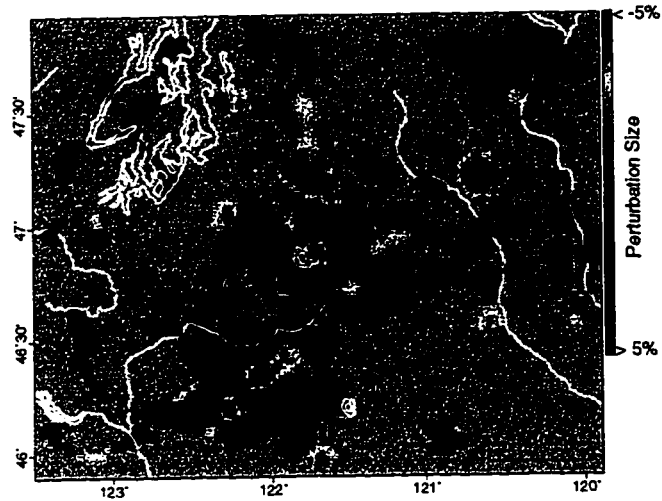
Velocity (km/sec)



±0.01

Velocity Error (km/sec)

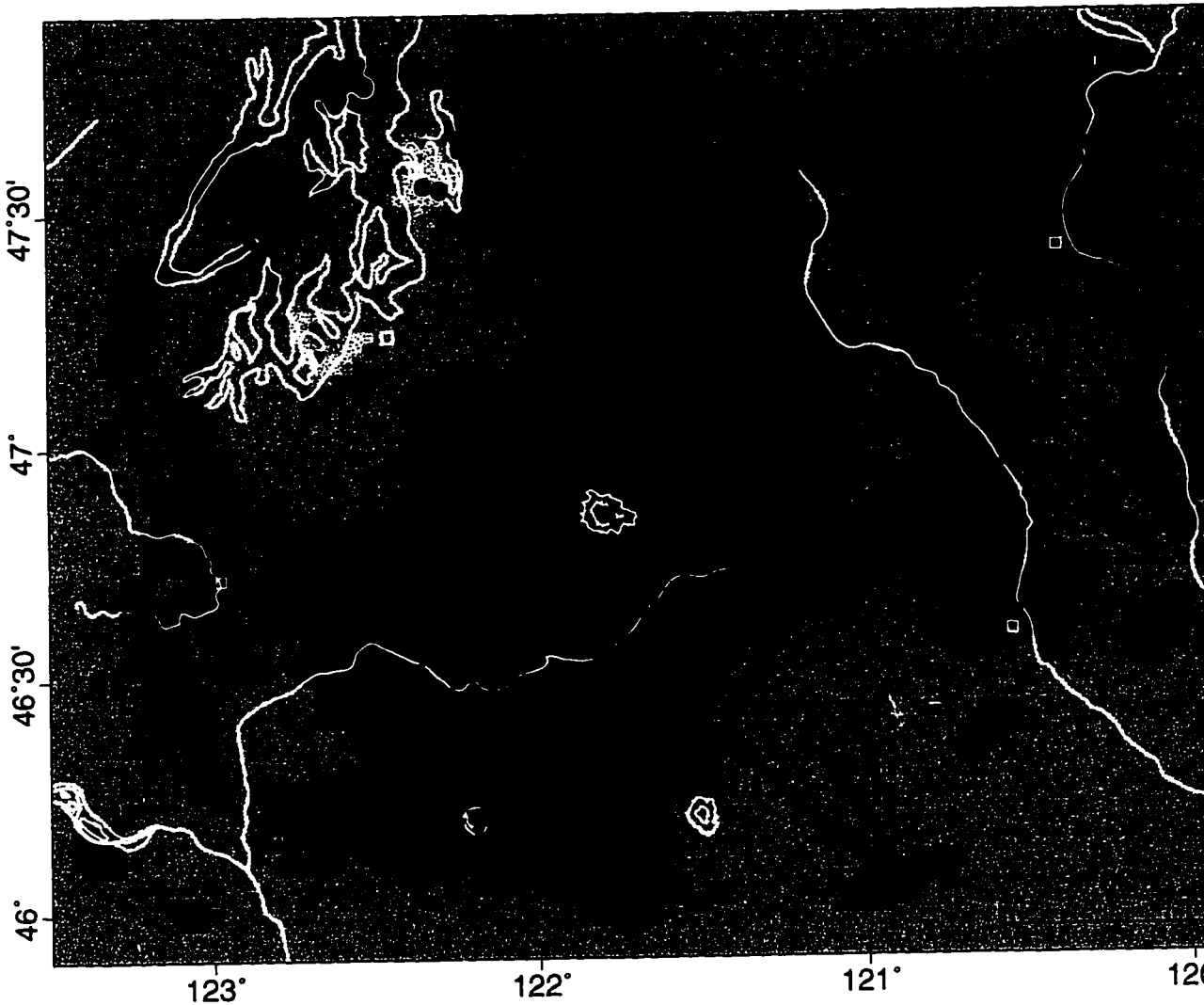
±0.25



Layer 3: 4 - 7 km

< 4.0
5.0
6.0
7.0

Velocity (km/sec)

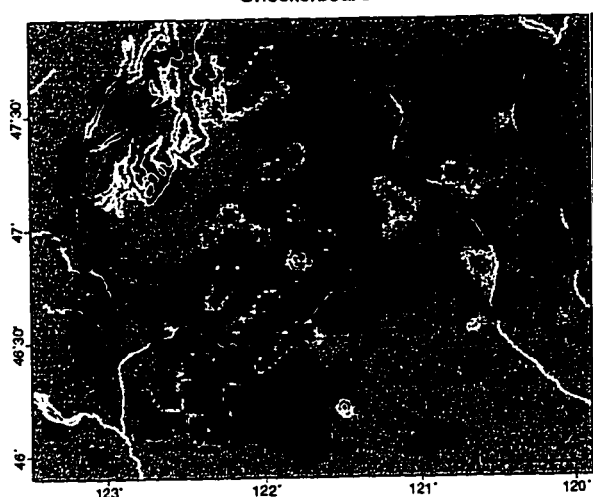


Checkerboard

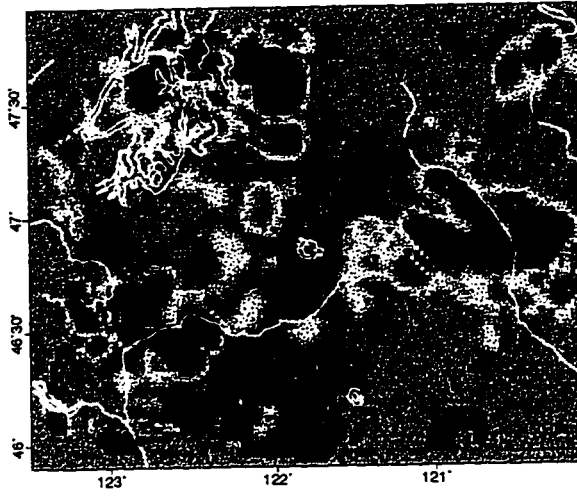
Jackknife Error

±0.01
±0.25

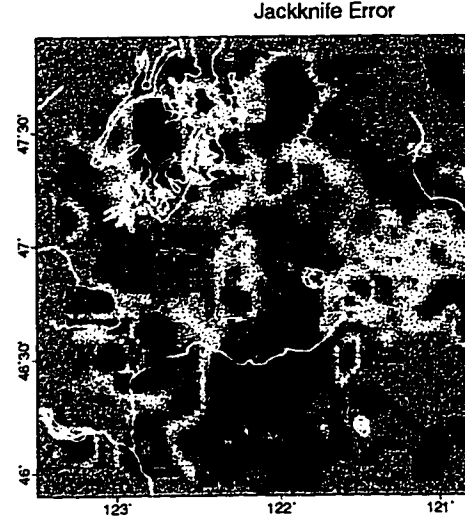
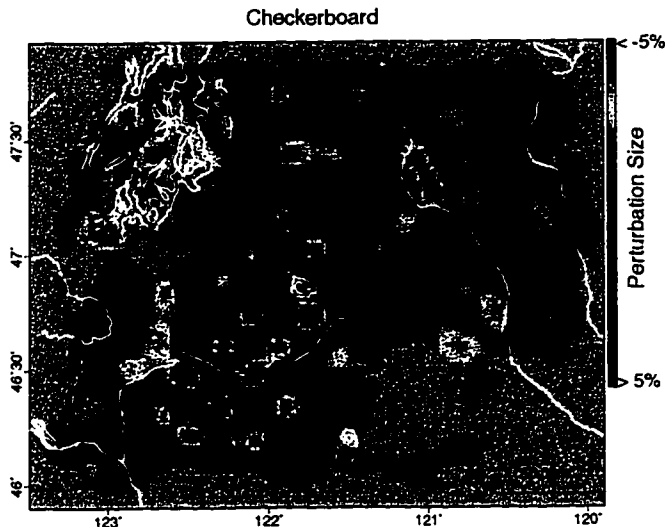
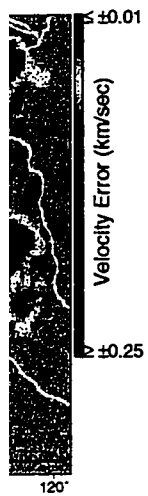
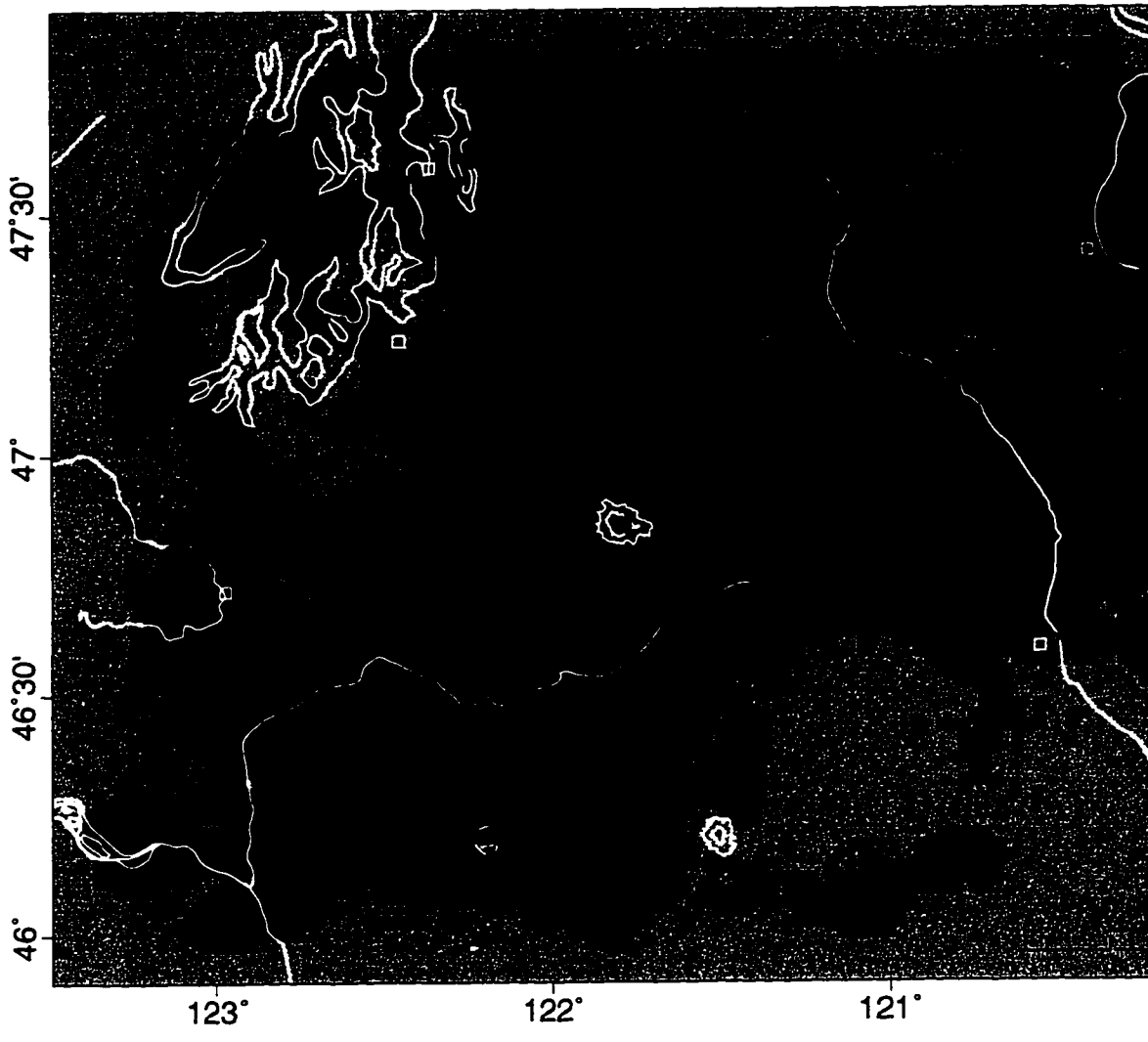
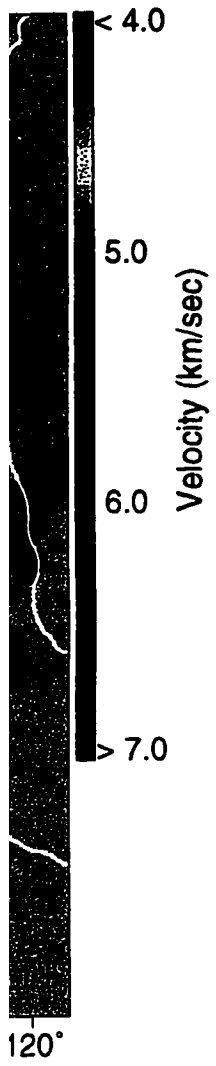
Velocity Error (km/sec)



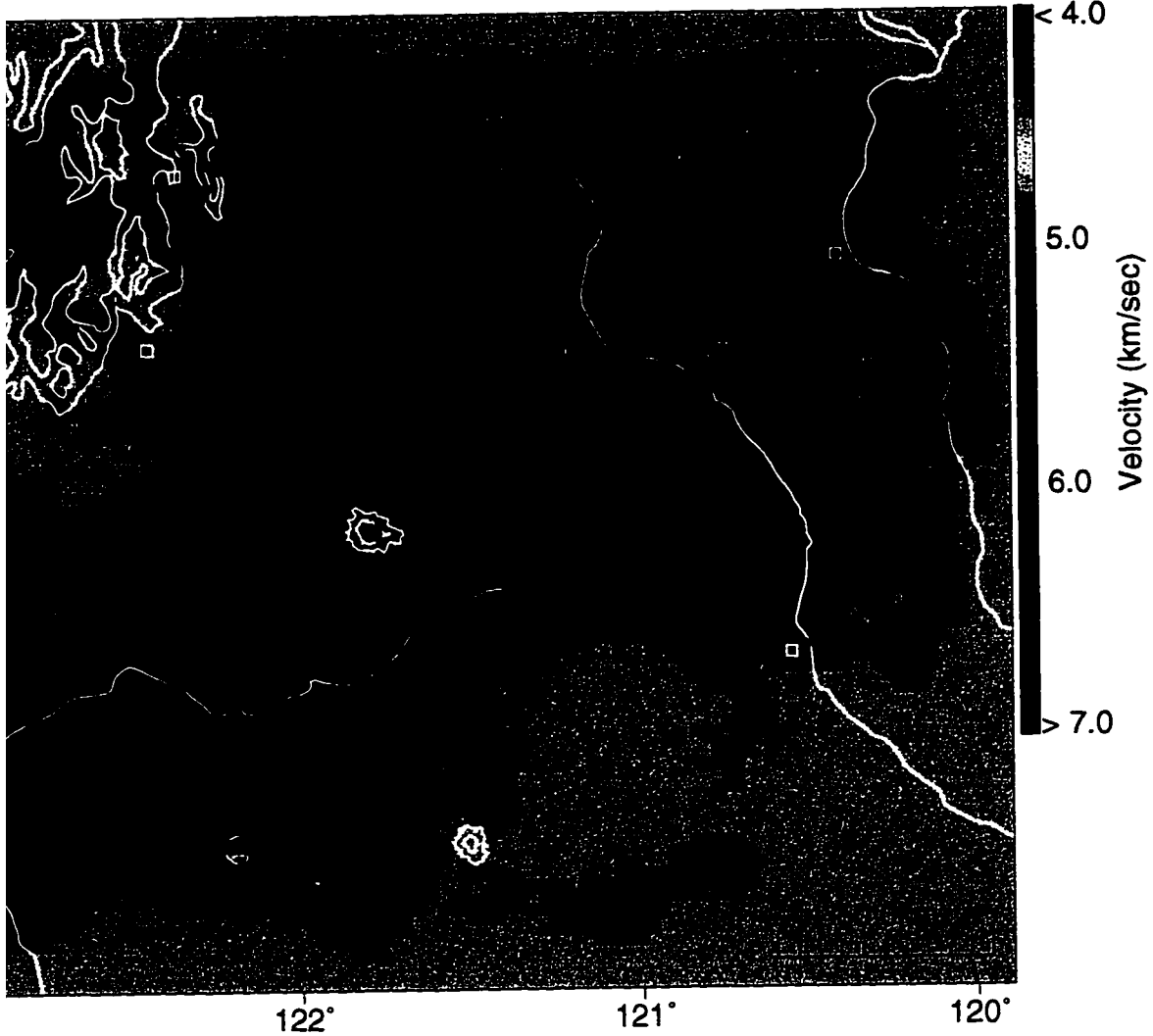
±5%
Perturbation Size
5%



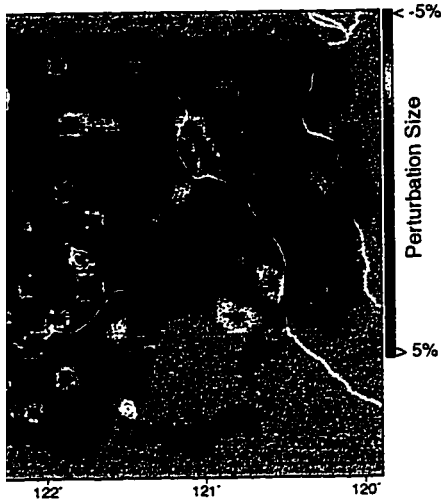
Layer 4: 7 - 10 km



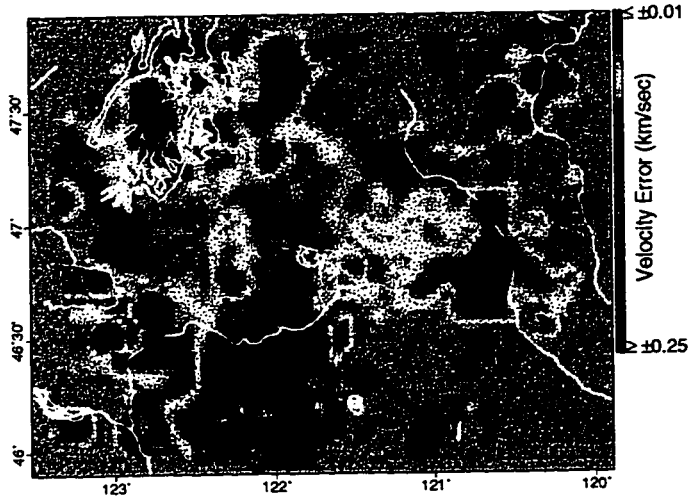
Layer 4: 7 - 10 km



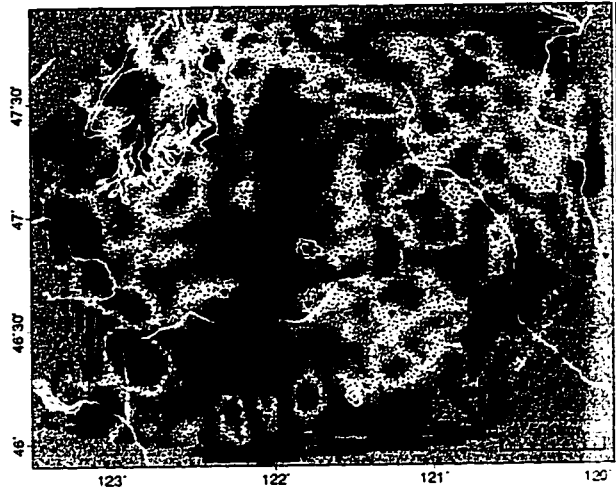
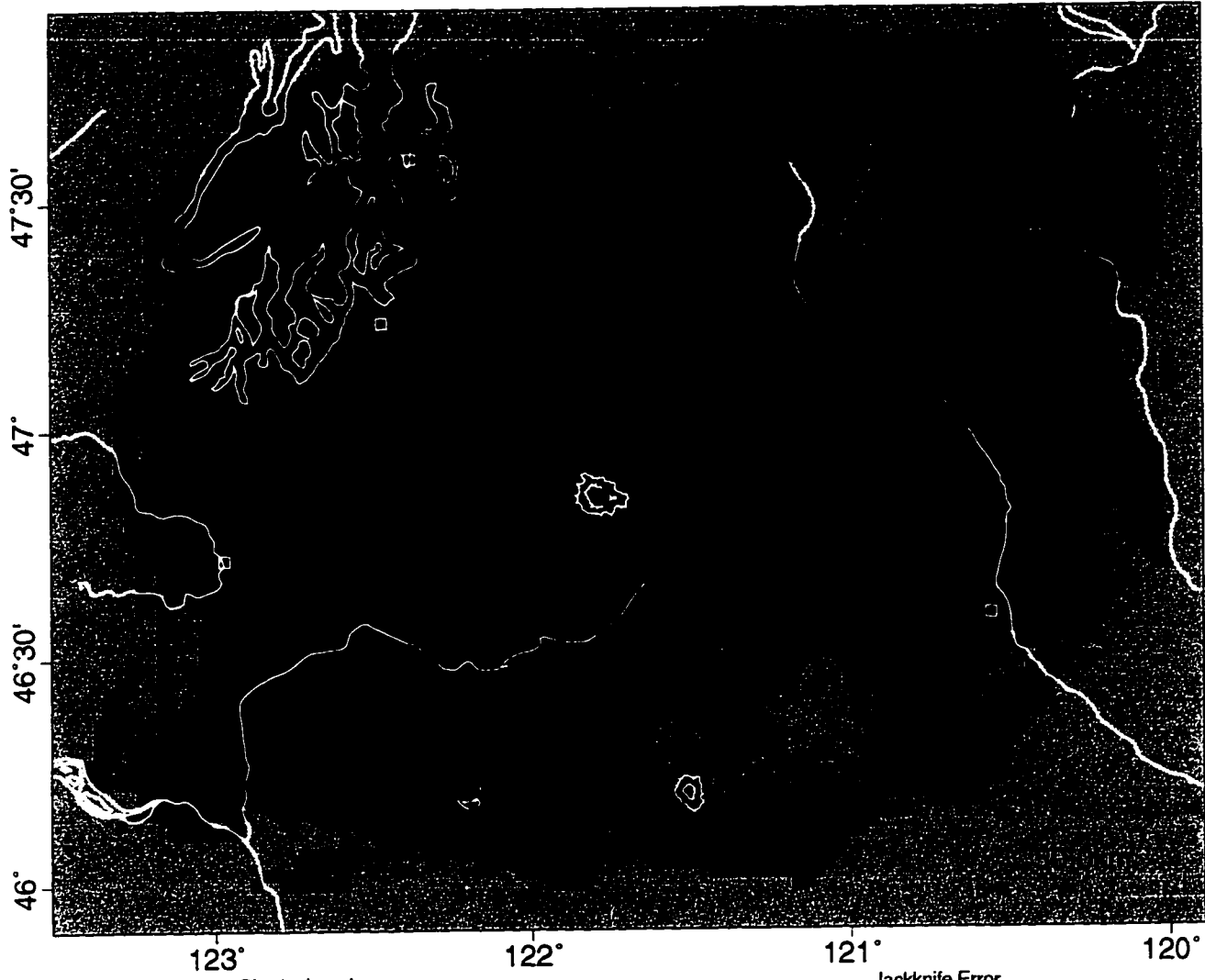
Checkerboard



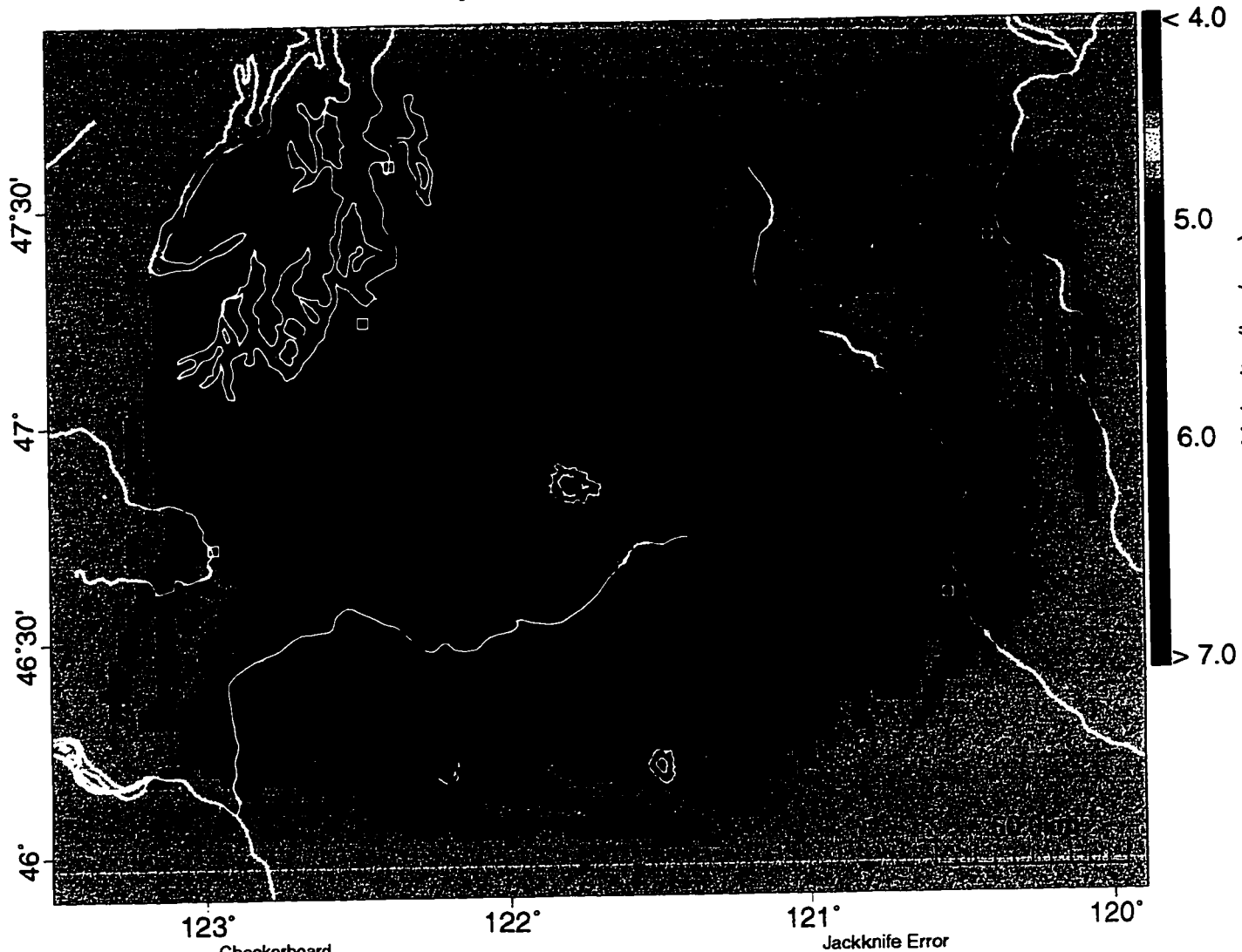
Jackknife Error



Layer 5: 10 - 14 km

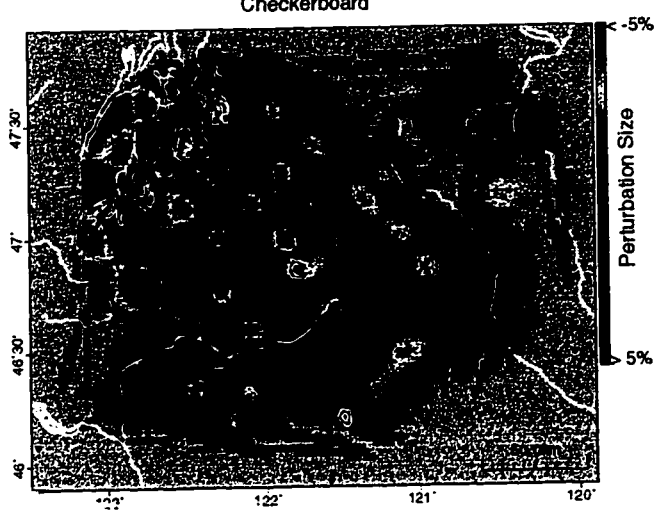


Layer 6: 14 - 18 km

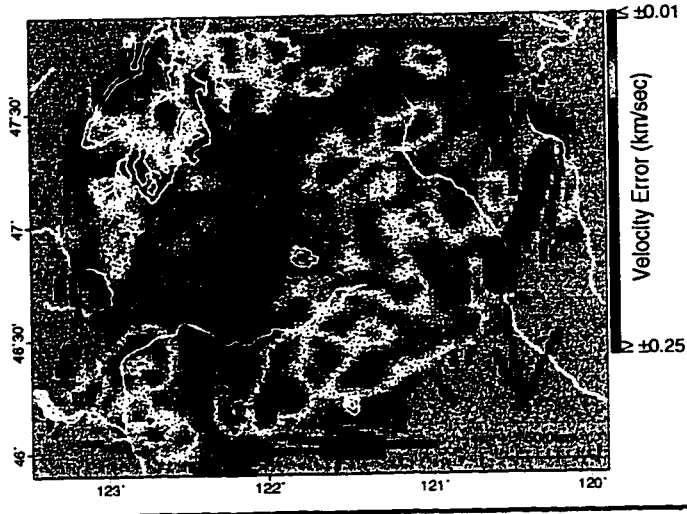


123° 122° 121° 120°
Checkerboard

Jackknife Error

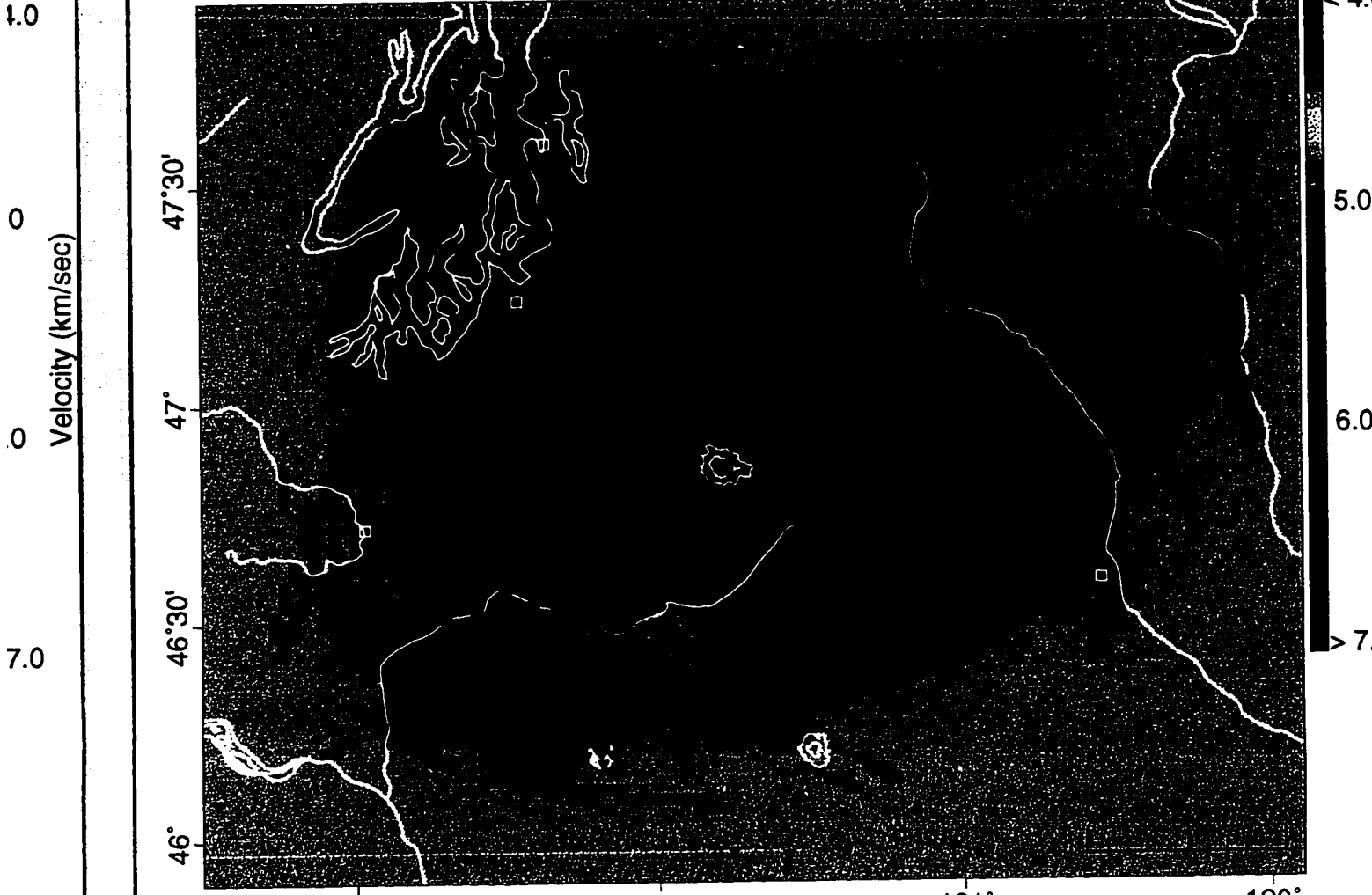


Perturbation Size



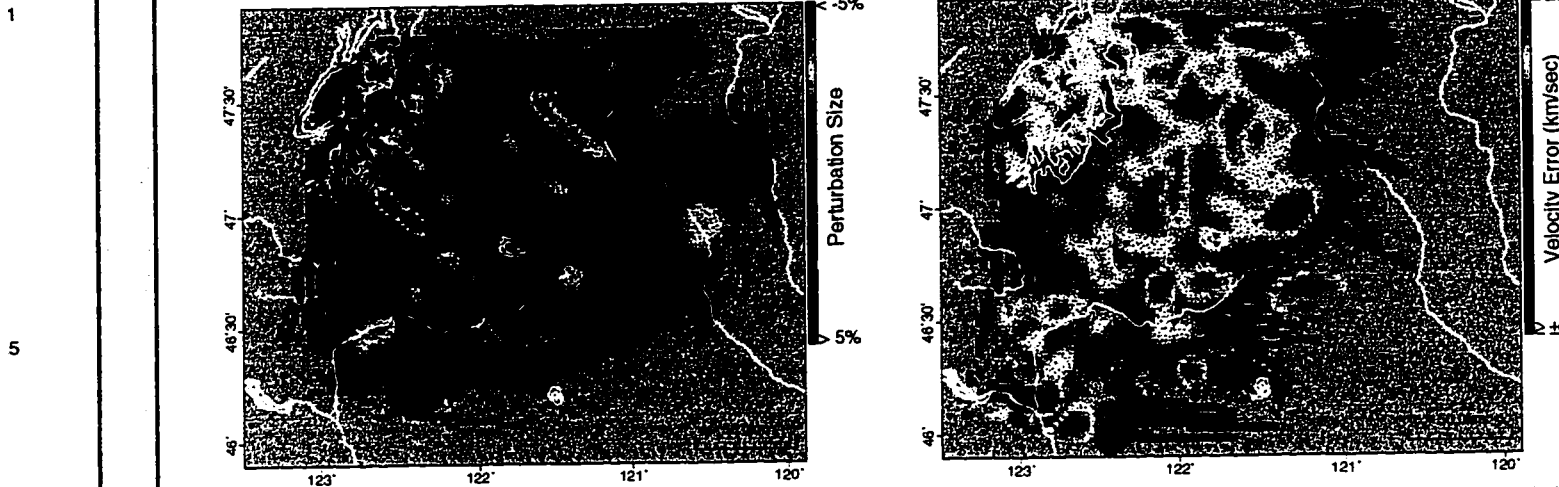
Velocity Error (km/sec)

Layer 7: 18 - 23 km



Checkerboard

Jackknife Error



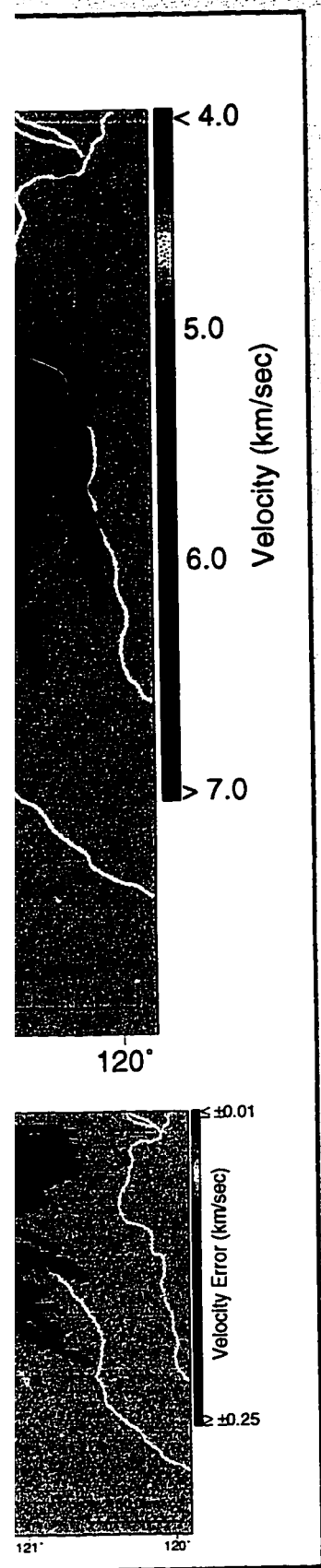


Plate 1: Seven horizontal slices through the velocity model discussed in Chapters IV. The figure is plotted using the program Xmap (Mantle, 1995)). The velocity scale for each layer is shown on the right. Velocities with values < 4.0 km/sec or > 7.0 km/sec are 'clipped', i.e. they are assigned the same value as the block with velocities of 4.0 or 7.0 km/sec. The yellow boxes in each layer are plots of the estimated resolution. The Checkerboard test (run using $\pm 10\%$ perturbations for checkers (each checker is 5 km \times 5 km) and $\pm 5\%$ perturbations with perturbations $> \pm 5\%$ clipped) and the estimated standard errors from the Jackknife test (run at 0.01 and 0.25 km/sec) (see Chapter II) are located in each layer are plotted as yellow boxes. The three dashed rectangular boxes in Layer 1 are related to the three cross-sectional profiles discussed in Chapter IV.

ven horizontal slices through the 3-D P-wave model discussed in Chapters IV and V (each plotted using the program Xmap8 (Lees, The velocity scale for each layer is identical. es with values < 4.0 km/sec or > 7.0 km/sec are ', i.e. they are assigned the same color as a with velocities of 4.0 or 7.0 km/sec. Beneath each e plots of the estimated resolution from the rboard test (run using $\pm 10\%$ perturbations kers (each checker is 5 km x 5 km), but plotted rturbations $> \pm 5\%$ clipped) and the esti- standard errors from the **Jackknife** test (clipped and 0.25 km/sec) (see Chapter II). Earthquakes in each layer are plotted as yellow circles. The dashed rectangular boxes in Layer 1 correspond three cross-sectional profiles discussed in r IV.